Study of the Transient Flow Behavior of Complex Fractures by Use of Semi-Analytical Models

by

Bailu Teng

A thesis submitted in partial fulfillment of the requirements for the degree of

Doctor of Philosophy

in

Petroleum Engineering

Department of Civil and Environmental Engineering
University of Alberta

ABSTRACT

Hydraulic fracturing treatment has been widely applied to enhance the well productivity in tight/shale formations, and history matching method is one of the most commonly used technique to help us obtain the information (e.g., fracture geometry and fracture conductivity) of the induced fractures. Due to the fact that the history matching work commonly requires running numerous fracture models to find the best match between the history production data and the simulated production data, it is highly necessary to work out a high computation-efficiency method to characterize the transient flow behavior of the hydraulic fractures in order to reduce the simulation time. Since the semi-analytical method has natural advantage in terms of computational efficiency, various semi-analytical models have been proposed in recent years to conduct the history matching work on the hydraulic fractures. At present, the existing semi-analytical models are normally developed for vertical planar fractures. However, due to the appearance of the complex stress field in the formations, a complex fracture can be induced after the fracturing treatment. This complex fracture can be a horizontal fracture (HF) with irregular geometry, a partially-penetrating-inclined fracture (PPIF), an orthogonal refracture, a reoriented refracture, or a non-uniform-width fracture. In order to conduct the history matching work on such complex fractures, it is imperative for us to develop the corresponding semi-analytical models to characterize the transient flow behavior of these complex fractures.

In this thesis, the author discretizes the complex fractures into small segments and characterizes the fluid flow in the fracture system with the numerical method (implicit finite difference method). Whereas, the fluid flow in the matrix system is characterized by an analytical method (Green function method). Coupling the numerical fracture flow equations with the analytical matrix flow equations yields the semi-analytical models for characterizing the transient flow

behavior of the complex fractures, including horizontal fractures, partially penetrating inclined fractures, reoriented refractures, and orthogonal refractures. Afterward, the author investigates the flow regimes that can be observed during the production period of the fractures by use of the proposed semi-analytical models. These flow regimes include wellbore after flow, fracture radial flow, bilinear flow, inclined formation linear flow, vertical elliptical flow, vertical pseudo-radial flow, inclined pseudo-radial flow, horizontal formation linear flow, horizontal elliptical flow, horizontal pseudo-radial flow, and boundary dominated flow. With the aid of these proposed models, the author also conducts history matching work on some real field cases to obtain the fracture conductivity and fracture dimension.

In addition, the author proposes a new fracture permeability model to characterize the relationship between the fracture permeability, fracture width, proppant-pack porosity, and proppant-pack permeability. The results calculated with the fracture permeability model show that the fluid flow in a fracture can be divided into viscous-shear dominated (VSD) regime, transition regime, and Darcy-flow dominated (DFD) regime. If Darcy parameter is sufficiently large, the effect of proppant-pack permeability on fracture permeability can be neglected and the fracture permeability can be calculated with viscous-shear-dominated fracture-permeability (VSD-FP) equation (i.e., $k_f = \beta_2 \phi_p w_f^2 / 12$), whereas, if Darcy parameter is sufficiently small, the effect of viscous shear on fracture permeability can be neglected and the fracture permeability can be calculated with the Darcy-flow-dominated fracture-permeability (DFD-FP) equation (i.e., $k_f = k_p$). Both the VSD-FP equation and DFD-FP equation are special forms of the proposed fracture permeability model.

PREFACE

This research is conducted under the guidance of my supervisor Dr. Huazhou Andy Li at the University of Alberta. The introduction in chapter 1, as well as the contributions and recommendations in chapter 7, are my original work.

Chapter 2 of this thesis is published as Teng, B. and Li, H. 2018. A Semi-Analytical Model for Characterizing the Pressure Transient Behavior of Finite-Conductivity Horizontal Fractures. *Transp. Porous. Med*. 123 (2): 367–402.

Chapter 3 of this thesis is published as Teng, B. and Li, H. 2018. Pressure Transient Behavior of Partially-Penetrating Inclined Fractures with a Finite conductivity. *SPE J.*, 24 (2):811-833.

Chapter 4 of this thesis is published as Teng, B., and Li, H. 2019. Transient Flow Behavior of Reoriented Refractures with the Consideration of the Interference from the Initial Fractures. *J. Petrol. Sci. Eng.*, 177: 921-940.

Chapter 5 of this thesis is published as Teng, B. and Li, H. 2019. A Semi-Analytical Model for Evaluating the Performance of a Refractured Vertical Well with an Orthogonal Refracture. *SPE J.*, 24 (2): 891-911.

Chapter 6 of this thesis is submitted to *SPE Journal* for peer review which is titled as A Novel Analytical Fracture Permeability Model Dependent on Both Fracture Width and Proppant-Pack Properties by Teng, B., Li, H., and Yu, H.

For the articles in Chapters 2 through 6, I was responsible for developing the models, writing code, analyzing data, and drafting manuscripts. Dr. Huazhou Andy Li was the supervisory author and was involved in the research and writing the manuscripts. For Chapter 6, Haisheng Yu constructs a fracture model with Comsol for validating the proposed fracture permeability model.

DEDICATION

This dissertation is dedicated to my parents.

ACKNOWLEDGMENTS

I would like to acknowledge Dr. Huazhou Andy Li for providing me the opportunity of studying at the University of Alberta and for his guidance throughout my Ph.D. study. I also thank him for the continuous support throughout my Ph.D. study;

I would also like to thank my committee members, Dr. Yongsheng Ma, Dr. Juliana Leung, Dr. Nobuo Maeda, Dr. Abhijit Dandekar, Dr. Ergun Kuru, and Dr. Huanzhou Li for sparing their precious time to review my dissertation and provide constructive comments;

I thank Dr. Zhehui Jin, Dr. William Zhang, and Dr. Lijun Deng for serving as my candidacy exam committee members;

I am heartily thankful to my parents and my wife whose continuous support helpes me overcome numerous obstacles during these years;

I am grateful to all my friends and colleagues that I have met in Canada. They enrich my life in Edmonton and help significantly expand my knowledge and vision; and

Last but not least, I would like to express my gratitude to China Scholarship Council (CSC) and Natural Science and Engineering Research Council (NSERC) for the financial support.

TABLE OF CONTENTS

LIST OF TABLES

LIST OF FIGURES

CHAPTER 1 INTRODUCTION

1.1 Background

Hydraulic-fracturing technology has been extensively applied to the low-permeability reservoirs to improve the reservoir productivity. History matching method is a commonly used technique to enhance our knowledge about the fluid and rock properties. Although the numerical simulation method is a powerful tool to conduct history matching work on different fracture patterns, it is normally more computationally demanding than the semi-analytical method. In recent years, many scholars have developed different semi-analytical approaches that are based on the Green function method to conduct the history matching work on different fracture patterns. Gringarten and Ramey (1973) derived the Green functions of different instantaneous sources under different boundary conditions. With the aids of these Green functions, Gringarten and Ramey (1974a) and Gringarten and Ramey (1974b) studied the pressure distribution within a reservoir that is induced by an infinite-conductivity vertical fracture and an infinite-conductivity horizontal fracture, respectively. By discretizing a vertical fracture into small planes, Rodriguez *et al*. (1984) developed a semi-analytical solution for characterizing the transient flow behavior of a vertical well intersecting with a partially penetrating fracture. Due to the presence of pre-existing natural fractures, a hydraulic fracturing treatment can create complex fracture networks. Zhou *et al*. (2014) introduced a semi-analytical approach to simulate the well performance from such complex fracture networks by use of the plane-source function. Yang *et al*. (2015) derived a slab-source function in the Laplace domain and applied this function to construct a semi-analytical model to evaluate the performance of a horizontal well with multiple fractures in tight formations. More studies about the semi-analytical method can be referred to Luo and Tang (2015), Chen *et al*. (2016), Jia *et al*. (2016), and Xiao *et al*. (2017). In addition to the above-mentioned fracture

patterns which can be well handled with the existing semi-analytical models, some complex fractures, such as horizontal fracture (HF), partially penetrating inclined fracture (PPIF), reoriented refracture, orthogonal refracture, and non-uniform width fracture (NUWF), can be frequently observed in the real field cases. However, we are still lacking the corresponding semi-analytical models to simulate the transient flow behavior of such complex fractures.

1.2 Literature Review

1.2.1 Horizontal Fracture (HF)

A hydraulic fracture always opens perpendicular to the least principal stress (Hubbert and Willis, 1957), which implies that the fractures are normally vertical because the horizontal stresses are typically less than the vertical stress. In practice, the HF, however, is far more common than what is generally believed. Field studies have shown that the HFs are frequently observed in shallow, tectonically-active and high-reservoir-pressure formations (Wahl and Campbell, 1963; Wahl, 1965; Chhina *et al*., 1987; Wright *et al*., 1997; Nicholl and Glass, 2001; Smith and Montgomery, 2015). There are heavy oil reservoirs in the south Fort McMurry (Alberta, Canada), locating at a depth of 250-300 m and having been widely hydraulically fractured; the fracturing treatments likely induce HFs in these reservoirs (AccuMap, 2013).

1.2.2 Partially Penetrating Inclined Fracture (PPIF)

Figure 1-1 shows two real field cases that a PPIF is observed. Figure 2a shows the microseismic events monitored from the 3rd stage fracturing treatment of Ridgewood-5 well (Johnson *et al*., 2010). The interpretation result of the microseismic map illustrates that a sub-horizontal fracture is induced after the fracturing treatment. This induced fracture has an inclination angle of 80^{o} corresponding to the vertical direction, and it has a length of 407 ft and a height of 59 ft. However, the target payzone is 68 ft thick, which is 9 ft larger than the fracture height, indicating

that this fracture is not only inclined but also partially penetrating. Figure 2b presents the downhole tiltmeter data of a fractured vertical well and the interpretation of these monitored data (Wright *et al*., 1998). As is shown in this figure, the interval of the two tilt peaks along the *Y*-axis represents the height of the fracture, indicating that this fracture's height is 160 ft, which is 120 ft less than the payzone thickness. In addition, the existence of the difference between these two peaks along *X*-axis demonstrates that the fracture is not perfectly vertical.

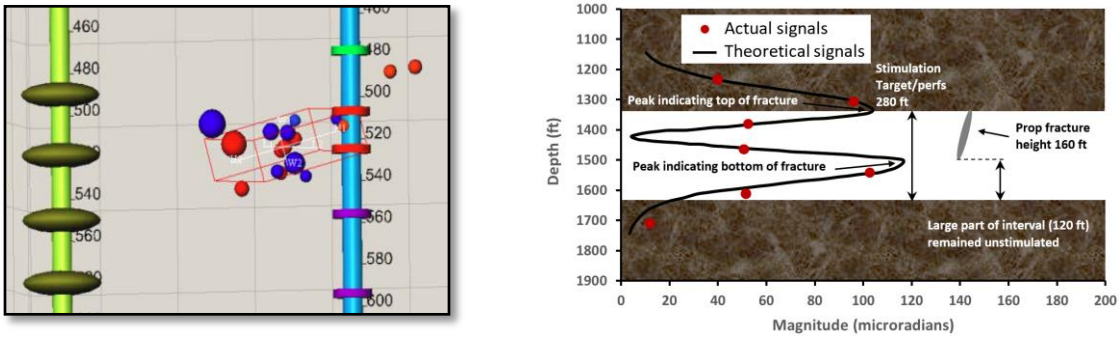

(a) (b)

Figure 1-1. Field examples where a PPIF is observed: (a) microseismic data show a PPIF with a significant inclination angle (adapted from Johnson *et al*., 2010); and (b) tiltmeter data show a PPIF with a poor growth along the inclined direction (adapted from Wright *et al*., 1998).

1.2.3 Reoriented Refracture

Field studies have shown that the stress in the formations frequently exhibits a non-uniform depletion due to the production of the initial fractures, leading to a stress reorientation region in the vicinity of these fractures (Wright, *et al*., 1994; Siebrits *et al*., 1998; Roussel and Sharma, 2012; Asalkhuzina *et al*., 2017; Xia *et al*., 2017). Thus, a refracturing treatment in this stress reorientation region can create a reoriented refracture which has a certain azimuth with respect to the initial fractures (Wright and Conant, 1995; Wolhart *et al*., 2007; Aghighi *et al*., 2009; Benedict and Miskimins, 2009; Xu *et al*., 2017). **Figure 1-2** illustrates the fracture orientations in the eastern part of the Lost Hills field, which is adapted from Wright *et al*. (1994). The shaded arcs represent the range of the fracture azimuths that were monitored over all of the fractured

wells, and the fracture in the elliptical box represents a reoriented refracture. As this figure shows, the orientations of the initial fractures are all close to an average azimuth of N55^{o}E, whereas the refracture exhibits a fracture azimuth around N85^{o}E.

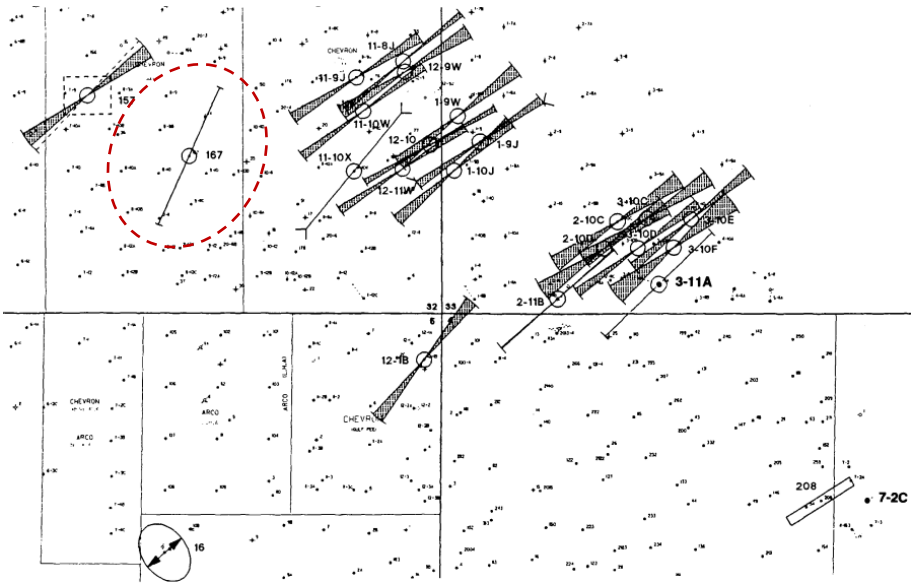

Figure 1-2. Fracture orientations in the eastern part of the Lost Hills field (adapted from Wright *et al*., 1994).

1.2.4 Orthogonal Refracture

The refracturing treatment has been widely used to repair or replace an inadequate initial fracturing treatment (Branch and Drennan, 1991; Lantz *et al*., 2007; Benedict and Miskimins, 2009; Potapenko *et al*., 2009; Ruhle, 2016). The existence of stress reorientation due to the production from a good initial fracture provides another motivation for the refracturing treatment (Wright *et al*., 1994; Siebrits *et al*., 1998; Aghighi *et al*., 2009; Roussel and Sharma, 2010; Zhao *et al*., 2016). Numerical simulations show that, during the production of a fractured vertical well, the stress parallel to the initial fracture will undergo a much faster reduction than that orthogonal to the initial fracture. If the stress changes due to the depletion of the formation pressure can overcome the effect of the initial horizontal stress deviator, the direction of the minimum horizontal stress will be turned into the direction of the maximum horizontal stress within an

elliptical area around the initial fracture. As such, a stress reversal region can be observed in the vicinity of the wellbore (Siebrits *et al*., 2000; Weng and Siebrits, 2007; Wolhart *et al*., 2007; Jiang *et al*., 2016; Gala and Sharma, 2017). As is generally acknowledged that the hydraulic fractures always propagate along the direction perpendicular to the direction of least principal stress (Hubbert and Willis, 1957; Daneshy, 1978; Medlin and Masse, 1984), a refracturing treatment on a fractured well with stress reversal region will probably result in an orthogonal refracture to the initial fracture.

1.2.5 Fracture Permeability

A hydraulic fracture is commonly packed with proppants, and the fracture permeability can be approximated with the proppant-pack permeability if the particle size is sufficiently small compared to the fracture width. **Table1-1** summarizes some of the equations that have been widely used to calculate the proppant-pack permeability (Carman, 1937; Krumbein and Monk, 1943; Carman, 1956; Berg, 1970; van Baaren, 1979; and Glover *et al*., 2006).

Table 1-1. Equations that can be used to calculate the proppant-pack permeability.

Name	Equation	Notes (the meanings and the units of the symbols are only used for the equations shown in this table)
Krumbein and Monk equation (Krumbein and Monk, 1943)	$k_p = 760D^2 \exp\left(-1.31\sigma_D\right)$	k_p = permeability, D D = geometric mean grain diameter, mm σ_D = standard deviation of grain size in phi units
Kozeny-Carman equation (Carman, 1937; Carman, 1956)	$k_p = \frac{cD^2\phi_p^3}{\left(1-\phi_p\right)^2}$	k_p = permeability, mD c = proportionality and unit factor, mD/mm^2 D = geometric mean grain diameter, mm ϕ_p = porosity

Berg equation (Berg, 1970)	$k_p = 80.8 \times 10^{-1.385\gamma} \times D^2 \phi_p^{5.1}$	k_p = permeability, D γ = sorting term in phi units D = geometric mean grain diameter, mm ϕ_p = porosity
van Baaren equation (van Baaren, 1979)	$k_p = 10 D_d^2 \phi_p^{(3.64+m)} C^{-3.64}$	k_p = permeability, mD D_d = dominant grain size, μm ϕ_p = porosity m = cementation exponent C = sorting index which ranges from 0.7 to 1.0
RGPZ equation (Glover *et al*., 2006)	$k_p = \frac{D^2 \phi_p^{3m}}{4am^2}$	k_p = permeability, m^2 D = geometric mean grain diameter, m ϕ_p = porosity a = parameter that equals to 8/3 for three dimensional samples composed of quasi-spherical grains m = cementation exponent

In practice, both the proppant-pack properties and the fracture width can exert their influences on the fracture permeability. This is espscially true for a propped NUWF, along which the permeability distribution can be significantly impacted by the fracture width as well as the proppant-pack. However, there is still no existing equation characterizing the relationship between the fracture permeability, the proppant-pack properties, and the fracture width.

1.2.6 Semi-Analytical Method

At present, there are three types of methods that can be used to characterize the transient flow behavior of a fracture, including analytical methods, semi-analytical methods, and numerical methods. In practice, the analytical methods are only applicable to characterize the transient flow behavior of simple field cases, such as linear flow, radial flow, or infinite conductivity fractures (Cinco-Ley and Samaniego-V, 1981; Rodriguez *et al*., 1984). However, for the scenarios of complex fractures, the analytical methods are normally not applicable anymore. Although the

numerical method can be used to simulate the transient flow behavior of complex fractures, it can be not so attractive to use the numerical method to conduct history matching work on a complex fracture. This is because conducting history matching work may require constructing and solving hundreds of fracture models to find the best match between the simulated data and the field data. Using the numerical method to construct and solve so many fracture models can be very time-consuming. The semi-analytical method is a combination of the analytical method and the numerical method. In the semi-analytical method, we only need to discretize the fracture system. Therefore, using the semi-analytical method to construct complex fracture models can be more convenient than using the numerical method. In addition, since only the fracture system is discretized, compared to the numerical method, the semi-analytical method requires building and solving much fewer linear equations at each timestep to characterize the transient flow behavior. However, at present, there are still no available semi-analytical models to characterize the transient flow behavior of the HF, PPIF, reoriented refracture, and orthogonal refracture.

1.3 Problem Statements

The following technical problems require to be addressed in this thesis:

- The complex fractures, such as HF, PPIF, reoriented refracture, and orthogonal refracture, can be frequently observed in the real filed cases. But we are still lacking the corresponding semi-analytical models to characterize the transient flow behavior of these fractures;
- Recognizing the flow regimes of a fracture can help us determine the fracture pattern. However, the flow regimes that can be observed during the production of an HF or PPIF have not been reported in the previous studies; and
- Since both the fracture width and the proppant-pack properties can impact the fracture permeability, it can be inaccurate to approximate the fracture permeability with a constant

value of the proppant-pack permeability. At present, there is no available fracture permeability model that accounts for the influences of the fracture width and proppant-pack properties on the fracture permeability.

1.4 Objectives

In this research, the author aims to develop a series of semi-analytical models to simulate the transient flow behavior of various complex fractures. The overall research objectives are listed as follows:

- Develop the semi-analytical models for modeling complex fractures, including HF, PPIF, reoriented refracture, and orthogonal refracture. As such one can utilize these proposed models to conduct the history matching work on these complex fractures;
- Recognize the flow regimes that can be observed during the production of HFs and PPIFs. These recognized flow regimes can help us determine whether a fracture is an HF or a PPIF; and
- Develop a fracture permeability model that can account for the influences of viscous shear and proppant-pack properties on the fracture permeability.

1.5 Thesis Structure

The structure of this paper-based dissertation can be summarized as follows:

In Chapter 1, the author introduces the background, literature review of complex fractures, problem statements, objectives, and thesis structure. Chapter 2 includes a semi-analytical model for characterizing the transient flow behavior of HFs. With the aid of this model, the author investigates the flow regimes that can be observed during the production of HFs. The author also studies the skin factors that are induced by the HFs. In Chapter 3, the author proposes a semi-analytical model to study the pressure transient behavior of PPIF. This model is applicable to the

scenarios that the fracture pattern cannot be determined a priori. By use of this proposed model, the author conducts history matching work on a real field case to obtain the fracture dimensions and fracture conductivity. The production of the fluid from the initial fracture can induce stress change in the fields. In such case, if the refracture treatment is conducted in the vicinity of the initial fracture we can obtain a reoriented refractures, whereas, if the refracturing treatment is conducted on the initial fractures, we can obtain an orthogonal refracture. In Chapters 4 and 5, the author develops semi-analytical models to evaluate the performance of reoriented refractures and orthogonal refractures, respectively. In practice, the fracture width can be non-uniform along the propagation direction of the fractures, and in Chapter 6, the author hence proposes a new fracture permeability model to calculate the fracture permeability which is a function of the fracture width as well as proppant-pack properties. Chapter 7 includes the contributions out of this research and recommendations for future research.

1.6 References

AccuMap, IHS, 2013.

Aghighi, M.A., Rahman, S.S., and Rahman, M.M. 2009. Effect of Formation Stress Distribution on Hydraulic Fracture Reorientation in Tight Gas Sands. Paper SPE 122723 presented at Asia Pacific Oil and Gas Conference & Exhibition, Jakarta, Indonesia, 4-6 August.

Asalkhuzina, G.F., Davletbaev, A.Ya., Fedorov, A.I., Yuldasheva, A.R., Efremov, A.N., Sergeychev, A.V., and Ishkin, D.Z. 2017. Identification of Refracturing Reorientation using Decline-Analysis and Geomechanical Simulator. Paper SPE 187750 presented at SPE Russian Petroleum Technology Conference, Moscow, Russia, 16-18 October.

Benedict, D., and Miskimins, J.L. 2009. The Effects of Hydraulic Fracture Reorientation. Paper SPE 119355 presented at SPE Hydraulic Fracturing Technology Conference, The Woodlands, Texas, 19-21 January.

Berg, R.R. 1970. Method for Determining Permeability from Reservoir Rock Properties. *Trans. GCAGS* 20: 303-335.

Branch, G.A., and Drennan, K.M. 1991. Refracture Stimulations in the Norge Marchand Unit: A Case Study. Paper SPE 21642 presented at SPE Production Operations Symposium, Oklahoma City, Oklahoma, 7-9 April.

Brown P.R. 1981. A Non-Interactive Method for the Automatic Generation of Finite Element Meshes Using the Schwarz-Christoffel Transformation. *Comput. Methods Appl. Mech. Eng.* 25 (1): 101-126.

Carman, P.C. 1937. Fluid Flow through Granular Beds. *Trans. IChemE* 75: 32-48.

Carman, P.C. 1956. *Flow of Gases through Porous Media*. Butterworths, London.

Cinco-Ley, H., and Samaniego-V., F. 1981. Transient Pressure Analysis for Fractured Wells. *J. Pet. Tech.* 33 (9) 1749-1766.

Daneshy, A.A. 1978. Hydraulic Fracture Propagation in Layered Formations. *SPE J.* 18 (1) 33-41.

Gala, D.P., and Sharma, M.M. 2017. Effect of Fluid Type and Composition on Changes in Reservoir Stresses Due to Production: Implications for Refracturing. Paper ARMA-2017-0042 presented at 51st U.S. Rock Mechanics/Geomechanics Symposium, San Francisco, California, USA, 25-28 June.

Glover, P.W., Zadjali, I.I., and Frew, K.A. 2006. Permeability Prediction from MICP and NMR Data Using an Electro-Kinetic Approach. *Geophysics* 71(4): 49-60.

Hubbert, M.K., and Willis, D.G. 1957. Mechanics of Hydraulic Fracturing. *Trans. AIME* 210: 153-168.

Jiang, W., Cai, B., Li, Y., He, C., Yan, X., and Xu, Z. 2016. Optimum Time and Critical Re-Orientation Pressure of Re-Fracturing. Paper SPE 181837 presented at SPE Asia Pacific Hydraulic Fracturing Conference, Beijing, China, 24-26 August.

Johnson, R.L., Scott, M.P., Jeffrey, R.G., Chen, Z., Bennett, L., Vandenborn, C.B., and Tcherkashnev, S. 2010. Evaluating Hydraulic Fracture Effectiveness in a Coal Seam Gas Reservoir from Surface Tiltmeter and Microseismic Monitoring. Paper SPE 133063 presented at SPE Annual Technical Conference and Exhibition, Florence, Italy, 19-22 September.

Krumbein, W.C. and Monk, G.D. 1943. Permeability as a Function of Size parameters of Unconsolidated Sand. *Trans. AIME* 151 (1): 153-163.

Lantz, T.G., Greene, D., Eberhard, M., Norrid, S., and Pershall, R. 2007. Refracture Treatments Proving Successful In Horizontal Bakken Wells: Richland Count, Montana. Paper SPE 108117 presented at Rocky Mountain Oil & Gas Technology Symposium, Denver, Colorado, U.S.A., 16-18 April.

Medlin, W.L., and Masse, L. 1984. Laboratory Experiments in Fracture Propagation. *SPE J.* 24 (03): 256-268.

Nicholl, M.J., and Glass, R.J. 2001. Simulation of Immiscible Viscous Displacement within the Plane of a Horizontal Fracture. Paper ARMA-01-0205 presented at the 38th U.S. Symposium on Rock Mechanics (USRMS), Washington, D.C., 7-10 July.

Potapenko, D.I., Tinkham, S.K., Lecerf, B., Fredd, C.N., Samuelson, M.L., Gillard, M.R., Le Calvez, J.H., and Daniels, J.L. 2009. Barnett Shale Refracture Stimulations Using a Novel Diversion Technique. Paper SPE 119636 presented at SPE Hydraulic Fracturing Technology Conference, The Woodlands, Texas, 19-21 January.

Rodriguez, F., Horne, R.N., and Cinco-Ley, H. 1984. Partially Penetrating Fractures: Pressure Transient Analysis of an Infinite Conductivity Fracture. Paper SPE 12743 presented at SPE California Regional Meeting, Long Beach, California, 11-13 April.

Roussel, N.P., and Sharma, M.M. 2010. Quantifying Transient Effects in Altered-Stress Refracturing of Vertical Wells. *SPE J.* 15 (3): 770-782.

Roussel, N.P., and Sharma, M.M. 2012. Role of Stress Reorientation in the Success of Refracture Treatments in Tight Gas Sands. *SPE Prod. Oper.* 27 (4): 346-355.

Ruhle, W. 2016. Refracturing: Empirical Results in the Bakken Formation. Paper URTEC 2461740 presented at Unconventional Resources Technology Conference, San Antonio, Texas, USA, 1-3 August.

Siebrits, E., Elbel, J.L., Detournay, E., Detouray-Piette, C., Christianson, M., Robinson, B.M., and Diyashev, I.R. 1998. Parameters Affecting Azimuth and Length of a Secondary Fracture During a Refracture Treatment. Paper SPE 48928 presented at SPE Annual Technical Conference and Exhibition, New Orleans, Louisiana, 27-30 September.

Siebrits, E., Elbel, J.L., Hoover, R.S., Diyashev, I.R., Griffin, L.G., Demntrius, S.L., Wright, C.A., Davidson, B.M., Steinsberger, N.P., and Hill, D.G. 2000. Refracture Reorientation Enhances Gas Production in Barnett Shale Tight Gas Wells. Paper SPE 63030 presented at SPE Annual Technical Conference and Exhibition, Dallas, Texas, 1-4 October.

Singh, K., and Whitson, C.H. 2010. Gas-Condensate Pseudopressure in Layered Reservoirs. *SPE Res. Eval. Eng*. 13 (02): 203-213.

Smith, M.B., and Montgomery, C. 2015. *Hydraulic Fracturing.* CRC Press.

van Baaren, J.P. 1979. Quick-Look Permeability Estimates Using Sidewall Samples and Porosity Logs. Transaction of the 6th Annual European Logging Symposium, Society of Professional Well Log Analysts.

van Everdingen, A.F., and Hurst, W. 1949. The Application of the Laplace Transformation to Flow Problems in Reservoirs. *Trans. AIME* 1 (12): 305-324.

Wahl, H.A., and Campbell, J.M. 1963. Sand Movement in Horizontal Fractures. *SPE J.* 15 (11): 1239-1246.

Weng, X., and Siebrits, E. 2007. Effect of Production-Induced Stress Field on Refracture Propagation and Pressure Response. Paper SPE 106043 presented at SPE Hydraulic Fracturing Technology Conference, College Station, Texas, U.S.A., 29-31 January.

Wolhart, S.L., and Mclntosh, G.E., Zoll, M.B., and Weijers, L. 2007. Surface Tiltmeter Mapping Shows Hydraulic Fracture Reorientation in the Codell Formation, Wattenberg Field,

Colorado. Paper SPE 110034 presented at SPE Annual Technical Conference and Exhibition, Anaheim, California, U.S.A., 11-14 November.

Wolhart, S.L., Mclntosh, G.E., Zoll, M.B., and Weijers, L. 2007. Surface Tiltmeter Mapping Shows Hydraulic Fracture Reorientation in the Codell Formation, Wattenberg Field, Colorado. Paper SPE 106043 presented at SPE Hydraulic Fracturing Technology Conference, College Station, Texas, U.S.A., 29-31 January.

Wright, C.A., and Conant, R.A. 1995. Hydraulic Fracture Reorientation in Primary and Secondary Recovery from Low-Permeability Reservoirs. Paper SPE 30484 presented at SPE Annual Technical Conference and Exhibition, Dallas, Texas, 22-25 October.

Wright, C.A., Conant, R.A., Stewart, D.W., and Byerly, P.M. 1994. Reorientation of Propped Refracture Treatments. Paper SPE 28078 presented at Rock Mechanics in Petroleum Engineering, Delft, Netherlands, 29-31 August.

Wright, C.A., Davis, E.J., Golich G.M., Ward, J.F., Demetrius, S.L., Minner, W.A., and Weijers, L. 1998. Downhole Tiltmeter Fracture Mapping: Finally Measuring Hydraulic Fracture Dimensions. Paper SPE 46194 presented at SPE Western Regional Meeting, Bakersfield, California, 10-13 May.

Wright, C.A., Davis, E.J., Weijers, L., Minner, W.A., Hennigan, C.M., and Golich, G.M. 1997. Horizontal Hydraulic Fractures: Oddball Occurrences or Practical Engineering Concern? Paper SPE 38324 presented at SPE Western Regional Meeting, Long Beach, California, 25-27 June.

Xia, K., Mondal. S., Fonseca, E., and Jones, R. 2017. Understanding Stress Reorientation Process in Shale Gas Play and Its Impact on Refracturing Time Window. Paper ARMA-2017-1012 presented at 51st U.S. Rock Mechanics/Geomechanics Symposium, San Francisco, California, USA, 25-28 June.

Xu, Y., Yu, W., and Sepehrnoori, K. 2017. Modeling Dynamic Behaviors of Complex Fractures in Conventional Reservoir Simulators. Paper URTEC-2670513 presented at SPE/AAPG/SEG Unconventional Resources Technology Conference, Austin, Texas, USA, 24-26 July.

Yu, W., Wu, K., and Sepehrnoori, K. 2016. A Semianalytical Model for Production Simulation from Nonplanar Hydraulic-Fracture Geometry in Tight Oil Reservoirs. *SPE J.* 21 (3) 1028-1040.

Zhao, B., Zhang, G., and Lin, Q. 2016. The Application of Cryogenic Treatment during Refracture Process - Laboratory Studies. Paper ARMA-2016-552 presented at 50th U.S. Rock Mechanics/Geomechanics Symposium, Houston, Texas, 26-29 June.

CHAPTER 2 A SEMI-ANALYTICAL MODEL FOR CHARACTERIZING THE PRESSURE TRANSIENT BEHAVIOR OF FINITE-CONDUCTIVITY HORIZONTAL FRACTURES

A version of this chapter has been published in *Transport in Porous Media*.

Summary

Hydraulic fracturing may induce horizontal fractures in shallow, tectonically-active or high-reservoir-pressure formations. Studying the pressure transient behavior of the horizontal fractures can provide insights into the size and shape of the formations as well as their productivities. However, our knowledge about the pressure transient behavior of a horizontal fracture is far from adequate. In this study, a semi-analytical model is proposed to characterize the pressure transient behavior of finite-conductivity horizontal fractures in bounded reservoirs. Specifically, we discretize the horizontal fracture into rectangle plane elements, each of which is treated as a plane source (in this work, a plane source indicates a rectangle plane, and the oil flows from the matrix to this plane). The transient flow in the fracture systems can be numerically characterized with the finite difference method, whereas the transient flow in the matrix system can be analytically simulated with the Green function method; as such, the flow behavior both in the fracture and matrix can be modeled. Subsequently, we construct the mathematical model by coupling the finite-difference formulations for the fracture system and the analytical functions for the matrix system. This semi-analytical model is arranged into a matrix format and can be readily solved with the Gaussian elimination method. The key features of the proposed approach can be summarized as: it can model an irregular horizontal fracture by discretizing the horizontal fracture into small elements, such that the real fracture configuration can be better captured; the fracture conductivity can be taken into consideration, and the non-uniform influx distribution along the fracture can be modeled to better honor the actual flow behavior from the matrix to the fracture. We also apply the semi-analytical method to analyze the flow regimes of single-phase oil flow from a circular horizontal fracture and an elliptical horizontal fracture in a bounded reservoir; the flow regimes such as wellbore after flow, bilinear flow, formation linear flow, early

pseudo-radial flow, late pseudo-radial flow, elliptical flow, and boundary dominated flow can be observed during oil production. In addition, we examine the influences of formation thickness, fracture's vertical position, fracture conductivity, and wellbore storage on the pressure dynamics of a circular horizontal fracture. It is found that the early pseudo-radial flow results from two different flow scenarios: one is near the edge of the horizontal fracture when the formation thickness is small, while the other one is surrounding the horizontal fracture in the vertical direction when the formation thickness is sufficiently large. The wellbore storage mainly exerts influences on the early production period, and its duration tends to be longer as the fracture conductivity decreases. Furthermore, the flow regimes and pseudoskin factor are comprehensively investigated for an elliptical horizontal fracture and an irregular-shaped horizontal fracture that may be induced by the stress heterogeneity in the reservoirs.

Keywords: Horizontal fracture; Pressure transient behavior; Semi-analytical model; Finite conductivity; Non-uniform flux; Irregular geometry

Keywords: Horizontal fracture; Pressure transient behavior; Semi-analytical model; Finite conductivity; Non-uniform flux; Irregular geometry

2.1 Introduction

Hydraulic-fracturing technology has been widely applied to the low-permeability reservoirs to improve the oil and gas productivity. Pressure transient analysis (PTA) is a commonly used tool to enhance our understanding about the flow behavior of hydraulically fractured wells in these reservoirs and help the industries evaluate their well performances. Numerical simulation is a powerful tool for characterizing the transient flow behavior of different fracture patterns. However, it is normally more computationally demanding than the analytical/semi-analytical

method. In the past, many scholars have developed different analytical and semi-analytical approaches to conduct PTA on different fracture patterns.

Gringarten and Ramey (1974) modeled the unsteady-state pressure distribution from a single infinite-conductivity vertical fracture in horizontally infinite reservoirs. The vertical fracture is divided into small segments, and each segment is assumed as a uniform flux source. By coupling the transient flow in the fractures and that in the reservoir matrix, Cinco-Ley *et al*. (1978) developed a vertical fracture model which can take the fracture conductivity into consideration. In the unconventional reservoirs, a complex fracture network may ensue after the fracturing treatment due to the presence of stress anisotropy and pre-existing natural fractures; following this scenario, Zhou *et al*. (2014) proposed a semi-analytical approach to simulate the production from complex fracture networks by use of a plane-source function. Yang *et al*. (2015) evaluated the performance of horizontal well with multiple fractures by using a slab-source function in Laplace domain; in their method, the fracture configuration can be better characterized by discretizing the fracture into thin slabs. Chen *et al*. (2016) investigated the pressure response of multiple-stage fractured horizontal well with secondary-fracture networks; in their work, the transient flows in natural fractures, hydraulic fractures, and reservoir matrix are coupled to construct a semi-analytical solution. Besides, there are numerous analytical/semi-analytical methods that can provide us with the pressure transient information about various vertical fracture models, such as bi-wing fractures, multi-stage hydraulic fractures and fracture networks (Warren and Root, 1963; Gringarten and Ramey, 1974; Cinco-Ley and Samaniego-V, 1981; Chen, 1990; Chen *et al*., 1991; Ozkan and Raghavan, 1991; Chen and Raghavan, 1997; Valko and Amini, 2007; Brown *et al*., 2009; Ozkan *et al*., 2011).

A hydraulic fracture always opens perpendicular to the least principal stress (Hubbert and Willis, 1957), which implies that the fractures are normally vertical because the horizontal stresses are typically less than the vertical stress. In practice, the horizontal hydraulic fracture, however, is far more common than what is generally believed. Field studies have shown that, the horizontal fractures are frequently observed in shallow, tectonically-active and high-reservoir-pressure formations (Wahl and Campbell, 1963; Wahl, 1965; Chhina *et al*., 1987; Wright *et al*., 1997; Nicholl and Glass, 2001; Smith and Montgomery, 2015). There are heavy oil reservoirs in the south Fort McMurry (Alberta, Canada), locating at a depth of 250-300 m and having been widely hydraulically fractured; the fracturing treatments likely induce horizontal fractures in these reservoirs (AccuMap, 2013). Conducting PTA on the horizontal fractures is very important for the industries to accurately assess the productivity of such fractures. Unfortunately, there have been very limited studies dedicated to thoroughly understanding the pressure transient behavior of a horizontal fracture. Gringarten and Ramey (1974) presented a pressure transient solution for a circular horizontal fracture with uniform influx and infinite conductivity in an unbounded reservoir; their model could accommodate the effects including partial penetration and restricted entry. But their assumption of uniform influx into the fracture will cease to be physically meaningful when the boundary effect cannot be neglected. Valko and Economides (1997) introduced a semi-analytical method to model the pressure response of a circular horizontal fracture in a horizontally infinite reservoir, and the influx difference can be considered by integrating the withdrawal rates along the radius of the fracture. However, this method also bears stringent restrictions because it requires the fracture being exactly circular, which is over idealized especially for the reservoirs where the stress heterogeneity is present. Although further knowledge about PTA of horizontal fractures can also be found in Ogunsanya *et al*. (2006) and

Larsen (2011), their models require that the fractures are either rectangle or circular; such requirement restricts the applications of their methods in modeling the horizontal fracture with irregular geometries. In addition, the assumption of uniform influx distribution in their models will lead to inaccurate results of the PTA of the horizontal fractures with low or moderate fracture conductivity. It is thus of significant importance to develop a more inclusive semi-analytical model that can well capture the flow dynamics of horizontal fractures.

In this work, we introduce a semi-analytical method to model the pressure transient behavior of horizontal fractures that have arbitrary geometries. Besides, the non-uniform influx distribution along the fracture and the fracture conductivity have also been accounted for in the semi-analytical method in order to better honor the reality. We first validate our method against Eclipse on an irregular horizontal fracture model. Subsequently, we apply the semi-analytical method to analyze the flow regimes of single phase oil flow from the horizontal fractures in a bounded reservoir. The major flow regimes are successfully distinguished from the calculation results. Sensitivity analysis is further conducted to investigate the influences of the following factors on the pressure transients of a circular horizontal fracture: formation thickness, fracture's vertical position, fracture conductivity, and wellbore storage. Additionally, the pressure response and of an elliptical horizontal fracture and an irregular-shaped horizontal fracture are thoroughly studied. The pseudoskin factors, which can be used to determine the difference of production capacity between the elliptical/irregular-shaped horizontal fracture and the circular horizontal fracture, are also evaluated with the proposed model.

2.2. Methodology

This research considers a vertical well with a horizontal fracture that produces single-phase oil from a box-shaped reservoir. This box-shaped reservoir has impermeable boundaries for all sides.

Since the impermeable boundary condition is used in this proposed model, the entire production period, including the boundary dominated flow which only occurs at the late production period, can be characterized with this model. We made the following assumptions to obtain a semi-analytical model to characterize the fluid flow in such a reservoir:

- The fluid and rock properties are homogeneous and isotropic both in the fracture system and matrix system;
- The bounded reservoir has a box shape and sealed by impermeable boundaries both along the horizontal direction and the vertical direction;
- The horizontal fracture has finite conductivity and is parallel to the upper and lower boundary;
- Only single-phase-oil flow is considered in this model;
- The horizontal fracture is assumed to have uniform distribution of fracture width and fracture conductivity across different parts of the fracture, and the fracture width and fracture conductivity remain unchanged as the pressure varies;
- The temperature variation in the reservoir is neglected; and
- The influence of gravity is neglected.

It is noted that, although the assumptions, including single-phase oil flow, isotropic matrix permeability, and a horizontal fracture with uniform and constant width and conductivity, are used in this proposed model, this model is not limited to model such a simplified scenario. The single-phase oil flow can be extended to single-phase gas flow or even two-phase flow (e.g., gas condensate) by applying the concept the pseudo-pressure and pseudo time (Singh and Whitson, 2010). The permeability anisotropy can be considered with the approach introduced by (Spivey and Lee, 1998). In addition, the non-uniform distribution of fracture width and fracture

conductivity, and the variation of fracture width and fracture conductivity caused by pressure change, can be readily incorporated into this model by applying the method introduced by Yu and Wu (2016). In practice, one can extend this general model to a specific scenario based on the actual reservoir conditions.

2.2.1 Fluid Flow inside Horizontal Fracture

As shown in **Figure 2-1**, we discretize the fracture system into N_f elements to capture the configuration of an irregular horizontal fracture. Figure 2-1a presents the irregular horizontal fracture in a bounded reservoir, Figure 2-1b illustrates the discretized horizontal fracture, and Figure 2-1c shows a fracture element and its neighboring elements. The width of the fracture is far smaller than the dimension of the fracture along the horizontal direction; thus, the fluid flow in the fracture can be simplified as a 2-dimensional flow. The flow equations for a single fracture element that is not connected with the wellbore can be expressed as:

$$\begin{aligned} &\frac{\partial}{\partial x}\left(\beta\frac{\Delta y w k_{fx}}{\mu B}\frac{\partial p}{\partial x}\right)_{i,j}\Delta x_{i,j}+\frac{\partial}{\partial y}\left(\beta\frac{\Delta x w k_{fy}}{\mu B}\frac{\partial p}{\partial y}\right)_{i,j}\Delta y_{i,j} \\ &+q_{sc_{i,j}}=\left(\frac{\Delta x\Delta y w\phi_f c_{tf}}{B}\right)_{i,j}\frac{\partial p_{i,j}}{\partial t} \end{aligned} \tag{2-1}$$

where Equation (2-1) is obtained from the continuity equation, which is introduced in **Appendix 2A**, Δx and Δy are dimensions of the fracture element, w is fracture width, k_f is fracture permeability, μ is fluid viscosity, B is formation volume factor, q_{sc} is withdrawal rate from the reservoir matrix to the fracture element under standard conditions, p is pressure, c_{tf} is total compressibility of the fracture system, ϕ_f is fracture porosity, t is time, β is unit conversion factor whose numerical value is 0.0853 and it has a unit of $(m^2 \cdot s)/(mD \cdot d)$. Applying finite difference approximation to Equation (1) and making the variables dimensionless, one can rewrite Equation (2-1) as:

$$\frac{C_{fD}}{\Delta x_D^2 w_D C_s}\left(2p^n_{fD_{i,j}} - p^n_{fD_{i+1,j}} - p^n_{fD_{i-1,j}}\right) + \frac{C_{fD}}{\Delta y_D^2 w_D C_s}\left(2p^n_{fD_{i,j}} - p^n_{fD_{i,j+1}} - p^n_{fD_{i,j-1}}\right) + \frac{2\pi h_D}{\Delta x_D \Delta y_D w_D C_s} q^n_{fD_{i,j}} = \frac{1}{\Delta t_D}\left(p^{n-1}_{fD_{i,j}} - p^n_{fD_{i,j}}\right) \tag{2-2}$$

where the definitions of the variables are tabulated in **Table 2-1**: p_D is dimensionless pressure, p_{fD} is dimensionless fracture pressure, p_f is fracture pressure, k_m is matrix permeability, h is reservoir thickness, q_w indicates the well production rate under standard condition which is a positive number, p_i is initial reservoir pressure, q_D is dimensionless flux, t_D is dimensionless time, l_r is reference length, c_{tm} is total compressibility in matrix system, ϕ_m is porosity in matrix system, x_D, y_D and z_D are dimensionless lengths, w_D is dimensionless fracture width, h_D is dimensionless formation thickness, r_w is radius of wellbore, r_D is dimensionless radius of wellbore, γ is a dimensionless coefficient, C is wellbore storage coefficient, C_D is dimensionless wellbore storage coefficient, C_s is a dimensionless variable defined in this work, and C_{fD} is dimensionless fracture conductivity.

In particular, for the well-element (the fracture element that is penetrated by the well), the flow equation is written as:

$$\frac{C_{fD}}{\Delta x_D^2 w_D C_s}\left(2p^n_{fD_{i,j}} - p^n_{fD_{i+1,j}} - p^n_{fD_{i-1,j}}\right) + \frac{C_{fD}}{\Delta y_D^2 w_D C_s}\left(2p^n_{fD_{i,j}} - p^n_{fD_{i,j+1}} - p^n_{fD_{i,j-1}}\right) + \frac{2\pi h_D}{\Delta x_D \Delta y_D w_D C_s}\left(q^n_{fD_{i,j}} - q^n_{f-wD}\right) = \frac{1}{\Delta t_D}\left(p^{n-1}_{fD_{i,j}} - p^n_{fD_{i,j}}\right) \tag{2-3}$$

where $q_{f\text{-}wD}$ is dimensionless flux from well-element to wellbore. At each timestep, we need to solve for the following unknowns: the dimensionless pressures and withdrawal rates at the discretized fracture elements, and the dimensionless flux from the well-element to the wellbore. It is noted that the withdrawal rate at each fracture element is represented with a unique influx $q^n_{fD_{i,j}}$, enabling us to consider the non-uniform influx distribution along the whole fracture.

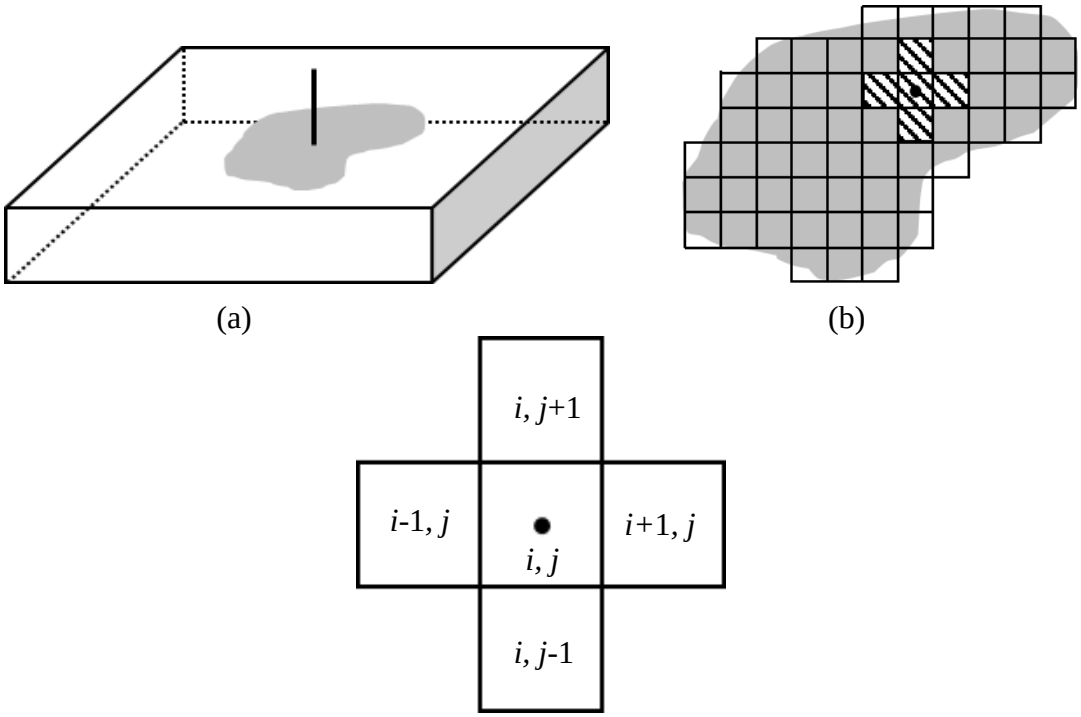

Figure 2-1. Discretization of a horizontal fracture: (a) schematic of an irregular horizontal fracture in a reservoir; (b) the discretized horizontal fracture represented with multiple fracture elements; and (c) one fracture element denoted by (*i*, *j*) and its neighboring elements.

Table 2-1. Definition of dimensionless variables used in this work.

$p_D = \frac{2\pi\beta k_m h \Delta p}{q_w B \mu}$	$p_{fD} = \frac{2\pi\beta k_m h \Delta p_f}{q_w B \mu}$
$q_D = \frac{q}{q_w}$	$t_D = \frac{\beta k_m t}{\phi_m \mu c_{tm} l_r^2}$
$x_D = \frac{x}{l_r}$	$y_D = \frac{y}{l_r}$
$z_D = \frac{z}{l_r}$	$w_D = \frac{w}{l_r}$
$h_D = \frac{h}{l_r}$	$r_D = \frac{r_w}{l_r}$
$\gamma = \frac{B r_w^2}{l_r^2}$	$C_D = \frac{C}{2\pi h \phi_m c_{tm} r_w^2}$

$$C_s = \frac{\phi_f c_{tf}}{\phi_m c_{tm}} \qquad C_{fD} = \frac{k_f w}{k_m l_r}$$

where $\Delta p = p_i - p$, and $\Delta p_f = p_i - p_f$

2.2.2 Analytical Solution in the Reservoir Matrix

The horizontal fracture is discretized into N_f fracture elements, and each of the fracture element can be treated as a plane source. Based on the results provided in **Appendix 2B**, in a bounded reservoir, the pressure response at position (x, y, z) at time t due to the contribution by a continuous plane source with a withdrawal rate of q_{sc} can be calculated by,

$$\begin{aligned} & p_i - p(x,y,z,t) = \\ & \frac{Bq_{sc}}{\phi_m c_{tm} x_e y_e z_e} \int_0^{t-t_0} \left\{ 1 + \frac{4x_e}{\pi \Delta x} \sum_{m=1}^{\infty} \frac{1}{m} \exp\left[-\frac{m^2 \pi^2 \alpha (t - t_0 - \tau)}{x_e^2} \right] \sin \frac{m\pi \Delta x}{2x_e} \cos \frac{m\pi x_0}{x_e} \cos \frac{m\pi x}{x_e} \right\} \\ & \cdot \left\{ 1 + \frac{4y_e}{\pi \Delta y} \sum_{m=1}^{\infty} \frac{1}{n} \exp\left[-\frac{m^2 \pi^2 \alpha (t - t_0 - \tau)}{y_e^2} \right] \sin \frac{m\pi \Delta y}{2y_e} \cos \frac{m\pi y_0}{y_e} \cos \frac{m\pi y}{y_e} \right\} \\ & \cdot \left\{ 1 + 2\sum_{m=1}^{\infty} \exp\left[-\frac{m^2 \pi^2 \alpha (t - t_0 - \tau)}{z_e^2} \right] \cos \frac{m\pi z_0}{z_e} \cos \frac{m\pi z}{z_e} \right\} \mathrm{d}\tau \end{aligned} \tag{2-4}$$

where x_e, y_e, and z_e are dimensions of the reservoir, α is diffusivity, x_0, y_0, and z_0 indicate the center position of the plane source, and t_0 is the time when the plane source becomes activated. During the production period, the withdrawal rate of a fracture element is time-dependent, and the pressure response at a given position caused by the horizontal fractures can be obtained by collecting the responses from all the fracture elements. As a result, the dimensionless pressure at position (x_D, y_D, z_D) at n^{th} timestep can be expressed as:

$$
\begin{aligned}
p_D^n\left(x_D,y_D,z_D,t_D^n\right) &= p_D^{n-1}+\frac{2\pi}{x_{eD}y_{eD}}\sum_{k=1}^{k=Nf}\sum_{l=1}^{l=n}\left(q_{fD,k}^{l}-q_{fD,k}^{l-1}\right)\int_{t_D^{n-1}-t_D^{l-1}}^{t_D^n-t_D^{l-1}} \\
&\left\{1+\frac{4x_{eD}}{\pi\Delta x_{D,k}}\sum_{m=1}^{\infty}\frac{1}{m}\exp\left[-\frac{m^2\pi^2\left(t_D^n-t_D^{l-1}-\tau_D\right)}{x_{eD}^2}\right]\sin\frac{m\pi\Delta x_{D,k}}{2x_{eD}}\cos\frac{m\pi x_{0D,k}}{x_{eD}}\cos\frac{m\pi x_D}{x_{eD}}\right\} \\
&\cdot\left\{1+\frac{4y_{eD}}{\pi\Delta y_{D,k}}\sum_{m=1}^{\infty}\frac{1}{m}\exp\left[-\frac{m^2\pi^2\left(t_D^n-t_D^{l-1}-\tau_D\right)}{y_{eD}^2}\right]\sin\frac{m\pi\Delta y_{D,k}}{2y_{eD}}\cos\frac{m\pi y_{0D,k}}{y_{eD}}\cos\frac{m\pi y_D}{y_{eD}}\right\} \\
&\cdot\left\{1+2\sum_{m=1}^{\infty}\exp\left[-\frac{m^2\pi^2\left(t_D^n-t_D^{l-1}-\tau_D\right)}{z_{eD}^2}\right]\cos\frac{m\pi z_{0D,k}}{z_{eD}}\cos\frac{m\pi z_D}{z_{eD}}\right\}\mathrm{d}\tau_D
\end{aligned}
\tag{2-5}
$$

As introduced in Appendix 2B, with the aid of Equation (2-5), we can readily build the relationship between the dimensionless pressures of the fracture elements and the dimensionless withdrawal rates of the fracture elements as follows:

$$
p_{fD,g}^n\left(x_{0D,g},y_{0D,g},z_{0D,g},t_D^n\right)=p_{fD,g}^{n-1}+\sum_{k=1}^{k=Nf}\sum_{l=1}^{l=n}\left(q_{fD,k}^{l}-q_{fD,k}^{l-1}\right)G_{l,k,g} \tag{2-6}
$$

where G is defined in Appendix 2B.

2.2.3 Solution Methodology

Based on the well model introduced by Peaceman (1990), we build the relationship between the dimensionless bottomhole pressure and the dimensionless pressure of the well-element,

$$
p_{wD}^n-p_{nwD}^n=\frac{w_D}{C_{fD}}q_{f-wD}^n\ln\frac{r_{eqD}}{r_{wD}} \tag{2-7}
$$

where p_{wD} is dimensionless wellbore pressure, p_{nwD} is dimensionless pressure of the well-element, r_{eq} is equivalent radius defined in Peaceman (1990), and r_{eqD} is defined as $r_{eq}/\,l_r$. In addition, we take the wellbore storage effect into account with the method provided in van Everdingen and Hurst (1949):

$$
1-\frac{\gamma C_D}{\Delta t_D^n}\left(p_{wD}^n-p_{wD}^{n-1}\right)=q_{f-wD}^n \tag{2-8}
$$

where γ is a dimensionless variable defined in Table 2-1, and C_D is dimensionless wellbore storage coefficient. Equation (2-7) and (2-8) can also be rearranged into a matrix form as:

$$\begin{bmatrix} \boldsymbol{C} & 1 & -\dfrac{w_D}{C_{fD}}\ln\dfrac{r_{eqD}}{r_{wD}} \\ \boldsymbol{0}_{1\times 2N_f} & \dfrac{\gamma C_D}{\Delta t_D^n} & 1 \end{bmatrix} \cdot \begin{bmatrix} \boldsymbol{p}_{fD} \\ \boldsymbol{q}_{fD} \\ p_{wD}^n \\ q_{f-wD}^n \end{bmatrix} = \begin{bmatrix} 0 \\ 1+\dfrac{\gamma C_D}{\Delta t_D^n} p_{wD}^{n-1} \end{bmatrix} \tag{2-9}$$

where

$$\boldsymbol{C} = \begin{bmatrix} \boldsymbol{0}_{1\times N_f} & \underbrace{0\cdots 0}^{n_w-1} \quad -1 \quad \underbrace{0\cdots 0}_{N_f} \end{bmatrix} \tag{2-10}$$

On the basis of the continuity of pressure and flux, we combine Equation (2-2) (or Equation (2-3)) Equations (2-6) and Equation (2-9) to obtain the following equation in a matrix format:

$$\begin{bmatrix} \boldsymbol{A} & \boldsymbol{0}_{N_f\times 1} & \boldsymbol{a} \\ \boldsymbol{B} & \boldsymbol{0}_{N_f\times 1} & \boldsymbol{0}_{N_f\times 1} \\ \boldsymbol{C} & 1 & -\dfrac{w_D}{C_{fD}}\ln\dfrac{r_{eqD}}{r_{wD}} \\ \boldsymbol{0}_{1\times 2N_f} & \dfrac{\gamma C_D}{\Delta t_D^n} & 1 \end{bmatrix} \cdot \begin{bmatrix} \boldsymbol{p}_{fD} \\ \boldsymbol{q}_{fD} \\ p_{wD}^n \\ q_{f-wD}^n \end{bmatrix} = \begin{bmatrix} \boldsymbol{RHS}_1 \\ \boldsymbol{RHS}_2 \\ 0 \\ 1+\dfrac{\gamma C_D}{\Delta t_D^n} p_{wD}^{n-1} \end{bmatrix} \tag{2-11}$$

where the matrices of $\boldsymbol{A}$, $\boldsymbol{a}$, $\boldsymbol{p}_{fD}$, $\boldsymbol{q}_{fD}$, and $\boldsymbol{RHS}_1$ are defined in Appendix 2A, and the matrices $\boldsymbol{B}$ and $\boldsymbol{RHS}_2$ are defined in Appendix 2B. Equation (2-11) has $2N_f$ +2 unknowns (N_f dimensionless pressures, N_f dimensionless withdrawal rates, one dimensionless bottomhole pressure and one dimensionless flux from the well-element to the wellbore) and $2N_f$ +2 linear equations. As such, the system of the linear equations shown in Equation (2-11) is closed and can be readily solved with the Gaussian elimination method. It is worth mentioning that Equation (2-11) is constructed for constant production rate condition and this model can also be used to model constant bottomhole pressure condition with minor modifications. For constant bottomhole pressure

condition, p_{wD} in Equation (2-11) is a constant value. After removing the wellbore storage equation in Equation (2-11), there will be $2N_f$ +1 unknowns (N_f dimensionless pressures, N_f dimensionless withdrawal rates, and one dimensionless flux from the well-element to the wellbore) and $2N_f$ +1 linear equations. The dimensionless flux from the well-element to the wellbore equals to the well production rate under constant buttonhole pressure condition.

2.3. Comparison to Commercial Software

We compare the results calculated by the proposed semi-analytical method against those by a commercial software (Eclipse) on an irregular horizontal fracture model. **Figure 2-2** shows a top view and a side view of the reservoir model where a well is producing oil through an irregular horizontal fracture within the reservoir. The dimensions of the reservoir are 1600×1000×40 m, and the dimensions of the grids used to discretize the reservoir are 20×20×10 m. The fracture has an area of 40800 m^2 along the horizontal direction, and it is located in the center of the payzone. The fracture considered in Eclipse is described with 102 cells, whereas the horizontal fracture considered in the semi-analytical method is also discretized into 102 elements and each element has dimensions of 20×20m. In the vertical direction, we apply local grid refinement in Eclipse to model the fracture, and the fracture width is 0.001 m both in Eclipse and the proposed model. In the reservoir model, the fracture conductivity is 500 mD·m, the oil viscosity is 1mPa·s, and the initial reservoir pressure is 30 MPa. The wellbore storage effect is neglected in this section.

The proposed method is compared against Eclipse under both the constant production rate condition and the constant bottomhole pressure condition. For constant pressure rate condition, the comparison is conducted on two scenarios: in scenario #1, the well keeps producing oil with a constant production rate of 20 m^3/day, a matrix porosity of 0.01, and a matrix permeability of 10 mD; and in scenario #2, the well keeps producing oil with a constant production rate of 100

m^3/day, a matrix porosity of 0.10, and a matrix permeability of 10 mD. Under the constant bottomhole pressure condition, the comparison is also conducted on two scenarios: scenario #3, the well keeps producing oil with a constant bottomhole pressure of 10 MPa, a matrix porosity of 0.10, and a matrix permeability of 0.1 mD; and scenario #4, the well keeps producing oil with a constant production rate of 10 MPa, a matrix porosity of 0.10, and a matrix permeability of 1 mD. **Figure 2-3** compares the pressure response (under constant production rate condition) and production rates (under constant bottomhole pressure condition) obtained with the semi-analytical method and those obtained with Eclipse. As seen from Figure 2-3, both the pressure response plots in Figure 2-3a and the production rate plots in Figure 2-3b obtained with the semi-analytical approach are in excellent agreement with the results given by Eclipse.

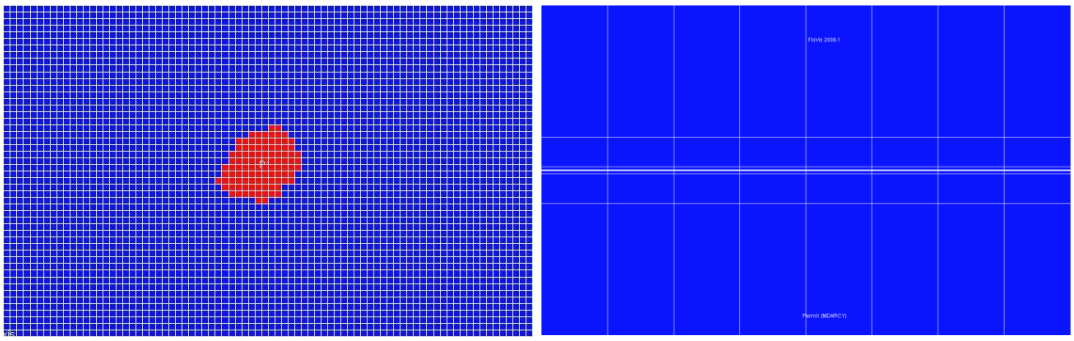

(a) (b)

Figure 2-2. The irregular-shaped horizontal fracture model used in Eclipse. The red cells represent the horizontal fracture, while the blue cells represent the reservoir: (a) top view of the irregular horizontal fracture model; and (b) side view of the refined cells to model the irregular-shaped horizontal fracture.

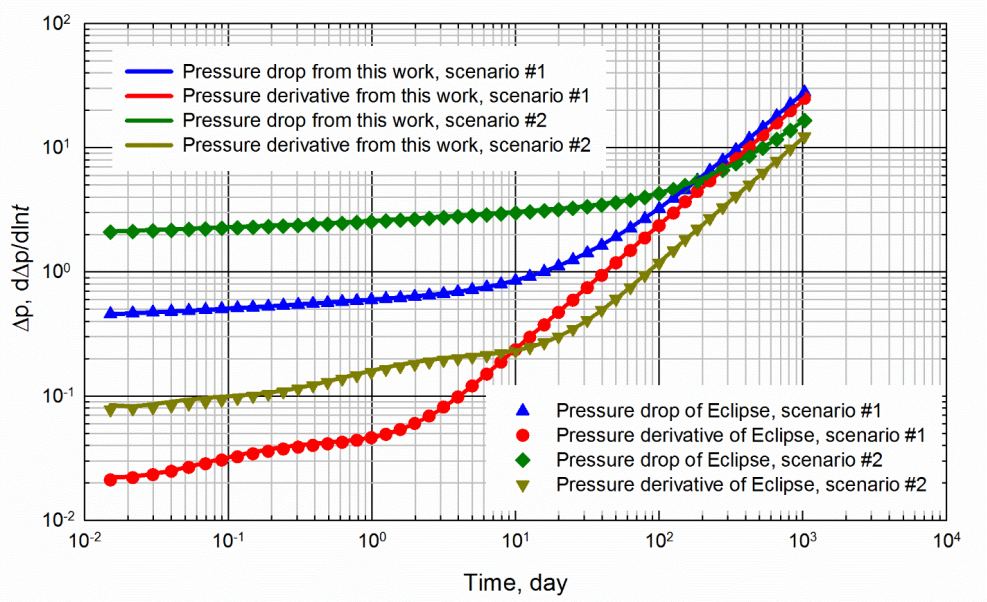

(a)

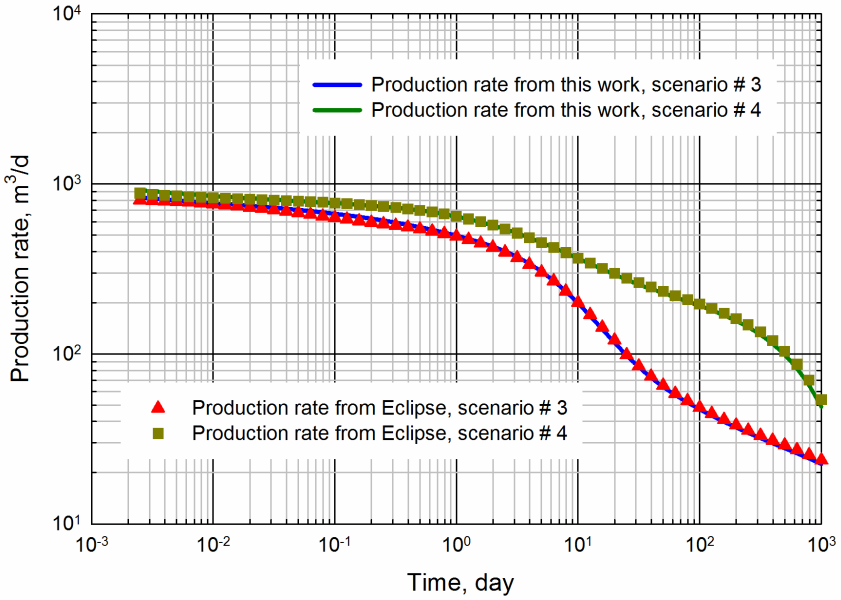

(b)

Figure 2-3. Comparison between the results obtained by the proposed method against those by Eclipse under constant production rate condition and constant bottomhole pressure condition: (a) the comparison is conducted under constant production rate condition on two scenarios: in scenario #1, the constant production rate is 20 m^3/day, the matrix porosity is 0.01, and the matrix permeability is 10 mD; and in scenario #2, the constant production rate is 100 m^3/day, the matrix porosity is 0.1, and the matrix permeability is 10 mD; (b) the comparison is conducted under constant bottomhole pressure condition on two scenarios: in scenario #3, the constant bottomhole pressure is 10 MPa, the matrix porosity is 0.1, and the matrix permeability is 0.1 mD; and in scenario #4, the constant bottomhole pressure is 10 MPa, the matrix porosity is 0.1, and the matrix permeability is 1 mD.

2.4. Results and Discussion

In practice, the growth of a horizontal fracture is closely related with the stress field of the reservoir and the fracturing operations. Since the geometry of horizontal fractures could vary from one reservoir to another, it is impossible to investigate the transient flow behavior of the horizontal fractures with all the possible geometries in this work. Herein, we select two representative geometries of the horizontal fracture in the case studies. We thoroughly study the pressure transient behavior of a circular horizontal fracture and an elliptical horizontal fracture in a bounded reservoir. In addition, we also provide a case study conducted on an irregular-shaped horizontal fracture and calculate the pressure response and pseudoskin of this fracture using the proposed model.

Figure 2-4 shows a side view of a horizontal fracture in a formation. In this figure, z_{vD} represents the relative vertical position of the horizontal fracture in a formation, and $z_{vD} = 0.5$ indicates that the horizontal fracture is located in the center across the thickness of the payzone. **Figure 2-5** presents the schematics of an elliptical horizontal fracture and a circular horizontal fracture. In this figure, a_D is dimensionless semi-major axis, and b_D is dimensionless semi-minor axis. a_D being equal to b_D represents that the fracture is circular; otherwise, the fracture is elliptical. The reference length l_f is assigned to be equal to the length of semi-major axis.

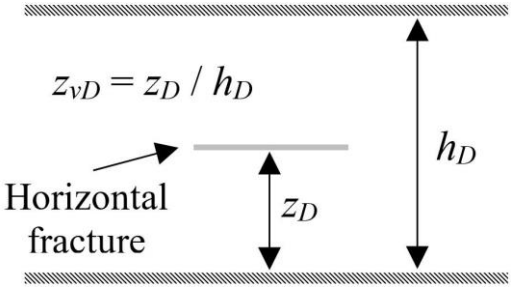

Figure 2-4. Side view of a horizontal fracture in a formation, which also shows the definition of z_{vD}, i.e., relative vertical position of the fracture in the formation.

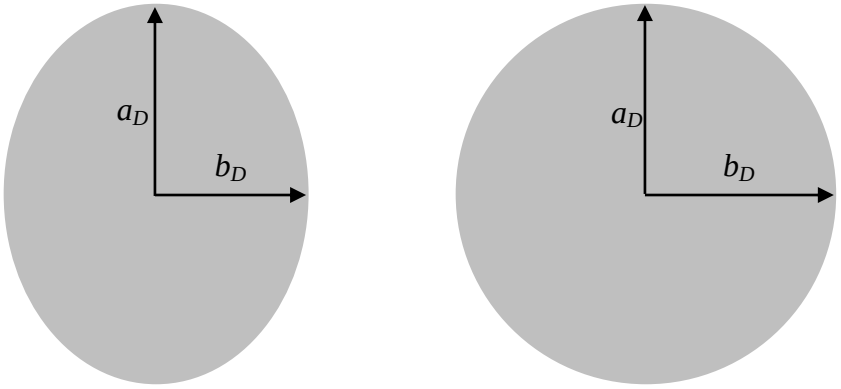

(a) (b)

Figure 2-5. Schematics of an elliptical horizontal fracture (a) and a circular horizontal fracture (b). a_D is dimensionless semi-major axis, and b_D is dimensionless semi-minor axis. As for a circular horizontal fracture $a_D = b_D$.

2.4.1 Flow Regimes of Horizontal Fractures

Prior to the sensitivity analysis carried out later, we first examine the influence of the number of fracture elements discretized on the simulation outputs. We discretize a circular fracture (or an elliptical fracture) into 103, 137, 177 and 221 square (or rectangle for an elliptical fracture) elements, respectively, and calculate the pressure drops and pressure derivatives of this fracture in the bounded reservoir. The following dimensionless data are used: $x_{eD} = 20$, $y_{eD} = 20$, $h_D = 0.2$, $z_{vD} = 0.5$, $a_D = 1$, $b_D = 1$, $w_D = 1.33\times10^{-5}$, $C_{fD} = 1$, $C_s = 10$, $C_D = 0$, and $\gamma = 5.3\times10^{-7}$.

Figure 2-6 illustrates the influence of the number of fracture elements discretized on the pressure drops and pressure derivatives of a circular horizontal fracture. It can be observed from Figure 2-6 that the pressure drops and pressure derivatives tend to undergo little change if the number of fracture elements is more than 137. Therefore, we discretize the horizontal fracture into 137 elements in the following studies. To analyze the flow regimes that can take place in the horizontal fracture, we use the following dimensionless numbers in the benchmark horizontal fracture model: $x_{eD} = 20$, $y_{eD} = 20$, $h_D = 0.2$, $z_{vD} = 0.5$, $a_D = 1$, $b_D = 1$, $w_D = 1.33\times10^{-5}$, $C_{fD} = 1$, $C_s = 10$, $C_D = 5$, and $\gamma = 5.3\times10^{-7}$. This benchmark horizontal fracture is circular.

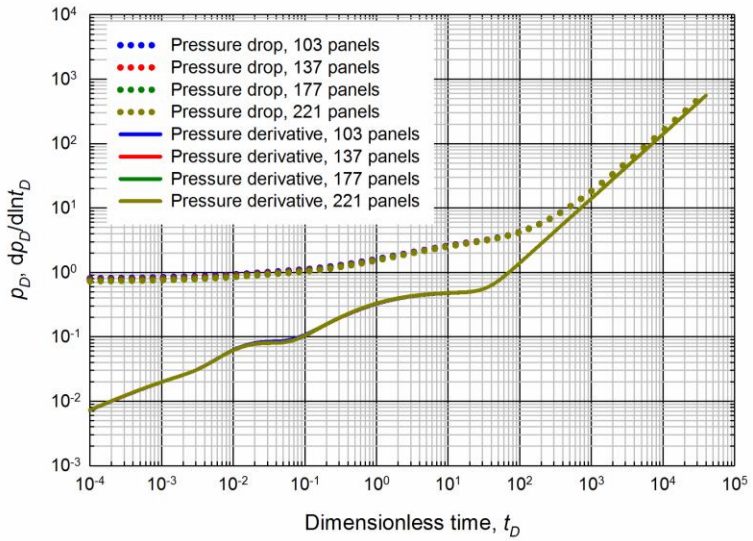

Figure 2-6. Impact of the number of the fracture elements, which are used to discretize a circular horizontal fracture, on the pressure drops and pressure derivatives that are calculated with the semi-analytical method.

Figure 2-7 presents the flow regimes that can be distinguished for the oil flow in the benchmark circular horizontal fracture model, namely: (1) wellbore after flow, (2) formation linear flow, (3) early pseudo-radial flow (4) late pseudo-radial flow, and (5) boundary dominated flow. At the very early production period, the wellbore storage exhibits a significant influence on the pressure drops as well as the pressure derivatives, and one can observe an inverted "V" shape from the pressure derivative curve during this period. Following the wellbore after flow, a half unit slope, which indicates a formation linear flow from the matrix to the fracture, can be distinguished from the pressure derivative curve. This is similar to the pressure transient behavior of a vertical fracture at the early production period (Cinco-Ley and Samaniego-V, 1981). Afterwards, one can observe two zero-slope periods, which indicate the early pseudo-radial flow and the late pseudo-radial flow, respectively. **Figure 2-8** illustrates the schematics of the formation linear flow, the early pseudo-radial flow, and the late pseudo-radial flow. As is shown in Figure 2-8a, the fluid flows perpendicularly to the horizontal fracture in the formation linear flow period. The early pseudo-radial flow of the first kind as shown in Figure 2-8b can be observed in the formations

that have small thickness, while the early pseudo-radial flow of the second kind as shown in Figure 2-8c can be observed only if the formations thickness is sufficiently large.

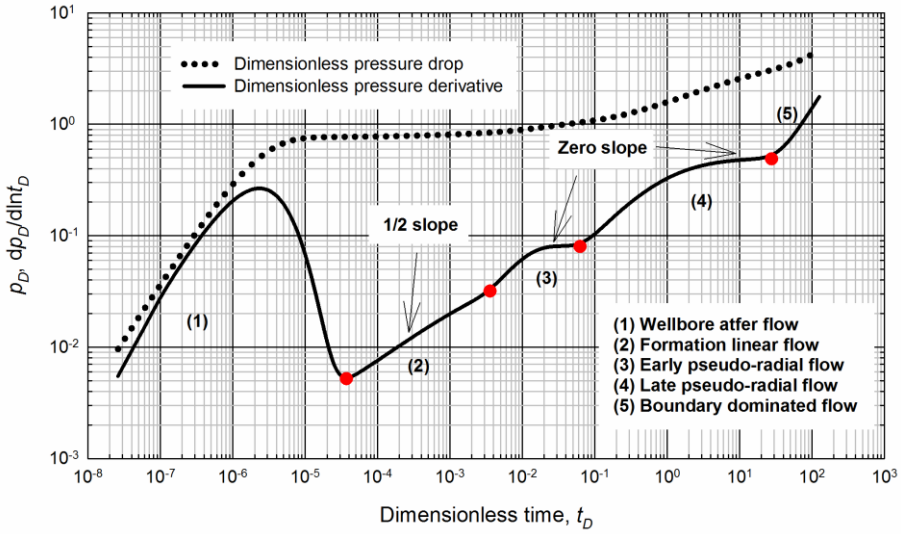

Figure 2-7. Identification of the flow regimes that can take place in a circular horizontal fracture in a bounded reservoir.

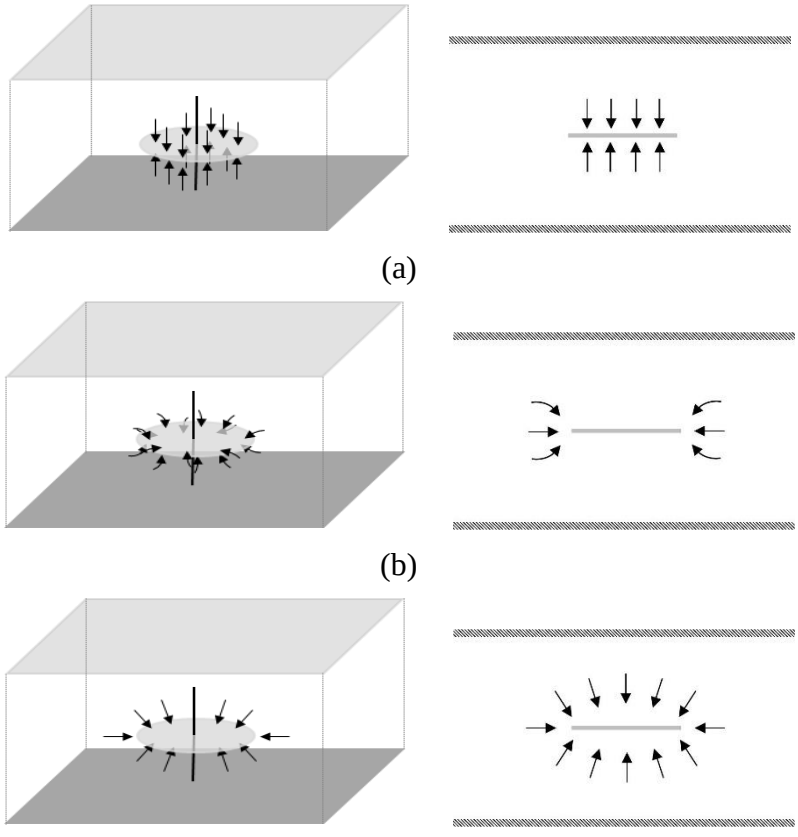

(a)

(b)

(c)

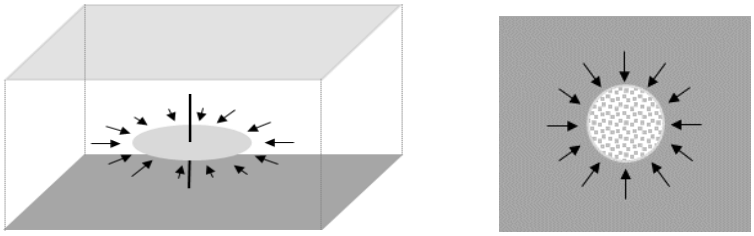

(d)

Figure 2-8. Schematics of different flow regimes: (a) 3D view and side view of the linear flow; (b) 3D view and side view of the first kind of early pseudo-radial flow ; (c) 3D view and side view of the second kind of early pseudo-radial flow; and (d) 3D view and top view of the late pseudo-radial flow.

It is noted that the flow regimes of a horizontal fracture can heavily depend on the input values of the parameters that are chosen in the cases studies. **Figure 2-9** shows the pressure drops and pressure derivatives of a horizontal fracture that are calculated with another set of data, i.e., x_{eD} = 3, y_{eD} = 3, h_D = 0.2, z_{vD} = 0.5, a_D = 1, b_D =0.02, w_D = 1.33×10^{-5}, C_{fD} = 50, C_s = 10, C_D =5, and γ = 5.3×10^{-7}. In this figure, one can also identify five flow regimes, namely: (1) wellbore after flow, (2) bilinear flow, (3) formation linear flow, (4) elliptical flow, and (5) boundary dominated flow. This horizontal fracture is elliptical and it has a much larger semi-major axis than its semi-minor axis, such that one can identify a bilinear flow period on the pressure derivative curve. **Figure 2-10** shows the schematics of different flow regimes of a horizontal fracture. As shown in Figure 2-10a, the appearance of the bilinear flow indicates that a fracture linear flow and a matrix-fracture linear flow take place simultaneously in the reservoir. Figure 2-10b presents the schematic of the elliptical flow; during this elliptical flow period, the transient flow of the horizontal fracture is very similar to that of a horizontal well (Escobar and Montealegre, 2007).

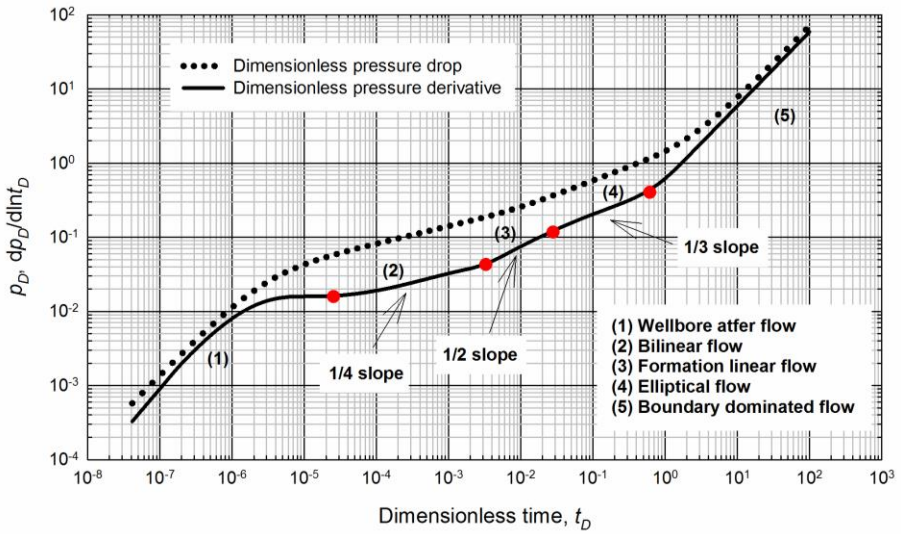

Figure 2-9. Identification of the flow regimes that can take place in an elliptical horizontal fracture in a bounded reservoir.

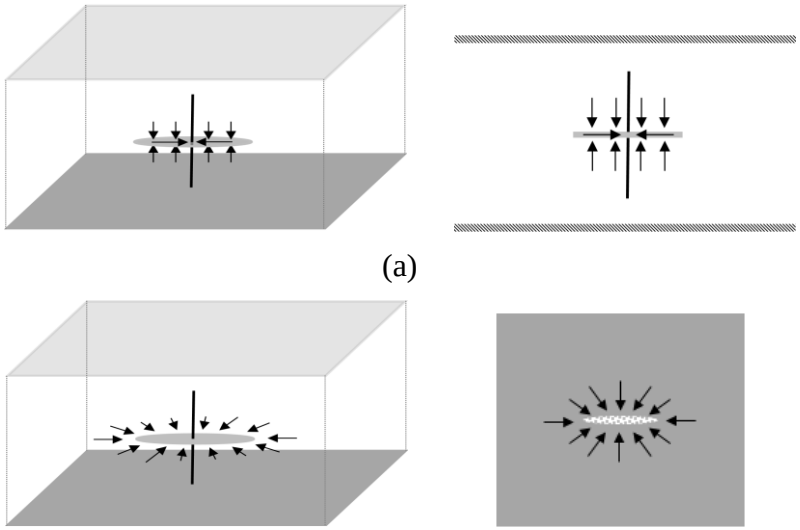

(a)

(b)

Figure 2-10. Schematics of different flow regimes of a horizontal fracture: (a) 3D view and side view of the bilinear flow; and (b) 3D view and top view of the elliptical flow.

2.4.2 Sensitivity Analysis of Circular Horizontal Fractures

Hereafter, we carry out detailed sensitivity analysis to examine the influences of the following parameters on the pressure transients of the benchmark circular horizontal fracture model: formation thickness, fracture's vertical position, fracture conductivity, and wellbore storage. As for the sensitivity analysis conducted on a specific parameter, its values are made different from

what is used in the aforementioned benchmark model. **Table 2-2** summaries the values of the parameter used for the sensitivity analysis.

Table 2-2. Parameter values used in the sensitivity analysis.

	Figure 2-11	Figure 2-12	Figure 2-13	Figure 2-14
x_{eD}	20	20	20	20
y_{eD}	20	20	20	20
a_D	1	1	1	1
b_D	1	1	1	1
w_D	1.33×10^{-5}	1.33×10^{-5}	1.33×10^{-5}	1.33×10^{-5}
C_s	10	10	10	10
γ	5.3×10^{-7}	5.3×10^{-7}	5.3×10^{-7}	5.3×10^{-7}
h_D	0.2/0.4/0.6/0.8/1	0.2	0.2	0.2
z_{vD}	0.5	0.1/0.2/0.3/0.4/0.5	0.5	0.5
C_{fD}	1	1	0.5/1/2/5/10	1
C_D	5	5	5	5/10/15/20/25

2.4.2.1 Formation Thickness

Different formation thickness values are considered in the sensitivity analysis: h_D = 0.2, 0.4, 0.6, 0.8 and 1.0. **Figure 2-11** shows the pressure drops and pressure derivatives that are calculated with the semi-analytical method for the horizontal fracture models with different formation thicknesses. As one can observe in this figure, the dimensionless pressure increases as the formation thickness increases. But this does not imply that the physical wellbore pressure will undergo a higher drop in a thicker formation. This is only because that the dimensionless pressure defined in this work is proportional to the formation thickness (See Table 2-1).

It is interesting to note that, although we can distinguish an early pseudo-radial flow from the pressure derivative plots calculated for the dimensionless thickness of 0.2 and 0.6, respectively, the mechanisms of these two early pseudo-radial flows are different. The early pseudo-radial flow that occurs in the formation thickness of 0.2 is corresponding to the early pseudo-radial flow of the first kind as shown in Figure 2-8b, while the early pseudo-radial flow that occurs in the formation thickness of 0.6 is corresponding to the early pseudo-radial flow of the second kind as

shown in Figure 2-8c. If the formation thickness is small (e.g., h_D = 0.2), the early pseudo-radial flow of the first kind can be observed near the edge of the horizontal fracture; whereas, if the formation thickness is sufficiently large (e.g., h_D = 0.6), the early pseudo-radial flow of the second kind can be observed surrounding the horizontal fracture along the vertical direction. When the formation thickness is 0.4, the pressure derivative plot (i.e., the red curve in Figure 2-11) presents a transition stage between these two kinds of early pseudo-radial flow. On the pressure derivative plot of h_D = 0.4, the "dip" section indicates that the early pseudo-radial flow of the second kind is imminent, and the zero-slope section indicates that the early pseudo-radial flow of the first kind occurs in the formation. If the dimensionless formation thickness reaches up to 0.8 or even higher, one can observe a negative-slop section on the pressure derivative plots. This implies that there is spherical flow component appearing in the formations.

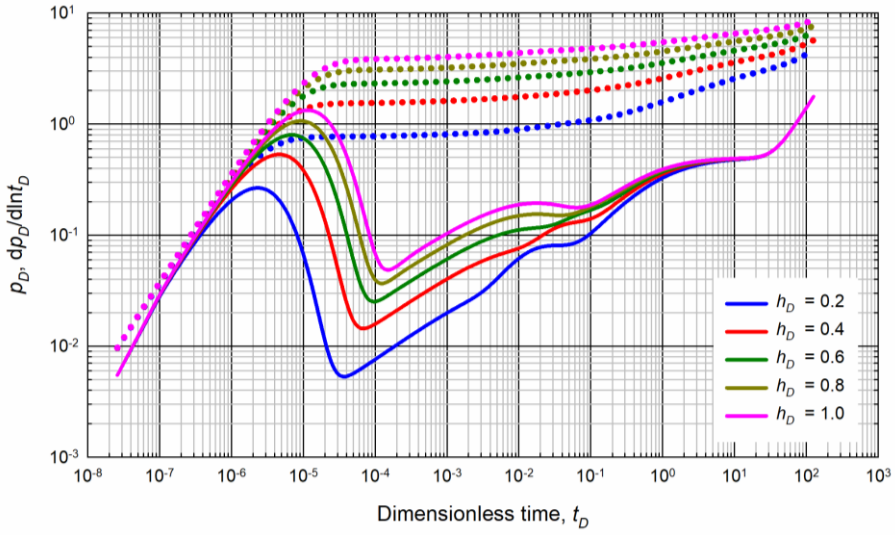

Figure 2-11. Impact of formation thickness on the pressure drops and their derivatives of a circular horizontal fracture. When h_D = 0.4, the early pseudo-radial flow of first and a "dip" can be observed on the pressure derivative plot.

2.4.2.2 Vertical Position

In the real field cases, the horizontal fracture may not be located in the central part across the payzone. Herein, we apply the semi-analytical method to examine the influence of the relative

vertical positions of the horizontal fracture on the pressure transient behavior. As the formation itself is symmetrical over the central plane of the formation, the calculations made for the fracture's vertical positions of z_{vD} = 0.1, 0.2, 0.3, 0.4 and 0.5 are sufficient for one to draw a complete picture about how the fracture's vertical position affects the pressure response. **Figure 2-12** illustrates the pressure drops and pressure derivatives of the horizontal fractures at different vertical locations across the payzone. It can be seen from Figure 2-12 that only negligible differences could be observed from the pressure drop plots. As for the pressure derivative plots, the main difference that can be observed appears during the periods of the formation linear flow and the early pseudo-radial flow. It can be also observed from Figure 2-12 that the formation linear flow ends earlier as the fracture vertical position takes a smaller value. This is because a smaller vertical-position value implies that the fracture is closer to the lower payzone boundary; this will allow the lower formation boundary to exert an earlier influence on the pressure response, resulting in the earlier termination of the linear flow period. In addition, when the horizontal fracture is located in a lower position, the distance between the upper formation boundary and the horizontal fracture may become large enough to enable the occurrence of the early pseudo-radial flow of the second kind. As a result, we can observe an early pseudo-radial flow of the second kind from the pressure derivative plot at z_{vD} = 0.1, followed by a "dip" section that indicates that an early pseudo-radial flow of the first kind is imminent.

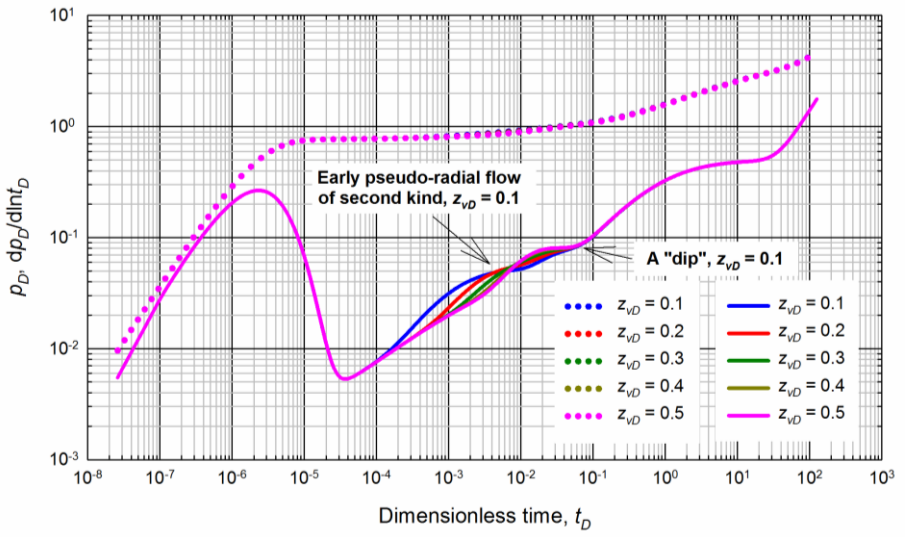

Figure 2-12. Impact of the relative vertical position of the circular horizontal fracture on the pressure drops and their derivatives. At z_{vD} = 0.1, we can observe an early pseudo-radial flow of the second kind as well as a "dip" on the pressure derivative plot.

2.4.2.3 Fracture Conductivity

Figure 2-13 depicts the pressure drops and pressure derivatives calculated with the semi-analytical method for the horizontal fracture model at different fracture conductivity of C_{fD} = 0.5, 1.0, 2.0, 5.0, and 10.0. One can see that the pressure drop increases as the fracture conductivity decreases. This is attributed to the fact that a lower fracture conductivity results in a higher flow resistance in the fracture. From the pressure derivative plots shown in Figure 2-13, one can observe that the duration of the wellbore storage effect tends to be longer as the fracture conductivity decreases. This is because, at the very early production period, the oil is mainly produced from the wellbore and the fracture, and the fracture can be regarded as an extension to the wellbore. A lower fracture conductivity indicates that there is more flow resistance in the fracture and the fluid will flow more slowly in the fracture; hence, the duration of the fluid flow from the fracture to the wellbore will be prolonged, and thus the duration of the wellbore storage period will also be prolonged.

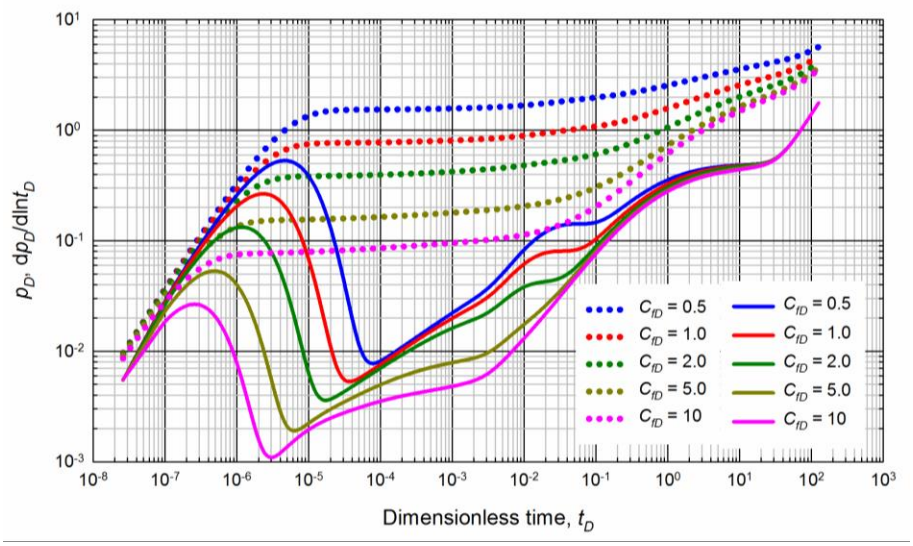

Figure 2-13. Impact of the fracture conductivities of the circular horizontal fracture on the pressure drops and their derivatives.

2.4.2.4 Wellbore Storage

The dimensionless wellbore storage coefficients are varied in an attempt to explore its influence on the pressure response of a horizontal fracture. **Figure 2-14** presents the pressure drops and pressure derivatives calculated by the semi-analytical model with these different dimensionless wellbore-storage coefficients of 5, 10, 15, 20 and 25**.** The pressure drop plots and pressure derivative plots shown in Figure 2-14 reveal that: the wellbore storage mainly exerts an influence on the early production period; a larger dimensionless wellbore storage coefficient will lead to a lower pressure drop and a longer duration of the wellbore storage effect; and the pressure drops as well as the pressure derivatives, which are calculated at different values of the dimensionless wellbore-storage coefficients, exhibit negligible difference after the wellbore after flow is terminated.

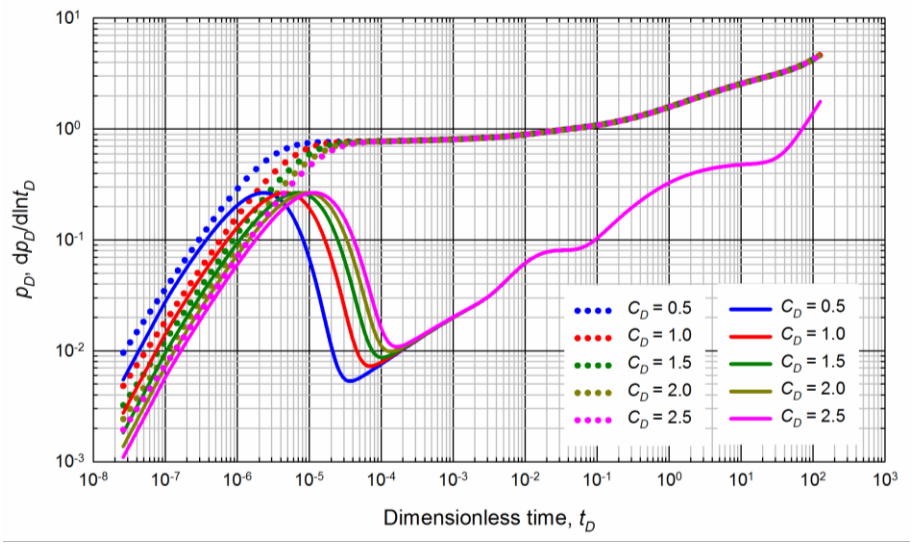

Figure 2-14. Impact of the wellbore storage coefficients on the pressure drops and their derivatives of the circular horizontal fracture.

2.4.3 Pressure Dynamics of Elliptical Horizontal Fractures

In practice, due to the impact of the stress heterogeneity in the formations, the propagation of a horizontal fracture along different horizontal directions can be very different. In such scenarios, an elliptical horizontal fracture might be created after the fracturing treatment. The production capacity of an elliptical fracture under steady-state condition has been previously studied by Crawford and Landrum (1954), and the effect of elliptical fractures on sweep efficiencies has also been investigated by Crawford *et al*. (1963). In addition, a circular horizontal fracture in a reservoir with horizontally heterogeneous permeability can be converted to an elliptical horizontal fracture in a reservoir with a homogeneous permeability. However, there is still no study made on the pressure transient behavior of an elliptical horizontal fracture. In this section, we study the pressure transient behavior of elliptical horizontal fractures with different axis ratios (semi-minor axis divide by semi-major axis) and calculate the pseudoskin factors for these elliptical fractures. The reference length l_f is set to be equal to $\sqrt{a \cdot b}$, where a is the semi-major axis and b is the semi-minor axis.

Figure 2-15 presents the pressure drops and pressure derivatives calculated with the semi-analytical model for the elliptical horizontal fractures with different axis ratios. The axis ratio is varied from 0.2 to 1, while the area of the elliptical fracture keeps unchanged. From the pressure derivative plots shown in Figure 2-15, one can find that the axis ratio mainly exerts an influence on the early pseudo-radial flow period. It should be noted that the dimensionless formation thickness used in the base case is 0.2, and based on the aforementioned arguments, the early pseudo-radial flow can be classified as the early pseudo-radial flow of the first kind which only occurs near the fracture edge (See Figure 2-8b). For an elliptical horizontal fracture, the distance from the fracture edge to the wellbore is non-uniform, leading to that the early pseudo-radial flow along the fracture edge appears at different times. As the axis ratio is decreased, the appearance time of the early pseudo-radial flow along the fracture edge becomes more non-uniform; hence, a smaller axis ratio renders the early pseudo-radial flow less distinguishable. In addition, the dimensionless pressure increases as the axis ratio decreases. This implies that, within relatively short production time, a circular fracture in a bounded reservoir has higher productivity than an elliptical fracture having the same fracture area. One should be cautious about the preconditions underlining these points, including the bounded reservoir and the relatively short production time, because if the reservoir is sufficiently large and the production time is sufficiently long, the productivity of a circular horizontal fracture and an elliptical fracture could be quite different.

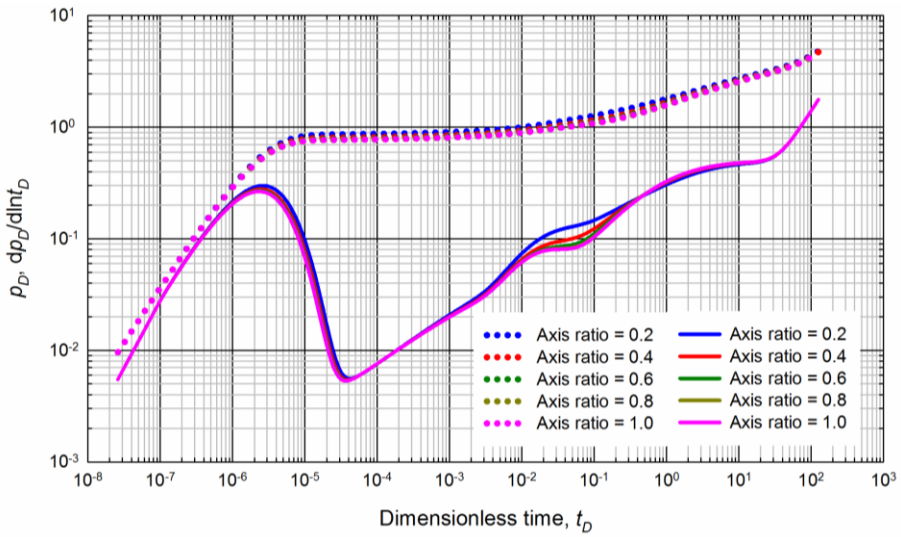

Figure 2-15. Impact of the axis ratios of the elliptical fracture on the pressure drops and their derivatives

The infinite-acting period indicates a period during which the reservoir boundaries exert negligible influence on the transient flow behavior. If the reservoir is sufficiently large, the infinite-acting period can last for a long time. During this period, the difference between the dimensionless bottomhole pressure of a circular horizontal fracture (axis ratio equals to 1.0) and that of an elliptical horizontal fracture remains unchanged at the late pseudo-radial flow (Valko and Economides, 1997). This enables us to reveal the relationship between the dimensionless bottomhole pressure of a circular horizontal fracture and that of an elliptical horizontal fracture at the late production period. We can use the concept of pseudoskin factor to express the dimensionless pressure difference between a circular horizontal fracture and an elliptical horizontal fracture (Reynolds *et al.*, 1984):

$$S = p_{w,non}\left(h_D, z_{vD}, C_{fD}\right) - p_{w,cir}\left(h_D, z_{vD}, C_{fD}\right) \tag{2-12}$$

where S is pseudoskin factor, $p_{w,cir}$ is the dimensionless bottomhole pressure of the circular horizontal fracture, and $p_{w,non}$ is the dimensionless bottomhole pressure of the non-circular horizontal fracture.

Figures 2-16 to **2-18** present the pseudoskin factors of the elliptical horizontal fractures calculated with different formation thicknesses, vertical positions, and conductivities. As one can see from these figures, the pseudoskin are commonly negative, indicating that at the late production period the elliptical horizontal fractures have higher well productivity compared with that of a circular horizontal fracture. A smaller pseudoskin factor represents a more significant increase in the well productivity. This is quite opposite to what is shown in Figure 2-15, in which an elliptical horizontal fracture has lower productivity than a circular horizontal fracture. This is attributed to the fact that, at the early production period, the produced oil is mainly from the reservoir near the wellbore, and a circular horizontal fracture is favorable for the oil to flow from the reservoir to the fracture; whereas, at the late production period, the oil is mainly produced from the reservoir section where is distant from the wellbore, and an elliptical fracture can penetrate further into the reservoir and stimulate a larger reservoir volume. A similar observation can also be found in Kucuk and Brigham (1979), in which one can see that an elliptical wellbore exhibits a higher productivity than a circular wellbore with an equivalent wellbore radius.

Figure 2-16 shows the pseudoskin factors of elliptical fractures with various axis ratios and formation thicknesses. As one can see, the pseudoskin factor of an elliptical fracture with a smaller axis ratio is smaller than that with a larger axis ratio. This is because the elliptical facture with a smaller axis can penetrate further into the reservoir than that with a larger axis ratio, resulting in a higher well productivity and a lower pseudoskin. In addition, the pseudoskin factor increases as the formation thickness increases, indicating that the elliptical horizontal fractures tend to enhance the well productivity more significantly in thinner formations.

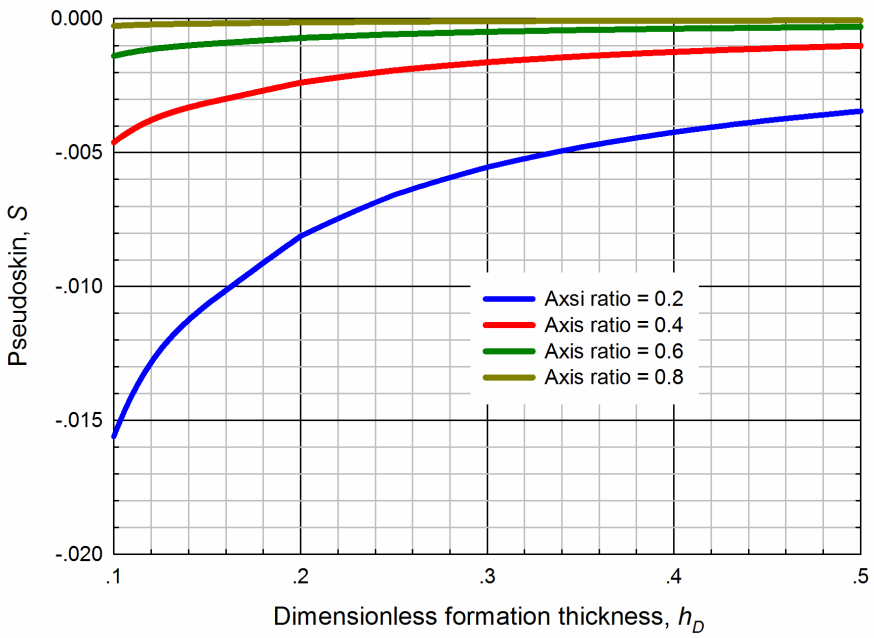

Figure 2-16. Variation of pseudoskin factors of elliptical horizontal fractures with various axis ratios vs. dimensionless formation thicknesses

Figure 2-17 shows the influence of the fracture's vertical position on the pseudoskin factor of the elliptical fractures under various axis ratios. As one can see from Figure 2-17, the pseudoskin factor keeps unchanged as the fracture's vertical position is varied. This is because the fracture's vertical position poses a major influence on the well productivity during the early production period, while it has a negligible influence on the well productivity during the late production period.

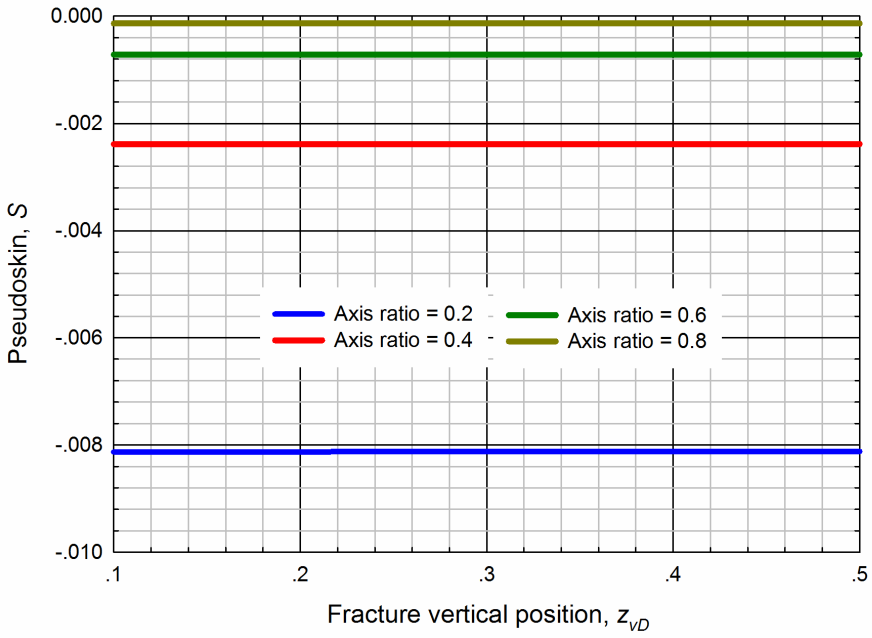

Figure 2-17. Pseudoskin factors of elliptical horizontal fractures with various axis ratios and vertical positions.

Figure 2-18 depicts the pseudoskin factors of elliptical horizontal fractures with various fracture conductivities and axis ratios. Figure 2-18 show that the pseudoskin factor decreases as the fracture conductivity increases. One can also observe that the pseudo skin factors show a more significant decrease if the axis ratio of the elliptical fracture is smaller. For example, if the dimensionless fracture conductivity increases from 0.1 to 50, the pseudoskin factor corresponding to an axis ratio of 0.2 decreases from -0.000982 to -0.145060, while the pseudoskin factor corresponding to an axis ratio of 0.8 only decreases from -0.000015 to -0.003249. In conclusion, a higher fracture conductivity will lead to a larger difference in the productivity between an elliptical fracture and a circular fracture. Such effect is more obvious for the elliptical fracture with a lower axis ratio.

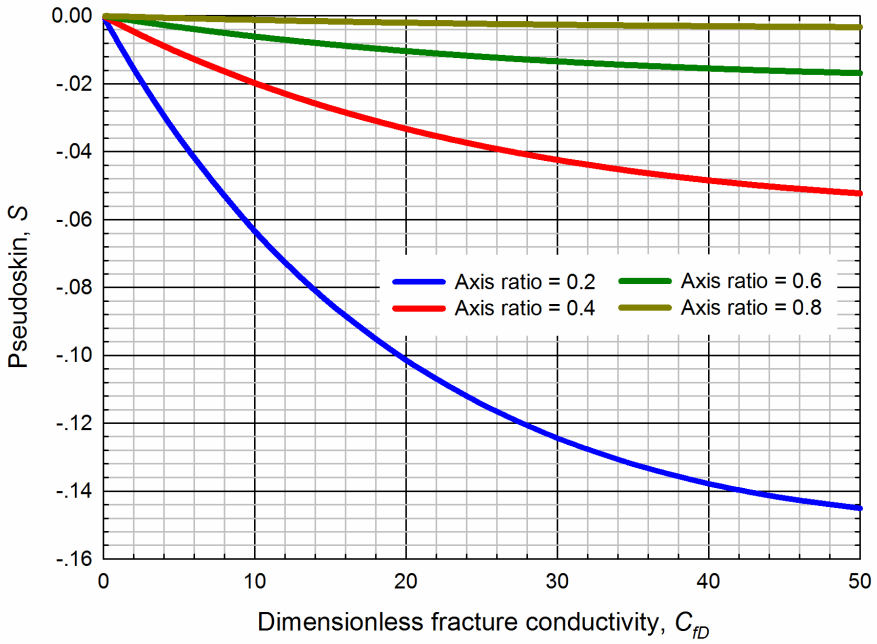

Figure 2-18. Pseudoskin factors of elliptical horizontal fractures with various axis ratios and dimensionless fracture conductivities.

2.4.4 Pressure Dynamics of an Irregular-shaped Horizontal Fracture

Figure 2-19a shows the schematic of an irregular-shaped horizontal fracture used in this work. Figure 2-19b presents the discretization of this fracture; this fracture has been also discretized into 137 elements. The reference length l_f is set to be equal to the radius of an imagined circular fracture which has an area equal to the area of the irregular-shaped fracture as shown in Figure 2-19.

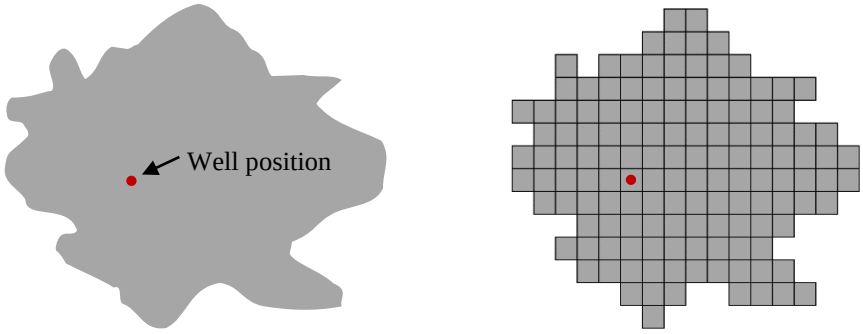

(a) (b)

Figure 2-19. The irregular-shaped horizontal fracture used in this work: (a) the schematic of the horizontal fracture; and (b) the discretization of the irregular-shaped horizontal fracture.

Figure 2-20 shows the pressure drops and pressure derivative of this irregular-shaped horizontal fracture with different dimensionless fracture conductivities. One can observe from Figure 2-20 that the pressure response of this irregular-shaped horizontal fracture is very similar to that of a circular horizontal fracture. We can also identify wellbore after flow, formation linear flow, early-pseudo radial flow, late pseudo-radial flow, and boundary dominated flow on the pressure derivative curves. In order to obtain a better understanding about the differences in the transient flow behavior between this irregular-shaped fracture and that of a circular fracture with an equivalent area, we also calculate the late-time pseudoskin factor for this irregular-shaped fracture at different dimensionless fracture conductivities. The calculation results are shown in **Figure 2-21**. As one can see from this figure, the pseudoskin factor is decreased as the fracture conductivity is increased, which is consistent with the trend presented in Figure 2-18. It is interesting to find that the pseudoskin factor is positive when the dimensionless fracture conductivity is less than 11, while the pseudoskin factor is negative when the dimensionless fracture conductivity is larger than 11. This implies that, with a small dimensionless fracture conductivity (e.g., $C_{fD} < 11$), this irregular-shaped horizontal fracture stimulates a smaller reservoir volume than a circular horizontal fracture; whereas, with a large dimensionless fracture conductivity (e.g., $C_{fD} > 11$), this irregular-shaped horizontal fracture stimulates a larger reservoir volume than a circular horizontal fracture.

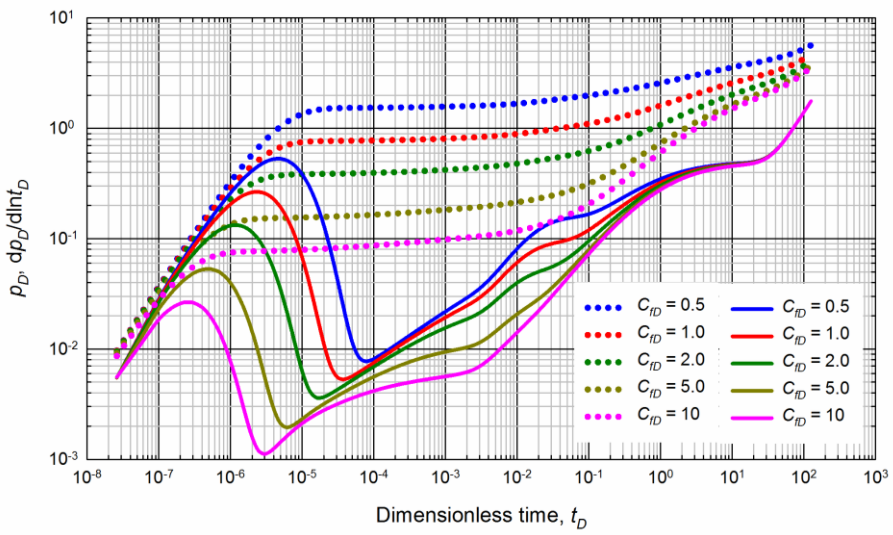

Figure 2-20. Pressure responses of the irregular-shaped horizontal fracture (shown in Figure 2-19) with different dimensionless fracture conductivities.

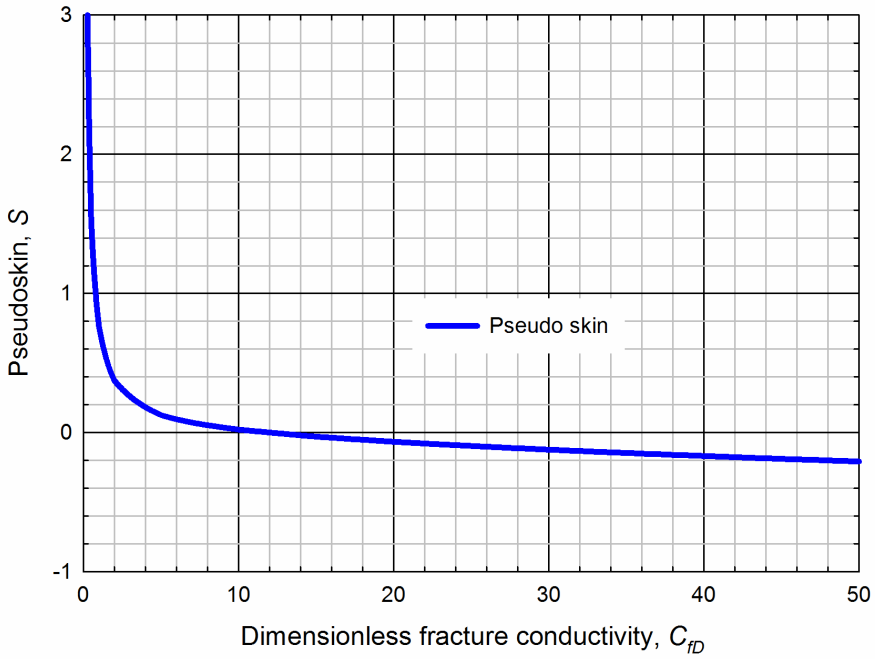

Figure 2-21. Pseudoskin factors of the irregular-shaped horizontal fracture (shown in Figure 2-19) with various dimensionless fracture conductivities.

2.5. Conclusions

In this work, a semi-analytical model is introduced and successfully applied to characterize the pressure transient behavior of finite-conductivity horizontal fractures in a bounded reservoir. With the use of the semi-analytical approach, we elucidate the influences of formation thickness,

fracture's vertical position, fracture conductivity, and wellbore storage on the pressure transient behavior of a circular horizontal fracture. The calculation results lead us to draw the following conclusions:

- The flow regimes that may be observed during the life of production of a circular horizontal fracture in a bounded reservoir are as follows: wellbore after flow, formation linear flow, early pseudo-radial flow, late pseudo-radial flow, and boundary dominated flow;
- At different formation thicknesses, the early pseudo-radial flows are induced by different flow mechanisms. An early pseudo-radial flow can be observed near the edge of the horizontal fractures when the formation thickness is small, while the early pseudo-radial flow can be observed surrounding the horizontal fracture in the vertical direction when the formation thickness becomes sufficiently large; and
- If the horizontal fracture is located near the lower or upper formation boundary, we can observe an early pseudo-radial flow that appears near the edge of the fracture, as well as an early pseudo-radial flow that surrounds the fracture along the vertical direction.

In addition, we study the pressure transient behavior of elliptical horizontal fractures and an irregular-shaped horizontal fracture. The major findings include the following:

- The axis ratio mainly exerts an influence on the early pseudo-radial flow period, and a smaller axis ratio renders the early pseudo-radial flow less distinguishable;
- The pseudoskin factors of the elliptical horizontal fracture are normally negative. This implies that an elliptical horizontal fracture can exhibit a higher productivity than a circular horizontal fracture at the late production period.

- The pseudoskin factor of an elliptical horizontal fracture decreases as its axis ratio decreases, indicating that an elliptical horizontal fracture has larger productivity with smaller axis ratio;
- The pseudoskin factor increases as the formation thickness increases, indicating that the elliptical horizontal fractures tend to enhance the well productivity more significantly in thinner formations;
- The fracture's vertical position has a negligible influence on the pseudoskin factor of the elliptical fractures; and
- The pressure response of the irregular-shaped horizontal fracture is similar to that of a circular horizontal fracture. In comparison to a circular horizontal fracture, this irregular-shaped fracture, which has the same area as the circular fracture, has positive pseudoskin factors with small dimensionless fracture conductivity while negative pseudoskin factors with larger dimensionless fracture conductivity.

Nomenclature

a = is semi-major axis, m

b = is semi-minor axis, m

a_D = dimensionless semi-major axis

b_D = dimensionless semi-minor axis

B = formation volume factor

c_f = fracture compressibility, MPa^{-1}

c_l = liquid compressibility, MPa^{-1}

c_{tf} = total compressibility of fracture, MPa^{-1}

c_{tm} = total compressibility of matrix, MPa^{-1}

C = wellbore storage coefficient, m^3/Mpa

C_s = a dimension coefficient defined in this work.

h = reservoir thickness, m

k_f = the fracture permeability, mD

k_m = matrix permeability, mD

l_r = reference length, m

N_f = number of the fracture elements

p = pressure, MPa

p_f = pressure in the fracture system, MPa

p_0 = reference pressure, MPa

$p_{w,cir}$ = dimensionless bottomhole pressure of the circular horizontal fracture

$p_{w,non}$ = dimensionless bottomhole pressure of the non-circular horizontal fracture

$q_{f\text{-}wD}$ = dimensionless flux from well-element to wellbore

q_{sc} = withdraw rate, m^3/d

q_w = production rate under standard condition, m^3/d

r_w = radius of the wellbore, m

r_{eq} = equivalent radius, m

s = Laplace operator

S = pseudoskin factor

t_0 = time when the source term becomes activated, day

t = time, day

u_x, u_y and u_z = Darcy flow rate, m/d

V_b = bulk volume, m^3

w = fracture width, m

x = x-coordinate, m

y = y-coordinate, m

z = z-coordinate, m

z_{vD} = fracture vertical position

α = diffusivity, m^2/d

β = unit conversion factor whose numerical value is 0.0853, $(m^2 \cdot s)/(mD \cdot d)$.

γ = a dimensionless coefficient

δ = influx of various dimensions, 1, m, m^2, or m^3

μ = viscosity, mPa·s

ρ = fluid density, kg/m^3

ρ_{sc} = fluid density under standard condition, kg/m^3

ϕ_0 = reference porosity

ϕ_f = porosity in the fracture

ϕ_m = matrix porosity

Subscripts and superscripts

f = fracture

i = initial condition

m = matrix

sc = standard condition

t = total

w = wellbore

Acknowledgements

The authors would like to acknowledge the financial supports provided by the Natural Science and Engineering Research Council of Canada (NSERC) as well as the financial supports from China Scholarship Council (CSC). The authors also thank Schlumberger for providing us the academic license of Eclipse.

Appendix 2A - Numerical Solution for the Oil Flow in the Horizontal Fracture

The 2D continuity equation is given as (Ertekin *et al*., 2001):

$$-\frac{\partial}{\partial x}\left(\rho u_x\right)-\frac{\partial}{\partial y}\left(\rho u_y\right)-\frac{\partial}{\partial z}\left(\rho u_z\right)+\frac{q_{sc}\rho_{sc}}{V_b}=\frac{\partial}{\partial t}\left(\rho\phi\right) \tag{2A-1}$$

where ρ is fluid density, u_x, u_y and u_z are Darcy flow rate, V_b is bulk volume, and for a single fracture element $V_b = w\Delta x_{i,j}\Delta y_{i,j}$. Equation (2A-1) is a partial differential equation, and one can solve it with finite difference method. Implicit finite difference method is utilized in this work because the results of implicit finite difference method are more stable than the explicit finite difference method. The finite difference approximation in this work is based on 5-point scheme, which has a truncation error proportional to $(\Delta x)^2$ (or $(\Delta y)^2$) and Δt. The implicit finite difference approximation based on the 5-point scheme can provide sufficiently accurate results for simulating the transient fracture flow. Multiplying Equation (2A-1) by the bulk volume gives:

$$-\frac{\partial}{\partial x}\left(\rho u_x w\Delta y\right)_{i,j}\Delta x_{i,j}-\frac{\partial}{\partial y}\left(\rho u_y w\Delta x\right)_{i,j}\Delta y_{i,j}+q_{sc_{i,j}}\rho_{sc}=\left(\Delta x\Delta y w\right)_{i,j}\frac{\partial}{\partial t}\left(\rho\phi\right) \tag{2A-2}$$

Based on Darcy equation, we have,

$$\begin{aligned} u_x &= -\beta\frac{k_{fx}}{\mu}\frac{\partial p}{\partial x} \\ u_y &= -\beta\frac{k_{fy}}{\mu}\frac{\partial p}{\partial y} \end{aligned} \tag{2A-3}$$

and the formation volume factor is defined as:

$$B=\frac{\rho_{sc}}{\rho} \tag{2A-4}$$

For a slightly compressible fluid, we have

$$\rho=\rho_0\left[1+c_l\left(p-p_0\right)\right] \tag{2A-5}$$

where c_l is fluid compressibility, p_0 and ρ_0 are reference pressure and reference density, respectively. For the porous media, we have

$$\phi = \phi_0 \left[1 + c_f \left(p - p_0 \right) \right] \tag{2A-6}$$

The fracture total compressibility is given as:

$$c_{tf} = c_f + c_l \tag{2A-7}$$

where ϕ_0 is reference porosity, and c_f is compressibility of the matrix or fracture. Inserting Equations (2A-3) to (2A-7) into Equation (2A-2) yields:

$$\begin{aligned} &\frac{\partial}{\partial x}\left(\beta \frac{\Delta y w k_{fx}}{\mu B} \frac{\partial p}{\partial x} \right)_{i,j} \Delta x_{i,j} + \frac{\partial}{\partial y}\left(\beta \frac{\Delta x w k_{fy}}{\mu B} \frac{\partial p}{\partial y} \right)_{i,j} \Delta y_{i,j} \\ &+ q_{sc_{i,j}} = \left(\frac{\Delta x \Delta y w \phi_f c_{tf}}{B} \right)_{i,j} \frac{\partial p_{i,j}}{\partial t} \end{aligned} \tag{2A-8}$$

Applying the finite difference approximation to the first term on the left-hand side of Equation (2A-8), one can have:

$$\frac{\partial}{\partial x}\left(\beta \frac{\Delta y w k_x}{\mu B} \frac{\partial p}{\partial x} \right)_{i,j} \approx \frac{1}{\Delta x_{i,j}} \left[\left(\beta \frac{\Delta y w k_x}{\mu B} \frac{\partial p}{\partial x} \right)_{i+\frac{1}{2},j} - \left(\beta \frac{\Delta y w k_x}{\mu B} \frac{\partial p}{\partial x} \right)_{i-\frac{1}{2},j} \right] \tag{2A-9}$$

where

$$\left(\frac{\partial p}{\partial x} \right)_{i+\frac{1}{2},j} \approx \frac{p_{i+1,j} - p_{i,j}}{\Delta x_{i+\frac{1}{2},j}} \tag{2A-10}$$

and

$$\left(\frac{\partial p}{\partial x} \right)_{i-\frac{1}{2},j} \approx \frac{p_{i,j} - p_{i-1,j}}{\Delta x_{i-\frac{1}{2},j}} \tag{2A-11}$$

Thus, Equation (2A-9) can be written as:

$$\frac{\partial}{\partial x}\left(\beta\frac{\Delta y w k_{fx}}{\mu B}\frac{\partial p}{\partial x}\right)_{i,j}\Delta x_{i,j}= \left(\beta\frac{\Delta y w k_{fx}}{\mu B\Delta x}\right)_{i+\frac{1}{2},j}\left(p^{n}_{i+1,j}-p^{n}_{i,j}\right)-\left(\beta\frac{\Delta y w k_{fx}}{\mu B\Delta x}\right)_{i-\frac{1}{2},j}\left(p^{n}_{i,j}-p^{n}_{i-1,j}\right) \tag{2A-12}$$

Similarly, the second term on the left-hand side of Equation (2A-8) can be rewritten as:

$$\frac{\partial}{\partial y}\left(\beta\frac{\Delta x w k_{fy}}{\mu B}\frac{\partial p}{\partial y}\right)_{i,j}\Delta y_{i,j}= \left(\beta\frac{\Delta x w k_{fy}}{\mu B\Delta y}\right)_{i,j+\frac{1}{2}}\left(p^{n}_{i,j+1}-p^{n}_{i,j}\right)-\left(\beta\frac{\Delta x w k_{fy}}{\mu B\Delta y}\right)_{i,j-\frac{1}{2}}\left(p^{n}_{i,j}-p^{n}_{i,j-1}\right) \tag{2A-13}$$

Applying backward-difference approximation on the time derivative, one can obtain:

$$\frac{\partial p_{i,j}}{\partial t}\approx\frac{p^{n}_{i,j}-p^{n-1}_{i,j}}{\Delta t} \tag{2A-14}$$

The backward-difference approximation of the flow equation can be written as:

$$\begin{aligned}&\left(\beta\frac{\Delta y w k_{fx}}{\mu B\Delta x}\right)_{i+\frac{1}{2},j}\left(p^{n}_{i+1,j}-p^{n}_{i,j}\right)-\left(\beta\frac{\Delta y w k_{fx}}{\mu B\Delta x}\right)_{i-\frac{1}{2},j}\left(p^{n}_{i,j}-p^{n}_{i-1,j}\right)\\ &+\left(\beta\frac{\Delta x w k_{fy}}{\mu B\Delta y}\right)_{i,j+\frac{1}{2}}\left(p^{n}_{i,j+1}-p^{n}_{i,j}\right)-\left(\beta\frac{\Delta x w k_{fy}}{\mu B\Delta y}\right)_{i,j-\frac{1}{2}}\left(p^{n}_{i,j}-p^{n}_{i,j-1}\right)\\ &+q_{sc_{i,j}}=\left(\frac{\Delta x\Delta y w\phi_{f}c_{tf}}{B\Delta t}\right)_{i,j}\left(p^{n}_{i,j}-p^{n-1}_{i,j}\right)\end{aligned} \tag{2A-15}$$

Equation (2A-15) can be used to characterize the transient flow in the fracture system. This equation is also applicable if the fracture has non-uniform fracture width and fracture conductivity distribution. In this work, we assume that the fracture width and fracture conductivity are both uniform along the fracture; thus, Equation (2A-15) can be simplified as:

$$\beta\frac{\Delta y_{i,j}wk_f}{\mu B\Delta x}\left(p^n_{i+1,j}-2p^n_{i,j}+p^n_{i-1,j}\right)+\beta\frac{\Delta x_{i,j}wk_f}{\mu B\Delta y}\left(p^n_{i,j+1}-2p^n_{i,j}+p^n_{i,j-1}\right)$$
$$+q_{sc_{i,j}}=\frac{\Delta x_{i,j}\Delta y_{i,j}w\phi_f c_{tf}}{B\Delta t}\left(p^n_{i,j}-p^{n-1}_{i,j}\right) \tag{2A-16}$$

In particular, for the well-element, the approximated flow equation can be written as:

$$\beta\frac{\Delta y_{i,j}wk_f}{\mu B\Delta x}\left(p^n_{i+1,j}-2p^n_{i,j}+p^n_{i-1,j}\right)+\beta\frac{\Delta x_{i,j}wk_f}{\mu B\Delta y}\left(p^n_{i,j+1}-2p^n_{i,j}+p^n_{i,j-1}\right)$$
$$+q_{sc_{i,j}}-q_{f-w}=\frac{\Delta x_{i,j}\Delta y_{i,j}w\phi_f c_{tf}}{B\Delta t}\left(p^n_{i,j}-p^{n-1}_{i,j}\right) \tag{2A-17}$$

Non-dimensionalizing the variables in Equation (2A-16) and (2A-17) based on Table 2-1 yields,

$$\frac{C_{fD}}{\Delta x_D^2 w_D C_s}\left(2p^n_{fD_{i,j}}-p^n_{fD_{i+1,j}}-p^n_{fD_{i-1,j}}\right)+\frac{C_{fD}}{\Delta y_D^2 w_D C_s}\left(2p^n_{fD_{i,j}}-p^n_{fD_{i,j+1}}-p^n_{fD_{i,j-1}}\right)$$
$$+\frac{2\pi h_D}{\Delta x_D\Delta y_D w_D C_s}q^n_{fD_{i,j}}=\frac{1}{\Delta t_D}\left(p^{n-1}_{fD_{i,j}}-p^n_{fD_{i,j}}\right) \tag{2A-18}$$

and

$$\frac{C_{fD}}{\Delta x_D^2 w_D C_s}\left(2p^n_{fD_{i,j}}-p^n_{fD_{i+1,j}}-p^n_{fD_{i-1,j}}\right)+\frac{C_{fD}}{\Delta y_D^2 w_D C_s}\left(2p^n_{fD_{i,j}}-p^n_{fD_{i,j+1}}-p^n_{fD_{i,j-1}}\right)$$
$$+\frac{2\pi h_D}{\Delta x_D\Delta y_D w_D C_s}\left(q^n_{fD_{i,j}}-q^n_{f-wD}\right)=\frac{1}{\Delta t_D}\left(p^{n-1}_{fD_{i,j}}-p^n_{fD_{i,j}}\right) \tag{2A-19}$$

Rearranging Equation (2A-18) and (2A-19) gives the following:

$$\left(\frac{2C_{fD}}{\Delta x_D^2 w_D C_s}+\frac{2C_{fD}}{\Delta y_D^2 w_D C_s}+\frac{1}{\Delta t_D}\right)p^n_{fD_{i,j}}-\frac{2C_{fD}}{\Delta x_D^2 w_D C_s}p^n_{fD_{i-1,j}}-\frac{C_{fD}}{\Delta y_D^2 w_D C_s}p^n_{fD_{i,j-1}}$$
$$-\frac{2C_{fD}}{\Delta x_D^2 w_D C_s}p^n_{fD_{i+1,j}}-\frac{C_{fD}}{\Delta y_D^2 w_D C_s}p^n_{fD_{i,j+1}}+\frac{2\pi h_D}{\Delta x_D\Delta y_D w_D C_s}q^n_{fD_{i,j}}=\frac{1}{\Delta t_D}p^{n-1}_{fD_{i,j}} \tag{2A-20}$$

$$\left(\frac{2C_{fD}}{\Delta x_D^2 w_D C_s}+\frac{2C_{fD}}{\Delta y_D^2 w_D C_s}+\frac{1}{\Delta t_D}\right)p^n_{fD_{i,j}}-\frac{2C_{fD}}{\Delta x_D^2 w_D C_s}p^n_{fD_{i-1,j}}-\frac{C_{fD}}{\Delta y_D^2 w_D C_s}p^n_{fD_{i,j-1}}$$
$$-\frac{2C_{fD}}{\Delta x_D^2 w_D C_s}p^n_{fD_{i+1,j}}-\frac{C_{fD}}{\Delta y_D^2 w_D C_s}p^n_{fD_{i,j+1}}+\frac{2\pi h_D}{\Delta x_D\Delta y_D w_D C_s}q^n_{fD_{i,j}}-\frac{2\pi h_D}{\Delta x_D\Delta y_D w_D C_s}q^n_{f-wD}=\frac{1}{\Delta t_D}p^{n-1}_{fD_{i,j}} \tag{2A-21}$$

As such, in Equation (2A-20) and (2A-21), the dimensionless pressures, dimensionless withdrawal rates and dimensionless flux from fracture to wellbore on the LHS become the unknowns. The flow equations for the N_f facture elements can be then written in a matrix form,

$$\begin{bmatrix} \boldsymbol{A} & \boldsymbol{a} \end{bmatrix} \cdot \begin{bmatrix} \boldsymbol{p}_{fD} \\ \boldsymbol{q}_{fD} \\ q^n_{f-wD} \end{bmatrix} = \boldsymbol{RHS}_1 \tag{2A-22}$$

where

$$\boldsymbol{a} = \begin{bmatrix} \left.\begin{matrix} 0 \\ \vdots \\ 0 \end{matrix}\right\} n_w - 1 \\ -\dfrac{2\pi h_D}{\Delta x_D \Delta y_D w_D C_s} \\ 0 \\ 0 \\ \vdots \\ 0 \end{bmatrix}_{N_f \times 1}, \quad \boldsymbol{p}_{fD} = \begin{bmatrix} p^n_{fD_1} \\ \vdots \\ p^n_{fD_{nw}} \\ \vdots \\ p^n_{fD_{N_f}} \end{bmatrix}_{N_f \times 1}, \quad \boldsymbol{q}_{fD} = \begin{bmatrix} q^n_{fD_1} \\ \vdots \\ q^n_{fD_{nw}} \\ \vdots \\ q^n_{fD_{N_f}} \end{bmatrix}_{N_f \times 1}, \text{ and } \boldsymbol{RHS_1} = \begin{bmatrix} \dfrac{1}{\Delta t_D} p^{n-1}_{fD_1} \\ \vdots \\ \dfrac{1}{\Delta t_D} p^{n-1}_{fD_{nw}} \\ \vdots \\ \dfrac{1}{\Delta t_D} p^{n-1}_{fD_{N_f}} \end{bmatrix}_{N_f \times 1},$$

where $\boldsymbol{A}$ is a matrix with a dimension of $N_f \times 2N_f$, and it represents the coefficients of the dimensionless pressures and the coefficients of dimensionless withdrawal rates of the fracture elements in Equation (2A-20) and (2A-21), and n_w is the number of the well-element.

Appendix 2B - Analytical Solution for the Oil Flow in the Reservoir Matrix

Figure 2B-1 shows a line source in a bounded reservoir and a plane source in a bounded reservoir, respectively. In a 2D reservoir, the pressure response at position x at time t caused by an instantaneous line source which is activated at time t_0 is given by Gringarten and Ramey (1973):

$$p_i - p(x,t) = \frac{\delta}{\phi_m c_{tm}} \frac{1}{x_e} \left\{ 1 + 2\sum_{m=1}^{\infty} \exp\left[-\frac{m^2 \pi^2 \alpha (t - t_0)}{x_e^2} \right] \cos\frac{m\pi x_0}{x_e} \cos\frac{m\pi x}{x_e} \right\} \qquad (2B\text{-}1)$$

where δ is the withdrawal rate per unit length, unit area or unit volume. Equation (2B-1) is derived using the Green function method. Similarly, the following equation can be used to predict the pressure response at position x at time t caused by an instantaneous plane source which is activated at time t_0,

$$p_i - p(x,t) = \frac{\delta}{\phi_m c_{tm}} \frac{x_f}{x_e} \left\{ 1 + \frac{4x_e}{\pi \Delta x} \sum_{m=1}^{\infty} \frac{1}{n} \exp\left[-\frac{m^2 \pi^2 \alpha (t - t_0)}{x_e^2} \right] \sin\frac{m\pi \Delta x}{2x_e} \cos\frac{m\pi x_0}{x_e} \cos\frac{m\pi x}{x_e} \right\} \qquad (2B\text{-}2)$$

where Δx is the width of the plane source.

Figure 2B-2 shows a plane source in a 3D bounded reservoir. According to the Newman product principle, the pressure response of an instantaneous plane source in a 3D reservoir can be obtained by the product of a plane source in X direction and a plane source in Y direction and a line source in Z direction:

$$
\begin{aligned}
&p_i - p(x,y,z,t) = \\
&\frac{\delta}{\phi_m c_{tm}} \frac{x_f}{x_e} \left\{ 1 + \frac{4x_e}{\pi \Delta x} \sum_{m=1}^{\infty} \frac{1}{m} \exp\left[-\frac{m^2 \pi^2 \alpha (t - t_0)}{x_e^2} \right] \sin \frac{m\pi \Delta x}{2x_e} \cos \frac{m\pi x_0}{x_e} \cos \frac{m\pi x}{x_e} \right\} \\
&\cdot \frac{y_f}{y_e} \left\{ 1 + \frac{4y_e}{\pi \Delta y} \sum_{m=1}^{\infty} \frac{1}{m} \exp\left[-\frac{m^2 \pi^2 \alpha (t - t_0)}{y_e^2} \right] \sin \frac{m\pi \Delta y}{2y_e} \cos \frac{m\pi y_0}{y_e} \cos \frac{m\pi y}{y_e} \right\} \\
&\cdot \frac{1}{z_e} \left\{ 1 + 2 \sum_{m=1}^{\infty} \exp\left[-\frac{m^2 \pi^2 \alpha (t - t_0)}{z_e^2} \right] \cos \frac{m\pi z_0}{z_e} \cos \frac{m\pi z}{z_e} \right\}
\end{aligned}
\tag{2B-3}
$$

The pressure response at point (x, y, z) at time t due to the contribution by a continuous plane source with a withdrawal rate of q_{sc} can be calculated by:

$$
\begin{aligned}
&p_i - p(x,y,z,t) = \frac{q(t)}{\phi_m c_{tm}} \int_0^{t-t_0} \\
&\frac{x_f}{x_e} \left\{ 1 + \frac{4x_e}{\pi \Delta x} \sum_{m=1}^{\infty} \frac{1}{m} \exp\left[-\frac{m^2 \pi^2 \alpha (t - t_0 - \tau)}{x_e^2} \right] \sin \frac{m\pi \Delta x}{2x_e} \cos \frac{m\pi x_0}{x_e} \cos \frac{m\pi x}{x_e} \right\} \\
&\cdot \frac{y_f}{y_e} \left\{ 1 + \frac{4y_e}{\pi \Delta y} \sum_{m=1}^{\infty} \frac{1}{m} \exp\left[-\frac{m^2 \pi^2 \alpha (t - t_0 - \tau)}{y_e^2} \right] \sin \frac{m\pi \Delta y}{2y_e} \cos \frac{m\pi y_0}{y_e} \cos \frac{m\pi y}{y_e} \right\} \\
&\cdot \frac{1}{z_e} \left\{ 1 + 2 \sum_{m=1}^{\infty} \exp\left[-\frac{m^2 \pi^2 \alpha (t - t_0 - \tau)}{z_e^2} \right] \cos \frac{m\pi z_0}{z_e} \cos \frac{m\pi z}{z_e} \right\} \mathrm{d}\tau
\end{aligned}
\tag{2B-4}
$$

where

$$
q(t) = \frac{q(t)}{x_f y_f} = \frac{B q_{sc}(t)}{x_f y_f} \tag{2B-5}
$$

Thus, Equation (2B-4) can be written as:

$$
\begin{aligned}
p_i - p(x,y,z,t) &= \frac{Bq_{sc}(t)}{\phi_m c_{tm} x_e y_e z_e}\int_0^{t-t_0} \\
&\left\{1+\frac{4x_e}{\pi\Delta x}\sum_{m=1}^{\infty}\frac{1}{m}\exp\left[-\frac{m^2\pi^2\alpha(t-t_0-\tau)}{x_e^2}\right]\sin\frac{m\pi\Delta x}{2x_e}\cos\frac{m\pi x_0}{x_e}\cos\frac{m\pi x}{x_e}\right\} \\
&\cdot\left\{1+\frac{4y_e}{\pi\Delta y}\sum_{m=1}^{\infty}\frac{1}{m}\exp\left[-\frac{m^2\pi^2\alpha(t-t_0-\tau)}{y_e^2}\right]\sin\frac{m\pi\Delta y}{2y_e}\cos\frac{m\pi y_0}{y_e}\cos\frac{m\pi y}{y_e}\right\} \\
&\cdot\left\{1+2\sum_{m=1}^{\infty}\exp\left[-\frac{m^2\pi^2\alpha(t-t_0-\tau)}{z_e^2}\right]\cos\frac{m\pi z_0}{z_e}\cos\frac{m\pi z}{z_e}\right\}\mathrm{d}\tau
\end{aligned}
\tag{2B-6}
$$

In the production period, the withdrawal rate of a plane source is time-dependent. The pressure response at position (x, y, z) at time t^n caused by a time-dependent continuous plane source is,

$$
\begin{aligned}
p_i - p(x,y,z,t^n) &= \frac{B}{\phi_m c_{tm} x_e y_e z_e}\sum_{l=1}^{l=n}\left(q_{sc}^{l}-q_{sc}^{l-1}\right)\int_0^{t^n-t^{l-1}} \\
&\left\{1+\frac{4x_e}{\pi\Delta x}\sum_{m=1}^{\infty}\frac{1}{m}\exp\left[-\frac{m^2\pi^2\alpha(t^n-t^{l-1}-\tau)}{x_e^2}\right]\sin\frac{m\pi\Delta x}{2x_e}\cos\frac{m\pi x_0}{x_e}\cos\frac{m\pi x}{x_e}\right\} \\
&\cdot\left\{1+\frac{4y_e}{\pi\Delta y}\sum_{m=1}^{\infty}\frac{1}{m}\exp\left[-\frac{m^2\pi^2\alpha(t^n-t^{l-1}-\tau)}{y_e^2}\right]\sin\frac{m\pi\Delta y}{2y_e}\cos\frac{m\pi y_0}{y_e}\cos\frac{m\pi y}{y_e}\right\} \\
&\cdot\left\{1+2\sum_{m=1}^{\infty}\exp\left[-\frac{m^2\pi^2\alpha(t^n-t^{l-1}-\tau)}{z_e^2}\right]\cos\frac{m\pi z_0}{z_e}\cos\frac{m\pi z}{z_e}\right\}\mathrm{d}\tau
\end{aligned}
\tag{2B-7}
$$

Since we discretize the horizontal fracture into N_f fracture elements, the pressure response at a given position (x, y, z) should be the summation of the pressure responses caused by all of the elements, leading to the following:

$$
\begin{aligned}
p_i - p\left(x,y,z,t^n\right) &= \frac{B}{\phi_m c_{tm} x_e y_e z_e}\sum_{k=1}^{k=Nf}\sum_{l=1}^{l=n}\left(q_{f,k}^{l}-q_{f,k}^{l-1}\right)\int_0^{t^n-t^{l-1}} \\
&\left\{1+\frac{4x_e}{\pi\Delta x_k}\sum_{m=1}^{\infty}\frac{1}{m}\exp\left[-\frac{m^2\pi^2\alpha\left(t^n-t^{l-1}-\tau\right)}{x_e^2}\right]\sin\frac{m\pi\Delta x_k}{2x_e}\cos\frac{m\pi x_{0,k}}{x_e}\cos\frac{m\pi x}{x_e}\right\} \\
&\cdot\left\{1+\frac{4y_e}{\pi\Delta y_k}\sum_{m=1}^{\infty}\frac{1}{m}\exp\left[-\frac{m^2\pi^2\alpha\left(t^n-t^{l-1}-\tau\right)}{y_e^2}\right]\sin\frac{m\pi\Delta y_k}{2y_e}\cos\frac{m\pi y_{0,k}}{y_e}\cos\frac{m\pi y}{y_e}\right\} \\
&\cdot\left\{1+2\sum_{m=1}^{\infty}\exp\left[-\frac{m^2\pi^2\alpha\left(t^n-t^{l-1}-\tau\right)}{z_e^2}\right]\cos\frac{m\pi z_{0,k}}{z_e}\cos\frac{m\pi z}{z_e}\right\}\mathrm{d}\tau
\end{aligned}
\tag{2B-8}
$$

Equation (2B-8) can be written in a dimensionless form,

$$
\begin{aligned}
p_D^n\left(x_D,y_D,z_D,t_D^n\right) &= \frac{2\pi}{x_{eD}y_{eD}}\sum_{k=1}^{k=Nf}\sum_{l=1}^{l=n}\left(q_{fD,k}^{l}-q_{fD,k}^{l-1}\right)\int_0^{t_D^n-t_D^{l-1}} \\
&\left\{1+\frac{4x_{eD}}{\pi\Delta x_{D,k}}\sum_{m=1}^{\infty}\frac{1}{m}\exp\left[-\frac{m^2\pi^2\left(t_D^n-t_D^{l-1}-\tau_D\right)}{x_{eD}^2}\right]\sin\frac{m\pi\Delta x_{D,k}}{2x_{eD}}\cos\frac{m\pi x_{0D,k}}{x_{eD}}\cos\frac{m\pi x_D}{x_{eD}}\right\} \\
&\cdot\left\{1+\frac{4y_{eD}}{\pi\Delta y_{D,k}}\sum_{m=1}^{\infty}\frac{1}{m}\exp\left[-\frac{m^2\pi^2\left(t_D^n-t_D^{l-1}-\tau_D\right)}{y_{eD}^2}\right]\sin\frac{m\pi\Delta y_{D,k}}{2y_{eD}}\cos\frac{m\pi y_{0D,k}}{y_{eD}}\cos\frac{m\pi y_D}{y_{eD}}\right\} \\
&\cdot\left\{1+2\sum_{m=1}^{\infty}\exp\left[-\frac{m^2\pi^2\left(t_D^n-t_D^{l-1}-\tau_D\right)}{z_{eD}^2}\right]\cos\frac{m\pi z_{0D,k}}{z_{eD}}\cos\frac{m\pi z_D}{z_{eD}}\right\}\mathrm{d}\tau_D
\end{aligned}
\tag{2B-9}
$$

Based on Equation (2B-9), one can have,

$$
\begin{aligned}
p_D^{n-1}\left(x_D,y_D,z_D,t_D^{n-1}\right) &= \frac{2\pi}{x_{eD}y_{eD}}\sum_{k=1}^{k=Nf}\sum_{l=1}^{l=n-1}\left(q_{fD,k}^{l}-q_{fD,k}^{l-1}\right)\int_0^{t_D^{n-1}-t_D^{l-1}} \\
&\left\{1+\frac{4x_{eD}}{\pi\Delta x_{D,k}}\sum_{m=1}^{\infty}\frac{1}{m}\exp\left[-\frac{m^2\pi^2\left(t_D^{n-1}-t_D^{l-1}-\tau_D\right)}{x_{eD}^2}\right]\sin\frac{m\pi\Delta x_{D,k}}{2x_{eD}}\cos\frac{m\pi x_{0D,k}}{x_{eD}}\cos\frac{m\pi x_D}{x_{eD}}\right\} \\
&\cdot\left\{1+\frac{4y_{eD}}{\pi\Delta y_{D,k}}\sum_{m=1}^{\infty}\frac{1}{m}\exp\left[-\frac{m^2\pi^2\left(t_D^{n-1}-t_D^{l-1}-\tau_D\right)}{y_{eD}^2}\right]\sin\frac{m\pi\Delta y_{D,k}}{2y_{eD}}\cos\frac{m\pi y_{0D,k}}{y_{eD}}\cos\frac{m\pi y_D}{y_{eD}}\right\} \\
&\cdot\left\{1+2\sum_{m=1}^{\infty}\exp\left[-\frac{m^2\pi^2\left(t_D^{n-1}-t_D^{l-1}-\tau_D\right)}{z_{eD}^2}\right]\cos\frac{m\pi z_{0D,k}}{z_{eD}}\cos\frac{m\pi z_D}{z_{eD}}\right\}\mathrm{d}\tau_D
\end{aligned}
\tag{2B-10}
$$

Combining Equation (2B-9) with Equation (2B-10), one can have:

$$
\begin{aligned}
p_D^n\left(x_D,y_D,z_D,t_D^n\right)&=p_D^{n-1}+\frac{2\pi}{x_{eD}y_{eD}}\sum_{k=1}^{k=Nf}\sum_{l=1}^{l=n}\left(q_{fD,k}^{l}-q_{fD,k}^{l-1}\right)\int_{t_D^{n-1}-t_D^{l-1}}^{t_D^n-t_D^{l-1}}\\
&\left\{1+\frac{4x_{eD}}{\pi\Delta x_{D,k}}\sum_{m=1}^{\infty}\frac{1}{m}\exp\left[-\frac{m^2\pi^2\left(t_D^n-t_D^{l-1}-\tau_D\right)}{x_{eD}^2}\right]\sin\frac{m\pi\Delta x_{D,k}}{2x_{eD}}\cos\frac{m\pi x_{0D,k}}{x_{eD}}\cos\frac{m\pi x_D}{x_{eD}}\right\}\\
&\cdot\left\{1+\frac{4y_{eD}}{\pi\Delta y_{D,k}}\sum_{m=1}^{\infty}\frac{1}{m}\exp\left[-\frac{m^2\pi^2\left(t_D^n-t_D^{l-1}-\tau_D\right)}{y_{eD}^2}\right]\sin\frac{m\pi\Delta y_{D,k}}{2y_{eD}}\cos\frac{m\pi y_{0D,k}}{y_{eD}}\cos\frac{m\pi y_D}{y_{eD}}\right\}\\
&\cdot\left\{1+2\sum_{m=1}^{\infty}\exp\left[-\frac{m^2\pi^2\left(t_D^n-t_D^{l-1}-\tau_D\right)}{z_{eD}^2}\right]\cos\frac{m\pi z_{0D,k}}{z_{eD}}\cos\frac{m\pi z_D}{z_{eD}}\right\}\mathrm{d}\tau_D
\end{aligned}
\tag{2B-11}
$$

As for a given fracture element, we use the dimensionless pressure at the center of this fracture element to represent the average pressure within this fracture element. Based on Equation (2B-11), the dimensionless pressure at the center of the fracture element can be obtained by:

$$
\begin{aligned}
p_{fD,g}^n\left(x_{0D,g},y_{0D,g},z_{0D,g},t_D^n\right)&=p_{fD,g}^{n-1}+\frac{2\pi}{x_{eD}y_{eD}}\sum_{k=1}^{k=Nf}\sum_{l=1}^{l=n}\left(q_{fD,k}^{l}-q_{fD,k}^{l-1}\right)\int_{t_D^{n-1}-t_D^{l-1}}^{t_D^n-t_D^{l-1}}\\
&\left\{1+\frac{4x_{eD}}{\pi\Delta x_{D,k}}\sum_{m=1}^{\infty}\frac{1}{m}\exp\left[-\frac{m^2\pi^2\left(t_D^n-t_D^{l-1}-\tau_D\right)}{x_{eD}^2}\right]\sin\frac{m\pi\Delta x_{D,k}}{2x_{eD}}\cos\frac{m\pi x_{0D,k}}{x_{eD}}\cos\frac{m\pi x_{0D,g}}{x_{eD}}\right\}\\
&\cdot\left\{1+\frac{4y_{eD}}{\pi\Delta y_{D,k}}\sum_{m=1}^{\infty}\frac{1}{m}\exp\left[-\frac{m^2\pi^2\left(t_D^n-t_D^{l-1}-\tau_D\right)}{y_{eD}^2}\right]\sin\frac{m\pi\Delta y_{D,k}}{2y_{eD}}\cos\frac{m\pi y_{0D,k}}{y_{eD}}\cos\frac{m\pi y_{0D,g}}{y_{eD}}\right\}\\
&\cdot\left\{1+2\sum_{m=1}^{\infty}\exp\left[-\frac{m^2\pi^2\left(t_D^n-t_D^{l-1}-\tau_D\right)}{z_{eD}^2}\right]\cos\frac{m\pi z_{0D,k}}{z_{eD}}\cos\frac{m\pi z_{0D,g}}{z_{eD}}\right\}\mathrm{d}\tau_D
\end{aligned}
\tag{2B-12}
$$

where, ($x_{0D,g}$, $y_{0D,g}$, $z_{0D,g}$) indicates the position of the center of the g^{th} fracture element (g= 1, 2,…N_f), and $p_{fD,g}$ indicates the dimensionless average pressure of the g^{th} fracture element. For convenience, Equation (2B-12) can be also written as:

$$
p_{fD,g}^n\left(x_{0D,g},y_{0D,g},z_{0D,g},t_D^n\right)=p_{fD,g}^{n-1}+\sum_{k=1}^{k=Nf}\sum_{l=1}^{l=n}\left(q_{fD,k}^{l}-q_{fD,k}^{l-1}\right)G_{l,k,g} \tag{2B-13}
$$

where

$$
\begin{aligned}
G_{l,k,g} &= \frac{2\pi}{x_{eD}y_{eD}}\int_{t_D^{n-1}-t_D^{l-1}}^{t_D^{n}-t_D^{l-1}} \\
&\cdot\left\{1+\frac{4x_{eD}}{\pi\Delta x_{D,k}}\sum_{m=1}^{\infty}\frac{1}{m}\exp\left[-\frac{m^2\pi^2\left(t_D^n-t_D^{l-1}-\tau_D\right)}{x_{eD}^2}\right]\sin\frac{m\pi\Delta x_{D,k}}{2x_{eD}}\cos\frac{m\pi x_{0D,k}}{x_{eD}}\cos\frac{m\pi x_{0D,g}}{x_{eD}}\right\} \\
&\cdot\left\{1+\frac{4y_{eD}}{\pi\Delta y_{D,k}}\sum_{m=1}^{\infty}\frac{1}{m}\exp\left[-\frac{m^2\pi^2\left(t_D^n-t_D^{l-1}-\tau_D\right)}{y_{eD}^2}\right]\sin\frac{m\pi\Delta y_{D,k}}{2y_{eD}}\cos\frac{m\pi y_{0D,k}}{y_{eD}}\cos\frac{m\pi y_{0D,g}}{y_{eD}}\right\} \\
&\cdot\left\{1+2\sum_{m=1}^{\infty}\exp\left[-\frac{m^2\pi^2\left(t_D^n-t_D^{l-1}-\tau_D\right)}{z_{eD}^2}\right]\cos\frac{m\pi z_{0D,k}}{z_{eD}}\cos\frac{m\pi z_{0D,g}}{z_{eD}}\right\}\mathrm{d}\tau_D
\end{aligned}
\tag{2B-14}
$$

Moving the unknowns in Equation (2B-13) to the left-hand side, one can have:

$$
p_{fD,g}^{n}-\sum_{k=1}^{k=Nf}q_{fD,k}^{n}G_{n,k,g}=p_{fD,g}^{n-1}+\left(\sum_{k=1}^{k=Nf}\sum_{l=1}^{l=n-1}q_{fD,k}^{l}G_{l,k,g}-\sum_{k=1}^{k=Nf}\sum_{l=1}^{l=n}q_{fD,k}^{l-1}G_{l,k,g}\right) \tag{2B-15}
$$

As a result, one can formulate the dimensionless pressures of the fractures elements and dimensionless withdrawal rates of the fracture elements into a matrix form:

$$
\boldsymbol{B}\cdot\begin{bmatrix}\boldsymbol{p}_{fD}\\ \boldsymbol{q}_{fD}\end{bmatrix}=\boldsymbol{RHS}_2 \tag{2B-16}
$$

where

$$
\boldsymbol{B}=\begin{bmatrix}
\underbrace{1\quad 0\quad 0\quad 0\quad\cdots\quad 0\quad 0}_{Nf} & \underbrace{G_{n,1,1}\cdots G_{n,k,1}\cdots G_{n,Nf,1}}_{Nf}\\
 & \vdots\\
\underbrace{0\quad\cdots\quad 0}_{g-1}\ \underbrace{1\quad 0\quad\cdots\quad 0}_{Nf} & \underbrace{G_{n,1,g}\cdots G_{n,k,g}\cdots G_{n,Nf,g}}_{Nf}\\
 & \vdots\\
\underbrace{0\quad 0\quad\cdots\quad 0\quad 0\quad 0\quad 1}_{Nf} & \underbrace{G_{n,1,Nf}\cdots G_{n,k,Nf}\cdots G_{n,Nf,Nf}}_{Nf}
\end{bmatrix}_{N_f\times 2N_f}
\tag{2B-17}
$$

$$\boldsymbol{RHS}_2 = \begin{bmatrix} p_{fD,1}^{n-1} + \left(\sum_{k=1}^{k=Nf} \sum_{l=1}^{l=n-1} q_{fD,k}^{l} G_{l,k,1} - \sum_{k=1}^{k=Nf} \sum_{l=1}^{l=n} q_{fD,k}^{l-1} G_{l,k,1} \right) \\ \vdots \\ p_{fD,g}^{n-1} + \left(\sum_{k=1}^{k=Nf} \sum_{l=1}^{l=n-1} q_{fD,k}^{l} G_{l,k,g} - \sum_{k=1}^{k=Nf} \sum_{l=1}^{l=n} q_{fD,k}^{l-1} G_{l,k,g} \right) \\ \vdots \\ p_{fD,Nf}^{n-1} + \left(\sum_{k=1}^{k=Nf} \sum_{l=1}^{l=n-1} q_{fD,k}^{l} G_{l,k,Nf} - \sum_{k=1}^{k=Nf} \sum_{l=1}^{l=n} q_{fD,k}^{l-1} G_{l,k,Nf} \right) \end{bmatrix}_{N_f \times 1} \tag{2B-18}$$

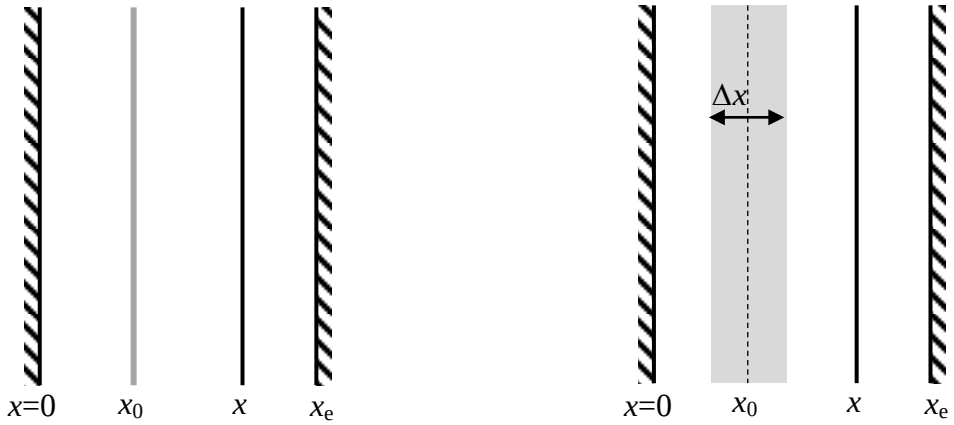

Figure 2B-1. A line source and a plane source in a 2D reservoir: **(**a) a line source in a bounded reservoir; and (b) a plane source in a bounded reservoir.

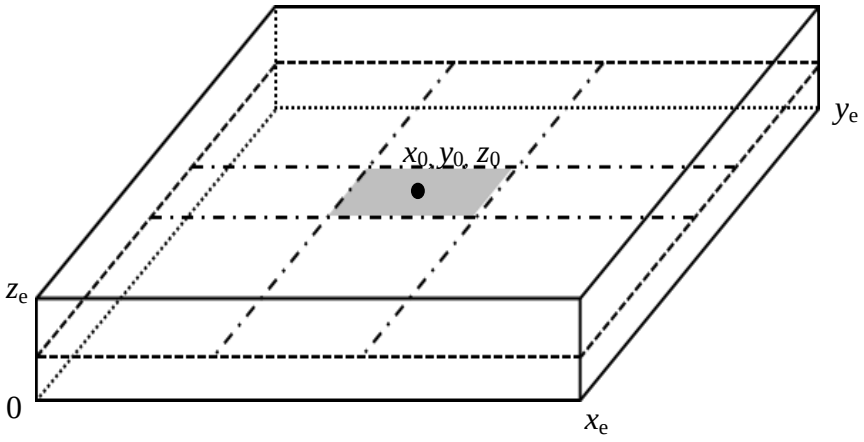

Figure 2B-2. A plane source in a 3D bounded reservoir.

References

AccuMap, IHS, 2013.

Brown, M.L., Ozkan, E., Raghavan, R.S., and Kazemi, H. Practical Solutions for Pressure Transient Responses of Fractured Horizontal Wells in Unconventional Reservoirs. *SPE Res. Eval. Eng.* 14 (05): 663-676 (2009).

Chen, C., and Raghavan, R. A Multiply-Fractured Horizontal Well in a Rectangular Drainage Region. *SPE J.* 2 (04): 455-465 (1997).

Chen, H.Y. *Well Behavior in Naturally Fractured Reservoirs*. PhD Dissertation, Texas A&M University, College Station, Texas (1990).

Chen, H.Y., Poston, S.W., and Raghavan, R. An Application of the Product Solution Principle for Instantaneous Source and Green's Functions. *SPE Form. Eval.* 6 (02): 161-167 (1991).

Chen, Z., Liao, X., Zhao, X., Lv, S., and Zhu, L. A Semianalytical Approach for Obtaining Type Curves of Multiple-Fractured Horizontal Wells with Secondary-Fracture Networks. *SPE J.* 21 (02): 538-549 (2016).

Chhina, H.S., Luhning, R.W., Bilak, R.A., and Best, D.A. A Horizontal Fracture Test in the Athabasca Oil Sands. Paper PETSOC-87-38-56 presented at Annual Technical Meeting, Calgary, Alberta, June 7 – 10 (1987).

Cinco-Ley, H., and Samaniego-V., F. Transient Pressure Analysis for Fractured Wells. *J. Pet. Tech.* 33 (09): 1749-1766 (1981).

Cinco-Ley, H., Samaniego-V., F., and Dominguez-A., N. Transient Pressure Behavior for a Well with a Finite-Conductivity Vertical Fracture. *SPE J.* 18 (04): 253-264 (1978).

Crawford, P.B., and Landrum, B.L. Estimated Effect of Horizontal Fractures on Production Capacity. Paper SPE 441-G presented at Fall Meeting of the Petroleum Branch of AIME, San Antonio, Texas, 17-20 October (1954).

Crawford, P.B., Pinson, J., Simmons, J., and Landrum, B.L. Effect of Elliptical Fractures on Sweep Efficiencies in Water Flooding or Fluid Injection Programs. SPE-602-MS (1963).

Ertekin, T., Abou-Kassem, J.H., and King, G.R. *Basic Applied Reservoir Simulation*. SPE Textbook Series (2001).

Escobar, F.H., and Montealegre, M. Conventional Analysis for the Determination of the Horizontal Permeability from the Elliptical Flow of Horizontal Wells. Paper SPE 105928

presented at Production and Operations Symposium, Oklahoma City, Oklahoma, U.S.A., 31 March-3 April (2007).

Gringarten, A.C., and Ramey, H.J. The Use of Source and Green's Functions in Solving Unsteady-Flow Problems in Reservoirs. *SPE J.* 13 (05): 285-296 (1973).

Gringarten, A.C., and Ramey, H.J. Unsteady-State Pressure Distributions Created by a Well with a Single Infinite-Conductivity Vertical Fracture. *SPE J.* 14 (04): 347-360 (1974).

Gringarten, A.C., and Ramey, H.J. Unsteady-State Pressure Distributions Created by a Well with a Single Horizontal Fracture, Partial Penetration, or Restricted Entry. *SPE J.* 14 (04): 413-426 (1974).

Hubbert, M.K., and Willis, D.G. Mechanics of Hydraulic Fracturing. *Trans. AIME* 210: 153-168 (1957).

Kucuk, F., and Brigham, W.E. Transient Flow in Elliptical Systems. *SPE J.* 19 (06): 401-410 (1979).

Larsen, L. Horizontal Fractures in Single and Multilayer Reservoirs. Paper SPE 147004 presented at Canadian Unconventional Resources Conference, Calgary, Alberta, 15-17 November (2011).

Nicholl, M.J., and Glass, R.J. Simulation of Immiscible Viscous Displacement within the Plane of a Horizontal Fracture. Paper ARMA-01-0205 presented at the 38th U.S. Symposium on Rock Mechanics (USRMS), Washington, D.C., 7-10 July (2001).

Ogunsanya, B.O., Oetama, T.P., Lea, J.F., Heinze, L.R., and Adisoemarta, P.S. A Robust Type Curve Solution for Analyzing Pressure-Transient Behaviors of both Vertical and Horizontal Fracture Systems. Paper SPE 105979 presented at Nigeria Annual International Conference and Exhibition, Abuja, Nigeria, 31 July-2 August (2006).

Ozkan, E., and Raghavan, R. New Solutions for Well-Test-Analysis Problems: Part 1-Analytical Considerations. *SPE Form. Eval.* 6 (03): 359-368 (1991).

Ozkan, E., Brown, M.L., Raghavan, R., and Kazemi, H. Comparison of Fractured-Horizontal-Well Performance in Tight Sand and Shale Reservoirs. *SPE Res. Eval. Eng.* 14 (02): 248-259 (2011).

Peaceman, D.W. Interpretation of Wellblock Pressures in Numerical Reservoir Simulation: Part 3 - Off-Center and Multiple Wells within a Wellblock. *SPE Res. Eng.* 5 (02): 227-232 (1990).

Reynolds, A.C., Chen, J.C., and Raghavan, R. Pseudoskin Factor Caused by Partial Penetration. *J. Pet. Tech.* 36 (12): 2197-2210 (1984).

Singh, K., and Whitson, C.H. Gas-Condensate Pseudopressure in Layered Reservoirs. *SPE Res. Eval. Eng*. 13 (02): 203-213 (2010).

Smith, M.B., and Montgomery, C. *Hydraulic Fracturing.* CRC Press (2015).

Spivey, J.P. and Lee, W.J. New Solutions for Pressure Transient Response for a Horizontal or a Hydraulically Fractured Well at an Arbitrary Orientation in an Anisotropic Reservoir. Paper SPE 49236 presented at SPE Annual Technical Conference and Exhibition, New Orleans, Louisiana, 27-30 September (1998).

Valko, P., and Economides, M.J. Transient Behavior of Finite Conductivity Horizontal Fractures. *SPE J*. 2 (02): 213-222 (1997).

Valko, P.P., and Amini, S. The Method of Distributed Volumetric Sources for Calculating the Transient and Pseudosteady-State Productivity of Complex Well-Fracture Configurations. Paper 106276 presented at SPE Hydraulic Fracturing Technology Conference, College Station, Texas, 29-31 January (2007).

van Everdingen, A.F., and Hurst, W. The Application of the Laplace Transformation to Flow Problems in Reservoirs. *Trans*. *AIME* 1 (12): 305-324 (1949).

Wahl, H.A. Horizontal Fracture Design Based on Propped Fracture Area. *SPE J*. 17 (6): 723-730 (1965).

Wahl, H.A., and Campbell, J.M. Sand Movement in Horizontal Fractures. *SPE J.* 15 (11): 1239-1246 (1963).

Warren, J.E., and Root, P.J. The Behavior of Naturally Fractured Reservoirs. *SPE J*. 3 (03): 245-255 (1963).

Wright, C.A., Davis, E.J., Weijers, L., Minner, W.A., Hennigan, C.M., and Golich, G.M. Horizontal Hydraulic Fractures: Oddball Occurrences or Practical Engineering Concern? Paper SPE 38324 presented at SPE Western Regional Meeting, Long Beach, California, 25-27 June (1997).

Yang, D., Zhang, F., Styles, J.A., and Gao, J. Performance Evaluation of a Horizontal Well With Multiple Fractures by Use of a Slab-Source Function. *SPE J*. 20 (03): 652-662 (2015).

Yu, W., Wu, K., and Sepehrnoori, K. A Semianalytical Model for Production Simulation from Nonplanar Hydraulic-Fracture Geometry in Tight Oil Reservoirs. *SPE J*. 21 (3) 1028-1040 (2016).

Zhou, W., Banerjee, R., Poe, B.D., and Spath, J. Semianalytical Production Simulation of Complex Hydraulic-Fracture-Networks. *SPE J*. 19 (01): 6-18 (2014).

CHAPTER 3 PRESSURE TRANSIENT BEHAVIOR OF PARTIALLY-PENETRATING INCLINED FRACTURES WITH A FINITE CONDUCTIVITY

A version of this chapter has been published in *SPE Journal.*

Summary

Field studies have shown that, if an inclined fracture has a significant inclination angle from the vertical direction or the fracture has a poor growth along the inclined direction, this fracture probably cannot fully penetrate the formations, resulting in a partially-penetrating inclined fracture (PPIF) in these formations. It is necessary for the petroleum industries to conduct pressure transient analysis on such fractures to properly understand the major mechanisms governing the oil production from these fractures. In this work, we develop a semi-analytical model to characterize the pressure transient behavior of a finite-conductivity PPIF. We discretize the fracture into small panels, and each of these panels is treated as a plane source. The fluid flow in the fracture system is numerically characterized with finite difference method, while the fluid flow in the matrix system is analytically characterized on the basis of Green's function method. As such, a semi-analytical model for characterizing the transient flow behavior of a PPIF can be readily constructed by coupling the transient flow in the fracture and that in the matrix. With the aid of the proposed model, we carry out a detailed study about the transient flow behavior of the PPIFs. Our calculation results show that, a PPIF with a finite conductivity in a bounded reservoir may exhibit the following flow regimes: wellbore afterflow, fracture radial flow, bilinear flow, inclined formation linear flow, vertical elliptical flow, vertical pseudo-radial flow, inclined pseudo-radial flow, horizontal formation linear flow, horizontal elliptical flow, horizontal pseudo-radial flow, and boundary dominated flow. A negative slope period can appear on the pressure derivative curve, which is ascribed to a converging flow near the wellbore. Even with a small dimensionless fracture conductivity, a PPIF can exhibit a horizontal formation linear flow. In addition to PPIFs, the proposed model can also be used to simulate the pressure transient

behavior of fully penetrating vertical fractures, partially penetrating vertical fractures, fully penetrating inclined fractures, and horizontal fractures.

3.1. Introduction

Hydraulic-fracturing technology has been widely used to improve the well productivity in the low-permeability reservoirs. It has been generally acknowledged that the hydraulic fractures are perpendicular to the least principal stress (Hubbert and Willis, 1957; Daneshy, 1978; Medlin and Masse, 1984; Chun and Ghassemi, 2012). Since the least principal stress is not always parallel or perpendicular to the plane of the formations, the fracture treatment can induce an inclined fracture in the formations (Daneshy, 1973; Wright, 1994; Cipolla and Wright, 2000).

Numerical simulation is a powerful tool for evaluating the performance of the vertical and horizontal fractures (Conlin *et al*., 1990; Al-Anazi *et al*., 2013). However, in terms of modeling an inclined fracture, the numerical simulation is time-consuming and inconvenient to use because it requires applying the local-grid-refinement technique or unstructured grids to capture the configuration of such fractures. In recent studies, various semi-analytical models have been proposed to characterize the transient flow behavior of complex fractures (Medeiros *et al*., 2008; Medeiros *et al*., 2010; Yu *et al*., 2016). Cinco-ley *et al.* (1975) derived an instantaneous plane source function to model the transient flow of a slightly compressible fluid toward a fully-penetrating inclined fracture (FPIF) by assuming the fracture has an infinite conductivity. In their work, the influence of fracture's inclination angle together with the formation thickness on the pressure response of the FPIF is comprehensively investigated. Dinh and Tiab (2009) developed a step-by-step procedure for pressure transient analysis of an FPIF; they found that the FPIF exhibits flow regimes similar to the counterpart of a vertical fracture. Following the work of Cinco-ley *et al.* (1975), Dinh and Tiab (2010) introduced a type-curve-matching technique to

interpret the pressure transient data of an FPIF, and successfully obtained the rock and fluid properties with this technique. Habte *et al.* (2010) studied the pressure response of a uniform-flux hydraulic fracture which is both inclined and asymmetrical; they claimed that three flow regimes (i.e., linear flow, early-radial flow and pseudo-radial flow) can be observed when the asymmetry is not significant. Rbeawi and Tiab (2012a) predicted the pressure dynamics of a horizontal well with multiple FPIFs based on a plane source function; a set of type curves of pressure drops and pressure derivatives were obtained in their work. Jia *et al*. (2016) further developed a semi-analytical model to study the pressure transient behavior of the FPIFs. In their model, the flux variation along the horizontal direction in the fracture, as well as the fracture conductivity, can be taken into account.

Even though great effects have been invested to study the pressure transients of the inclined fractures, most of these works ignore the scenario that an inclined fracture cannot always fully penetrate the formations. **Figure 3-1** shows two real field cases that a partially-penetrating inclined fracture (PPIF) is observed. Figure 3-1a shows the microseismic events monitored from the 3rd stage fracturing treatment of Ridgewood-5 well (Johnson *et al*. 2010). The interpretation result of the microseismic map illustrates that a sub-horizontal fracture is induced after the fracturing treatment. This induced fracture has an inclination angle of 80^{o} corresponding to the vertical direction, and it has a length of 407 ft and a height of 59 ft. However, the target payzone is 68 ft thick, which is 9 ft larger than the fracture height, indicating that this fracture is not only inclined but also partially penetrating. This real field case presents that an inclined fracture cannot fully penetrate a formation if it has a sufficiently large inclination angle with respect to the vertical direction. Figure 3-1b presents the downhole tiltmeter data of a fractured vertical well and the interpretation of these monitored data (Wright *et al*. (1998). As is shown in this figure,

the interval of the two tilt peaks along the *Y*-axis represents the height of the fracture, indicating that this fracture's height is 160 ft, which is 120 ft less than the payzone thickness. In addition, the existence of the difference between these two peaks along *X*-axis demonstrates that the fracture is not perfectly vertical. Figure 3-1b shows such a scenario that, albeit a fracture has an insignificant inclination angle, it cannot fully penetrate a formation if this fracture has a poor growth along the inclined direction. More reports on the sub-horizontal fractures or poorly grown fractures along the inclined direction can be referred to Minner *et al*. (2002), Jeffrey *et al*. (2009), Baig and Urbancic (2012), Pandey and Agreda (2014), and Mukuhira *et al*. (2016).

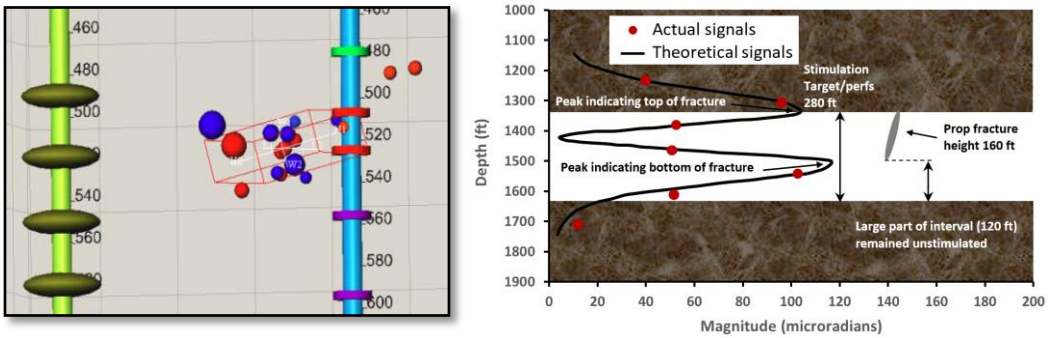

(a) (b)

Figure 3-1. Field examples where a PPIF is observed: (a) microseismic data show a PPIF with a significant inclination angle (adapted from Johnson *et al*., 2010); and (b) tiltmeter data show a PPIF with a poor growth along the inclined direction (adapted from Wright *et al*., 1998).

Since the PPIFs truly exist in the real field cases, it is necessary to develop a corresponding technique to conduct pressure transient analysis of the PPIFs. Cinco-ley *et al.* (1975) derived an inclined plane source function based on Newman product method. Although this function was mainly used to characterize the pressure transient behavior of an FPIF in their work, they claimed that this derived function could also be used to model a PPIF in an infinite reservoir. Based on the plane source function provided in Cinco-ley *et al.* (1975), Rbeawi and Tiab (2012b) and Rbeawi and Tiab (2013) investigated the performance of a horizontal well intersected with multiple PPIFs. They defined the flow regimes predicted by their models and studied the

influence of inclination angle and penetrating ratio on the pressure response. These previous works provide us with a preliminary knowledge about the transient flow behaviors of the PPIFs. However, all these works assume that the fractures have infinite conductivity and ignore the pressure drop and flux variation along the fractures, which will lead to inaccurate results for pressure transient analysis of low/moderate-conductivity PPIFs. Currently, the literature lacks a technique which can provide us with a comprehensive insight into the pressure transient behavior of a PPIF that has finite conductivity and nonuniform flux distribution.

In this work, we provide a thorough investigation of the pressure dynamics of a finite-conductivity PPIF on the basis of a semi-analytical model. With the aid of the proposed model, we depict the flux distribution along the fracture to illustrate the variation of flux distribution at different fracture conductivities. Subsequently, we identify the flow regimes of the PPIF and analyze the influences of inclination angle, penetrating ratio, fracture conductivity and wellbore storage on the pressure transient behavior.

3.2. Methodology

In this work, we study the pressure transient behavior of a vertical well intersected with a rectangle-shaped PPIF in a box-shaped reservoir, as shown in **Figure 3-2**. It is worth mentioning that, although only a rectangle-shaped PPIF is studied in this work, the proposed model can also be used to model the pressure transient behavior of a PPIF with an arbitrary geometry by discretizing the fracture into small panels. In practical applications, a reliable fracture geometry, which is based on the interpretation of microseismic and tiltmeter data, could be used to best capture the real fracture geometry for transient flow analysis. As shown in Figure 3-2, this fracture is parallel to X-axis, θ is the inclination angle of the fracture with respect to the vertical

direction (i.e., *Z*-axis), *X*, *Y*, and *Z* are the axes. In order to construct a semi-analytical model, we make the following assumptions:

- The reservoir is box-shaped and sealed by impermeable boundaries;
- The properties in the matrix and fracture systems are assumed to be homogeneous;
- This model is derived in an isotropic permeability matrix system;
- Since the fracture width is far smaller than the fracture length, the oil flow in the fracture system is simplified as a 2D flow;
- The PPIF has a rectangular shape and assigned to be located at the center of the reservoir;
- The oil is produced with a constant rate and the oil enters the wellbore only through the fracture;
- In the fracture system, the flux variations both along the horizontal direction and inclined direction are taken into account;
- The wellbore storage effect is considered in the model.

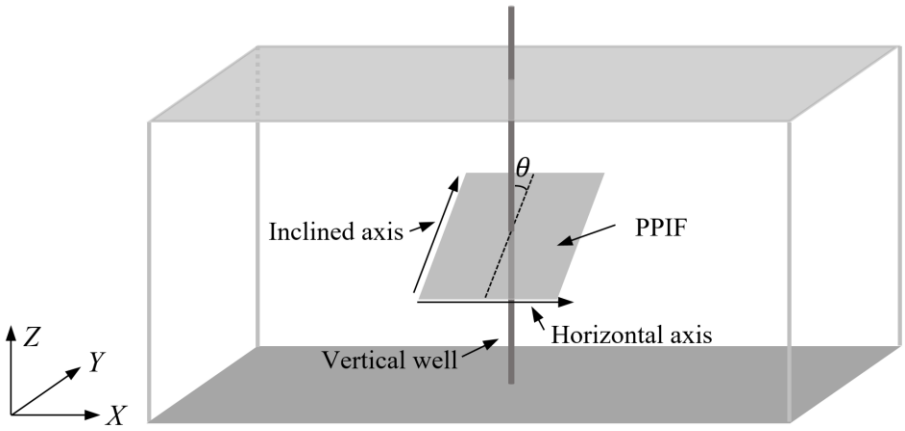

Figure 3-2. Schematic of a PPIF intersecting with a vertical well in a box-shaped reservoir.

3.2.1 Definition of the Dimensionless Parameters

For the convenience of analysis and discussion, we define the following dimensionless variables:

$$p_D = \frac{2\pi\beta k_m h\left(p_i - p\right)}{q_w B\mu},\ p_{fD} = \frac{2\pi\beta k_m h\left(p_i - p_f\right)}{q_w B\mu} \tag{3-1}$$

$$t_D = \frac{\beta k_m t}{\phi_m \mu c_{tm} x_{f/2}^2} \tag{3-2}$$

$$q_D = \frac{q}{q_w},\ q_{f-wD} = \frac{q_{f-w}}{q_w}, \tag{3-3}$$

$$x_D = \frac{x}{x_{f/2}},\ y_D = \frac{y}{x_{f/2}},\ z_D = \frac{z}{x_{f/2}}, l_D = \frac{l}{x_{f/2}}, \tag{3-4}$$

$$h_D = \frac{h}{x_{f/2}},\ w_D = \frac{w}{x_{f/2}},\ r_{wD} = \frac{r_w}{x_{f/2}},\ r_{eqD} = \frac{r_{eq}}{x_{f/2}}, \tag{3-5}$$

$$\gamma = \frac{0.0434 B r_w^2}{x_{f/2}^2},\ C_{wD} = \frac{C_w}{2\pi h \phi_m c_{tm} r_w^2}, \tag{3-6}$$

$$C_s = \frac{\phi_f c_{tf}}{\phi_m c_{tm}}, \tag{3-7}$$

$$C_f = k_f w,\ C_{fD} = \frac{C_f}{k_m x_{f/2}}, \tag{3-8}$$

$$\lambda = \frac{h_f}{h}, \tag{3-9}$$

where p_D is dimensionless pressure, β is unit conversion factor which equals to 0.0853, k_m is matrix permeability, h is formation thickness, p_i is initial reservoir pressure, p is pressure, q_w is well production rate under standard condition, B is formation volume factor, μ is oil viscosity, p_{fD} is dimensionless fracture pressure, p_f is fracture pressure, t_D is dimensionless time, t is time, ϕ_m is matrix porosity, c_{tm} is matrix total compressibility, $x_{f/2}$ is half fracture length along the horizontal direction, q_D is dimensionless flux, q is flux rate from the matrix to fracture, $q_{f\text{-}wD}$ is dimensionless flux from fracture to the wellbore, $q_{f\text{-}w}$ is flux from fracture to the wellbore under

standard condition, x_D, y_D, and z_D are dimensionless Cartesian coordinates, x, y, and z are Cartesian coordinates, l_D is dimensionless space position along the inclination direction of the fracture, l is space position along the inclination direction of the fracture, h_D is dimensionless formation thickness, w_D is dimensionless fracture width, w is fracture width, r_{wD} is dimensionless wellbore radius, r_w is wellbore radius, r_{eqD} is dimensionless equivalent radius, r_{eq} is equivalent radius, γ is a dimensionless coefficient defined in this work, C_{wD} is dimensionless wellbore storage coefficient, C_w is wellbore storage coefficient, C_s is dimensionless coefficient defined in this work, ϕ_f is effective porosity in the fracture system, c_{tf} is fracture's total compressibility, C_f is fracture conductivity, k_f is fracture permeability, C_{fD} is dimensionless fracture conductivity, λ is penetrating ratio, and h_f is fracture height.

3.2.2 Numerical Formulation of the Fracture System

As mentioned in the assumptions, the flux variations both along the horizontal direction and the inclined direction are taken into account in the proposed model; thus, the fracture should be discretized along both directions. **Figure 3-3** shows the discretized fracture. In this figure, x_f is fracture length along horizontal direction, l_f is fracture length along inclined direction, and h_f is fracture height in vertical direction. We discretize the PPIF into N_f ($N_f = N_i \times N_j$) panels and these panels have the same dimension of $\Delta x \times \Delta l$, where Δx and Δl represent fracture panel's lengths along the horizontal direction and inclination direction, respectively. The transient flow equation for the fracture system can be expressed as:

$$\frac{\partial^2 p_f}{\partial x^2} + \frac{\partial^2 p_f}{\partial l^2} + \frac{B\mu q}{\beta \Delta x \Delta l w k_f} = \frac{\mu \phi_f c_{tf}}{\beta k_f} \frac{\partial p_f}{\partial t}, \tag{3-10}$$

where l indicates the spatial position along the inclination direction of a PPIF, the third term on the left-hand side of Equation (3-10) represents the influx from the matrix to the fracture. Converting Equation (3-10) into dimensionless format and applying finite difference

approximation to this equation, one can have the approximated flow equation for panel (i, j) at the n^{th} timestep:

$$\begin{aligned}&\left(\frac{2}{\Delta x_D^2}+\frac{2}{\Delta l_D^2}+\frac{w_D C_s}{C_{fD}}\frac{1}{\Delta t_D^n}\right)p^n_{fD_{i,j}}-\frac{1}{\Delta x_D^2}p^n_{fD_{i-1,j}}-\frac{1}{\Delta x_D^2}p^n_{fD_{i+1,j}}\\&-\frac{1}{\Delta l_D^2}p^n_{fD_{i,j-1}}-\frac{1}{\Delta l_D^2}p^n_{fD_{i,j+1}}+\frac{2\pi h_D}{\Delta x_D \Delta l_D C_{fD}}q^n_{D_{i,j}}=\frac{w_D C_s}{C_{fD}\Delta t_D^n}p^{n-1}_{fD_{i,j}}\end{aligned}, \tag{3-11}$$

where $i = 1 \cdots N_i$, and $j = 1 \cdots N_j$. Applying Equation (3-11) to the N_f fracture panels and arranging these fracture flow equations into a matrix format yields:

$$\boldsymbol{A}\cdot\boldsymbol{p}_f^n+\boldsymbol{B}_1\odot\boldsymbol{q}^n-q^n_{f-wD}\cdot\boldsymbol{B}_2=\boldsymbol{C}\odot\boldsymbol{p}_f^{n-1}, \tag{3-12}$$

where $\odot$ is Hadamard product operator, $q_{f\text{-}wD}$ is dimensionless flux from fracture to the wellbore, and the matrices of $\boldsymbol{A}$, $\boldsymbol{p}_f$, $\boldsymbol{B}_1$, $\boldsymbol{q}^n$, $\boldsymbol{B}_2$, and $\boldsymbol{C}$ are defined in **Appendix 3A**.

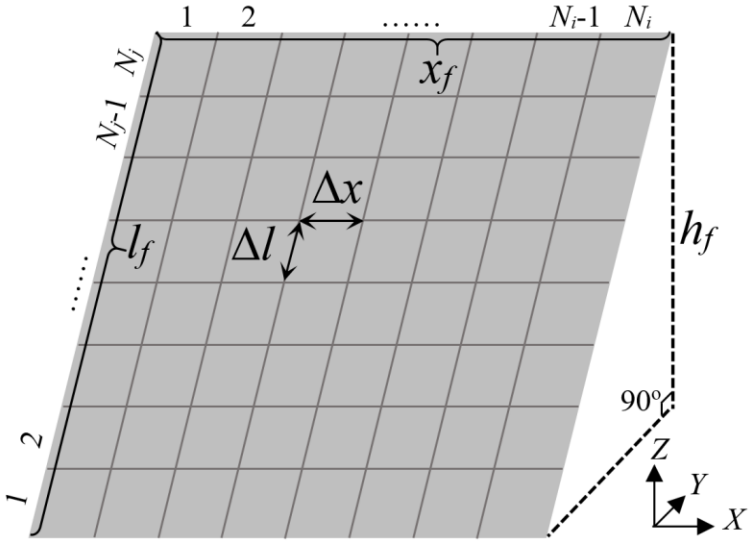

Figure 3-3. Discretization of the PPIF along both the horizontal axis and inclined axis.

3.2.3 Analytical Solution of the Matrix System

The PPIF is discretized into N_f panels in our work, and each of the fracture panels can be regarded as a plane source. Based on the Green's function and Newman product method, one can obtain the pressure response at an arbitrary position within the reservoir which is caused by a

continuous plane source. As is presented in **Appendix 3B**, the analytical solution of an inclined plane source, fracture panels (i, j), in a bounded reservoir can be written as:

$$
\begin{aligned}
&p_i - p\left(x,y,z,t^n\right) = \frac{B}{\phi_m c_{tm}\Delta x\Delta y}\frac{\Delta x}{x_e y_e z_e}\sum_{k=1}^{k=n} q^k \int_{t^{k-1}}^{t^k} \\
&\left\{1+\frac{4x_e}{\pi\Delta x}\sum_{m=1}^{\infty}\frac{1}{m}\exp\left[-\frac{m^2\pi^2\alpha\left(t^n-\tau\right)}{x_e^2}\right]\sin\frac{m\pi\Delta x}{2x_e}\cos\frac{m\pi x_{0_{i,j}}}{x_e}\cos\frac{m\pi x}{x_e}\right\} \\
&\cdot\int_{l_{i,j}=0}^{l_{i,j}=\Delta l}\left\{1+2\sum_{m=1}^{\infty}\exp\left[-\frac{m^2\pi^2\alpha\left(t^n-\tau\right)}{y_e^2}\right]\cos\frac{m\pi y\left(l_{i,j}\right)}{y_e}\cos\frac{m\pi y}{y_e}\right\} \\
&\cdot\left\{1+2\sum_{m=1}^{\infty}\exp\left[-\frac{m^2\pi^2\alpha\left(t^n-\tau\right)}{z_e^2}\right]\cos\frac{m\pi z\left(l_{i,j}\right)}{z_e}\cos\frac{m\pi z}{z_e}\right\}\mathrm{d}l_{i,j}\mathrm{d}\tau
\end{aligned}
\quad , \tag{3-13}
$$

where α is diffusivity defined as $\alpha = k_m / \mu\phi_m c_{tm}$, x_e, y_e, and z_e are reservoir dimensions, $x_{0_{i,j}}$ represents the center position of the fracture panel (i, j) along x-axis, $l_{i,j}$ represents space position along the inclination direction of fracture panel (i, j), $y(l_{i,j})$ and $z(l_{i,j})$ represent y and z coordinates at space position $l_{i,j}$. Equation (3-13) characterizes the pressure response caused by a single fracture panel, and one can calculate the pressure response caused by the entire PPIF by collecting the pressure response from all the panels. The equation is given as:

$$
\begin{aligned}
&p_i - p\left(x,y,z,t^n\right) = \frac{B}{\phi_m c_{tm}\Delta x\Delta y}\frac{\Delta x}{x_e y_e z_e}\sum_{i=1}^{i=N_i}\sum_{j=1}^{j=N_j}\sum_{k=1}^{k=n} q_{i,j}^k \int_{t^{k-1}}^{t^k} \\
&\left\{1+\frac{4x_e}{\pi\Delta x}\sum_{m=1}^{\infty}\frac{1}{m}\exp\left[-\frac{m^2\pi^2\alpha\left(t^n-\tau\right)}{x_e^2}\right]\sin\frac{m\pi\Delta x}{2x_e}\cos\frac{m\pi x_{0_{i,j}}}{x_e}\cos\frac{m\pi x}{x_e}\right\} \\
&\cdot\int_{l_{i,j}=0}^{l_{i,j}=\Delta l}\left\{1+2\sum_{m=1}^{\infty}\exp\left[-\frac{m^2\pi^2\alpha\left(t^n-\tau\right)}{y_e^2}\right]\cos\frac{m\pi y\left(l_{i,j}\right)}{y_e}\cos\frac{m\pi y}{y_e}\right\} \\
&\cdot\left\{1+2\sum_{m=1}^{\infty}\exp\left[-\frac{m^2\pi^2\alpha\left(t^n-\tau\right)}{z_e^2}\right]\cos\frac{m\pi z\left(l_{i,j}\right)}{z_e}\cos\frac{m\pi z}{z_e}\right\}\mathrm{d}l_{i,j}\mathrm{d}\tau
\end{aligned}
\tag{3-14}
$$

On the basis of Equation (3-14), the pressure response caused by a PPIF at an arbitrary position in a bounded reservoir can be readily calculated; thus, if we use the pressure at a panel's center position to approximate this panel's average pressure, the dimensionless pressure of fracture panel (I, J), where $I = 1^{\cdots} N_i$ and $J = 1^{\cdots} N_j$, has the following relationship with the fluxes of the N_f fracture panels:

$$
\begin{aligned}
p_{fD_{I,J}}\left(x_{0D_{I,J}}, y_{0D_{I,J}}, z_{0D_{I,J}}, t_D^n\right) &= \frac{2\pi}{\Delta y_D x_{eD} y_{eD}} \sum_{i=1}^{i=N_i} \sum_{j=1}^{j=N_j} \sum_{k=1}^{k=n} q_{D_{i,j}}^k \int_{t_D^{k-1}}^{t_D^k} \\
&\left\{1+\frac{4x_{eD}}{\pi\Delta x_D}\sum_{m=1}^{\infty}\frac{1}{m}\exp\left[-\frac{m^2\pi^2\left(t_D^n-\tau_D\right)}{x_{eD}^2}\right]\sin\frac{m\pi\Delta x_D}{2x_{eD}}\cos\frac{m\pi x_{0D_{i,j}}}{x_{eD}}\cos\frac{m\pi x_{0D_{I,J}}}{x_{eD}}\right\} \\
&\cdot\int_{l_{D_{i,j}}=0}^{l_{D_{i,j}}=\Delta l_D}\left\{1+2\sum_{m=1}^{\infty}\exp\left[-\frac{m^2\pi^2\left(t_D^n-\tau_D\right)}{y_{eD}^2}\right]\cos\frac{m\pi y_D\left(l_{D_{i,j}}\right)}{y_{eD}}\cos\frac{m\pi y_{0D_{I,J}}}{y_{eD}}\right\} \\
&\cdot\left\{1+2\sum_{m=1}^{\infty}\exp\left[-\frac{m^2\pi^2\left(t_D^n-\tau_D\right)}{z_{eD}^2}\right]\cos\frac{m\pi z_D\left(l_{D_{i,j}}\right)}{z_{eD}}\cos\frac{m\pi z_{0D_{I,J}}}{z_{eD}}\right\}\mathrm{d}l_{D_{i,j}}\,\mathrm{d}\tau_D
\end{aligned}
\tag{3-15}
$$

Applying Equation (3-15) to all of the fracture panels, we can have N_f equations which reveal the relationship between the dimensionless pressure and dimensionless fluxes of the fracture panels. These matrix flow equations can also be arranged into a matrix format, which is given as follows:

$$
\boldsymbol{p}_f^n - \boldsymbol{G}\boldsymbol{q}^n = \boldsymbol{D}\,, \tag{3-16}
$$

where the matrices of $\boldsymbol{G}$ and $\boldsymbol{D}$ are defined in **Appendix 3A**.

3.2.4 Wellbore Storage and Wellbore Representation

In this work, the wellbore storage effect is considered with the method provided by van Everdingen and Hurst (1949):

$$
1-\frac{\gamma C_{wD}}{\Delta t_D^n}\left(p_{wD}^n - p_{wD}^{n-1}\right) = q_{f-wD}^n\,, \tag{3-17}
$$

where p_{wD} is dimensionless bottomhole pressure, γ and C_{wD} are defined in Equation (3-6). According to the well model introduced by Peaceman (1983), the dimensionless bottomhole pressure and dimensionless pressure of the well-panel have the following relationship:

$$p_{wD}^{n} - p_{wpD}^{n} = \frac{w_D}{C_{fD}} q_{f-wD}^{n} \ln \frac{r_{eqD}}{r_{wD}}, \tag{3-18}$$

where p_{wpD} is dimensionless pressure of the well-panel, w_D, C_{fD}, r_{eqD} and r_{wD} are defined in Equations (3-5) and (3-8). The equivalent radius r_{eq} in a homogeneous permeability reservoir can be calculated with the following equation given by Peaceman (1983):

$$r_{eq} = 0.14\left[\left(\Delta x\right)^2 + \left(\Delta l\right)^2\right]^{0.5} \tag{3-19}$$

3.2.5 Solution Methodology

Based on the continuity of the flux and pressure, one can group the fracture flow equations, matrix flow equations, wellbore storage effect equation and wellbore representation equation to construct a system of linear equations to characterize the transient flow behavior of a PPIF. This system of linear equations can be written as follow:

$$\begin{cases} \boldsymbol{A} \cdot \boldsymbol{p}_f^n + \boldsymbol{B}_1 \odot \boldsymbol{q}^n - q_{f-wD}^n \cdot \boldsymbol{B}_2 = \boldsymbol{C} \odot \boldsymbol{p}_f^{n-1} \\ \boldsymbol{p}_f^n - \boldsymbol{G}\boldsymbol{q}^n = \boldsymbol{D} \\ 1 - \dfrac{\gamma C_D}{\Delta t_D^n}\left(p_{wD}^n - p_{wD}^{n-1}\right) = q_{f-wD}^n \\ p_{wD}^n - p_{wpD}^n = \dfrac{w_D}{C_{fD}} q_{f-wD}^n \ln \dfrac{r_{eqD}}{r_{wD}} \end{cases} \tag{3-20}$$

In this system of linear equations, there are the following unknowns at each timestep:

- N_f dimensionless pressures of the fracture panels: $p_{fD_{i,j}}$, $i = 1 \cdots N_i$, and $j = 1 \cdots N_j$;
- N_f dimensionless fluxes that flow from the matrix to the fracture panels: $q_{D_{i,j}}$, $i = 1 \cdots N_i$, and $j = 1 \cdots N_j$;

- 1 dimensionless flux from the well-panel to the wellbore: $q_{f\text{-}wD}$;
- 1 dimensionless bottomhole pressure: p_{wD}.

The governing equations at each timestep include the following:

- N_f fracture flow equations which are given by Equations (3-12);
- N_f matrix flow equations which are given by Equation (3-16);
- 1 wellbore storage effect equation which is given by Equation (3-17);
- 1 wellbore representation equation which is given by Equation (3-18).

In total, there are $2N_f + 2$ unknowns and $2N_f + 2$ governing equations, and one can solve these equations with the Gaussian elimination method.

3.3. Validation of the Proposed Model

Prior to the validations being carried out later, we first examine the influence of the number of discretized fracture panels on the simulation outputs. We discretize the PPIF into 135 (15×9), 143 (13×11), 165 (15×11), 187 (17×11), and 195 (15×13) panels, respectively, and calculate the pressure response of the PPIF in a bounded reservoir. The following dimensionless fracture and reservoir data are used in this model: $x_{eD} = 20$, $y_{eD} = 20$, $h_D = 0.5$, $x_{fD} = 2$, $\theta = 45^o$, $\lambda = 0.5$, $C_{fD} = 5$, $C_s = 10$, $C_{wD} = 0$, $w_D = 1\times10^{-5}$, and $\gamma = 1.30\times10^{-8}$. **Figure 3-4** presents the pressure drops and pressure derivatives calculated with the proposed model under different numbers of fracture panels. As one can see, the pressure drops and pressure derivatives undergo negligible changes when the number of fracture panels is more than 165; therefore, the number of fracture panels of 165 (15×11) is used in the following studies.

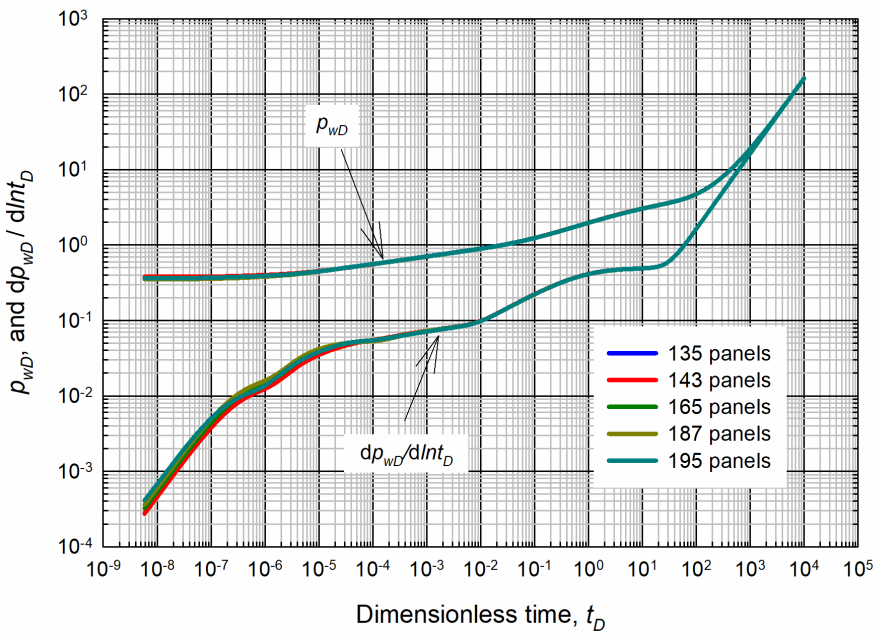

Figure 3-4. Impact of the number of fracture panels on the outputs of the semi-analytical model.

3.3.1 Validation against Semi-analytical Models

We first validate the proposed model against those of Cinco-ley *et al.* (1975) and Rbeawi and Tiab (2013), respectively. It is noted that since the two existing methods, i.e., Cinco-ley *et al.* (1975) and Rbeawi and Tiab (2013), assume the fracture has infinite conductivity and neglect the flux variation along the fracture, the comparison is conducted on a PPIF model with infinite conductivity and uniform flux distribution. The dimensionless data used in this part are as follows: x_{eD} = 20, y_{eD} = 20, h_D = 1, x_{fD} = 2, θ = 15°, λ = 0.1, C_{wD} = 0, w_D = 1×10^{-5}, and γ = 1.30×10^{-8}. **Figure 3-5** compares the results obtained with the proposed model against those obtained with Cinco-ley *et al.* (1975) and Rbeawi and Tiab (2013). Overall, the calculated results from our model agree well with those from Cinco-ley *et al.* (1975) and Rbeawi and Tiab (2013), except a deviation showing up at the late production stage. This is because that the plane source function used in Cinco-ley *et al.* (1975) and Rbeawi and Tiab (2013) is derived under an infinite boundary condition, while the plane source function used in this work is derived under a bounded reservoir condition, The deviation occurs at the late production time indicates the boundary effect.

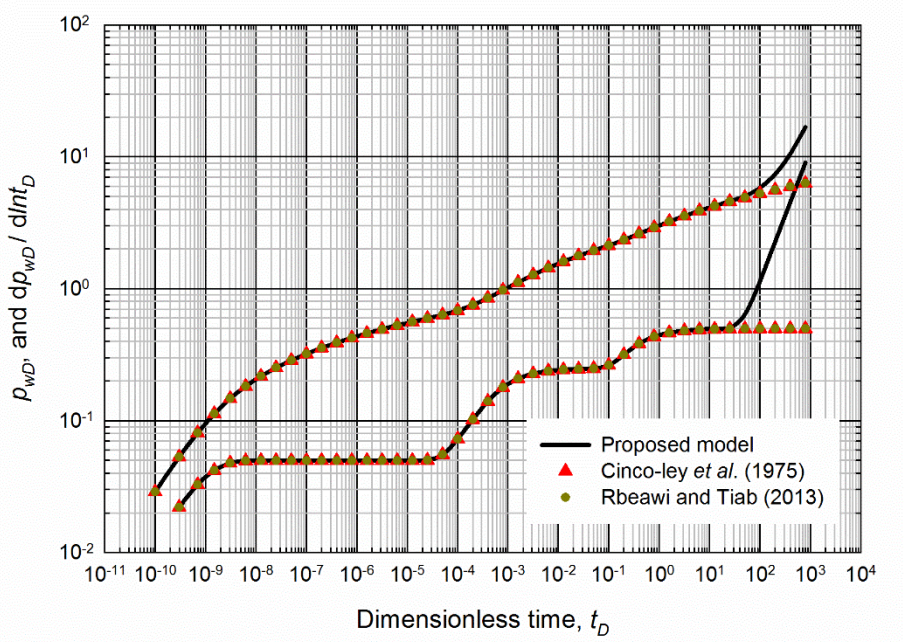

Figure 3-5. Comparison between the pressure drops and pressure derivatives calculated by the proposed model and those by Cinco-ley *et al.* (1975) and Rbeawi and Tiab (2013).

3.3.2 Validation against Numerical Software

In practice, the fracture conductivity is normally not infinite and the flux distribution along the fracture cannot be simplified as uniform; therefore, we also validate the proposed model against a numerical simulator (Eclipse) which can take the fracture conductivity and flux variation into consideration. **Figure 3-6.a** gives a top view of the overall grid system of the reservoir model built in Eclipse. As shown in Figure 3-6.a, the PPIF is located at the center of the reservoir, and local-grid-refinement technique is applied to model the fracture. Figure 3-6.b shows a side view of the locally refined grid system. The red cells are assigned with a higher permeability to represent the PPIF. The reservoir has a dimension of 1000×1000×5 m, and we discretize the reservoir into 50×50×5 cells. A local grid system comprised of 5×1×3 cells is refined into a system of 5×300×60 cells to model the fracture. The validation is conducted on two scenarios. Scenario #1 considers a matrix permeability (k_m) of 1 mD, and scenario #2 considers a matrix permeability (k_m) of 100 mD. The other fluid and rock properties used both in Eclipse and the

proposed model are as follows: c_{tm} = 0.0012 MPa^{-1}, ϕ_m = 0.2, k_f = 200 mD, C_w = 0 bbl/psi, C_f = 10 mD·m, c_{tf} = 0.0012 MPa^{-1}, ϕ_f = 0.2, p_i = 30 MPa, q_w = 5 m^3/d, μ = 1 mPa·s, B = 0.985 (dead oil), r_w = 0.05 m, x_f = 100 m, l_f = 20.22 m, and θ =81.5^o. **Figure 3-7** compares the pressure drops and pressure derivatives calculated with the proposed model and Eclipse, respectively. One can find that the results obtained with the proposed model agree well with the results obtained with Eclipse on both scenarios. The validations shown in Figures 3-5 and 3-7 indicate that the proposed semi-analytical model is reliable in modeling the pressure transient behavior of a finite-conductivity PPIF in a bounded reservoir.

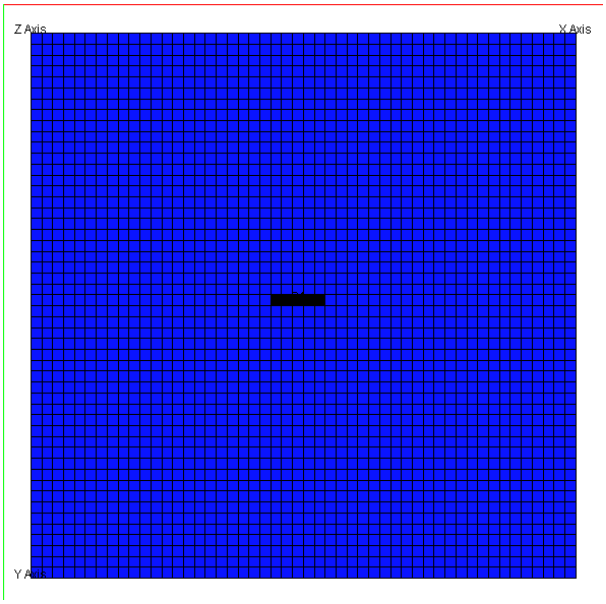

(a)

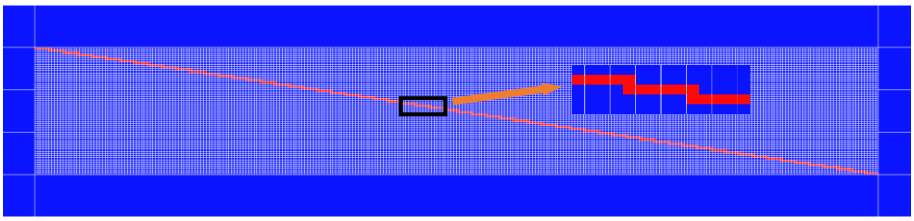

(b)

Figure 3-6. Reservoir model build in the Eclipse: (a) top view of the overall grid system; and (b) side view of the locally refined grid system.

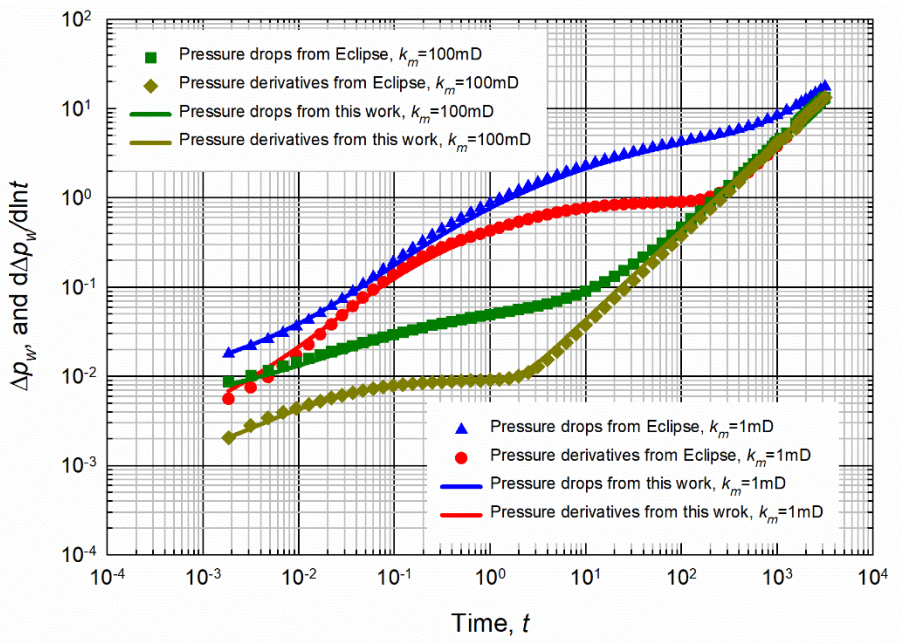

Figure 3-7. Comparison between the pressure drops and pressure derivatives calculated by the proposed model and those by Eclipse on two scenarios: scenario #1 k_m = 1 mD, and scenario #2 k_m = 100 mD.

3.4. Result and Discussion

In this section, we first show the calculated flux distribution along the PPIF with different fracture conductivities. Subsequently, we identify the flow regimes that can be observed during the production of a PPIF and study the influences of fracture's inclination angle, penetrating ratio, fracture conductivity, and wellbore storage on the pressure response. The following dimensionless numbers are used in the benchmark PPIF model: x_{eD} = 20, y_{eD} = 20, h_D = 0.5, x_{fD} = 2, θ = 45°, λ = 0.7, C_{fD} = 5, C_s = 10, C_{wD} = 20, $w_D = 1\times10^{-5}$, B = 1.2, and $\gamma = 1.30\times10^{-8}$.

3.4.1 Flux Distribution along the Fracture

In the previous studies, the uniform-flux models, together with the 2D-nonuniform-flux models, have been widely used for characterizing the transient flow behavior of the hydraulic fractures (Cinco-Ley and Samaniego-V, 1981; Rodriguez *et al*. 1984; Larsen and Hegre, 1994; Restrepo and Tiab, 2009; Zhou *et al*. 2014). The uniform-flux models are normally applied to simulate the transient flow of infinite-conductivity fractures by assuming that the fractures have uniform flux

distribution along both the horizontal and inclined directions; while the 2D-nonuniform-flux models, which take into account the flux variation along the horizontal direction of the fracture but still neglect the flux variation along the inclined direction, have been frequently utilized to model the pressure response of fully-penetrating fractures with finite conductivity. Since most of these models involving inclined fractures neglect the flux variation along the inclined direction, there is one question that requires to be answered: whether it is necessary to consider the flux variation along the inclined direction when modeling the pressure transient behavior of a finite-conductivity PPIF. **Figure 3-8** compares the pressure responses of the benchmark PPIF model which are calculated with the assumptions of uniform flux, nonuniform flux along the horizontal direction but uniform flux along the inclined direction, and nonuniform flux along both the horizontal direction and inclined direction, respectively. As one can see from this figure, a significant difference can be observed on the pressure drop curves and pressure derivative curves calculated with different assumptions. In practice, the flux variation along both the horizontal direction and the inclined direction should be physically present in the PPIF. Therefore, the proposed model, which can take into account the flux variation along both directions, can provide more realistic simulation results.

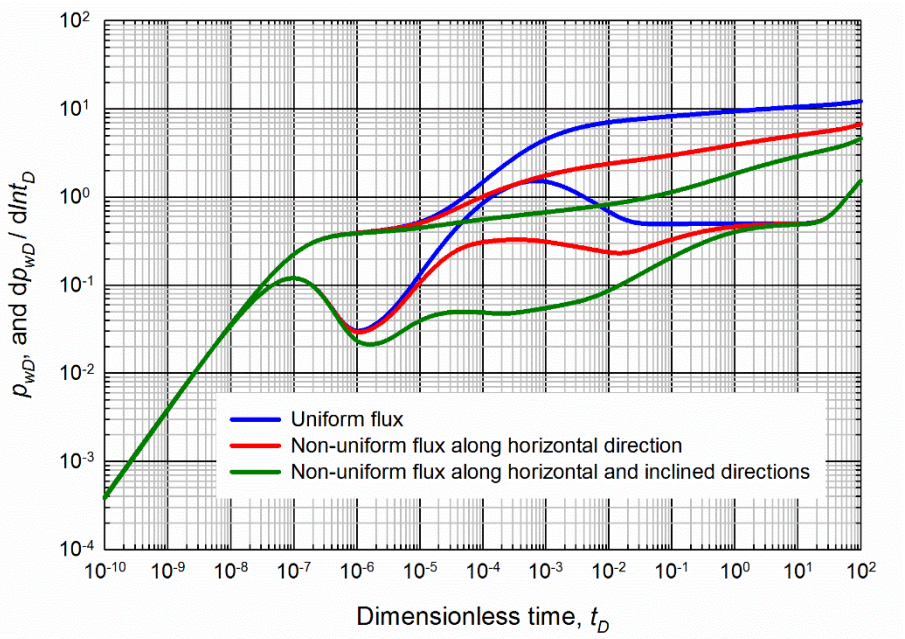

Figure 3-8. Comparison of pressure responses which are calculated based on the assumptions of uniform flux, nonuniform flux along horizontal direction but uniform flux along the inclination direction, and nonuniform flux both along the horizontal direction and inclined direction, respectively.

We also examine the effects of fracture conductivity on the flux distribution along the PPIF. **Figure 3-9** shows the flow distribution of the PPIF with dimensionless conductivities varying from 0.1 to 100 at the dimensionless time of 1×10^{-4}. At low fracture conductivities, such as C_{fD} = 0.1 in Figure 3-9a, the fluid enters the fracture mainly through the center of the PPIF, corresponding to the position of the wellbore. The maximum dimensionless flux, which is as high as 0.6532, can be observed at the wellbore, whereas the flux at the position away from the wellbore is negligible. This is ascribed to the fact that a smaller fracture conductivity will lead to a larger flow resistance in the fracture. As the fracture conductivity is increased, the flux variation along the fracture becomes smaller. At dimensionless fracture conductivity of 100, the maximum dimensionless flux is about 0.0124 that can be observed at the wellbore, while the minimum dimensionless flux is about 0.0044 which occurs at the fracture edge along the inclined direction (see Figure 3-9d).

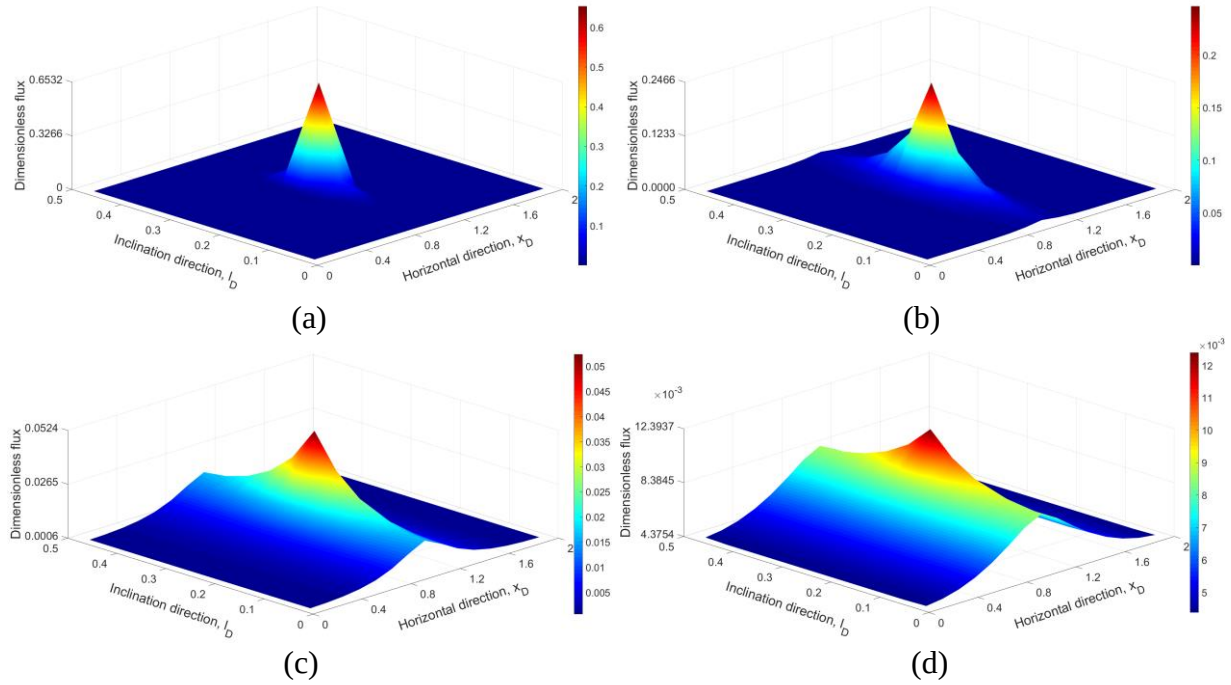

Figure 3-9. Flux distribution of the PPIF with different fracture conductivities at $t_D = 1\times10^{-4}$: (a) $C_{fD} = 0.1$; (b) $C_{fD} = 1$; (c) $C_{fD} = 10$; and (d) $C_{fD} = 100$.

Figure 3-10 presents the flux distribution of the PPIF with dimensionless conductivities varying from 0.1 to 100 at the dimensionless time of 1×10^{-3}. It is interesting to note that, as the fracture conductivity is increased, the flux along the fracture edge (i.e., $l_D = 0$ and $l_D = 0.5$) is increased, while the flux at the wellbore is decreased. In Figure 3-10d, the highest dimensionless flux, 0.0085, occurs at the fracture edge rather than the wellbore. This can be explained as follows: for a high-conductivity PPIF, the fluid near the wellbore will be rapidly drained. Subsequently, the produced fluid is mainly from the reservoir that is distant from the wellbore, and the fluid enters the fracture mainly through the fracture edge; therefore, for a high-conductivity fracture, the highest flux can occur at the fracture edge. The nonuniform flux distributions shown in Figures 3-9 and 3-10 provide a further justification that the flux variations both along the horizontal direction and the inclined direction should not be neglected in order to accurately model the transient flow behavior of a PPIF.

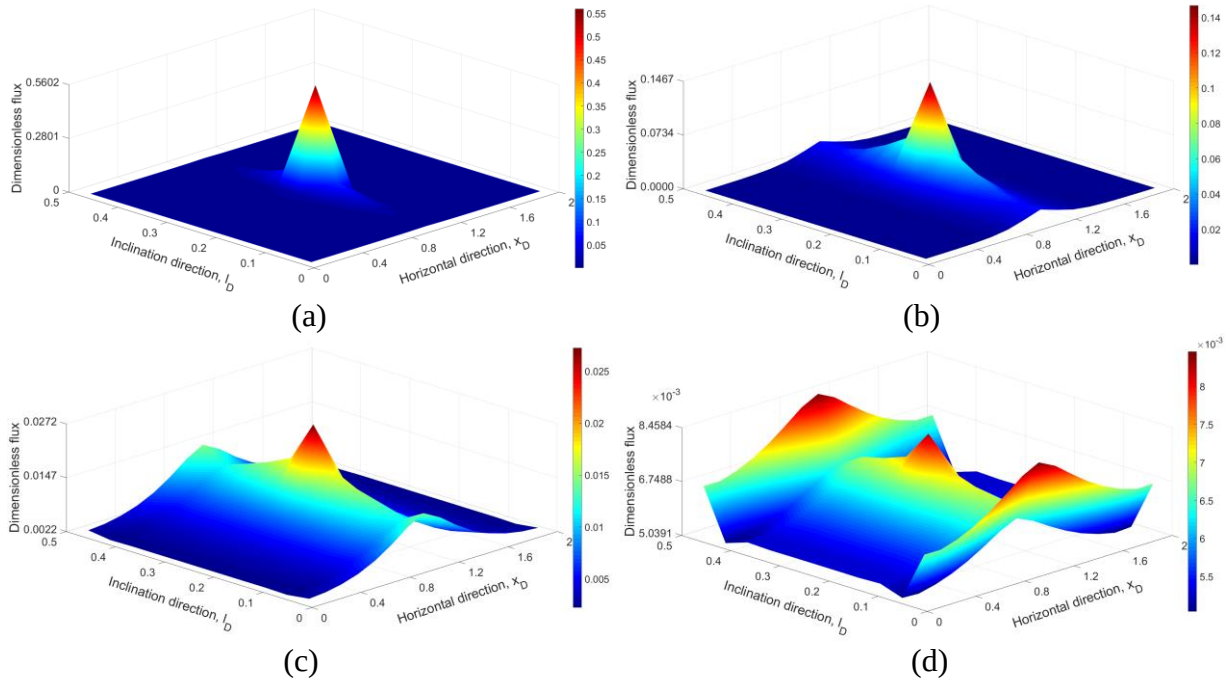

Figure 3-10. Flux distribution of the PPIF with different fracture conductivities at $t_D = 1 \times 10^{-3}$: (a) $C_{fD} = 0.1$; (b) $C_{fD} = 1$; (c) $C_{fD} = 10$; and (d) $C_{fD} = 100$.

3.4.2 Flow Regimes of a PPIF

The flow regimes can be distinguished by identifying the slopes on the pressure derivative curves. For instance, 1/4-slope indicates bilinear flow, 1/3-slope indicates elliptical flow, and 1/2-slope indicates linear flow (Cinco-Ley and Samaniego-V, 1981; Issaka *et al*., 2000; Chacon *et al*., 2004). **Figure 3-11** depicts the pressure drops and pressure derivatives of the benchmark PPIF that are calculated with the proposed semi-analytical model. In this figure, one can distinguish the following flow regimes during the production of the finite-conductivity PPIF in a bounded reservoir: (1) wellbore afterflow, (2) inclined formation linear flow, (3) inclined pseudo-radial flow, (4) horizontal elliptical flow, (5) horizontal pseudo-radial flow, and (6) boundary dominated flow. The wellbore afterflow only occurs at the early production period, which reflects the influence of the wellbore storage on the pressure transient behavior. **Figure 3-12** illustrates the flow behavior of various flow regimes that can possibly occur in a reservoir with a PPIF:

inclined formation linear flow, inclined pseudo-radial flow, horizontal elliptical flow, and horizontal pseudo-radial flow. The half-unit slope on the pressure derivative curve indicates that the flow regime is inclined formation linear flow. During this period, the fluid flows perpendicularly from the matrix to the fracture, as shown in Figure 3-12a. A schematic of the inclined pseudo-radial flow is shown in Figure 3-12b. During this period, the fluid flows radially to the fracture axis along the inclined direction. Following the inclined pseudo-radial flow, the pressure derivative plot exhibits a 1/3-slope, signifying that a horizontal elliptical flow, which has limited height around a PPIF, appears in the reservoir (see Figure 3-12c). Figure 3-12d illustrates the fluid flow at the horizontal pseudo-radial flow period, during which the fluid flows radially to the *Z*-axis along the vertical well. This flow regime can be observed only if the reservoir is large enough. Afterwards, the fluid flow enters the pseudo-steady state once the reservoir boundary starts exerting its influence on the pressure dynamics, leading to a unit slope on the pressure derivative curve; this corresponds to the boundary dominated flow.

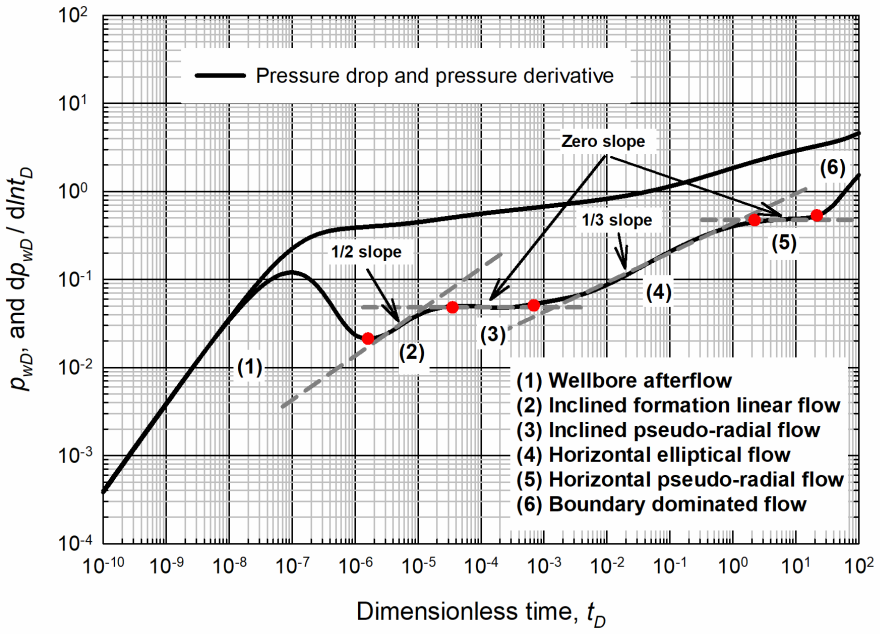

Figure 3-11. Identification of the flow regimes that can be observed during the production of the benchmark PPIF in a bounded reservoir.

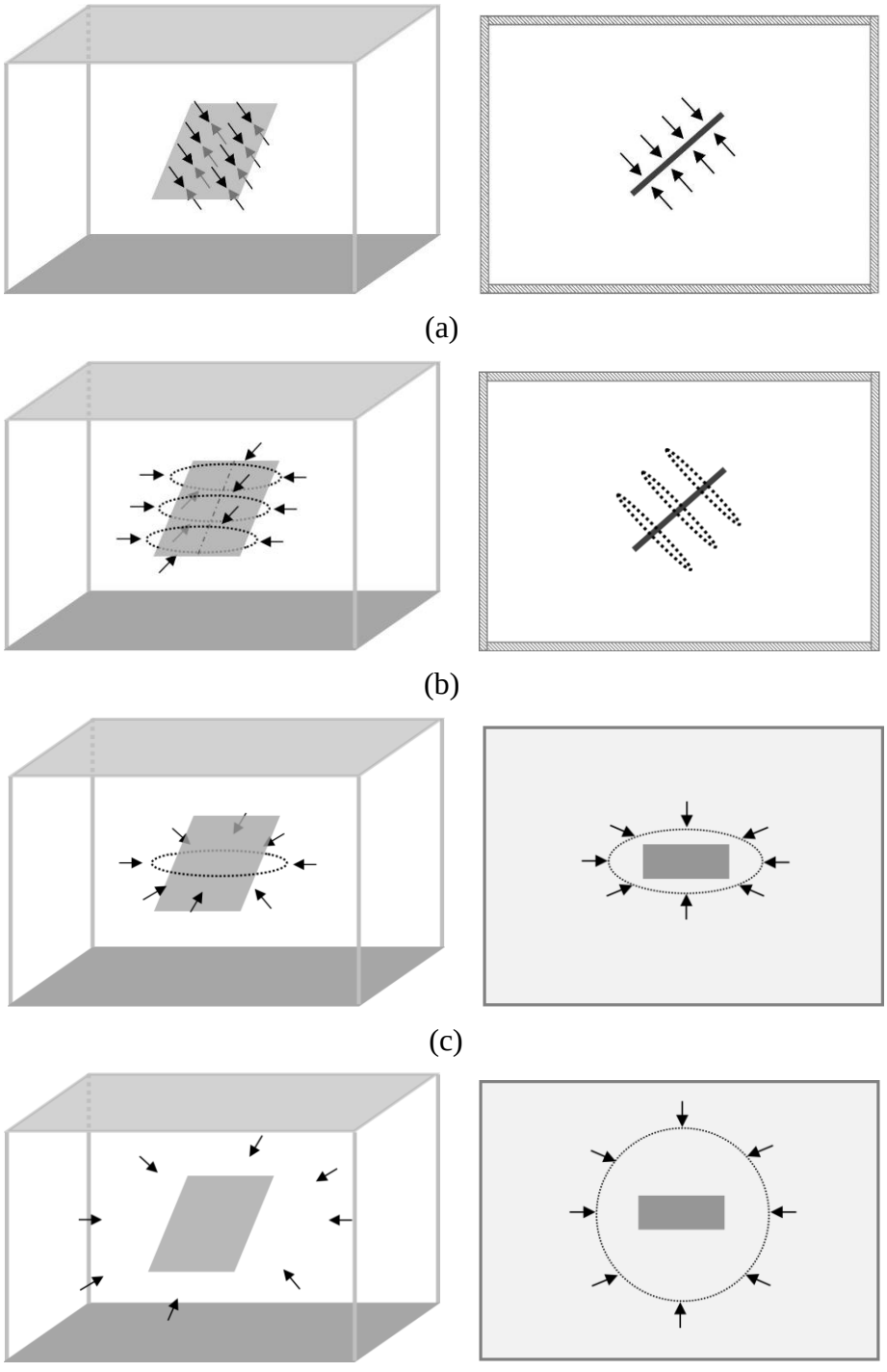

Figure 3-12. The flow behaviors of various flow regimes occurring during the production of PPIF: (a) inclined formation linear flow from 3D view and side view; (b) inclined pseudo-radial flow from 3D view and side view; (c) horizontal elliptical flow form 3D view and top view; and (d) horizontal pseudo-radial flow from 3D view and top view.

In practice, the flow regimes that can be observed during the production of a PPIF are heavily dependent on the input values of the parameters that are chosen in the case studies. **Figure 3-13** shows the pressure drops and pressure derivatives of a PPIF with a penetrating ratio of 0.3. All of the other input values are kept the same as those in the benchmark PPIF model. From this figure, one can find the following flow regimes on the pressure derivative plot: (1) wellbore afterflow, (2) vertical elliptical flow, (3) vertical pseudo-radial flow, (4) horizontal elliptical flow, (5) horizontal pseudo-radial flow, and (6) boundary dominated flow. **Figure 3-14** depicts the flow behavior of the vertical elliptical flow and the vertical pseudo-radial flow. It is noted that the upper and lower boundaries can exert significantly early-time effect on the flow regimes of a PPIF. Since this PPIF has a small penetrating ratio (0.3), the interval between the upper/lower formation boundary and the fracture is large enough to enable the appearance of an elliptical flow along the vertical direction (i.e. vertical elliptical flow), as in Figure 3-14a. As the production proceeds, this vertical elliptical flow gradually turns into a vertical pseudo-radial flow (i.e., pseudo-radial flow along the vertical direction, see Figure 3-14b), leading to the appearance of a zero slope period on the pressure derivative curve (see Figure 3-13).

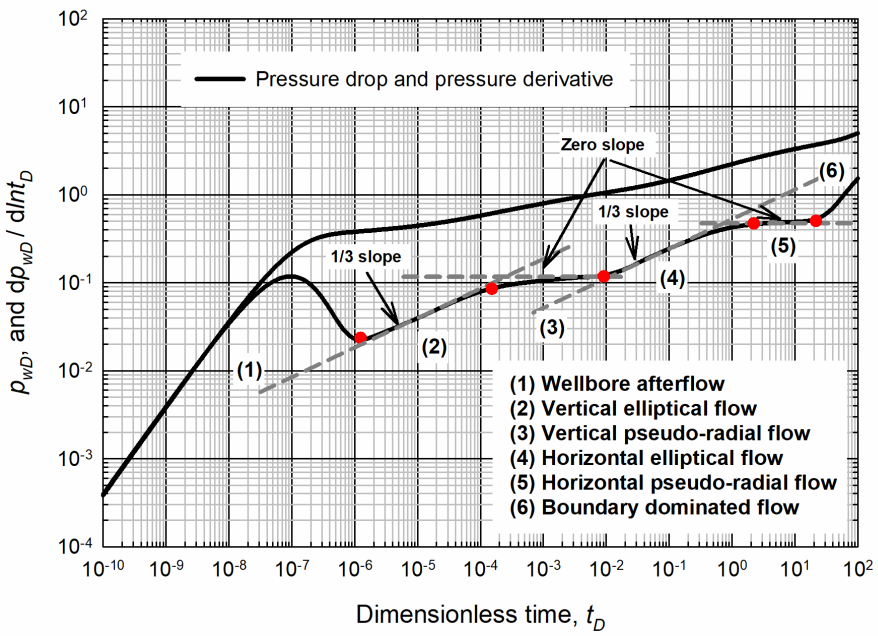

Figure 3-13. Identification of the flow regimes that can be observed during the production of a PPIF with a penetrating ratio of 0.3 in a bounded reservoir.

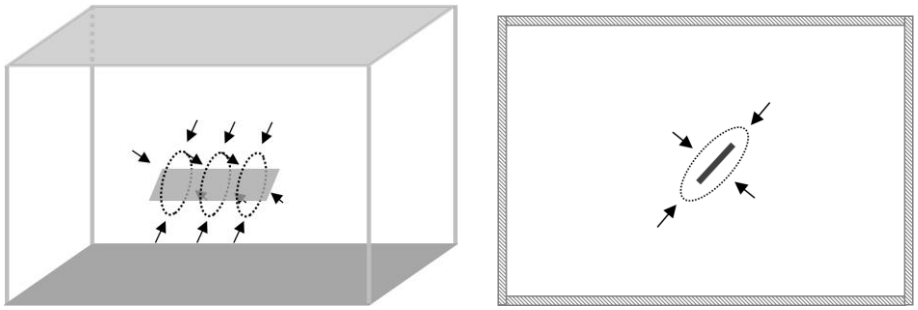

(a)

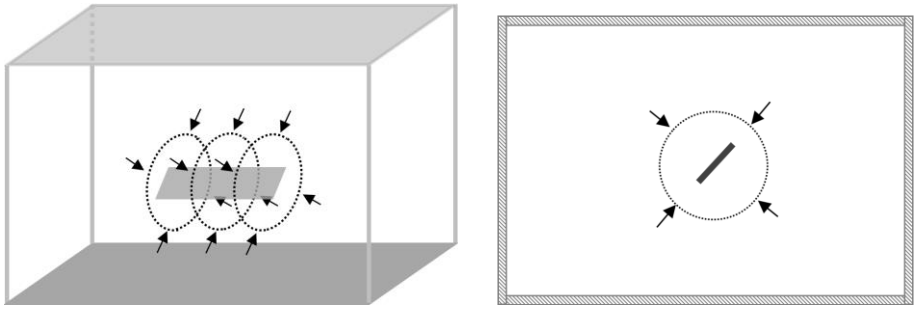

(b)

Figure 3-14. The flow behaviors of various flow regimes occurring during the production of PPIF: (a) vertical elliptical flow from 3D view and side view; and (b) vertical pseudo-radial flow from 3D view and side view.

Figure 3-15 illustrates the pressure drops and pressure derivatives of another PPIF model. Its difference with the benchmark PPIF model is that the penetrating ratio has been changed to 0.9 while the dimensionless fracture conductivity has been changed to 20. The following flow regimes can be identified on the pressure derivative plot: (1) wellbore afterflow, (2) fracture radial flow, (3) inclined pseudo-radial flow, (4) horizontal formation linear flow, (5) horizontal pseudo-radial flow, and (6) boundary dominated flow. It is interesting to note that a new flow regime, fracture radial flow, can be observed on the pressure derivative plot after the flow regime of wellbore afterflow. This flow regime can be observed only if the fracture conductivity and fracture inclined length are sufficiently large. **Figure 3-16a** illustrates the fracture radial flow, showing that the fluid in the fracture radially flows to the wellbore during this period. In addition, since this fracture has a high penetrating ratio (0.9), it is not possible for the vertical pseudo-radial flow to appear in the reservoir; therefore, the second zero-slope period should correspond to the inclined pseudo-radial flow, as indicated in Figure 3-12b. Following the inclined pseudo-radial flow, a horizontal formation linear flow is observed on the pressure derivative curve. Figure 3-16b shows the schematics of the horizontal formation linear flow which appears with limited height along the horizontal direction. Afterwards, one can also observe the horizontal pseudo-radial flow and boundary dominated flow.

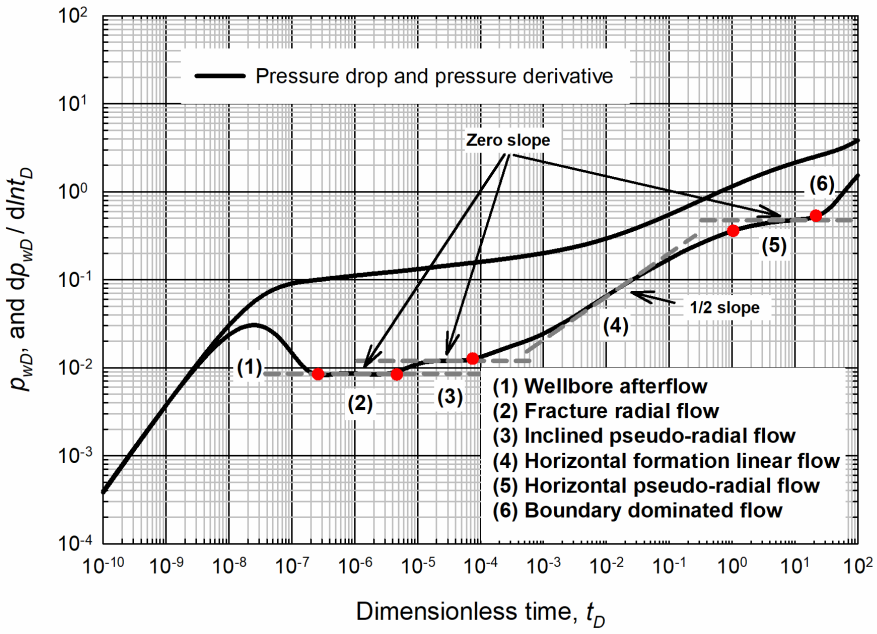

Figure 3- 15. Identification of the flow regimes that can be observed during the life of production of a PPIF with a penetrating ratio of 0.9 and dimensionless fracture conductivity of 20 in a bounded reservoir.

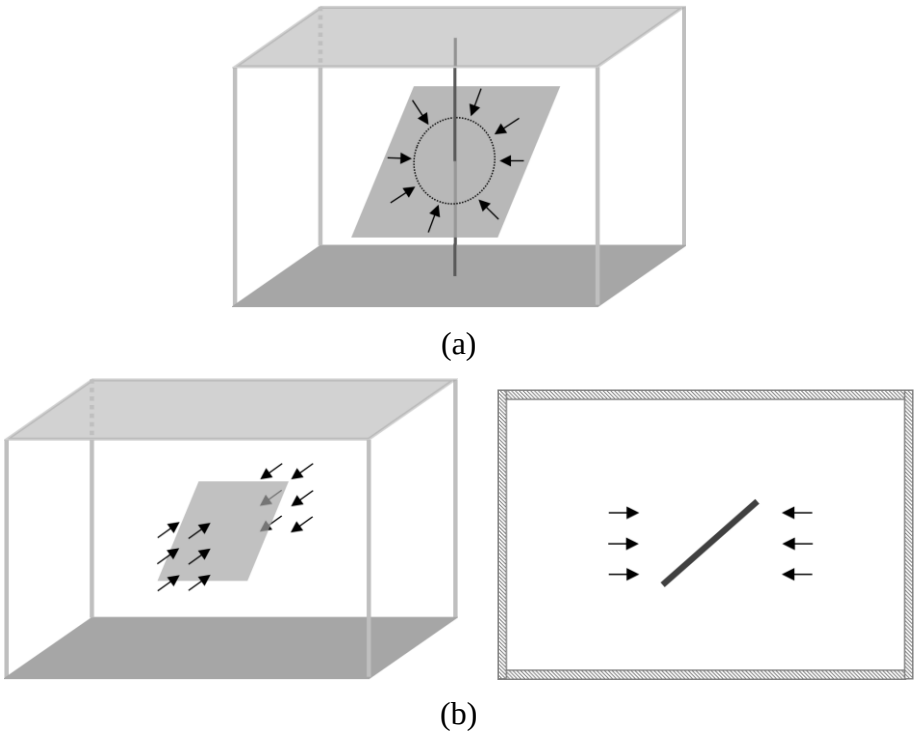

(a)

(b)

Figure 3-16. The flow behaviors of various flow regimes occurring during the production of PPIF: (a) fracture radial flow from 3D view; and (b) horizontal formation linear flow from 3D view and side view.

It is worth noting that, the flow regimes of a PPIF are similar to those of a vertical fracture if the coordinate system of a PPIF is rotated and gets adjusted to the coordinate system of a vertical fracture. For a vertical fracture, one can observe the formation-linear flow, elliptical flow, and pseudo-radial flow on the pressure derivative plot. If the horizontal dimension of a PPIF is sufficiently small, a PPIF from the top view is similar to a vertical fracture; therefore, it is reasonable to observe a horizontal formation linear flow (Figure 3-16b), horizontal elliptical flow (Figure 3-12c), and horizontal pseudo-radial flow (Figure 3-12d) during the production of a PPIF. In addition, a PPIF (Figure 3-14a) from the side view is similar to a vertical fracture from the top view; thus, with appropriate values of the parameters, we should also observe the inclined formation linear flow (Figure 3-12a), vertical elliptical flow (Figure 3-14a), and vertical pseudo-radial flow (Figure 3-14b) along the vertical direction of a PPIF.

3.4.3 Sensitivity Analysis

Thereafter, using the developed model, we carry out detailed sensitivity analysis studying the influences of the following parameters on the pressure transient behavior: fracture's inclination angle, penetrating ratio, and fracture conductivity. **Table 3-1** shows the values of the dimensionless parameters used in the sensitivity analysis. The values in bold text shown in Table 3-1 are the values used in the benchmark model.

Table 3-1. Dimensionless parameters used in the sensitivity analysis.

Inclination angle, θ	Penetrating ratio, λ	Dimensionless fracture conductivity, C_{fD}
15^o	0.1	0.5
30^o	0.3	1.0
45^o	0.5	2.0
60^o	**0.7**	**5.0**
75^o	0.9	10.0

3.4.3.1 Inclination Angle

The influence of the inclination angle on the pressure transient behavior is studied on two scenarios. The first scenario considers a PPIF with varied inclination angle but fixed fracture dimension, while the second scenario considers a PPIF with varied inclination angle but fixed penetration ratio. **Figure 3-17** illustrates the pressure drops and pressure derivatives of the PPIF with different inclination angles and fixed fracture dimension. From the pressure derivative curves in Figure 3-17, one can observe a 1/4-slope period or 1/2-slope period after the wellbore afterflow, which indicate the appearance of bilinear flow and inclined formation linear flow, respectively. During the bilinear flow, two flows occur simultaneously, i.e., a linear flow from the matrix to the fracture together with a linear flow from the fracture to the wellbore. A more detailed introduction about the bilinear flow can be referred to Cinco-Ley and Samaniego-V (1981). It is interesting to note that, a negative slope period can be observed after the bilinear flow (or inclined formation linear flow) with a larger inclination angle (e.g., $\theta = 75^o$). This is ascribed to a converging flow around the PPIF. **Figures 3-18a and 3-18b** show the side view of the schematics of the spherical flow around a point sink and converging flow around a PPIF. Comparing these two figures, one can see that the converging flow contains spherical flow component whose slope is -1/2 (Culham, 1974), resulting into a negative slope on the pressure derivative curve of a PPIF. Figure 3-18c shows the side view of a converging flow around a PPIF with a small inclination angle. The converging flow in Figure 3-18c exhibits less spherical flow component, and thus the negative slope period is less distinguishable for a small inclination angle (see Figure 3-17). Following the converging flow period, a 1/2-slope, which indicates a horizontal formation linear flow, appears on the pressure derivative curve with an inclination angle of 75^o. It is noted that a vertical fracture can exhibit a horizontal formation linear flow only

if the dimensionless fracture conductivity is sufficiently large; the studied dimensionless fracture conductivity (C_{fD} = 5) cannot satisfy the conditions causing the occurrence of the horizontal formation linear flow for a vertical fracture. Therefore, as the inclination angle decreases from 75° to 15°, the PPIF becomes closer to be vertical, and the flow regimes switch from a horizontal formation linear flow (1/2-slope) to a horizontal elliptical flow (1/3-slope).

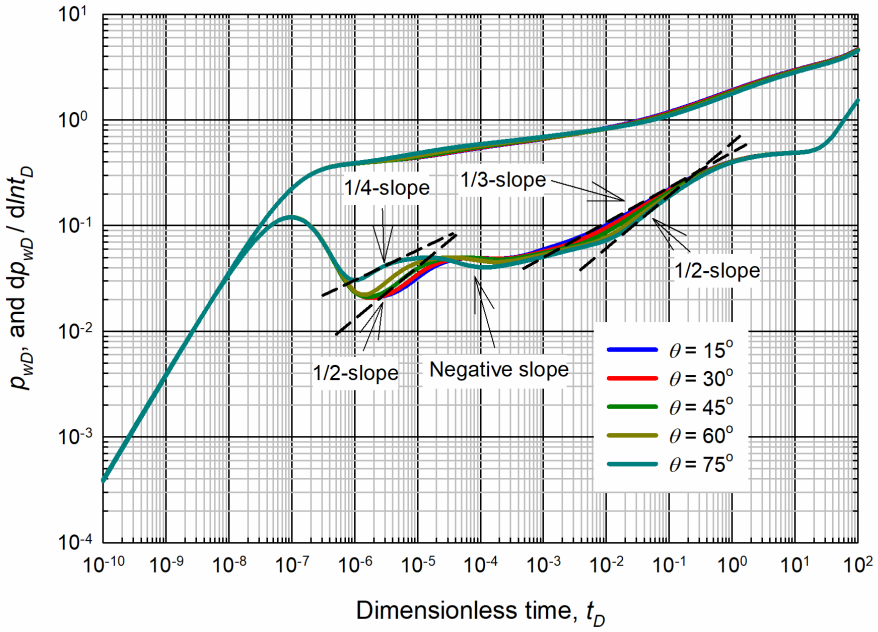

Figure 3-17. Impact of inclination angle on the pressure drops and pressure derivatives of a PPIF with fixed fracture dimension.

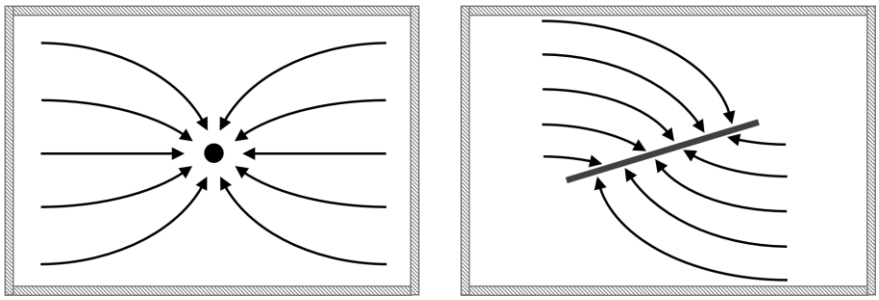

(a) (b)

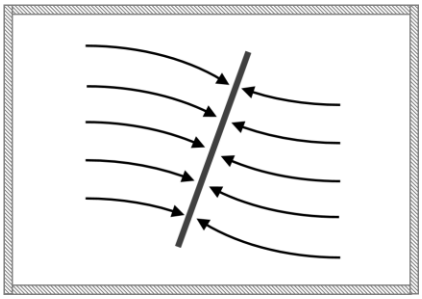

(c)

Figure 3-18. Schematics of the spherical flow and converging flow: (a) side view of spherical flow around a point sink; (b) side view of converging flow around a PPIF with a large inclination angle; and (c) side view of converging flow around a PPIF with a small inclination angle.

Figure 3-19 depicts the pressure drops and pressure derivatives of the PPIF with different inclination angles but fixed penetrating ratio. As shown in this figure, a negative slope period, corresponding to a converging flow, can also be observed after the inclined formation linear flow for the fractures with large inclination angles (e.g., $\theta = 60^{o}$ and 75^{o}). In addition, the horizontal formation linear flow is also changed into a horizontal elliptical flow as the inclination angle is varied from 75^{o} to 15^{o}. These two observations imply that: first, in a hydraulically fractured reservoir (no natural/secondary fracture), a negative slope period on the pressure derivative curve denotes that the hydraulic fracture is possible to be a PPIF with a large inclination angle; and second, since the PPIF with small dimensionless fracture conductivity (e.g., $C_{fD} = 5$) can exhibit a horizontal formation linear flow, the fracture conductivity can be over-estimated if a PPIF is mistakenly recognized as a vertical fracture.

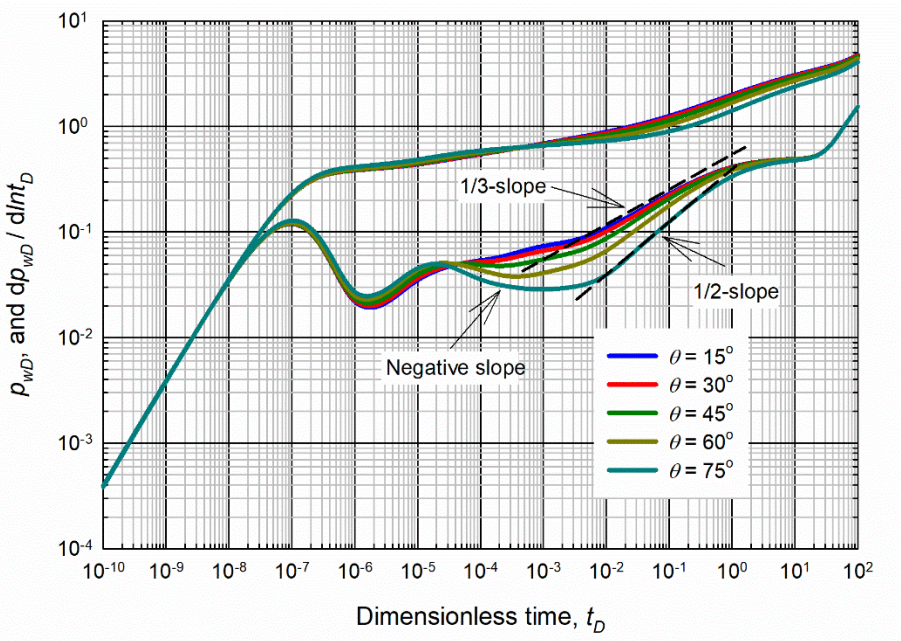

Figure 3-19. Impact of inclination angle on the pressure drops and pressure derivatives of a PPIF with a fixed penetrating ratio.

3.4.3.2 Penetrating Ratio

Different penetrating ratios, i.e., λ = 01, 0.3, 0.5, 0.7, and 0.9, are examined in an attempt to explore its influence on the pressure response of the PPIF. The pressure drops and pressure derivatives at different penetrating ratios, which are calculated with the proposed model, are presented in **Figure 3-20**. As one can see from the pressure drop curves, the penetrating ratio mainly influences the intermediate and late production periods of the pressure response. The pressure drop tends to be decreased as the penetrating ratio is increased. This is because the fracture has a larger contact area with the reservoir at a larger penetrating ratio, leading to a lower flow resistance between the reservoir and the fracture. In addition, as for the scenario with a penetrating ratio of 0.1, the PPIF has a small length along the inclination direction. Thus, the fluid tends to converge to the wellbore along the vertical direction. If the fracture conductivity is small (e.g., C_{fD} = 5), the fluid will also converge to the wellbore along the horizontal direction, leading to a 3D converging flow near the wellbore. This renders a negative slope period

appearing on the pressure derivative curve with λ = 0.1. It is also observed from Figure 3-20 that a negative slope period appears on the pressure derivative curve with a penetrating ratio of 0.9. Whereas, with the other penetrating ratios (λ = 0.3, 0.5, and 0.7), the negative slope period is absent. **Figure 3-21** compares the flux distribution along the PPIF with a penetrating ratio of 0.5 against that with a penetrating ratio of 0.9 at dimensionless time of 1×10^{-4}. As one can see in this figure, the fluxes near the wellbore with λ = 0.9 are larger than those with λ = 0.5. This signifies that, with a penetrating ratio of 0.9, the converging flow around the wellbore is more noticeable and the negative slope period is more distinguishable.

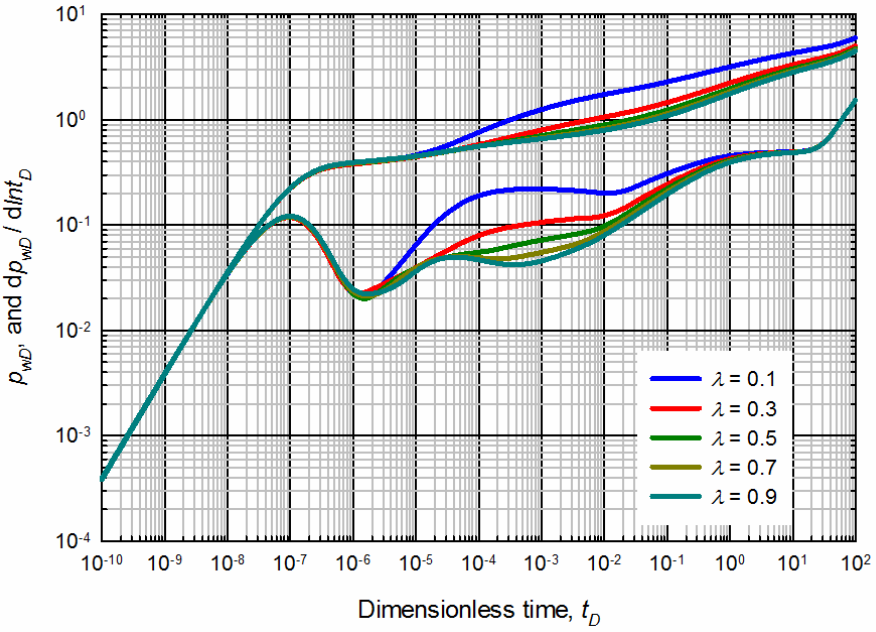

Figure 3-20. Impact of penetrating ratio on the pressure drops and pressure derivatives of a PPIF.

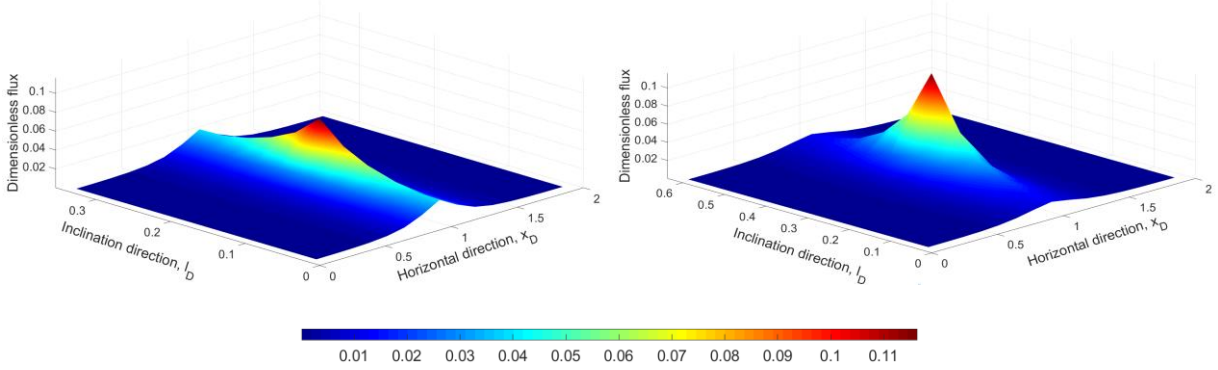

Figure 3-21. Comparison of the flux distribution of the PPIF with a penetrating ratio of 0.5 against that with a penetrating ratio of 0.9.

3.4.3.3 Fracture Conductivity

Figure 3-22 presents the pressure response of a PPIF at different fracture conductivities, i.e., C_{fD} =0.5, 1, 2, 5, and 10. As one can see from this figure, the fracture conductivity exerts a significant influence on the pressure drops as well as the pressure derivatives throughout the entire production period. A higher fracture conductivity leads to a smaller pressure drop, which is ascribed to a lower flow resistance in the fracture. One can also find that the negative slope period is more distinguishable with smaller dimensionless fracture conductivity. This can be explained as follows: the fluxes near the wellbore with smaller C_{fD} are larger than those with larger C_{fD} (see Figure 3-9); hence, with a smaller dimensionless fracture conductivity, a converging flow around the wellbore is more likely to occur, and thus the negative slope period can appear on the pressure derivative curve with small dimensionless fracture conductivity.

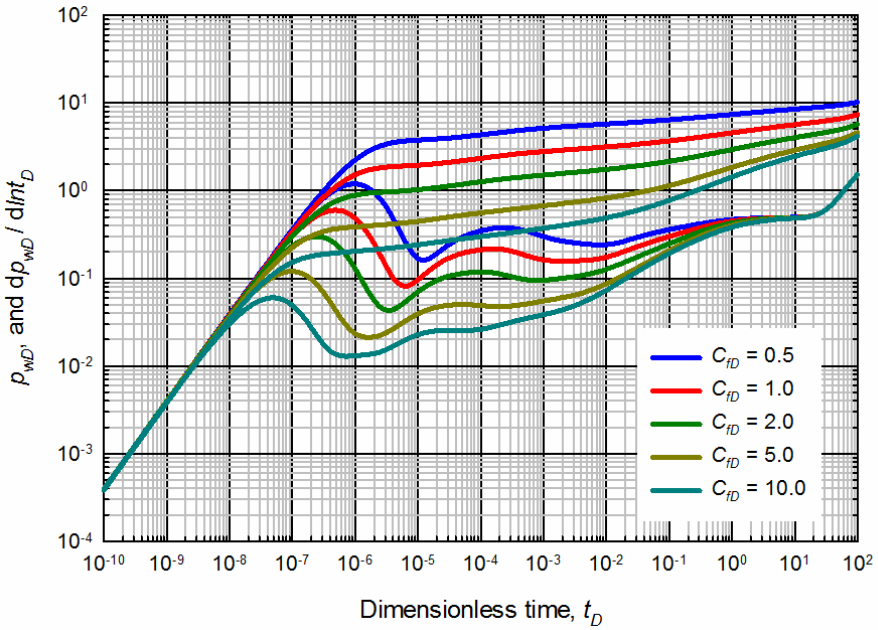

Figure 3-22. Impact of fracture conductivity on the pressure drops and pressure derivatives of a PPIF.

3.4.4 Application of the Proposed Model

In practice, a "critical" depth about 2000 ft can be regarded as the threshold, below which the hydraulic fracture is normally vertical (Wright *et al.*, 1997). Whereas, as for a shallow formation which is located at a depth less than 2000 ft, the vertical stress can be close to the horizontal stress; therefore, a fully penetrating vertical fracture (FPVF), partially penetrating vertical fracture (PPVF), fully penetrating inclined fracture (FPIF), PPIF, or even horizontal fracture (HF), can be induced after the fracturing treatment (see Figure 3-1a, in which a PPIF is induced at a depth of 516 m/1693 ft). If the tiltmeter monitoring or the microseismic monitoring is not utilized to determine the propagation, both along the horizontal direction and the vertical direction, of the fracture, it is difficult to recognize the fracture pattern from production data. In such cases, the utilization of a single fracture model for fitting the historical production data can lead to inaccurate results, while applying all the fracture models to fit the production data and find out the best-match curve can be a heavy workload. However, the proposed model can address this issue without prior knowledge about the fracture pattern. This is because, a vertical/horizontal fracture can be regarded as a PPIF with an inclination angle of $0^o/90^o$, and a fully penetrating fracture can be regarded as a PPIF with a penetrating ratio of 1. This indicates that this proposed model cannot only simulate exactly PPIFs, but also FPVFs, PPVFs, FPIFs, and HFs. Therefore, the proposed model is more advantageous since it can be used to fit the historical production data of a fractured well in the cases where the fracture pattern is not known beforehand.

Due to the fact that there is no available production data of a PPIF in previous studies, in this section, this proposed model is used to fit the pressure buildup data from a PPVF, which can be regarded as a PPIF with an inclination angle of 0^o. The known values of the parameters are summarized in **Table 3-2** (Rodriguez *et al*., 1984). The matrix permeability of k_m = 4.59 mD is

obtained with radial flow analysis by Rodriguez *et al.* (1984). The unknown parameters include horizontal fracture length (x_f), penetrating ratio (λ), fracture conductivity (C_f), and skin factor (S). The skin factor S can be expressed as:

$$S = P_{wD} - p_{wD}, \tag{3-21}$$

where P_{wD} is real dimensionless wellbore pressure which considers the skin factor. The history-matching work is conducted by varying these four unknown values of parameters. Table 3-3 shows the values of the parameters determined by history matching of the production data. **Figure 3-23** shows the measured pressure buildup data and the pressure buildup data calculated with the history-matched model. One can see from Figure 3-23 the calculated pressure buildup data show an excellent agreement with the pressure buildup data in Rodriguez *et al*. (1984). It is noted in Table 3-3 that a negative skin (-0.745) is obtained. This is because our proposed model assumes that the wellbore is restrictedly connected to the fracture, whereas the wellbore can be fully connected to the vertical fracture. This is the reason leading to that the pressure drop calculated with the proposed model can be higher than the real pressure drop, leading to a negative skin during the history matching. In addition, the values of the parameters (including C_w, C_s, and w) cannot be obtained with the history matching work since they only exert their influences on the pressure response at the very early production period and the measured pressure build-up data do not cover this period.

Table 3-2. Known values of the parameters of a PPVF in Rodriguez *et al*. (1984).

Parameter	Value	Parameter	Value
q_w, m^3/d	31.8	c_{tm}, MPa^{-1}	7.25×10^{-4}
h, m	78.6	ϕ_m	0.3
B, m^3/m^3	1.4	r_w, m	0.0762
μ, mPa·s	3	θ	0^o

Table 3-3. History matching results for the pressure buildup data.

Parameter	Value	Parameter	Value

x_f, m	55.8	λ	0.45
C_f, mD·m	768.4	S	-0.745

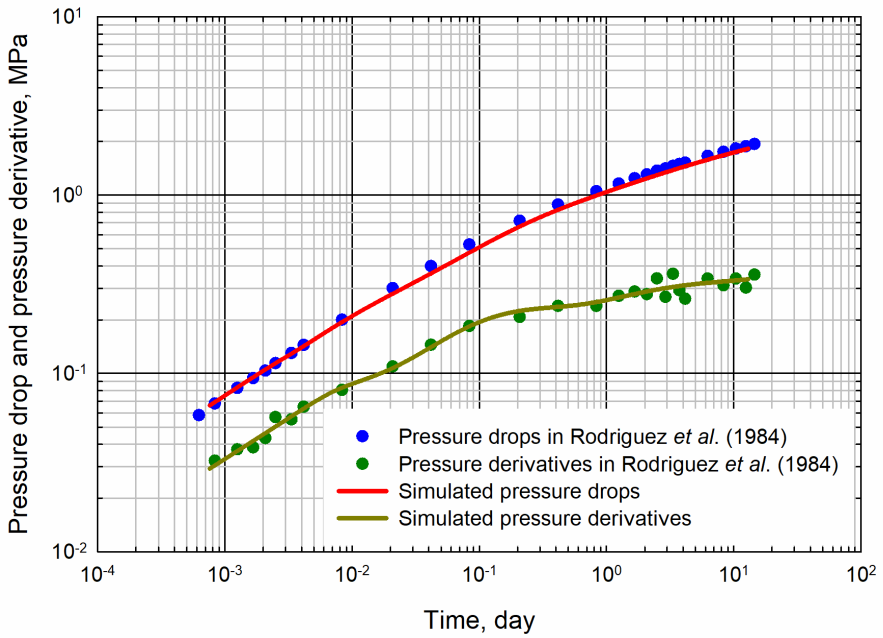

Figure 3-23. Comparison of the pressure buildup data in Rodriguez *et al*. (1984) and calculated ones using the history-matched model.

3.5. Conclusions

In this work, we develop a novel semi-analytical model to study the pressure transient behavior of a finite-conductivity PPIF in a bounded reservoir. With the aid of the proposed model, we depict the flux distribution along the fracture with different fracture conductivities and distinguish the flow regimes that can be observed during the production of a PPIF. In addition, we investigate the influence of inclination angle, penetrating ratio, and fracture conductivity on the pressure responses. Furthermore, we apply this proposed model to a real field case. These case studies lead us to draw the following conclusions:

- Under given reservoir and fracture properties, a PPIF with a finite conductivity in a bounded reservoir may exhibit the following flow regimes: wellbore afterflow, fracture radial flow, bilinear flow, inclined formation linear flow, vertical elliptical flow, vertical

pseudo-radial flow, inclined pseudo-radial flow, horizontal formation linear flow, horizontal elliptical flow, horizontal pseudo-radial flow, and boundary dominated flow;

- A converging flow near the wellbore can occur during the production of a PPIF, leading to a negative slope period on the pressure derivative curve. The negative slope period can be observed for three types of PPIF: first, the PPIF has a sufficient large inclination angle; second, the penetrating ratio of the PPIF is sufficiently small or sufficiently large; and third, the dimensionless fracture conductivity of the PPIF is sufficiently small;
- The PPIF can exhibit a horizontal formation linear flow even with a small dimensionless fracture conductivity (e.g., C_{fD} = 5). This implies that if a PPIF is mistakenly recognized as a vertical fracture, the fracture conductivity will be over-estimated;
- In addition to PPIFs, this proposed model can also be used to simulate the pressure transient behavior of FPVFs, PPVFs, FPIFs, and HFs. Hence the proposed model can be utilized in the cases where the fracture pattern is not known a priori; and
- By rotating the coordinate system of a PPIF, a PPIF in a bounded reservoir can be converted to a PPVF with an arbitrary azimuth in a bounded reservoir; such that this proposed semi-analytical model can also be used to simulate the pressure transient behavior of a PPVF with an arbitrary azimuth in a bounded reservoir.

Nomenclature

Δl = fracture panel's length along the inclination direction, m

Δl_D = dimensionless fracture panel's length along the inclination direction, m

Δx = fracture panel's length along the horizontal direction, m

Δx_D = dimensionless fracture panel's length along the horizontal direction, m

a, b, c, A= parameters defined in Appendix 3A

$\boldsymbol{A}$, $\boldsymbol{B}_1$, $\boldsymbol{B}_2$, $\boldsymbol{C}$, $\boldsymbol{D}$, $\boldsymbol{G}$, $\boldsymbol{p}_f$, $\boldsymbol{q}^n$ = matrices defined in Appendices A and B

B = formation volume factor, m^3/m^3

C_f = fracture conductivity, mD·m

C_{fD} = dimensionless fracture conductivity

C_s = dimensionless coefficient defined in this work

c_{tf} = fracture total compressibility, MPa^{-1}

c_{tm} = matrix total compressibility, MPa^{-1}

C_w = wellbore storage coefficient, bbl/psi

C_{wD} = dimensionless wellbore storage coefficient

h = formation thickness, m

h_D = dimensionless formation thickness

h_f = fracture height, m

k_f = fracture permeability, mD

k_m = matrix permeability, mD

l = space position along the inclination direction of the fracture, m

l_D = dimensionless space position along the inclination direction of the fracture

l_f = fracture length along inclined direction

$l_{i,j}$ = space position along the inclination direction of fracture panel (i, j), m

N_f = number of panels of the discretized fracture

N_i = number of panels of the discretized fracture along horizontal direction

N_j = number of panels of the discretized fracture along inclined direction

p = pressure, MPa

p_D = dimensionless pressure

p_f = fracture pressure, MPa

p_{fD} = dimensionless fracture pressure

p_i = initial reservoir pressure, MPa

p_w = bottomhole pressure

p_{wD} = dimensionless bottomhole pressure

P_{wD} = real dimensionless wellbore pressure

p_{wpD} = dimensionless pressure of the well-panel

q = flux rate form the matrix to the fractureunder standard condition, m^3/d

q_D = dimensionless flux

$q_{f\text{-}w}$ = flux from fracture to the wellbore under standard condition, m^3/d

$q_{f\text{-}wD}$ = dimensionless flux from fracture to the wellbore

q_w = well production rate under standard condition, m^3/d

r_{eq} = equivalent radius, m

r_{eqD} = dimensionless equivalent radius

r_w = wellbore radius, m

r_{wD} = dimensionless wellbore radius

S = skin factor

t = time, d

t_D = dimensionless time

w = fracture width, m

w_D = dimensionless fracture width

x, y and z = x-, y-, and z-coordinate

x_0, y_0, z_0 = center position coordinates of the line/plane source, m

x_{0D}, y_{0D}, z_{0D} = dimensionless center position coordinates of the line/plane source

x_D, y_D and z_D = dimensionless coordinate

x_e, y_e, and z_e = reservoir dimension, m

x_f = fracture length along horizontal direction, m

$x_{f/2}$ = half fracture length along horizontal direction, m

$y(l_{i,j})$, $z(l_{i,j})$ = the space coordinates at position $l_{i,j}$, m

α = diffusivity coefficient, m^2/d

β = unit conversion factor which equals to 0.0853

γ = dimensionless coefficient

δ = the instantaneous flux

θ = inclination angle

λ = penetrating ratio

μ = oil viscosity, mPa·s

ϕ_f = effective porosity in the fracture system

ϕ_m = matrix porosity

Subscripts and superscripts

f = fracture

i = initial condition

m = matrix

sc = standard condition

t = total

w = wellbore

Acknowledgements

The authors would like to acknowledge the financial supports provided by the Natural Science and Engineering Research Council of Canada (NSERC) as well as the financial supports provided by the China Scholarship Council (CSC). The authors also thank Schlumberger for providing us the academic license of Eclipse.

Appendix 3A - Numerical Formulation for the Oil Flow in the Fracture System

In the fracture system, the transient flow equation for the oil flow can be written as:

$$\frac{\partial^2 p_f}{\partial x^2}+\frac{\partial^2 p_f}{\partial l^2}+\frac{B\mu q}{\beta\Delta x\Delta l w k_f}=\frac{\mu\phi_f c_{tf}}{\beta k_f}\frac{\partial p_f}{\partial t} \tag{3A-1}$$

Writing Equation (3A-1) in a dimensionless form, one can have:

$$\frac{\partial^2 p_{fD}}{\partial x_D^2}+\frac{\partial^2 p_{fD}}{\partial l_D^2}-\frac{2\pi h_D}{\Delta x_D\Delta l_D C_{fD}}q_D=\frac{w_D C_s}{C_{fD}}\frac{\partial p_{fD}}{\partial t_D} \tag{3A-2}$$

At the time level t_D^n, applying finite difference approximation to the first term on the left-hand side of Equation (3A-2) gives:

$$\frac{\partial^2 p_{fD}}{\partial x_D^2}\approx\frac{1}{\Delta x_D}\left[\left(\frac{\partial p_{fD}^n}{\partial x_D}\right)_{i+1/2,j}-\left(\frac{\partial p_{fD}^n}{\partial x_D}\right)_{i-1/2,j}\right]\approx\frac{1}{\Delta x_D}\left[\frac{p_{fD_{i+1,j}}^n-p_{fD_{i,j}}^n}{\Delta x_{D_{i+1/2,j}}}-\frac{p_{fD_{i-1,j}}^n-p_{fD_{i,j}}^n}{\Delta x_{D_{i-1/2,j}}}\right] \tag{3A-3}$$

Since the fracture panels have a uniform dimension in this work, Equation (3A-3) can be simplified as:

$$\frac{\partial^2 p_{fD}}{\partial x_D^2}=\frac{1}{\Delta x_D^2}\left(p_{fD_{i+1,j}}^n-2p_{fD_{i,j}}^n+p_{fD_{i,j}}^n\right) \tag{3A-4}$$

Similarly, the second term on the left-hand side of Equation (3A-2) can be rewritten as:

$$\frac{\partial^2 p_{fD}}{\partial l_D^2}=\frac{1}{\Delta l_D^2}\left(p_{fD_{i,j+1}}^n-2p_{fD_{i,j}}^n+p_{fD_{i,j-1}}^n\right) \tag{3A-5}$$

Applying backward-difference approximation on the time derivative term, one can have:

$$\frac{w_D C_s}{C_{fD}}\frac{\partial p_{fD}}{\partial t_D}=\frac{w_D C_s}{C_{fD}}\frac{1}{\Delta t_D^n}\left(p_{fD_{i,j}}^n-p_{fD_{i,j}}^{n-1}\right) \tag{3A-6}$$

Inserting Equations (3A-4), (3A-5) and (3A-6) into Equation (3A-2), one can have:

$$\frac{1}{\Delta x_D^2}\left(p^n_{fD_{i+1,j}}-2p^n_{fD_{i,j}}+p^n_{fD_{i,j}}\right)+\frac{1}{\Delta l_D^2}\left(p^n_{fD_{i,j+1}}-2p^n_{fD_{i,j}}+p^n_{fD_{i,j-1}}\right)$$
$$-\frac{2\pi h_D}{\Delta x_D \Delta l_D C_{fD}} q^n_{D_{i,j}} = \frac{w_D C_s}{C_{fD}} \frac{1}{\Delta t^n_D}\left(p^n_{fD_{i,j}}-p^{n-1}_{fD_{i,j}}\right) \tag{3A-7}$$

Rearranging Equation (3A-7) gives the following:

$$\left(\frac{2}{\Delta x_D^2}+\frac{2}{\Delta l_D^2}+\frac{w_D C_s}{C_{fD}}\frac{1}{\Delta t^n_D}\right)p^n_{fD_{i,j}}-\frac{1}{\Delta x_D^2}p^n_{fD_{i-1,j}}-\frac{1}{\Delta x_D^2}p^n_{fD_{i+1,j}}$$
$$-\frac{1}{\Delta l_D^2}p^n_{fD_{i,j-1}}-\frac{1}{\Delta l_D^2}p^n_{fD_{i,j+1}}+\frac{2\pi h_D}{\Delta x_D \Delta l_D C_{fD}} q^n_{D_{i,j}} = \frac{w_D C_s}{C_{fD}\Delta t^n_D} p^{n-1}_{fD_{i,j}} \tag{3A-8}$$

For convenience, we define the following parameters:

$$a_{i-1,j}=a_{i+1,j}=\frac{1}{\Delta x_D^2},\ a_{i,j-1}=a_{i,j+1}=\frac{1}{\Delta l_D^2} \tag{3A-9}$$

$$b=\frac{2\pi h_D}{\Delta x_D \Delta l_D C_{fD}},\ c=\frac{w_D C_s}{C_{fD}}\frac{1}{\Delta t^n_D} \tag{3A-10}$$

$$A_{i,j}=a_{i-1,j}+a_{i+1,j}+a_{i,j-1}+a_{i,j+1}+c \tag{3A-11}$$

As such, Equation (3A-8) can be rewritten as:

$$A_{i,j}p^n_{fD_{i,j}}-a_{i-1,j}p^n_{fD_{i-1,j}}-a_{i+1,j}p^n_{fD_{i+1,j}}-a_{i,j-1}p^n_{fD_{i,j-1}}-a_{i,j+1}p^n_{fD_{i,j+1}}+bq^n_{D_{i,j}}=cp^{n-1}_{fD_{i,j}} \tag{3A-12}$$

It is noted that,

$$\begin{cases} i=1,\ a_{i-1,j}=0 \\ i=N_i,\ a_{i+1,j}=0 \end{cases} \text{ and } \begin{cases} j=1,\ a_{i,j-1}=0 \\ j=N_j,\ a_{i,j+1}=0 \end{cases} \tag{3A-13}$$

In particular, the approximated flow equation for the well-panel should be written as:

$$A_{i,j}p^n_{fD_{i,j}}-a_{i-1,j}p^n_{fD_{i-1,j}}-a_{i+1,j}p^n_{fD_{i+1,j}}-a_{i,j-1}p^n_{fD_{i,j-1}}-a_{i,j+1}p^n_{fD_{i,j+1}}+b\left(q^n_{D_{i,j}}-q^n_{f-wD}\right)=cp^{n-1}_{fD_{i,j}} \tag{3A-14}$$

Applying Equations (3A-12) and (3A-14) to all of the fracture panels and arranging these fracture flow equations into a matrix format gives:

$$\boldsymbol{A}\cdot\boldsymbol{p}_f^n+\boldsymbol{B}_1\odot\boldsymbol{q}^n-q_{f-wD}^n\cdot\boldsymbol{B}_2=\boldsymbol{C}\odot\boldsymbol{p}_f^{n-1}, \tag{3A-15}$$

where $\odot$ is Hadamard product operator, $\boldsymbol{A}$ is a matrix of the coefficients $A_{i,j}$, $a_{i\text{-}1,j}$, $a_{i+1,j}$, $a_{i,j\text{-}1}$, and $a_{i,j+1}$, whose dimension is $n_f \times n_f$,

$$\boldsymbol{p}_f^n=\begin{bmatrix} p_{fD_{1,1}}^n \\ \vdots \\ p_{fD_{i_w,j_w}}^n \\ \vdots \\ p_{fD_{N_i,N_j}}^n \end{bmatrix},\ \boldsymbol{B}_1=\begin{bmatrix} b \\ \vdots \\ b \end{bmatrix}_{N_f\times 1},\ \boldsymbol{q}^n=\begin{bmatrix} q_{D_{1,1}}^n \\ \vdots \\ q_{D_{N_i,N_j}}^n \end{bmatrix},\ \boldsymbol{B}_2=\begin{bmatrix} 0 \\ \vdots \\ 0 \\ b \\ 0 \\ \vdots \\ 0 \end{bmatrix},\ \boldsymbol{C}=\begin{bmatrix} c \\ \vdots \\ c \end{bmatrix}_{N_f\times 1}, \tag{3A-16}$$

where $(i_w,\ j_w)$ indicates the position of the well-panel, the subscripts $N_f \times 1$ indicates the dimensions of the corresponding matrices, and the position of constant b in matrix $\boldsymbol{B}_2$ is consistent with the position of pressure $p_{fD_{iw,jw}}^n$ in matrix $\boldsymbol{p}_f^n$.

Appendix 3B – Analytical Solution for the Oil Flow in the Matrix System

The instantaneous line source function and the instantaneous plane source function have been introduced in detail by Gringarten and Ramey (1973). These two functions are given as follows: the instantaneous line source function in 1-dimension (1-D) bounded reservoir:

$$\frac{\phi c\left[p_i - p(x,t)\right]}{\delta} = \frac{1}{x_e}\left\{1 + 2\sum_{m=1}^{\infty}\exp\left[-\frac{m^2\pi^2\alpha t}{x_e^2}\right]\cos\frac{m\pi x_0}{x_e}\cos\frac{m\pi x}{x_e}\right\} \quad \text{(3B-1)}$$

and the instantaneous plane source function in 1-D bounded reservoir:

$$\frac{\phi c\left[p_i - p(x,t)\right]}{\delta} = \frac{x_f}{x_e}\left[1 + \frac{4x_e}{\pi x_f}\sum_{m=1}^{\infty}\frac{1}{m}\exp\left(-\frac{m^2\pi^2\alpha t}{x_e^2}\right)\sin\frac{m\pi x_f}{2x_e}\cos\frac{m\pi x_0}{x_e}\cos\frac{m\pi x}{x_e}\right], \quad \text{(3B-2)}$$

where δ is the instantaneous flux, α is diffusivity which is defined as $\alpha = k_m/\mu\phi_m c_t$, x_e is reservoir dimensions along the 1-D X direction, and x_0 represents the center position of the line/plane source. A line source in a 3-D reservoir (see **Figure 3B-1**) can be visualized as the intersection of a plane source along X direction, a line source along Y direction, and a line source along Z direction. As introduced by Carslaw and Jaeger (1959) and Gringarten and Ramey (1973), the pressure function of an instantaneous line source in such a 3-D bounded reservoir can be described with Newman product method as:

$$\begin{aligned}&\text{A line source function in 3-D}\\ &= \text{A plane source function in } X \text{ direction}\\ &\times \text{A line source function in } Y \text{ direction}\\ &\times \text{A line source function in } Z \text{ direction}\end{aligned} \quad \text{(3B-3)}$$

Inserting Equations (3B-1) and (3B-2) into Equation (3B-3) gives the instantaneous line source function in a 3-D bounded reservoir:

$$
\begin{aligned}
&p_i - p(x,y,z,t) = \frac{\delta}{\phi_m c_{tm}} \\
&\cdot\frac{\Delta x}{x_e}\left[1+\frac{4x_e}{\pi\Delta x}\sum_{m=1}^{\infty}\frac{1}{m}\exp\left(-\frac{m^2\pi^2\alpha t}{x_e^2}\right)\sin\frac{m\pi\Delta x}{2x_e}\cos\frac{m\pi x_0}{x_e}\cos\frac{m\pi x}{x_e}\right] \\
&\cdot\frac{1}{y_e}\left\{1+2\sum_{m=1}^{\infty}\exp\left[-\frac{m^2\pi^2\alpha t}{y_e^2}\right]\cos\frac{m\pi y_0}{y_e}\cos\frac{m\pi y}{y_e}\right\} \\
&\cdot\frac{1}{z_e}\left\{1+2\sum_{m=1}^{\infty}\exp\left[-\frac{m^2\pi^2\alpha t}{z_e^2}\right]\cos\frac{m\pi z_0}{z_e}\cos\frac{m\pi z}{z_e}\right\}
\end{aligned}
\quad , \qquad \text{(3B-4)}
$$

where y_e and z_e are the reservoir dimensions along Y and Z directions, y_0 and z_0 represent the center position of the line source along Y and Z directions. **Figure 3B-2** shows a side view of a plane source, i.e., fracture panel (i, j). One can obtain the plane source function by integrating Equation (3B-4) along the inclined direction:

$$
\begin{aligned}
&p_i - p(x,y,z,t) = \frac{\delta}{\phi_m c_{tm}}\frac{\Delta x}{x_e y_e z_e} \\
&\cdot\left[1+\frac{4x_e}{\pi\Delta x}\sum_{m=1}^{\infty}\frac{1}{m}\exp\left(-\frac{m^2\pi^2\alpha t}{x_e^2}\right)\sin\frac{m\pi\Delta x}{2x_e}\cos\frac{m\pi x_{0_{i,j}}}{x_e}\cos\frac{m\pi x}{x_e}\right] \\
&\cdot\int_{l_{i,j}=0}^{l_{i,j}=\Delta l}\left\{1+2\sum_{m=1}^{\infty}\exp\left[-\frac{m^2\pi^2\alpha t}{y_e^2}\right]\cos\frac{m\pi y\left(l_{i,j}\right)}{y_e}\cos\frac{m\pi y}{y_e}\right\} \\
&\cdot\left\{1+2\sum_{m=1}^{\infty}\exp\left[-\frac{m^2\pi^2\alpha t}{z_e^2}\right]\cos\frac{m\pi z\left(l_{i,j}\right)}{z_e}\cos\frac{m\pi z}{z_e}\right\}\mathrm{d}l_{i,j}
\end{aligned}
\quad , \qquad \text{(3B-5)}
$$

where $x_{0_{i,j}}$ represents the center position of the fracture panel (i, j) along x-axis, Δl is the fracture length along the inclination direction, $l_{i,j}$ represent the spatial position along the inclination direction of fracture panel (i, j), and $y(l_{i,j})$ and $z(l_{i,j})$ indicate the space coordinates at position $l_{i,j}$. For a continuous plane source which has a constant flux rate, the pressure function is written as:

$$
\begin{aligned}
&p_i - p(x,y,z,t) = \frac{Bq}{\phi_m c_{tm} \Delta x \Delta y} \frac{\Delta x}{x_e y_e z_e} \int_{\tau_1}^{\tau_2} \\
&\left\{1 + \frac{4x_e}{\pi \Delta x} \sum_{m=1}^{\infty} \frac{1}{m} \exp\left[-\frac{m^2 \pi^2 \alpha (t-\tau)}{x_e^2}\right] \sin\frac{m\pi \Delta x}{2x_e} \cos\frac{m\pi x_{0_{i,j}}}{x_e} \cos\frac{m\pi x}{x_e}\right\} \\
&\cdot \int_{l_{i,j}=0}^{l_{i,j}=\Delta l} \left\{1 + 2\sum_{m=1}^{\infty} \exp\left[-\frac{m^2 \pi^2 \alpha (t-\tau)}{y_e^2}\right] \cos\frac{m\pi y(l_{i,j})}{y_e} \cos\frac{m\pi y}{y_e}\right\} \\
&\cdot \left\{1 + 2\sum_{m=1}^{\infty} \exp\left[-\frac{m^2 \pi^2 \alpha (t-\tau)}{z_e^2}\right] \cos\frac{m\pi z(l_{i,j})}{z_e} \cos\frac{m\pi z}{z_e}\right\} \mathrm{d}l_{i,j} \mathrm{d}\tau
\end{aligned}
\quad , \qquad \text{(3B-6)}
$$

where (τ_1, τ_2) indicates that the plane source is continued from time τ_1 to time τ_2. In practice, the flux rate of each fracture panel is time-dependent. Based on the superposition principle, one can calculate the pressure response caused by an inclined plane source that has a time-dependent flux rate with the following equation:

$$
\begin{aligned}
&p_i - p(x,y,z,t^n) = \frac{B}{\phi_m c_{tm} \Delta x \Delta y} \frac{\Delta x}{x_e y_e z_e} \sum_{k=1}^{k=n} q^k \int_{t^{k-1}}^{t^k} \\
&\left\{1 + \frac{4x_e}{\pi \Delta x} \sum_{m=1}^{\infty} \frac{1}{m} \exp\left[-\frac{m^2 \pi^2 \alpha (t-\tau)}{x_e^2}\right] \sin\frac{m\pi \Delta x}{2x_e} \cos\frac{m\pi x_{0_{i,j}}}{x_e} \cos\frac{m\pi x}{x_e}\right\} \\
&\cdot \int_{l_{i,j}=0}^{l_{i,j}=\Delta l} \left\{1 + 2\sum_{m=1}^{\infty} \exp\left[-\frac{m^2 \pi^2 \alpha (t-\tau)}{y_e^2}\right] \cos\frac{m\pi y(l_{i,j})}{y_e} \cos\frac{m\pi y}{y_e}\right\} \\
&\cdot \left\{1 + 2\sum_{m=1}^{\infty} \exp\left[-\frac{m^2 \pi^2 \alpha (t-\tau)}{z_e^2}\right] \cos\frac{m\pi z(l_{i,j})}{z_e} \cos\frac{m\pi z}{z_e}\right\} \mathrm{d}l_{i,j} \mathrm{d}\tau
\end{aligned}
\qquad \text{(3B-7)}
$$

Equation (3B-7) can be used to calculate the pressure response caused by a single fracture panel, while the pressure response caused by the entire fracture should be the summation of the pressure response from all of the panels, leading to the following:

$$
\begin{aligned}
p_i - p\left(x,y,z,t^n\right) &= \frac{B}{\phi_m c_{tm}\Delta x\Delta y}\frac{\Delta x}{x_e y_e z_e}\sum_{i=1}^{i=N_i}\sum_{j=1}^{j=N_j}\sum_{k=1}^{k=n} q_{i,j}^{k}\int_{t^{k-1}}^{t^k} \\
&\left\{1+\frac{4x_e}{\pi\Delta x}\sum_{m=1}^{\infty}\frac{1}{m}\exp\left[-\frac{m^2\pi^2\alpha\left(t-\tau\right)}{x_e^2}\right]\sin\frac{m\pi\Delta x}{2x_e}\cos\frac{m\pi x_{0_{i,j}}}{x_e}\cos\frac{m\pi x}{x_e}\right\} \\
&\cdot\int_{l_{i,j}=0}^{l_{i,j}=\Delta l}\left\{1+2\sum_{m=1}^{\infty}\exp\left[-\frac{m^2\pi^2\alpha\left(t-\tau\right)}{y_e^2}\right]\cos\frac{m\pi y\left(l_{i,j}\right)}{y_e}\cos\frac{m\pi y}{y_e}\right\} \\
&\cdot\left\{1+2\sum_{m=1}^{\infty}\exp\left[-\frac{m^2\pi^2\alpha\left(t-\tau\right)}{z_e^2}\right]\cos\frac{m\pi z\left(l_{i,j}\right)}{z_e}\cos\frac{m\pi z}{z_e}\right\}\mathrm{d}l_{i,j}\,\mathrm{d}\tau
\end{aligned}
\tag{3B-8}
$$

Rewriting Equation (3B-8) into a dimensionless form leads to:

$$
\begin{aligned}
p_D\left(x_D,y_D,z_D,t_D^n\right) &= \frac{2\pi}{\Delta y_D x_{eD} y_{eD}}\sum_{i=1}^{i=N_i}\sum_{j=1}^{j=N_j}\sum_{k=1}^{k=n} q_{D_{i,j}}^{k}\int_{t_D^{k-1}}^{t_D^k} \\
&\left\{1+\frac{4x_{eD}}{\pi\Delta x_D}\sum_{m=1}^{\infty}\frac{1}{m}\exp\left[-\frac{m^2\pi^2\left(t_D^n-\tau_D\right)}{x_{eD}^2}\right]\sin\frac{m\pi\Delta x_D}{2x_{eD}}\cos\frac{m\pi x_{0D_{i,j}}}{x_{eD}}\cos\frac{m\pi x_D}{x_{eD}}\right\} \\
&\cdot\int_{l_{D_{i,j}}=0}^{l_{D_{i,j}}=\Delta l_D}\left\{1+2\sum_{m=1}^{\infty}\exp\left[-\frac{m^2\pi^2\left(t_D^n-\tau_D\right)}{y_{eD}^2}\right]\cos\frac{m\pi y_D\left(l_{D_{i,j}}\right)}{y_{eD}}\cos\frac{m\pi y_D}{y_{eD}}\right\} \\
&\cdot\left\{1+2\sum_{m=1}^{\infty}\exp\left[-\frac{m^2\pi^2\left(t_D^n-\tau_D\right)}{z_{eD}^2}\right]\cos\frac{m\pi z_D\left(l_{D_{i,j}}\right)}{z_{eD}}\cos\frac{m\pi z_D}{z_{eD}}\right\}\mathrm{d}l_{D_{i,j}}\,\mathrm{d}\tau_D
\end{aligned}
\tag{3B-9}
$$

Based on Equation (3B-9), we can calculate the dimensionless pressure at an arbitrary position in the bounded reservoir. As such, at time t_D^n, the dimensionless pressure at the center position of fracture panel (*I*, *J*) can be expressed as:

$$
\begin{aligned}
&p_{fD_{I,J}}\left(x_{0D_{I,J}},y_{0D_{I,J}},z_{0D_{I,J}},t_D^n\right)=\frac{2\pi}{\Delta y_D x_{eD} y_{eD}}\sum_{i=1}^{i=N_i}\sum_{j=1}^{j=N_j}\sum_{k=1}^{k=n}q_{D_{i,j}}^k\int_{t_D^{k-1}}^{t_D^k}\\
&\left\{1+\frac{4x_{eD}}{\pi\Delta x_D}\sum_{m=1}^{\infty}\frac{1}{m}\exp\left[-\frac{m^2\pi^2\left(t_D^n-\tau_D\right)}{x_{eD}^2}\right]\sin\frac{m\pi\Delta x_D}{2x_{eD}}\cos\frac{m\pi x_{0D_{i,j}}}{x_{eD}}\cos\frac{m\pi x_{0D_{I,J}}}{x_{eD}}\right\}\\
&\cdot\int_{l_{D_{i,j}}=0}^{l_{D_{i,j}}=\Delta l_D}\left\{1+2\sum_{m=1}^{\infty}\exp\left[-\frac{m^2\pi^2\tau_D}{y_{eD}^2}\right]\cos\frac{m\pi y_D\left(l_{D_{i,j}}\right)}{y_{eD}}\cos\frac{m\pi y_{0D_{I,J}}}{y_{eD}}\right\}\\
&\cdot\left\{1+2\sum_{m=1}^{\infty}\exp\left[-\frac{m^2\pi^2\tau_D}{z_{eD}^2}\right]\cos\frac{m\pi z_D\left(l_{D_{i,j}}\right)}{z_{eD}}\cos\frac{m\pi z_{0D_{I,J}}}{z_{eD}}\right\}\mathrm{d}l_{D_{i,j}}\mathrm{d}\tau_D
\end{aligned}
\tag{3B-10}
$$

For convenience, we define that:

$$
\begin{aligned}
&G_{i,j}^k\left(I,J,t_D^k\right)=\frac{2\pi}{\Delta y_D x_{eD} y_{eD}}\int_{t_D^{k-1}}^{t_D^k}\\
&\left\{1+\frac{4x_{eD}}{\pi\Delta x_D}\sum_{m=1}^{\infty}\frac{1}{m}\exp\left[-\frac{m^2\pi^2\left(t_D^n-\tau_D\right)}{x_{eD}^2}\right]\sin\frac{m\pi\Delta x_D}{2x_{eD}}\cos\frac{m\pi x_{0D_{i,j}}}{x_{eD}}\cos\frac{m\pi x_{0D_{I,J}}}{x_{eD}}\right\}\\
&\cdot\int_{l_{D_{i,j}}=0}^{l_{D_{i,j}}=\Delta l_D}\left\{1+2\sum_{m=1}^{\infty}\exp\left[-\frac{m^2\pi^2\left(t_D^n-\tau_D\right)}{y_{eD}^2}\right]\cos\frac{m\pi y_D\left(l_{D_{i,j}}\right)}{y_{eD}}\cos\frac{m\pi y_{0D_{I,J}}}{y_{eD}}\right\}\\
&\cdot\left\{1+2\sum_{m=1}^{\infty}\exp\left[-\frac{m^2\pi^2\left(t_D^n-\tau_D\right)}{z_{eD}^2}\right]\cos\frac{m\pi z_D\left(l_{D_{i,j}}\right)}{z_{eD}}\cos\frac{m\pi z_{0D_{I,J}}}{z_{eD}}\right\}\mathrm{d}l_{D_{i,j}}\mathrm{d}\tau_D
\end{aligned}
\tag{3B-11}
$$

As such, Equation (3B-10) can be rewritten as:

$$
p_{fD_{I,J}}\left(x_{0D_{I,J}},y_{0D_{I,J}},z_{0D_{I,J}},t_D^n\right)=\sum_{i=1}^{i=N_i}\sum_{j=1}^{j=N_j}\sum_{k=1}^{k=n}q_{D_{i,j}}^k G_{i,j}^k\left(I,J,t_D^k\right) \tag{3B-12}
$$

It is noted that, at each timestep, all the parameters in term $G_{i,j}^k$ are known; hence the value of $G_{i,j}^k$ can be readily calculated by substituting the values of these parameters into Equation (3B-11). Applying Equation (3B-12) to all of the fracture panels and arranging these matrix flow equations into a matrix format gives:

$$
\boldsymbol{p}_f^n-\boldsymbol{G}\boldsymbol{q}^n=\boldsymbol{D}, \tag{3B-13}
$$

where the matrices $\boldsymbol{p}_f^n$ and $\boldsymbol{q}^n$ are defined in Equation (3A-16),

$$\boldsymbol{G}=\begin{bmatrix} G_{1,1}^k\left(1,1,t_D^n\right) & \cdots & G_{i,j}^k\left(1,1,t_D^n\right) \\ \vdots & \ddots & \vdots \\ G_{1,1}^k\left(N_i,N_j,t_D^n\right) & \cdots & G_{N_i,N_j}^k\left(N_i,N_j,t_D^n\right) \end{bmatrix}, \tag{3B-14}$$

and

$$\boldsymbol{D}=\begin{bmatrix} \sum_{i=1}^{i=N_i}\sum_{j=1}^{j=N_j}\sum_{k=1}^{k=n-1} q_{D_{i,j}}^k G_{i,j}^k\left(I,J,t_D^k\right) \\ \vdots \\ \sum_{i=1}^{i=N_i}\sum_{j=1}^{j=N_j}\sum_{k=1}^{k=n-1} q_{D_{i,j}}^k G_{i,j}^k\left(I,J,t_D^k\right) \end{bmatrix} \tag{3B-15}$$

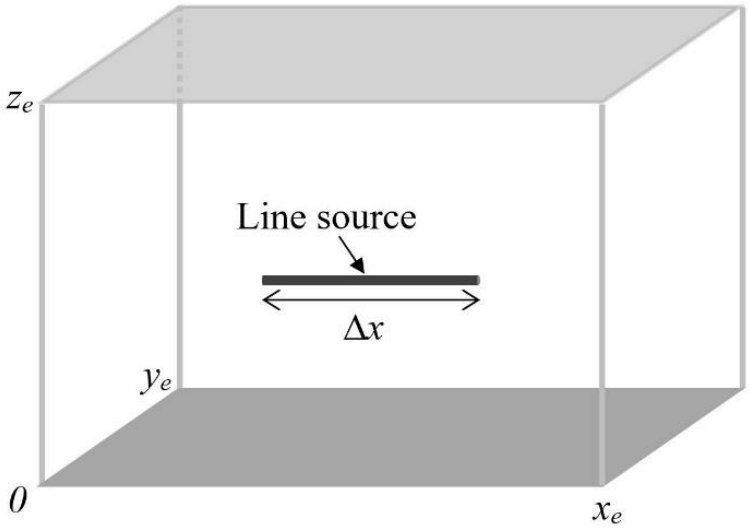

Figure 3B-1. 3D view of a line source in a bounded reservoir.

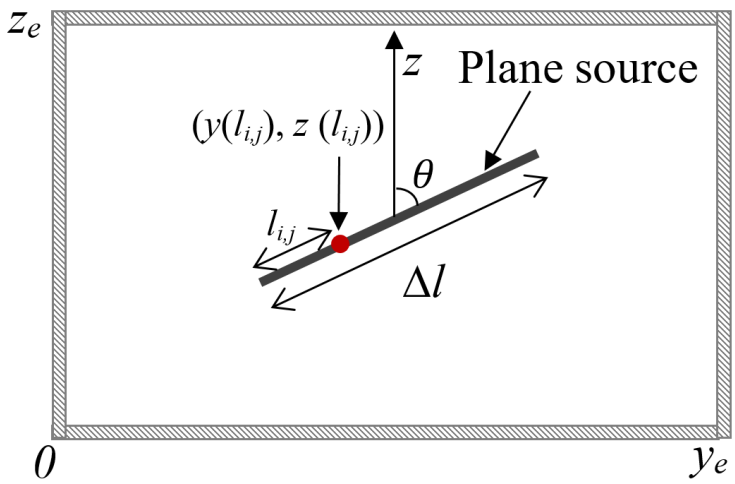

Figure 3B-2. Side view of an inclined plane source in a bounded reservoir.

References

Al-Anazi, H., Al-Kanaan, A., Pacheco, E., and Rahim, Z. 2013. Evaluation and Selection of Stimulation Methods in Horizontal Gas Wells for Production Optimization Using Numerical Modeling of Well Performances. Paper SPE 167090 presented at SPE Unconventional Resources Conference and Exhibition-Asia Pacific, Brisbane, Australia, 11-13 November.

Baig, A., and Urbancic, T.I. 2012. Structural Controls on Vertical Growth of Hydraulic Fractures as Revealed Through Seismic Moment Tensor Inversion Analysis. Paper SPE 159795 presented at SPE Annual Technical Conference and Exhibition, San Antonio, Texas, USA, 8-10 October.

Carslaw, H.S., and Jaeger, J.C. 1959. *Conduction of Heat in Solids*, second edition. Oxford, UK: Oxford University Press.

Chacon, A., Djebrouni, A., and Tiab, D. 2004. Determining the Average Reservoir Pressure from Vertical and Horizontal Well Test Analysis Using the Tiab's Direct Synthesis Technique. Paper SPE 88619 presented at SPE Asia Pacific Oil and Gas Conference and Exhibition, Perth, Australia, 18-20 October.

Chun, K.H., and Ghassemi, A. 2012. Fracture Propagation under Poroelastic Loading. Paper ARMA 2012-274 presented at 46th U.S. Rock Mechanics/Geomechanics Symposium, Chicago, Illinois, 24-27 June.

Cinco-Ley, H., and Samaniego-V., F. 1981. Transient Pressure Analysis for Fractured Wells. *J. Pet. Tech.* 33 (09): 1749-1766.

Cinco-Ley, H., Ramey, H.J., and Miller, F.G. 1975. Unsteady-State Pressure Distribution Created by a Well with an Inclined Fracture. Paper SPE 5591 presented at Fall Meeting of the Society of Petroleum Engineers of AIME, Dallas, Texas, 28 September-1 October.

Cipolla, C.L., and Wright, C.A. 2000. State-of-the-Art in Hydraulic Fracture Diagnostics. Paper SPE 64434 presented at SPE Asia Pacific Oil and Gas Conference and Exhibition, Brisbane, Australia, 16-18 October.

Conlin, J.M., Hale, J.L., Sabathier, J.C., Faure, F., and Mas, D. 1990. Multiple-Fracture Horizontal Wells: Performance and Numerical Simulation. Paper SPE 20960 presented at European Petroleum Conference, The Hague, Netherlands, 21-24 October.

Culham, W.E. 1974. Pressure Buildup Equations for Spherical Flow Regime Problems. *SPE J.* 14 (06): 545-555.

Daneshy, A.A. 1973. A Study of Inclined Hydraulic Fractures. *SPE J.* 13 (02): 61-68.

Daneshy, A.A. 1978. Hydraulic Fracture Propagation in Layered Formations. *SPE J.* 18 (01) 33-41.

Dinh, A.V., and Tiab, D. 2009. Transient-Pressure Analysis of a Well with an Inclined Hydraulic Fracture Using Tiab's Direct Synthesis Technique. Paper SPE 120545 presented at SPE Production and Operations Symposium, Oklahoma City, Oklahoma, 4-8 April.

Dinh, A.V., and Tiab, D. 2010. Transient-Pressure Analysis of a Well with an Inclined Hydraulic Fracture Using Type Curve Matching. *SPE Res. Eval. Eng.* 13 (06): 845-860.

Gringarten, A.C., and Ramey, H.J. 1973. The Use of Source and Green's Functions in Solving Unsteady-Flow Problems in Reservoirs. *SPE J.* 13 (05): 285-296.

Habte, A.D., Dinh, A.V., and Tiab, D. 2010. Pressure Analysis of a Well with an Inclined Asymmetric Hydraulic Fracture Using Type Curves. Paper SPE 140638 presented at Nigeria Annual International Conference and Exhibition, Tinapa - Calabar, Nigeria31 July - 7 August.

Hubbert, M.K., and Willis, D.G. 1957. Mechanics of Hydraulic Fracturing. *Trans. AIME* 210: 153-168.

Issaka, M.B., Zaoral, K., Ambastha, A.K., and Mattar, L., 2000. Determination of Horizontal Permeability Anisotropy from Horizontal Well Test. Paper presented at SPE Saudi Arabia Section Technical Symposium, Dhahran, Saudi Arabia, 21-23 October.

Jeffrey, R.G., Bunger, A. LeCampion, B., Zhang, X., Chen, Z., van As, A., Allision, D.P., Beer. W.D., Dudley, J.W., Siebrits, E., Thiercelin, M.J., and Mainguy, M. 2009. Measuring Hydraulic Fracture Growth in Naturally Fractured Rock. Paper SPE 124919 presented at SPE Annual Technical Conference and Exhibition, New Orleans, Louisiana, 4-7 October.

Jia, P., Cheng, L., Huang, S., Liu, H. 2016. Pressure-Transient Analysis of a Finite-Conductivity Inclined Fracture Connected to a Slanted Wellbore. *SPE J.* 21 (02): 522-537.

Johnson, R.L., Scott, M.P., Jeffrey, R.G., Chen, Z., Bennett, L., Vandenborn, C.B., and Tcherkashnev, S. 2010. Evaluating Hydraulic Fracture Effectiveness in a Coal Seam Gas Reservoir from Surface Tiltmeter and Microseismic Monitoring. Paper SPE 133063

presented at SPE Annual Technical Conference and Exhibition, Florence, Italy, 19-22 September.

Larsen, L., and Hegre, T.M. 1994. Pressure Transient Analysis of Multifractured Horizontal Wells. Paper SPE 28389 presented at SPE Annual Technical Conference and Exhibition, New Orleans, Louisiana, 25-28 September.

Medeiros, F., Kurtoglu, B., Ozkan, E., and Kazemi, H. 2010. Analysis of Production Data from Hydraulically Fractured Horizontal Wells in Shale Reservoirs. *SPE Res. Eval. Eng.* 13 (03): 559-568.

Medeiros, F., Ozkan, E., and Kazemi, H. 2008. Productivity and Drainage Area of Fractured Horizontal Wells in Tight Gas Reservoirs. *SPE Res. Eval. Eng.* 11 (05): 902-911.

Medlin, W.L., and Masse, L. 1984. Laboratory Experiments in Fracture Propagation. *SPE J.* 24 (03): 256-268.

Minner, W.A., Wright, C.A., Stanly, G.R., de Pater, C.J., Gorham, T.L., Eckerfield, L.D., and Hejl, K.A. 2002. Waterflood and Production-Induced Stress Changes Dramatically Affect Hydraulic Fracture Behavior in Lost Hills Infill Wells. Paper SPE 77536 presented at SPE Annual Technical Conference and Exhibition, San Antonio, Texas, 29 September-2 October.

Mukuhira, Y., Ito, T., Asanuma, H., and Haring, M. 2016. Stress State Analysis of a Fault Plane with Large Induced Seismicity. Paper ARMA-2016-360 presented at 50th U.S. Rock Mechanics/Geomechanics Symposium, Houston, Texas, 26-29 June.

Pandey, V.J., and Agreda, A.J. 2014. New Fracture-Stimulation Designs and Completion Techniques Result in Better Performance of Shallow Chittim Ranch Wells. *SPE Prod. Oper*. 29 (04): 288-309.

Peaceman, D.W. 1990. Interpretation of Wellblock Pressures in Numerical Reservoir Simulation with Nonsquare Grid Blocks and Anisotropic Permeability. *SPE J.* 23 (03): 531-543.

Rbeawi, S.AI, and Tiab, D. 2012a. Transient Pressure Analysis of a Horizontal Well with Multiple Inclined Hydraulic Fractures Using Type-Curve Matching. Paper SPE 149902 presented at SPE International Symposium and Exhibition on Formation Damage Control, Lafayette, Louisiana, USA, 15-17 February.

Rbeawi, S.AI, and Tiab, D. 2012b. Effect of Penetrating Ratio on Pressure Behavior of Horizontal Wells with Multiple-Inclined Hydraulic Fractures. Paper SPE 153788 presented at SPE Western Regional Meeting, Bakersfield, California, USA, 21-23 March.

Rbeawi, S.AI, and Tiab, D. 2013. Partially Penetrating Hydraulic Fractures: Pressure Responses and Flow Dynamics. Paper SPE 164500 presented at SPE Production and Operations Symposium, Oklahoma City, Oklahoma, USA, 23-26 March.

Restrepo, D.P., and Tiab, D. 2009. Multiple Fractures Transient Response. Paper SPE 121594 presented at Latin American and Caribbean Petroleum Engineering Conference, Cartagena de Indias, Colombia, 31 May-3 June.

Rodriguez, F., Horne, R.N., and Cinco-Ley, H. 1984. Partially Penetrating Fractures: Pressure Transient Analysis of an Infinite Conductivity Fracture. Paper SPE 12743 presented at SPE California Regional Meeting, Long Beach, California, 11-13 April.

Valko, P., and Economides, M.J. 1997. Transient Behavior of Finite Conductivity Horizontal Fractures. *SPE J*. 2 (02): 213-222.

van Everdingen, A.F., and Hurst, W. 1949. The Application of the Laplace Transformation to Flow Problems in Reservoirs. *Trans. AIME* 1 (12): 305-324.

Wright, C.A. 1994. Reorientation of Propped Refracture Treatments in the Lost Hills Field. Paper SPE 27896 presented at SPE Western Regional Meeting, Long Beach, California, 23-25 March.

Wright, C.A., Davis, E.J., Golich G.M., Ward, J.F., Demetrius, S.L., Minner, W.A., and Weijers, L. 1998. Downhole Tiltmeter Fracture Mapping: Finally Measuring Hydraulic Fracture Dimensions. Paper SPE 46194 presented at SPE Western Regional Meeting, Bakersfield, California, 10-13 May.

Wright, C.A., Davis, E.J., Weijers, L., Minner, W.A., Hennigan, C.M., and Golich, G.M. 1997. Horizontal Hydraulic Fractures: Oddball Occurrences or Practical Engineering Concern? Paper 38324 presented at SPE Western Regional Meeting, Long Beach, California, 25-27 June.

Yu, W., Wu, K., and Sepehrnoori, K. 2016. A Semianalytical Model for Production Simulation from Nonplanar Hydraulic-Fracture Geometry in Tight Oil Reservoirs. *SPE J*. 21 (3) 1028-1040.

Zhou, W., Banerjee, R., Poe, B.D., and Spath, J. 2014. Semianalytical Production Simulation of Complex Hydraulic-Fracture-Networks. *SPE J.* 19 (01): 6-18.

CHAPTER 4 A SEMI-ANALYTICAL MODEL FOR CHARACTERIZING THE FLUID TRANSIENT FLOW OF REORIENTED REFRACTURES

A version of this chapter has been published in *Journal of Petroleum Science and Engineering*.

Summary

In order to improve the field productivity, the industries can create new fractured wells to reduce the interval between the initial fractures (initial fracture indicates a fracture that is induced during the initial fracturing treatment). Production from the initial fractured wells can induce stress reorientation in the vicinity of the fractures. As such, a refracturing treatment in the stress reorientation region can lead to a reoriented refracture which has a certain azimuth with respect to the initial fractures. This azimuth can even be 90 degrees if the stress reorientation is sufficiently large. In addition to the conventional parameters (including refracture's length, refracture's conductivity, and the *in-situ* conditions), there are two more factors, the reorientation azimuth and the interference from the initial fracture, can exert significant influence on the transient flow behavior of the reoriented refractures. In such a case, the conventional analytical/semi-analytical models which neglect these two factors are no longer applicable to characterize the transient flow behavior from such a refracture.

In this work, we develop a novel semi-analytical model to characterize the transient flow behavior of a reoriented refracture considering the interference from the initial fractures. In this model, the fractures are explicitly represented with discretized segments. We apply finite difference approximation to the initial fractures and refractures, respectively, to simulate the transient flow in the fracture system. In addition, the fluid flow in the matrix system can be characterized by Green function and Newman product method. Based on the continuity of flux and pressure, we couple the fracture flow equations with the matrix flow equations to construct a semi-analytical model. With the aid of the proposed model, we conduct a thorough investigation of the transient flow behavior of reoriented refractures. It is observed that, at the early production period, two fracture pseudo-steady-state flows can appear due to the interference from the initial

fractures. The formation linear flow and bilinear flow can also be observed during the production period of a refractured well. In an anisotropic-permeability reservoir, the refracture's azimuth and position can exert a significant impact on the productivity of the fractures. There is a region in the vicinity of the initial fractures, within which an orthogonal refracture can lead to the highest field productivity.

4.1. Introduction

The field productivity in the tight and shale formations commonly undergo a rapid decline following the initial fracturing treatment [1, 2, 3]. As such, the refracturing treatment has been widely applied in such formations to improve the field productivity. The refracturing treatment can be summarized into two categories: first, refracturing a poor-growth initial fracture (a poor-growth fracture represent a fracture that has small fracture-length); and second, creating new fractures to reduce the interval between the initial fractures. This work focuses on the second category of the refracturing treatment. Field studies have shown that the stress in the formations frequently exhibits a non-uniform depletion due to the production from the initial fractures, leading to a stress reorientation region in the vicinity of these fractures [4, 5, 6, 7, 8]. Thus, a refracturing treatment in this stress reorientation region can create a reoriented refracture which has a certain azimuth with respect to the initial fractures [9, 10, 11, 12, 13]. This azimuth can even be 90 degrees if the stress reorientation is sufficiently large.

Warpinski and Branagan introduced the concept of altered-stress fracturing and claimed that a fracturing treatment taking advantage of the stress reorientation can create a favorable fracture orientation [14]. On the basis of the numerical simulation approach, Elbel and Mack investigated the stress changes caused by the production from the initial fractures. They also stated that the reorientation of the refracture is almost sure to occur if the horizontal stresses are essentially

equal [15]. Palmer studied the stress changes induced by the propped hydraulic fractures with an emphasis of its influence on the propagation of the refractures in coalbed-methane reservoirs [16]. These studies provided theoretical evidence of the reoriented refractures, and the existence of the reoriented refractures was subsequently verified in the Lost Hills field and the Codell formation [10, 17]. **Figure 4-1** illustrates the fracture orientations in the eastern part of the Lost Hills field, which is adapted from Wright *et al*. [17]. The shaded arcs represent the range of the fracture azimuths that were monitored over all of the fractured wells, and the fracture in the elliptical box represents a reoriented refracture. As this figure shows, the orientations of the initial fractures are all close to an average azimuth of N55^{o}E, whereas the refracture exhibits a fracture azimuth around N85^{o}E.

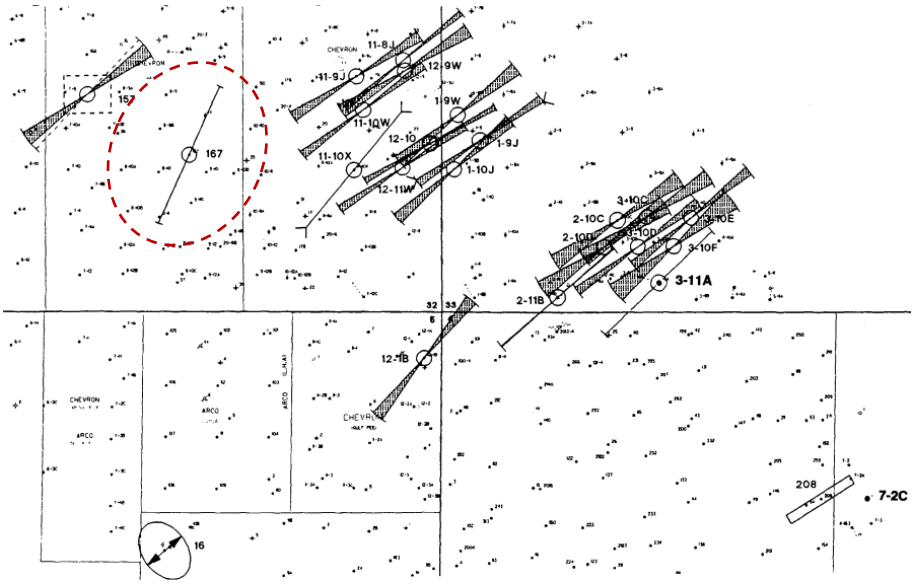

Figure 4-1. Fracture orientations in the eastern part of the Lost Hills field (adapted from [17]).

Since the reorientation of the refractures frequently occurs after the refracturing treatment, it is highly necessary to characterize transient flow behavior of the reoriented refractures. Characterizing the fluid transient flow can help the industries conduct history matching or predict production from such fractures. However, using the numerical method to characterize the fluid

transient flow of the reoriented refractures can be time-consuming. This is especially true when one wants to conduct history matching work on a refracture, which can require numerous runs of a reservoir model. Due to the facts that the semi-analytical method is efficient in computation and is convenient in constructing a fractured reservoir model, in recent years many semi-analytical models have been proposed to characterize the transient flow behavior from various fractures, including vertical fractures, inclined fractures, horizontal fractures, multi-stage fractures, and fracture-networks [18, 19, 20, 21,22]. However, there is still no available semi-analytical model to simulate the transient flow behavior of a reoriented refracture.

In this work, we introduce a semi-analytical model to characterize the transient flow behavior of a reoriented refracture. With the aid of this proposed model, we distinguish the different flow regimes of a reoriented refracture. The flux distribution along the refracture is examined at early production period. As such, one can have a direct insight into the interference of the initial fractures on the refractures. Hereafter, we carry out a thorough investigation about the influences of refracture's azimuth, refracture's position, and permeability anisotropy, on the field productivity. In addition, we depict the optimal reoriented azimuth map of a refracture with the consideration of the interference from the initial fractures.

4.2. Methodology

This work considers a reoriented refracture in the vicinity of the initial fractures. **Figure 4-2** shows an example of a fracture system containing a reoriented refracture and four initial fractures. In this figure, the initial fractures exhibit a relatively uniform azimuth while the refracture undergoes a significant reorientation with respect to the initial fractures. We discretize the initial fractures into n_1 segments and the refracture into n_2 segments. In order to characterize the transient flow behavior of the refracture, we make the following fundamental assumptions:

- The reservoir is infinite in *X*-*Y* plane and sealed by impermeable upper and lower boundaries;
- The initial fractures and the refractures fully penetrate the reservoir along the vertical direction;
- The well is producing single-phase oil;
- The initial reservoir pressure is a constant throughout the entire reservoir;
- The reservoir thickness, porosity, oil viscosity, and oil compressibility are both constant and homogeneous in the reservoir;
- The oil enters the wellbore only through the fractures; and
- The influence of the fracturing treatment on the reservoir pressure is neglected.

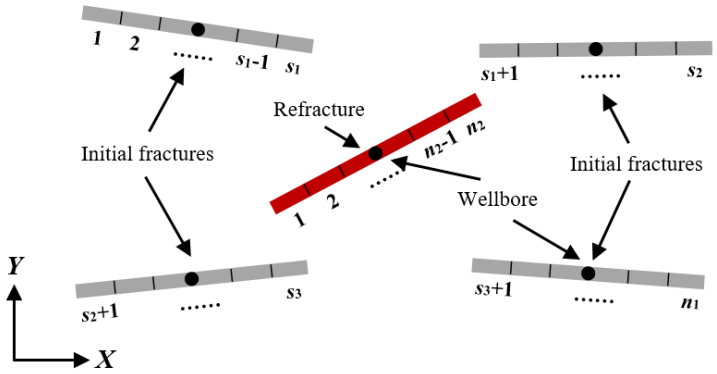

Figure 4-2. Discretization of the initial fractures and the reoriented refracture.

Since the permeability anisotropy along the horizontal direction is also considered in this work, we first convert the anisotropic-permeability system into an equivalent isotropic-permeability system by using the approach introduced by Spivey and Lee [23]. **Table 4-1** summaries the parameters used in the anisotropic-permeability system and their counterparts in the equivalent isotropic-permeability system. In this table, the parameters used in the anisotropic-permeability system are written in uppercase, whereas their counterparts in the equivalent isotropic-permeability system are written in lowercase (excluding C_F and C_f which indicate the fracture

conductivity in the anisotropic-permeability system and in the equivalent isotropic-permeability system, respectively).

Table 4-1. Conversion from an anisotropic-permeability system to an equivalent isotropic-permeability system.

Anisotropic system	Equivalent isotropic system
K_{mx}, K_{my} (K_{my}=R_K K_{mx})	$k_m = \sqrt{K_{mx}K_{my}} = R_K^{0.5} K_{mx}$
X	$x = \sqrt{\frac{k_m}{K_{mx}}} X = R_K^{0.25} X$
Y	$y = \sqrt{\frac{k_m}{K_{my}}} Y = R_K^{-0.25} Y$
Z	$z = Z$
L_f	$l_f = L_f \sqrt{R_K^{0.5} \cos^2\theta + R_K^{-0.5} \sin^2\theta}$
W_f	$\theta_1 = \arctan\left(R_K^{-0.5} \tan\theta\right)$ $\theta_2 = \arctan\left(R_K^{0.5} \tan\theta\right)$ $w_f = W_f \sqrt{R_K^{0.5} \sin^2\theta + R_K^{-0.5} \cos^2\theta} \cos\left(\theta_2 - \theta_1\right)$
C_F	$C_f = C_F \sqrt{R_K^{0.5} \cos^2\theta + R_K^{-0.5} \sin^2\theta}$

For the sake of convenience, we define the following dimensionless parameters:

$$t_D = \frac{\beta k_m t}{\phi_m \mu c_{tm} l_r^2} \tag{4-1}$$

$$x_D = \frac{x}{l_r},\ X_D = \frac{X}{l_r},\ y_D = \frac{y}{l_r},\ Y_D = \frac{Y}{l_r} \tag{4-2}$$

$$l_{fD} = \frac{l_f}{l_r}, L_{fD} = \frac{L_f}{l_r},\ l_D = \frac{l}{l_r}, w_{fD} = \frac{w_f}{l_r}, W_{fD} = \frac{W_f}{l_r} \tag{4-3}$$

$$C_s = \frac{\phi_f c_{tf}}{\phi_m c_{tm}},\ C_{wD} = \frac{C_w}{2\pi h \phi_m c_{tm} r_w^2},\ C_{fD} = \frac{C_f}{k_m l_r},\ C_{FD} = \frac{C_F}{k_m l_r} \tag{4-4}$$

$$\gamma = \frac{0.0434 B r_w^2}{l_r^2} \tag{4-5}$$

In addition, at constant BHP condition, we have:

$$p_{wD} = \frac{p_i - p_w}{p_i - p_r}, p_{fD} = \frac{p_i - p_f}{p_i - p_r} \tag{4-6}$$

$$q_{wD} = \frac{q_w B\mu}{2\pi\beta k_m h\left(p_i - p_r\right)},\ q_{fwD} = \frac{q_{fw} B\mu}{2\pi\beta k_m h\left(p_i - p_r\right)},\ q_{fD} = \frac{q_f B\mu}{2\pi\beta k_m h\left(p_i - p_r\right)} \tag{4-7}$$

whereas, at constant production rate condition, we have:

$$p_{wD} = \frac{2\pi\beta k_m h\left(p_i - p_w\right)}{q_r B\mu}, p_{fD} = \frac{2\pi\beta k_m h\left(p_i - p_f\right)}{q_r B\mu} \tag{4-8}$$

$$q_{wD} = \frac{q_w}{q_r}\ q_{fwD} = \frac{q_{fw}}{q_r}, q_{fD} = \frac{q_f}{q_r} \tag{4-9}$$

and

$$l_r = \frac{\sum_{m=1}^{m=N_1} L_{f_1^m} + \sum_{m=1}^{m=N_2} L_{f_2^m}}{2\left(N_1 + N_2\right)},\quad p_r = \frac{\sum_{m=1}^{m=N_1} p_{w_1^m} + \sum_{m=1}^{m=N_2} p_{w_2^m}}{N_1 + N_2},\ q_r = \frac{\sum_{m=1}^{m=N_1} q_{w_1^m} + \sum_{m=1}^{m=N_2} q_{w_2^m}}{N_1 + N_2} \tag{4-10}$$

The meaning of the terms showing up in the above equations can be referred to the nomenclature section.

4.2.1 Analytical Formulation of the Matrix Flow

The fractures are discretized into small segments and for each fracture segment there are two unknowns (i.e., fracture pressure, p_f, and flux rate from the matrix to the fracture segment q_f). In the matrix system, the relationship between p_f and q_f can be analytically characterized. In an infinite reservoir, the pressure change at time t at position (x, y) induced by a fully penetrating continuous line source (see **Figure 4-3a**) can be calculated with the Green function provided in Gringarten and Ramey [24]:

$$\Delta p\left(x,y,t\right)=\int_{\tau_1}^{\tau_2}\frac{qB}{\phi_m c_{tm} h}\left\{4\pi\eta_m\left(t-\tau\right)\exp\left[\frac{\left[x-x_0\right]^2+\left[y-y_0\right]^2}{4\eta_m\left(t-\tau\right)}\right]\right\}^{-1}\mathrm{d}\tau \tag{4-11}$$

where Δp indicates pressure change, the integration from τ_1 to τ_2 represents that the line source is continued from $t = \tau_1$ to $t = \tau_2$, and q is flux per unit length (m^2/d) from the matrix to the fracture. The fractures are discretized into small segments, as shown in Figure 4-3. For each fracture segment (see Figure 4-4b), q has the following relationship with q_f:

$$q_f=\int_l^{l+\Delta l} q\left(l\right)\mathrm{d}l \tag{4-12}$$

where Δl is the length of a fracture segment. With the aid of Equation (4-11), we can calculate the pressure change induced by a fracture segment by integrating Equation (4-11) along the propagation direction of this fracture segment:

$$\Delta p\left(x,y,t\right)=\int_{\tau_1}^{\tau_2}\int_l^{l+\Delta l_f}\frac{q\left(l\right)B}{\phi_m c_{tm} h}\left\{4\pi\eta_m\left(t-\tau\right)\exp\left[\frac{\left[x-x_0\left(l\right)\right]^2+\left[y-y_0\left(l\right)\right]^2}{4\eta_m\left(t-\tau\right)}\right]\right\}^{-1}\mathrm{d}l\mathrm{d}\tau \tag{4-13}$$

If the fracture segment is sufficiently small, the flux distribution along a single fracture segment can be approximately represented with an average value. Thus, Equation (4-13) can be rewritten as:

$$\Delta p(x,y,t)=\int_{\tau_1}^{\tau_2}\int_{l}^{l+\Delta l_f}\frac{q_f B}{\phi_m c_{tm}\Delta l_f h}\left\{4\pi\eta_m(t-\tau)\exp\left[\frac{\left[x-x_0(l)\right]^2+\left[y-y_0(l)\right]^2}{4\eta_m(t-\tau)}\right]\right\}^{-1}\mathrm{d}l\mathrm{d}\tau \quad (4\text{-}14)$$

Inserting the dimensionless parameters into Equation (4-14) gives:

$$\begin{aligned}&p_D(x_D,y_D,t_D)=q_{fD}\int_{\tau_{D1}}^{\tau_{D2}}\int_{l_D}^{l_D+\Delta l_{fD}}\\&\frac{1}{2\Delta l_{fD}}\left\{(t_D-\tau_D)\exp\left[\frac{\left[x_D-x_{0D}(l_D)\right]^2+\left[y_D-y_{0D}(l_D)\right]^2}{4(t_D-\tau_D)}\right]\right\}^{-1}\mathrm{d}l_D\mathrm{d}\tau_D\end{aligned} \quad (4\text{-}15)$$

For convenience, we use G_{fD} (x_D, y_D, t_D) to represent the integral term of Equation (4-15). As such, Equation (4-15) can be rewritten as:

$$p_D(x_D,y_D,t_D)=q_{fD}G_{fD}(x_D,y_D,t_D) \quad (4\text{-}16)$$

where p_D is dimensionless pressure, q_{fD} is dimensionless flux rate. The pressure change at the central position of a fracture segment can be calculated by collecting the changes induced by all of the fracture segments throughout the entire production period. As such, before the refracturing treatment we have:

$$p^n_{f_1D,i}\left(x_{f_1D,i},y_{f_1D,i},t^n_D\right)=\sum_{I=1}^{I=n_1}\sum_{k=1}^{k=n}q^k_{f_1D,I}G^k_{f_1D,I}\left(x_{f_1D,i},y_{f_1D,i},t^n_D\right) \quad (4\text{-}17)$$

where i = 1, 2…n_1 (x_{fD}, y_{fD}) indicates the central position of a fracture segment, and the superscripts k and n indicate the k^{th} and n^{th} timestep.

After the refracturing treatment we have:

$$\begin{aligned}p^n_{f_1D,i}\left(x_{f_1D,i},y_{f_1D,i},t^n_D\right)=&\sum_{I=1}^{I=n_1}\sum_{k=1}^{k=n}q^k_{f_1D,I}G^k_{f_1D,I}\left(x_{f_1D,i},y_{f_1D,i},t^n_D\right)\\&+\sum_{J=1}^{J=n_2}\sum_{k=K}^{k=n}q^k_{f_2D,J}G^k_{f_2D,J}\left(x_{f_1D,i},y_{f_1D,i},t^n_D\right)\end{aligned} \quad (4\text{-}18)$$

$$p^n_{f_2D,j}\left(x_{f_2D,j}, y_{f_2D,j}, t^n_D\right) = \sum_{I=1}^{I=n_1}\sum_{k=1}^{k=n} q^k_{f_1D,I} G^k_{f_1D,I}\left(x_{f_2D,j}, y_{f_2D,j}, t^n_D\right) + \sum_{J=1}^{J=n_2}\sum_{k=K}^{k=n} q^k_{f_2D,J} G^k_{f_2D,J}\left(x_{f_2D,j}, y_{f_2D,j}, t^n_D\right) \tag{4-19}$$

where $j = 1, 2 \ldots n_2$, and K indicates that the refractures are created at the end of the K^{th} timestep. Applying Equations (4-17) through (4-19) to all of the fracture segments and arranging these equations into a matrix format yields:

before the refracturing treatment,

$$\boldsymbol{p}^n_{f_1D} - \boldsymbol{G}^k_{f_1D,f_1} \cdot \boldsymbol{q}^k_{f_1D} = \boldsymbol{RHS}_1 \tag{4-20}$$

and after the refracturing treatment,

$$\begin{cases} \boldsymbol{p}^n_{f_1D} - \boldsymbol{G}^k_{f_1D,f_1} \cdot \boldsymbol{q}^k_{f_1D} - \boldsymbol{G}^k_{f_2D,f_1} \cdot \boldsymbol{q}^k_{f_2D} = \boldsymbol{RHS}_2 \\ \boldsymbol{p}^n_{f_2D} - \boldsymbol{G}^k_{f_1D,f_2} \cdot \boldsymbol{q}^k_{f_1D} - \boldsymbol{G}^k_{f_2D,f_2} \cdot \boldsymbol{q}^k_{f_2D} = \boldsymbol{RHS}_3 \end{cases} \tag{4-21}$$

where the matrices $\boldsymbol{p}$, $\boldsymbol{q}$, $\boldsymbol{G}$, and $\boldsymbol{RHS}$ are defined in **Appendix 4A**.

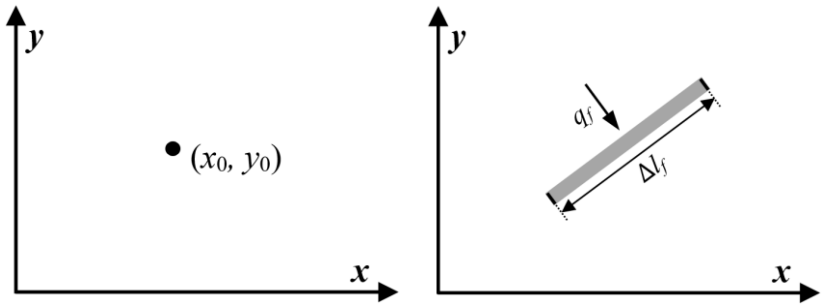

Figure 4-3. Schematics of a line source and a plane source: (a) top view of a line source in *x*-*y* plane (this line source fully penetrates the reservoir along the *z*-axis); and (b) top view of a fracture segment in *x*-*y* plane (this plane source fully penetrates the reservoir along the *z*-axis).

4.2.2 Numerical Formulation of the Fracture Flow

Flow Equation. The fracture width is far smaller than the fracture length, such that the transient flow in the fracture can be simplified as 1D flow. The 1D fracture flow equation that considers the flux from the matrix to the fracture is given as:

$$\frac{\partial}{\partial l}\left(w_f \eta_f \frac{\partial p_f}{\partial l} \right) + \frac{q(l,t)B}{h\phi_f c_{tf}} = w_f \frac{\partial p_f}{\partial t} \tag{4-22}$$

The fractures are discretized into small segments, and the segments of each fracture have uniform length, width, and properties; hence, Equation (4-22) can be numerically solved by applying finite difference approximation:

$$p^n_{f,i-1} - 2p^n_{f,i} + p^n_{f,i+1} + \frac{B\Delta l_f}{w_f \eta_f h \phi_f c_{tf}} q^n_{f,i} = \frac{\Delta l_f^2}{\eta_f \Delta t^n}\left(p^n_{f,i} - p^{n-1}_{f,i} \right) \tag{4-23}$$

Substituting the dimensionless definitions into Equation (4-23) gives:

$$p^n_{fD,i-1} - 2p^n_{fD,i} + p^n_{fD,i+1} - \frac{2\pi\Delta l_{fD}}{C_{fD}} q^n_{fD,i} = \frac{\Delta l^2_{fD} w_{fD} C_s}{C_{fD}\Delta t^n_D}\left(p^n_{fD,i} - p^{n-1}_{fD,i} \right) \tag{4-24}$$

Equation (4-24) can also be rearranged as:

$$p^n_{fD,i-1} - \left(2 + \frac{\Delta l^2_{fD} w_{fD} C_s}{C_{fD}\Delta t^n_D} \right) p^n_{fD,i} + p^n_{fD,i+1} - \frac{2\pi\Delta l_{fD}}{C_{fD}} q^n_{fD,i} = -\frac{\Delta l^2_{fD} w_{fD} C_s}{C_{fD}\Delta t^n_D} p^{n-1}_{fD,i} \tag{4-25}$$

In particular, the flow equation of the fracture segment that is connected to the wellbore (which is shown in **Figure 4-4a**) can be written as:

$$-\left(1 + \frac{\Delta l^2_{fD} w_{fD} C_s}{C_{fD}\Delta t^n_D} \right) p^n_{fD,i} + p^n_{fD,i+1} - \frac{2\pi\Delta l_{fD}}{C_{fD}}\left(q^n_{fD,i} - q^n_{fwD,i} \right) = -\frac{\Delta l^2_{fD} w_{fD} C_s}{C_{fD}\Delta t^n_D} p^{n-1}_{fD,i} \tag{4-26}$$

and the flow equation of the fracture segment at the fracture tip (which is shown in Figure 4-4b) can be written as:

$$p^n_{fD,i-1} - \left(1 + \frac{\Delta l^2_{fD} w_{fD} C_s}{C_{fD}\Delta t^n_D} \right) p^n_{fD,i} - \frac{2\pi\Delta l_{fD}}{C_{fD}} q^n_{fD,i} = -\frac{\Delta l^2_{fD} w_{fD} C_s}{C_{fD}\Delta t^n_D} p^{n-1}_{fD,i} \tag{4-27}$$

In addition, a reoriented refracture can result in an intersection between the initial fracture and the refracture (see **Figure 4-5a**). In such a case, the intersected fracture segment (*i* or *j*) is refined into

two smaller segments (i.e., *i*- and *i*+; *j*- and *j*+), as shown in Figure 4-5b. The flow equation that characterizes the transient flow behavior of the refined segment *i*- is given as:

$$\left(\frac{C_{fD}}{\Delta l_{fD}}\right)_{i-1,i-} p^n_{f_1D,i-1} + \left(\frac{C_{fD}}{\Delta l_{fD}}\right)_{i-,i+} p^n_{f_1D,i+} + \left(\frac{C_{fD}}{\Delta l_{fD}}\right)_{i-,j-} p^n_{f_2D,j-} + \left(\frac{C_{fD}}{\Delta l_{fD}}\right)_{i-,j+} p^n_{f_2D,j+}$$
$$-\left[\left(\frac{C_{fD}}{\Delta l_{fD}}\right)_{i-1,i-} + \left(\frac{C_{fD}}{\Delta l_{fD}}\right)_{i-,i+} + \left(\frac{C_{fD}}{\Delta l_{fD}}\right)_{i-,j-} + \left(\frac{C_{fD}}{\Delta l_{fD}}\right)_{i-,j+} + \frac{\Delta l_{f_1D,i-} w_{f_1D,i-} C_s}{\Delta t^n_D}\right] p^n_{f_1D,i-} \quad (4\text{-}28)$$
$$-2\pi q^n_{f_1D,i-} = -\frac{\Delta l_{f_1D,i-} w_{f_1D,i-} C_s}{\Delta t^n_D} p^{n-1}_{f_1D,i-}$$

where

$$\left(\frac{C_{fD}}{\Delta l_{fD}}\right)_{a,b} = 2\left[\left(\frac{\Delta l_{fD}}{C_{fD}}\right)_a + \left(\frac{\Delta l_{fD}}{C_{fD}}\right)_b\right]^{-1} \quad (4\text{-}29)$$

where the subscripts $a = i\text{-}1$ or *i*-, and $b = i+$, *j*- or *j*+. An equation that is similar to Equation (4-28) can be used to characterize the transient flow in the other three refined segments *i*+, *j*-, and *j*+. Applying the fracture flow Equations (4-25) through (4-28) to the fracture segments and arranging them into a matrix format gives:

before the refracturing treatment,

$$\boldsymbol{A}^n_{f_1} \cdot \boldsymbol{p}^n_{f_1D} + \boldsymbol{B}_{f_1} \odot \boldsymbol{q}^n_{f_1D} + \boldsymbol{C}_{f_1} \cdot \boldsymbol{q}^n_{fw_1D} = \boldsymbol{D}^n_{f_1} \odot \boldsymbol{p}^{n-1}_{f_1D} \quad (4\text{-}30)$$

and after the refracturing treatment,

$$\begin{cases} \boldsymbol{A}^n_{f_1} \cdot \boldsymbol{p}^n_{f_1D} + \boldsymbol{B}_{f_1} \odot \boldsymbol{q}^n_{f_1D} + \boldsymbol{C}_{f_1} \cdot \boldsymbol{q}^n_{fw_1D} = \boldsymbol{D}^n_{f_1} \odot \boldsymbol{p}^{n-1}_{f_1D} \\ \boldsymbol{A}^n_{f_2} \cdot \boldsymbol{p}^n_{f_2D} + \boldsymbol{B}_{f_2} \odot \boldsymbol{q}^n_{f_2D} + \boldsymbol{C}_{f_2} \cdot \boldsymbol{q}^n_{fw_2D} = \boldsymbol{D}^n_{f_2} \odot \boldsymbol{p}^{n-1}_{f_2D} \end{cases} \quad (4\text{-}31)$$

where $\odot$ is Hadamard product operator, and the definitions of the matrices of $\boldsymbol{A}_f$, $\boldsymbol{B}_f$, $\boldsymbol{C}_f$, $\boldsymbol{D}_f$, and $\boldsymbol{q}_{fwD}$ can be referred to **Appendix 4B**.

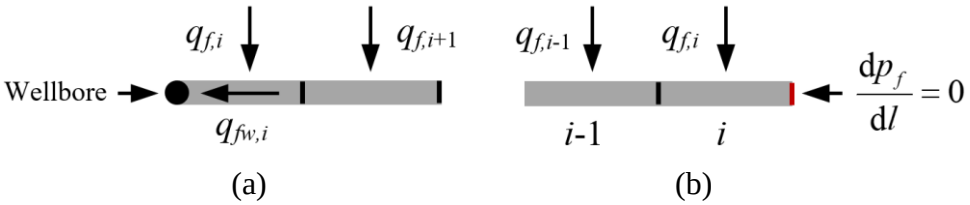

(a) (b)

Figure 4-4. Fracture segments that are located at special positions: (a) fracture segment that connects to the wellbore; and (b) fracture segment at the fracture tip.

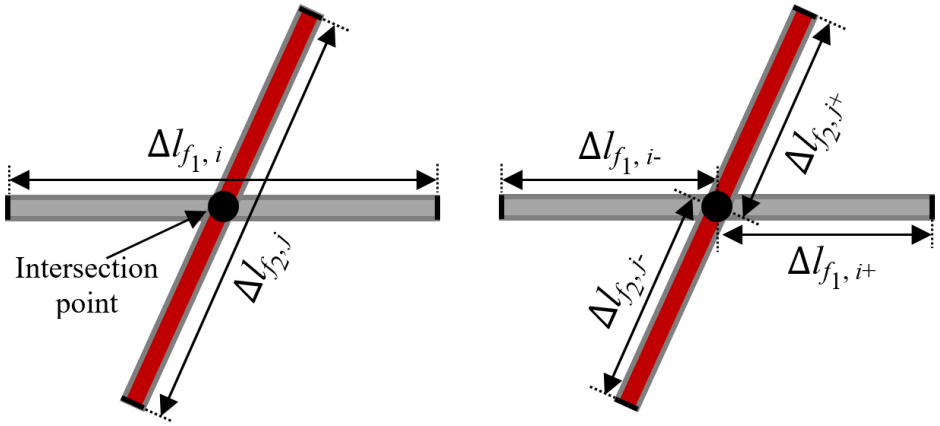

(a) (b)

Figure 4-5. Fracture segments at the intersection position: (a) fracture segments of the initial fracture and the refracture before being refined; and (b) fracture segments of the initial fracture and the refracture after being refined.

Production Constraints. The fractured well can produce oil under constant BHP condition or constant production rate condition. The constant BHP condition at the wellbore can be expressed as:

$$p_f\big|_{l=WB} = p_w \tag{4-32}$$

where *WB* represents the position of the wellbore; thus, the relationship between the production rate and the BHP can be written in the following dimensionless format:

$$\begin{cases} p_{fD,i-1}^{n} + \dfrac{\pi \Delta l_{fD}}{C_{fD}} q_{fwD,i-1}^{n} = p_{wD} \\ p_{fD,i}^{n} + \dfrac{\pi \Delta l_{fD}}{C_{fD}} q_{fwD,i}^{n} = p_{wD} \\ q_{fwD,i-1}^{n} + q_{fwD,i}^{n} - q_{wD}^{n} = 0 \end{cases} \tag{4-33}$$

where i and i-1 indicate the two fracture segments that are connected to the wellbore. The constant production rate condition can be characterized with:

$$\frac{\partial p_f}{\partial l}\Big|_{l=WB^+} + \frac{\partial p_f}{\partial l}\Big|_{l=WB^-} = \frac{q_w \mu w_f h}{k_f} \tag{4-34}$$

The wellbore storage effect can be taken into account based on the method provided by van Everdingen and Hurst [25] under constant production rate condition. As such, we can have the following equation at constant production rate condition:

$$\begin{cases} p_{fD,i-1}^{n} + \dfrac{\pi \Delta l_{fD}}{C_{fD}} q_{fwD,i-1}^{n} - p_{wD}^{n} = 0 \\ p_{fD,i}^{n} + \dfrac{\pi \Delta l_{fD}}{C_{fD}} q_{fwD,i}^{n} - p_{wD}^{n} = 0 \\ q_{fwD,i-1}^{n} + q_{fwD,i}^{n} + \dfrac{\gamma C_{wD}}{\Delta t_D^n} p_{wD}^{n} = q_{wD} + \dfrac{\gamma C_{wD}}{\Delta t_D^n} p_{wD}^{n-1} \end{cases} \tag{4-35}$$

Equation (4-33) can also be arranged into a matrix format as follows:

before the refracturing treatment,

$$\begin{cases} \boldsymbol{M}_{f_1} \cdot \boldsymbol{p}_{f_1 D}^{n} + \boldsymbol{F}_{f_1} \cdot \boldsymbol{q}_{fw_1 D}^{n} = \boldsymbol{BHP}_{f_1} \\ \boldsymbol{H}_{f_1} \cdot \boldsymbol{q}_{fw_1 D}^{n} - \boldsymbol{q}_{w_1 D}^{n} = \boldsymbol{0} \end{cases} \tag{4-36}$$

and after the refracturing treatment,

$$\begin{cases} \boldsymbol{M}_{f_1} \cdot \boldsymbol{p}^n_{f_1 D} + \boldsymbol{F}_{f_1} \cdot \boldsymbol{q}^n_{f w_1 D} = \boldsymbol{BHP}_{f_1} \\ \boldsymbol{M}_{f_2} \cdot \boldsymbol{p}^n_{f_2 D} + \boldsymbol{F}_{f_2} \cdot \boldsymbol{q}^n_{f w_2 D} = \boldsymbol{BHP}_{f_2} \\ \boldsymbol{H}_{f_1} \cdot \boldsymbol{q}^n_{f w_1 D} - \boldsymbol{q}^n_{w_1 D} = \boldsymbol{0} \\ \boldsymbol{H}_{f_2} \cdot \boldsymbol{q}^n_{f w_2 D} - \boldsymbol{q}^n_{w_2 D} = \boldsymbol{0} \end{cases} \tag{4-37}$$

Similarly, Equation (4-35) can also be arranged into a matrix format as follows:

before the refracturing treatment,

$$\begin{cases} \boldsymbol{M}_{f_1} \cdot \boldsymbol{p}^n_{f_1 D} + \boldsymbol{F}_{f_1} \cdot \boldsymbol{q}^n_{f w_1 D} - \boldsymbol{BHP}^n_{f_1} = \boldsymbol{0} \\ \boldsymbol{H}_{f_1} \cdot \boldsymbol{q}^n_{f w_1 D} + \boldsymbol{L}^n_{f_1} \odot \boldsymbol{p}^n_{w_1 D} = \boldsymbol{q}_{w_1 D} + \boldsymbol{L}^n_{f_1} \odot \boldsymbol{p}^{n-1}_{w_1 D} \end{cases} \tag{4-38}$$

and after the refracturing treatment,

$$\begin{cases} \boldsymbol{M}_{f_1} \cdot \boldsymbol{p}^n_{f_1 D} + \boldsymbol{F}_{f_1} \cdot \boldsymbol{q}^n_{f w_1 D} - \boldsymbol{BHP}^n_{f_1} = \boldsymbol{0} \\ \boldsymbol{M}_{f_2} \cdot \boldsymbol{p}^n_{f_2 D} + \boldsymbol{F}_{f_2} \cdot \boldsymbol{q}^n_{f w_2 D} - \boldsymbol{BHP}^n_{f_2} = \boldsymbol{0} \\ \boldsymbol{H}_{f_1} \cdot \boldsymbol{q}^n_{f w_1 D} + \boldsymbol{L}^n_{f_1} \odot \boldsymbol{p}^n_{w_1 D} = \boldsymbol{q}_{w_1 D} + \boldsymbol{L}^n_{f_1} \odot \boldsymbol{p}^{n-1}_{w_1 D} \\ \boldsymbol{H}_{f_2} \cdot \boldsymbol{q}^n_{f w_2 D} + \boldsymbol{L}^n_{f_2} \odot \boldsymbol{p}^n_{w_2 D} = \boldsymbol{q}_{w_2 D} + \boldsymbol{L}^n_{f_2} \odot \boldsymbol{p}^{n-1}_{w_2 D} \end{cases} \tag{4-39}$$

where the matrix M_f is defined in Appendix 4B, and the matrices $\boldsymbol{BHP}_f$, $\boldsymbol{F}_f$, $\boldsymbol{H}_f$, $\boldsymbol{L}_f$, $\boldsymbol{p}_{wD}$, and $\boldsymbol{q}_{wD}$ are defined in **Appendix 4C**.

4.2.3 Solution Methodology

On the basis of the continuity of flux and pressure, one can group the matrix flow equations, fracture flow equations and the production constraint equations to construct systems of linear equations that characterize the transient flow behavior of the refractures. At each timestep, we have the following unknowns in the systems of linear equations:

before the refracturing treatment,

- n_1 dimensionless pressures of the initial fracture panels, $p_{f_1 D}$;
- n_1 dimensionless fluxes from the matrix to the initial fracture panels: $q_{f_1 D}$;
- $2N_1$ dimensionless fluxes from the initial fractures to the wellbore, $q_{f w_1 D}$;

- N_1 dimensionless production rates at constant BHP condition (or N_1 dimensionless BHPs at constant production rate condition): p_{w_1D} (or q_{w_1D}).

and after the refracturing treatment,

- n_1+n_2 dimensionless pressures of the fracture panels, p_{f_1D} and p_{f_2D};
- n_1+n_2 dimensionless fluxes from the matrix to the fracture panels: q_{f_1D} and q_{f_2D};
- $2N_1$+$2N_2$ dimensionless fluxes from the fractures to the wellbore: q_{fw_1D} and q_{fw_2D};
- N_1+N_2 dimensionless production rates at constant BHP condition (or N_1+N_2 dimensionless BHPs at constant production rate condition): q_{w_1D} and q_{w_2D} (or p_{w_1D} and p_{w_2D}).

We also have the following equations at each timestep:

before the refracturing treatment,

- n_1 matrix flow equations given by Equation (4-17);
- n_1 fracture flow equations given by Equation (4-25);
- $3N_1$ equations that characterize the production constraint conditions given by Equation (4-33) or Equation (4-35).

and after the refracturing treatment,

- n_1+n_2 matrix flow equations given by Equations (4-18) and (4-19);
- n_1+n_2 fracture flow equations given by Equation (4-25);
- $3N_1$+$3N_2$ equations that characterize the production constraint conditions given by Equation (4-33) or Equation (4-35).

The systems of linear equations are close before or after the refracturing treatment. We solve them with the Gaussian elimination method. **Appendix 4D** provides these systems of linear equations in matrix format.

4.3. Validation of the Proposed Model

We validate the aforementioned model against a numerical simulator (Eclipse) under both constant production rate condition and constant BHP condition. In order to simulate the transient flow behavior of the fractures in an infinite reservoir, the reservoir model used in the Eclipse is set up with a sufficiently large size with dimensions of $5000 \times 5000 \times 15$ m^3. We also conduct sensitivity analysis on the grid size and we find that if the reservoir is discretized into more than $500 \times 500 \times 3$ cells (each cell has a dimension of $10 \times 10 \times 5$ m^3), the results from eclipse exhibit negligible difference with different numbers of cells. Therefore, the grid size used in Eclipse is $10 \times 10 \times 5$ m^3. **Figure 4-6a** shows a top view of the local grid system that contains the two fractures, and Figure 4-6b shows the refined cells that are used to characterize the fractures. As one can see in Figure 4-6a, the refracture is orthogonal to the initial fracture. The wellbores are located at the centers of the fractures and the distance between the wellbores is 70 m. Both the initial fracture and the refracture have a length of 50 m and a width of 0.1 m. The fluid and rock properties used are given as follows: c_{tm} = 0.0012 MPa^{-1}, ϕ_m = 0.2, K_{mx} = 0.2 mD, K_{my} = 0.1 mD, p_i = 30 MPa, μ = 1 mPa·s, C_w = 0, B = 0.985 (dead oil). The initial fracture and the refracture have the same properties and production constraints: K_f = 1000 mD, c_{tf} = 0.0012 MPa^{-1}, ϕ_f = 0.2, q_w = 0.5 m^3/d (constant production rate condition), and p_w = 5 MPa (constant BHP condition). The simulation is conducted with two production periods with each period lasting 500 production days. During the first production period, only the initial fracture is put into production and the cells that are used to characterize the refracture are assigned with a permeability equal to the matrix permeability. During the second production period, both the initial fracture and the refracture are put into production, and the cells of the refracture are assigned with a permeability of 1000 mD.

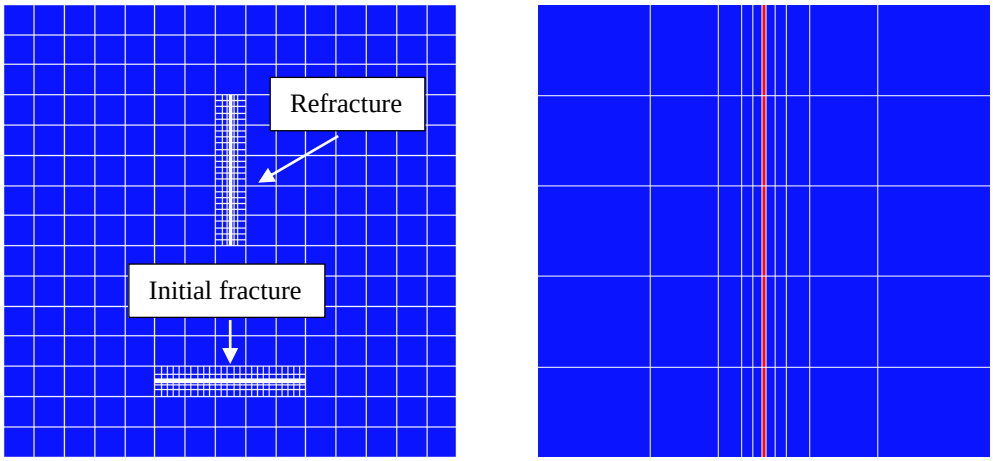

(a) (b)

Figure 4-6. Grid system used in the Eclipse model: (a) top view of the local grid system that characterizes the initial fracture and the refracture; and (b) zoom-in view of the refined grids.

Before we compare the results obtained with the proposed model to those obtained with Eclipse, we first examine the impact of the number of fracture segments on the outputs of our model. We discretize the fractures, including the initial fracture and the refracture, into 22, 26, 30 and 34 segments, respectively, and calculate the transient flow behavior of the fractures with the above-mentioned parameter values. **Figure 4-7** presents the pressure responses of the refracture (Figure 4-7a) and the field production rates (Figure 4-7b) that are calculated with the different numbers of fracture segments. In Figure 4-7, the field production rate q_t is defined as:

$$q_t = \sum_{m=1}^{m=N_1} q_{w_1^m} + \sum_{m=1}^{m=N_2} q_{w_2^m} \tag{4-40}$$

and the time t_2 is defined as:

$$t_2 = t - t_1 \tag{4-41}$$

where t is production time, and t_1 is the production time before the refracturing treatment (i.e., 500 days). Figure 4-7 shows that the simulation outputs become unchanged if the number of the fracture segments is larger than 30; therefore, we use 30 fracture segments in the subsequent calculations. **Figure 4-8** compares the pressure responses of the refracture (Figure 4-8a) and the

field production rates (Figure 4-8b) calculated with the proposed model against those calculated with Eclipse. As seen from this figure, the results obtained with the proposed model are in good agreement with those obtained with Eclipse. This implies that the proposed model is reliable in characterizing the transient flow behavior of a reoriented refracture.

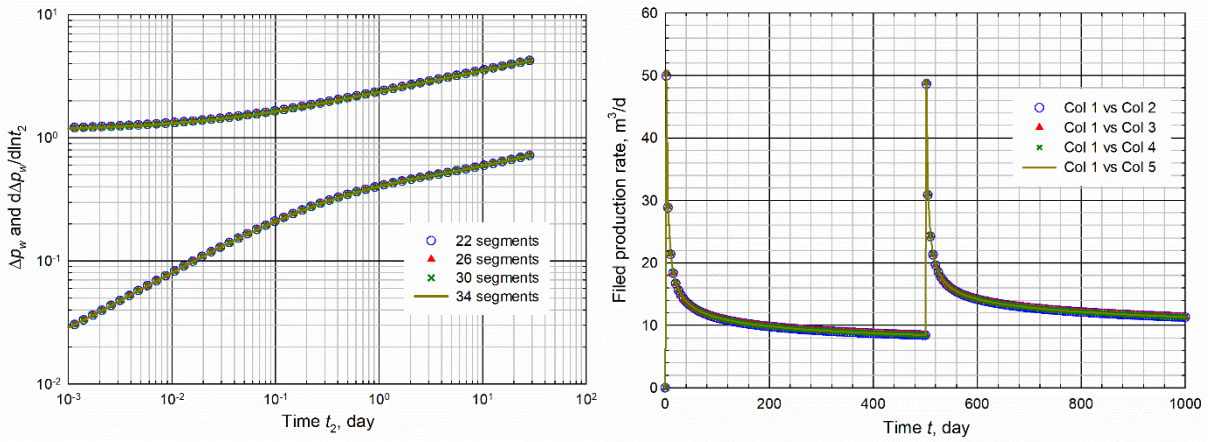

(a) (b)

Figure 4-7. Impact of the number of fracture segments on the outputs of the semi-analytical model: (a) pressure drops and pressure derivatives under constant production rate condition; and (b) field production rates under constant BHP condition.

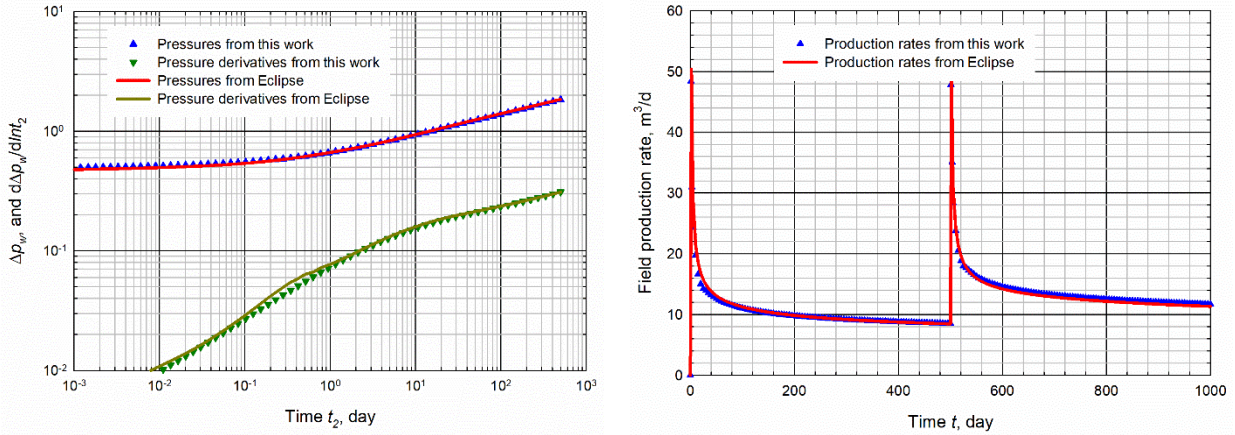

(a) (b)

Figure 4-8. Comparison between the pressure response and field production rates calculated with the proposed model and those by Eclipse: (a) pressure drops and pressure derivatives under constant production rate condition; and (b) field production rates under constant BHP condition.

4.4. Results and Discussion

In this section, a two-fracture system which contains a single initial fracture and a single refracture is studied. We distinguish the flow regimes that can be observed during the production period of a reoriented refracture. Hereafter, we study the influences of refracture's reoriented azimuth, refracture's position, and permeability anisotropy on the productivity of the fractures. Furthermore, we determine the reoriented azimuths of a refracture that can lead to the highest field productivity. The following benchmark dimensionless values for the initial fractures and the refractures are used in the following studies: $W_{f_1D} = 0.0001$, $W_{f_2D} = 0.0001$, $L_{f_1D} = 2$, $L_{f_2D} = 2$, $\gamma = 1.069 \times 10^{-8}$, $C_s = 1$, $C_{wD} = 1$, and the refracture is put into production at the dimensionless time of 10. It should be noted that although only a two-fracture system is studied in this work, this proposed model can also be used to characterize the transient flow behavior of multiple-fracture systems.

4.4.1 Flow Regimes

We consider a single initial fracture and a single reoriented refracture in order to illustrate the flow regimes that can be observed during the production period of a refracture. The ratio of the horizontal permeability R_K ($R_K = K_{my}/K_{mx}$) is 1. The flow regimes of the reoriented refracture are investigated under the constant production rate condition on two scenarios. Scenario #1 considers a refracture which is distant from the initial fracture and has a small dimensionless fracture conductivity, whereas scenario #2 considers a refracture which is in the vicinity of the initial fracture and has a large dimensionless fracture conductivity. **Figure 4-9** shows the schematic of the fracture system. The used data of the initial fracture are as follows: $X_{fw_1D} = 0$, $Y_{fw_1D} = 0$, $C_{F_1D} = 10$, $\theta_{f_1} = 0^o$). The used data of the refracture in the two scenarios are as follows: scenario #1, $X_{fw_2D} = 20$, $Y_{fw_2D} = 0$, $C_{F_2D} = 1$, and $\theta_{f_2} = 90^o$; and scenario #2, $X_{fw_2D} = 1.5$, $Y_{fw_2D} = 0.5$, $C_{F_2D} = 20$,

and $\theta_{f2} = 150^{o}$. **Figure 4-10** presents the pressure drop curves and the pressure derivative curves that are obtained with the proposed model for these two scenarios. As shown in Figure 4-10a, one can distinguish the following flow regimes in scenario #1: (1) wellbore after flow, (2) fracture pseudo-steady-state flow, (3) bilinear flow (1/4-slope), (4) early pseudo-radial flow, and (5) late pseudo-radial flow. It is noted that there are two pseudo-radial flow periods in this scenario. The early pseudo-radial flow occurs around the refracture, while the late pseudo-radial flow occurs around both the initial fracture and the refracture.

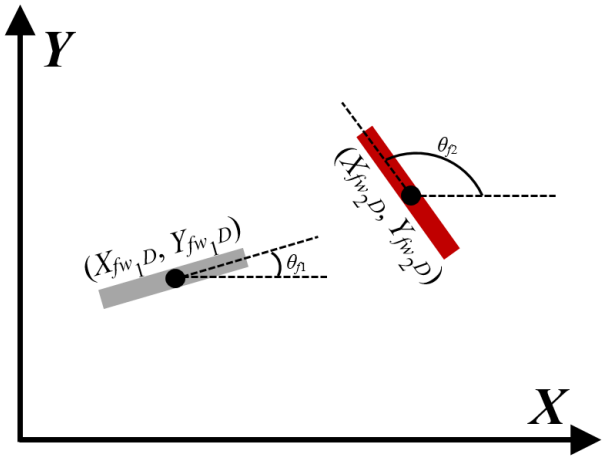

Figure 4-9. Schematic of the fracture system.

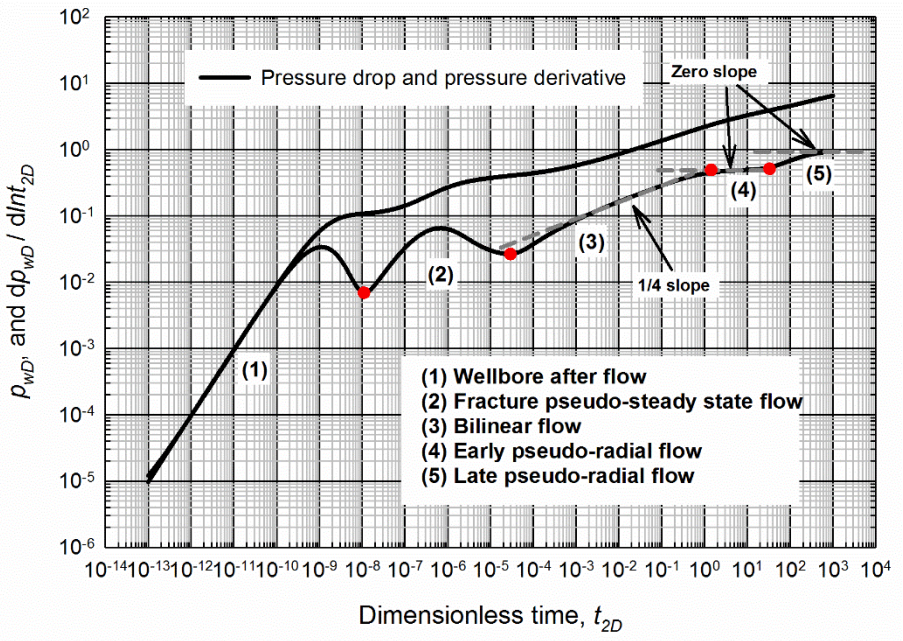

(a)

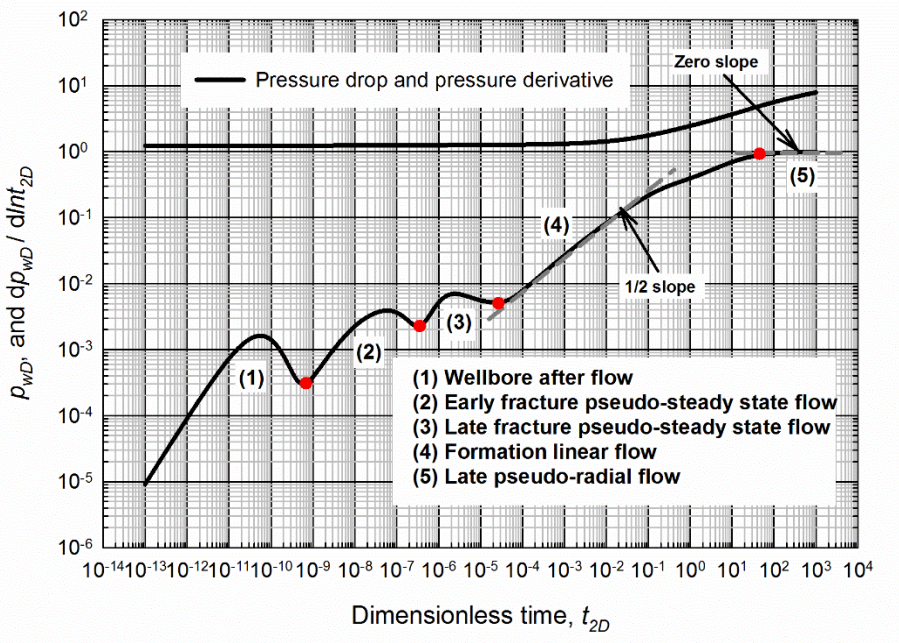

(b)

Figure 4-10. Identification of the flow regimes that can be observed during the production period of a reoriented refracture: (a) flow regimes of scenario #1; and (b) flow regimes of scenario #2.

As for the scenario #2 (Figure 4-10b), one can observe the following flow regimes: (1) wellbore after flow, (2) early fracture pseudo-steady-state flow, (3) late fracture pseudo-steady-state flow, (4) formation linear flow (1/2-slope), and (5) late pseudo-radial flow. The fracture pseudo-steady-state flow can be observed only if the wellbore storage effect is sufficiently small. An interesting observation is that there are two fracture pseudo-steady-state flow periods in Figure 4-10b. This is attributed to the interference from the initial fracture. **Figure 4-11** presents the flux distributions along the refracture and the pressure maps during these two fracture pseudo-steady-state flow periods. In Figures 4-11a and 4-11c, one can find that the wellbore position (l_{f2D} = 1) and the fracture toes (l_{f2D} = 0, and 2) exhibit a relatively higher flux than the other positions along the fracture. A similar observation can also be found in Yang *et al*. [21]. A positive flux indicates that the fluid flows from the matrix to the fracture, while a negative flux indicates that the fluid flows from the fracture to the matrix. As one can see in Figure 4-11a, the flux distribution during

the early fracture pseudo-steady-state flow can be divided into three sections: sections #1 and #3, the flux is increased as the time elapses; and section #2, the flux is decreased as the time elapses. One can also distinguish these three sections on the pressure map in Figure 4-11b. In Figure 4-11c which presents the flux distribution during the late fracture pseudo-steady-state flow period, the flux distribution along the refracture can be divided into two sections, namely, section #1 (the flux is decreased as time elapses) and section #2 (the flux is increased as time elapses). These two sections can also be distinguished on the pressure map in Figure 4-11d. In both Figures 4-11a and 4-11c, it is observed that the left branch of the refracture lateral that is nearer to the initial fracture exhibits smaller flux compared to the right branch of the refracture lateral.

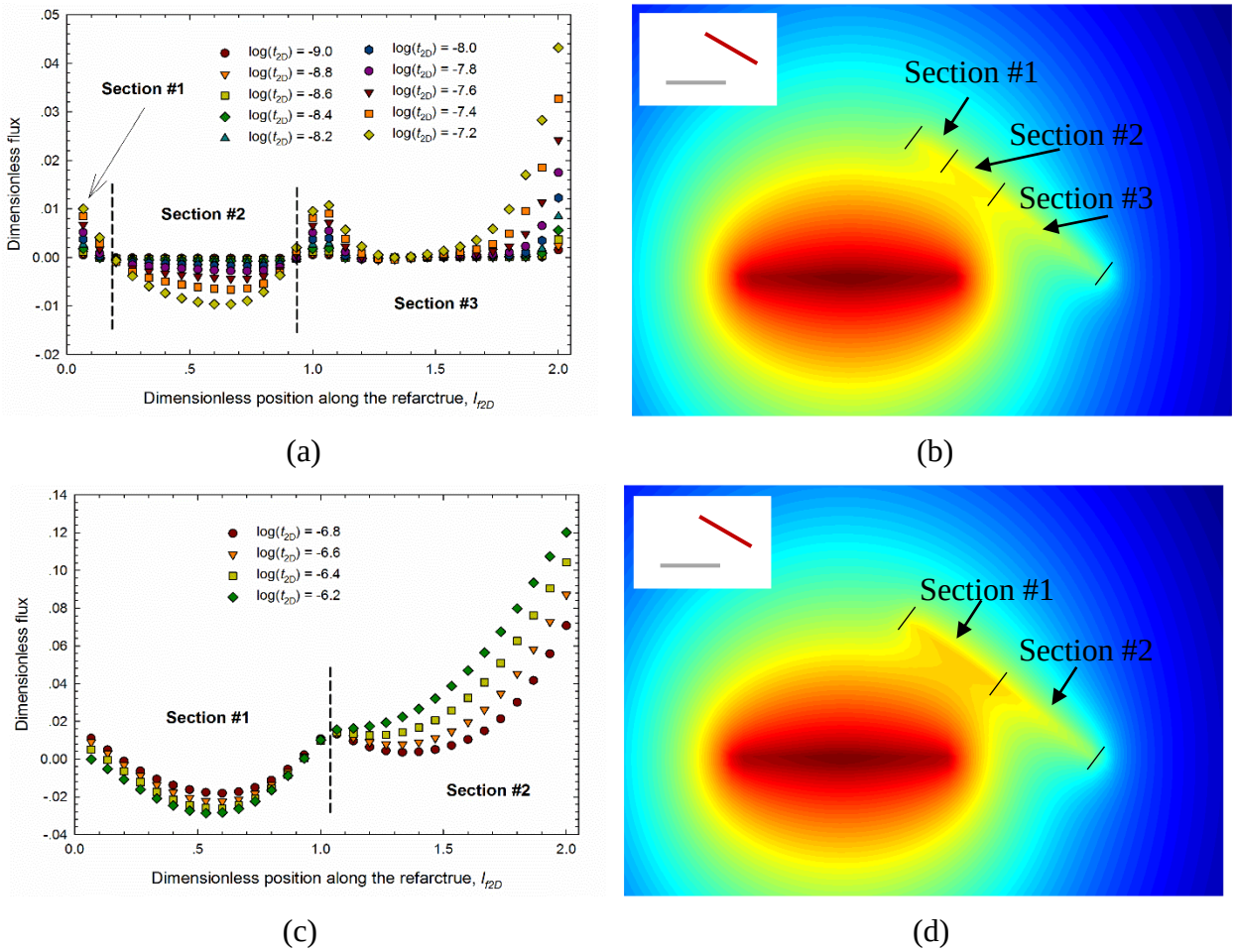

Figure 4-11. Flux distributions along the refracture and the pressure maps during these two fracture pseudo-steady-state flow periods: (a) flux distribution along the refracture during the

early fracture pseudo-steady state flow; (b) pressure map during the early fracture pseudo-steady state flow; (c) flux distribution along the refracture during the late fracture pseudo-steady state flow; (d) pressure map during the late fracture pseudo-steady state flow.

4.4.2 Sensitivity Analysis

The sensitivity analysis is also conducted with a single reoriented refracture and a single initial fracture. The influences of refracture' position, refracture's azimuth, and permeability anisotropy, on the transient flow behaviors are investigated under the constant BHP condition. In addition to the benchmark dimensionless values, we have $X_{fw_1D} = 0$, $Y_{fw_1D} = 0$, $C_{F_1D} = 10$, $\theta_{f_1} = 0^o$, $C_{F_2D} = 10$, and the other dimensionless values used in the sensitivity analysis are tabulated in **Table 4-2**.

Table 4-2. Dimensionless values used in Section 4.2 sensitivity analysis.

	(X_{fw_2D}, Y_{fw_2D})	θ_{f_2}	R_K
Section 4.2.1	(1.77, 1.77)	0, 45°, 90°	0.1, 1 , 10
Section 4.2.2	(2.50, 0), (1.77, 1.77), (0, 2.50)	45°	0.1, 1 , 10
Section 4.2.3	(2.50, 0), (1.77, 1.77), (0, 2.50)	0, 45°, 90°	1

4.4.2.1 Effect of Refracture's Azimuth and Permeability Ratio

Figure 4-12 shows the dimensionless field production rates with different refracture's azimuths and different permeability ratios, and **Figure 4-13** shows the dimensionless pressure maps for all these cases at dimensionless time of 20. As one can see in Figure 4-12a, with an R_K of 0.1, the field productivity will be most significantly enhanced if the refracture is orthogonal to the X-axis. As seen from Figures 4-13a to 4-13c, an orthogonal refracture (Figure 4-13c) can more significantly expand the low-pressure (or high-dimensionless-pressure) area than the refracture

that is not exactly orthogonal (Figures 4-13a and 4-13b). Figures 4-12b presents the dimensionless field production rates with different refracture's azimuths in a homogeneous permeability system (R_K = 1). In this figure, the field productivity undergoes slight changes as the azimuth is varied. From Figures 4-13d to 4-13f, one can also observe that the low-pressure (or high-dimensionless-pressure) area has not been much impacted by the variation in the refracture's azimuth. Figures 4-12c shows that, with an R_K of 10, a smaller reoriented azimuth can lead to a higher field productivity. Figures 4-13g to 4-13i compare the pressure maps with different refracture's azimuths with an R_K of 10. It can be readily observed that the low-pressure (or high-dimensionless-pressure) area with a non-reoriented refracture (Figure 4-13g) is larger than those with a reoriented refracture (Figures 4-13h and 4-13i).

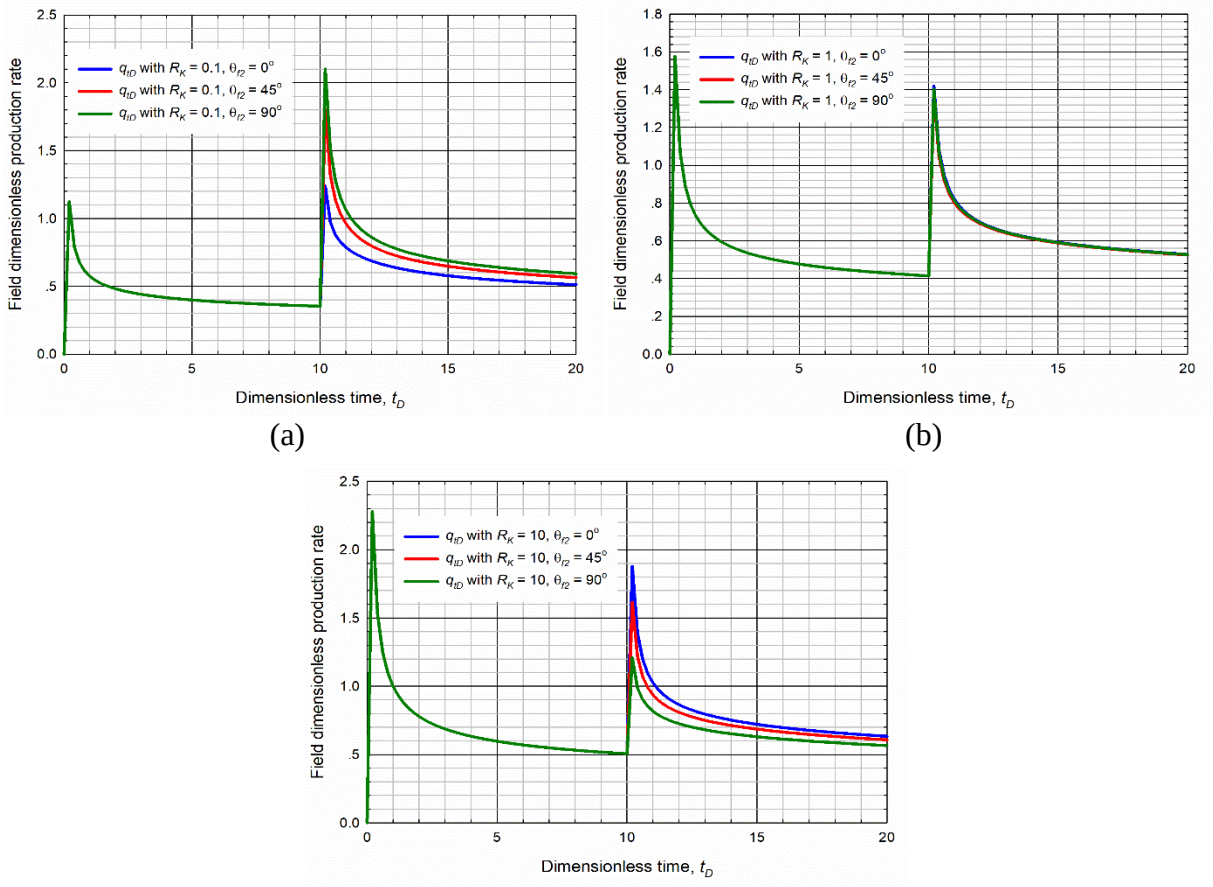

Figure 4-12. Dimensionless field production rates with different refracture's azimuths and different permeability ratios: (a) dimensionless field production rates with R_K = 0.1 and varied refracture's azimuth; (b) dimensionless field production rates with R_K = 1 and varied refracture's azimuth; (c) dimensionless field production rates with R_K = 10 and varied refracture's azimuth.

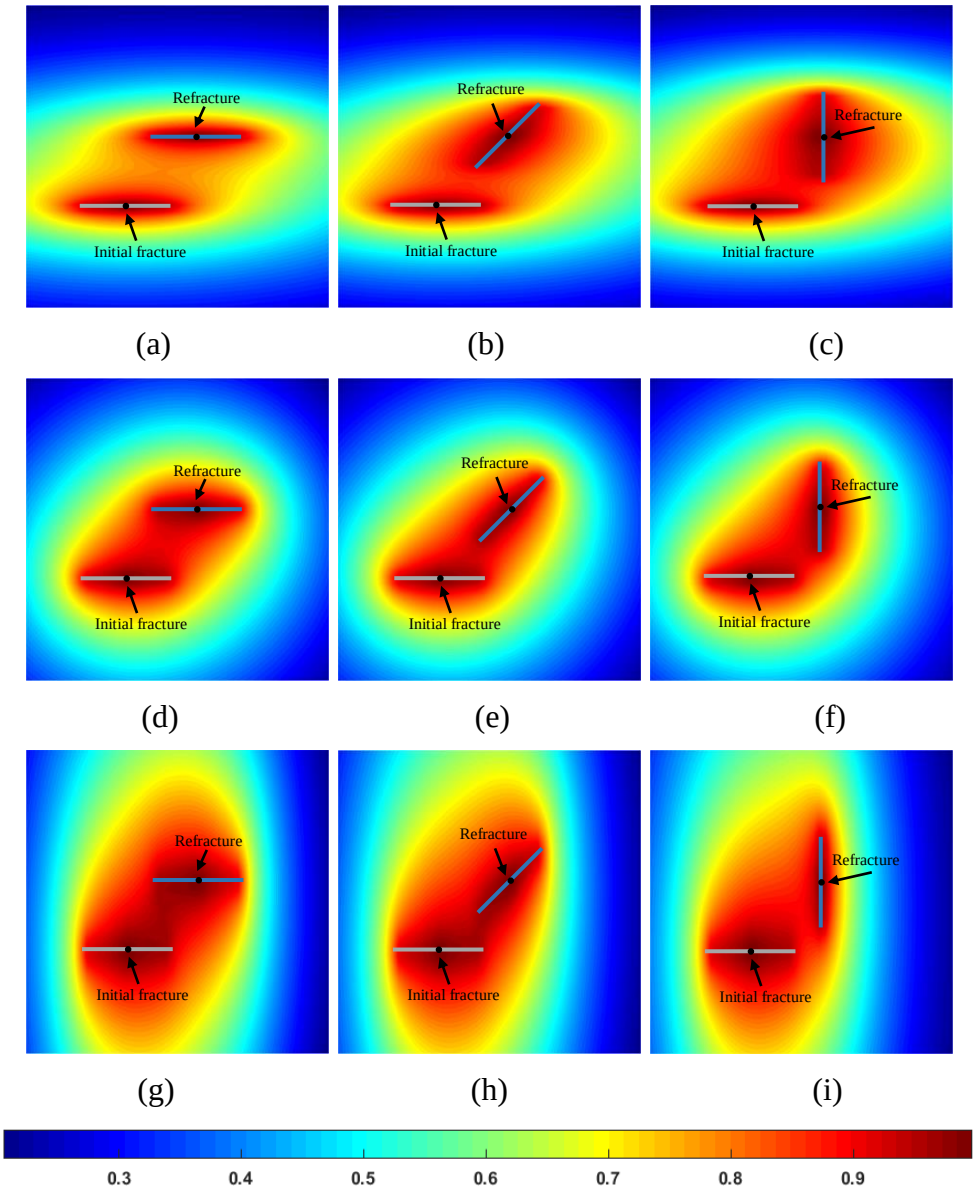

Figure 4-13. Dimensionless pressure maps with different refracture's azimuths and different permeability ratios: (a) R_K = 0.1, θ_{f2} = 0°; (b) R_K = 0.1, θ_{f2} = 45°; (c) R_K = 0.1, θ_{f2} = 90°; (d) R_K = 1, θ_{f2} = 0°; (e) R_K = 1, θ_{f2} = 45°; (f) R_K = 1, θ_{f2} = 90°; (g) R_K = 10, θ_{f2} = 0°; (h) R_K = 10, θ_{f2} = 45°; (i) R_K = 10, θ_{f2} = 90°.

4.4.2.2 Effects of Refracture's Position and Permeability Ratio

Figure 4-14 illustrates the dimensionless field production rates with different refracture's positions and different permeability ratios, and **Figure 4-15** depicts the dimensionless pressure maps for all these scenarios at dimensionless time of 20. The studied positions of the refracture include: position #1 (Figures 4-15a, 4-15d, and 4-15g), X_{fw_2D} = 2.50, Y_{fw_2D} = 0; position #2 (Figures 4-15b, 4-15e, and 4-15h), X_{fw_2D} = 1.77, Y_{fw_2D} = 1.77; and position #3 (Figures 4-15c, 4-15f, and 4-15i), X_{fw_2D} = 0, Y_{fw_2D} = 2.50. As shown in Figures 4-14a, with an R_k of 0.1, the filed productivity is increased as the refracture's position is changed from position #1 to position #3. This is attributed to that, the interference from the initial fracture towards the refracture is decreased as the refracture's position changes from position #1 to position #3 (see Figures 4-15a to 4-15c). In the homogeneous reservoir where R_K = 1, both the filed productivity (see Figure 4-14b) and the low-pressure area (see Figures 4-15d to 4-15f) undergo slight changes as the refracture's position is changed. As shown in Figures 4-14c where R_K = 10, the field productivity with position #1 illustrates a higher value than those with positions #2 and #3. This observation can be readily explained with the pressure maps shown by Figures 4-15g through 4-15i, where one can see that the interference between the fractures is increased as the refracture's position is varied from position #1 to position #3.

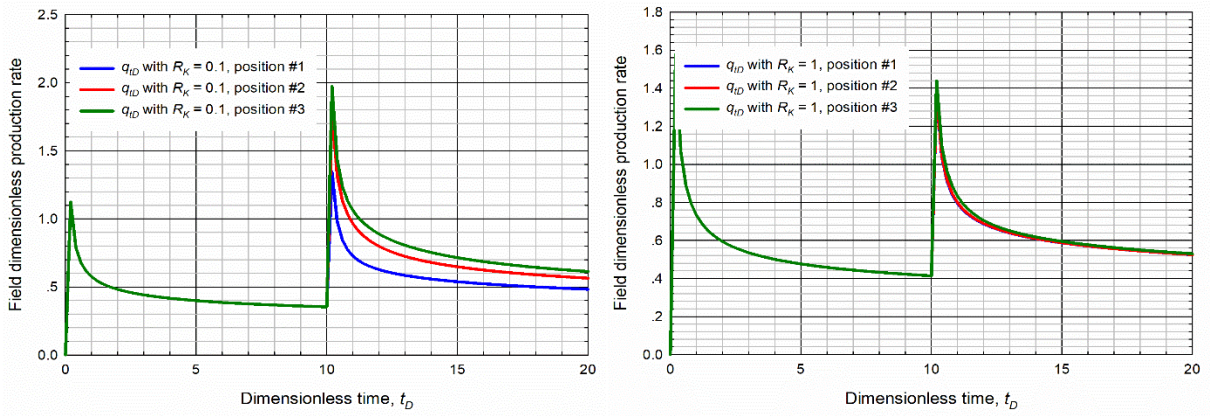

(a) (b)

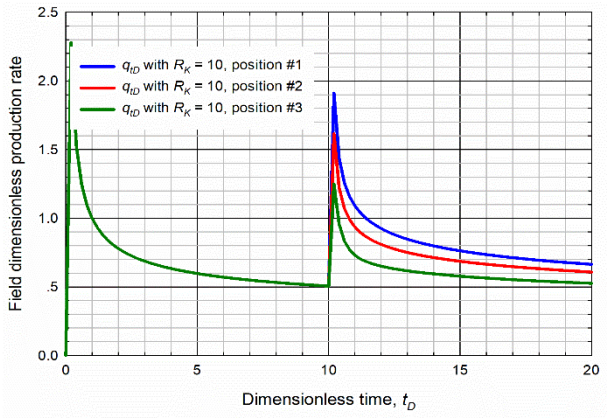

(c)

Figure 4-14. Dimensionless field production rates with different refracture's positions and different permeability ratios: (a) dimensionless field production rates with R_K = 0.1 and varied refracture's position; (b) dimensionless field production rates with R_K = 1 and varied refracture's position; (c) dimensionless field production rates with R_K = 10 and varied refracture's position.

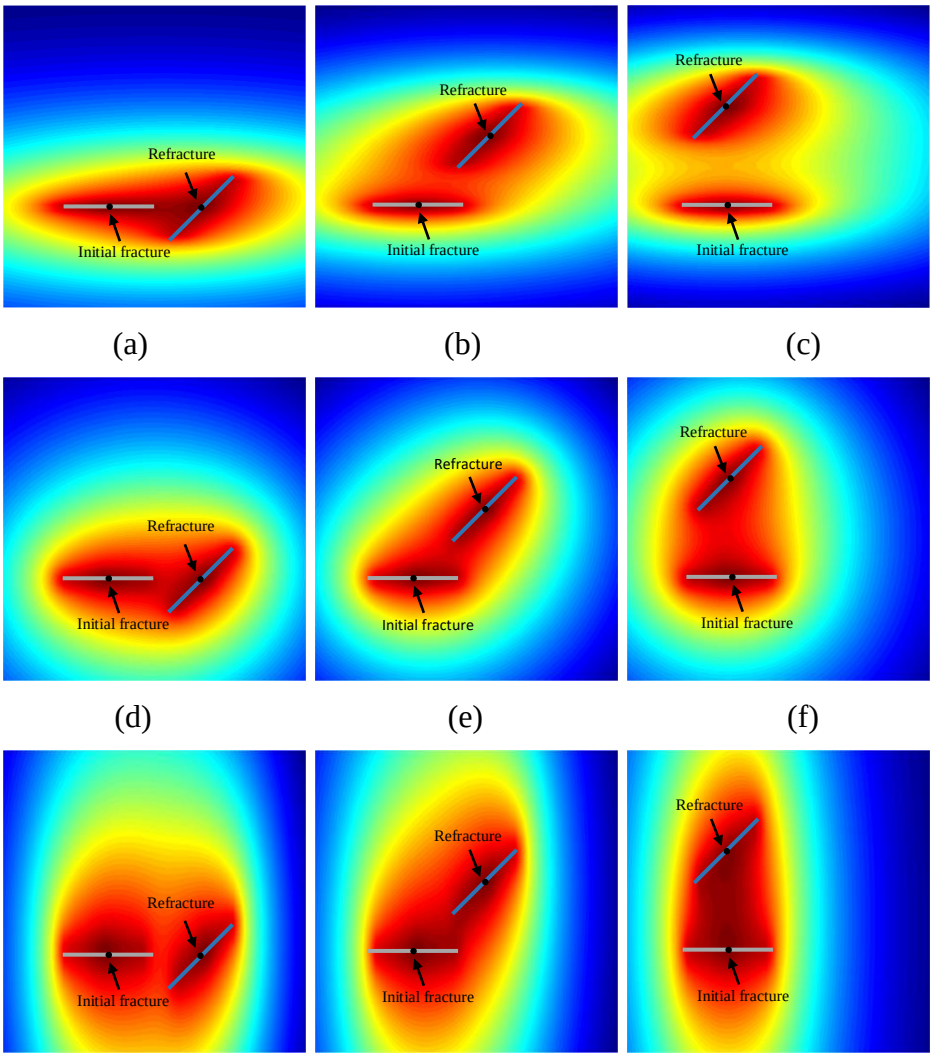

(a) (b) (c)

(d) (e) (f)

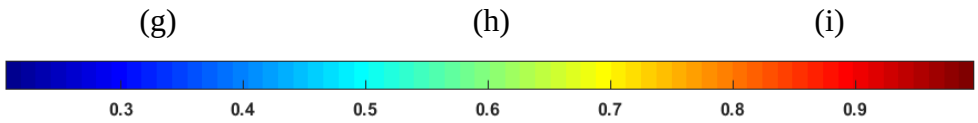

Figure 4-15. Dimensionless pressure maps with different refracture's positions and different permeability ratios: (a) R_K = 0.1, position #1; (b) R_K = 0.1, position #2; (c) R_K = 0.1, position #3; (d) R_K = 1, position #1; (e) R_K = 1, position #2; (f) R_K = 1, position #3; (g) R_K = 10, position #1; (h) R_K = 10, position #2; (i) R_K = 10, position #3.

4.4.3 Optimal Reorientation Azimuth

In practice, with the refracture being located at a relative position with respect to the initial fracture, different reorientation azimuths of the refracture can lead to different filed productivities. We assume that the reorientation azimuth that can lead to the highest field productivity is the optimal reorientation azimuth. Consequently, we carry out a comprehensive study of the optimal reorientation azimuth of the refracture. It should be noted that the reorientation of a refracture should be heavily dependent of the stress field; but in this section, the study is conducted with the assumption that the optimal reorientation azimuth can be induced for all of the studied cases under a given stress field.

Figure 4-16 shows the top view of the optimal-reorientation-azimuth maps of the refracture at different relative positions with respect to a single initial fracture. In addition to the benchmark dimensionless parameters, the following values are used: X_{fw_1D} = 0, Y_{fw_1D} = 0, C_{F_1D} = 10, θ_{f_1} = 0^o, and C_{F_2D} = 0.1, 1, 10, and 100. The refracture's azimuth is varied from 0^o to 180^o with an interval of 5^o. Since the refracture's position and reorientation azimuth are symmetric with respect to the wellbore of the initial fracture, a quarter of the coordinate system is sufficient to represent the entire coordinate system. It is observed in Figure 4-17 that, there is a region in the vicinity of the initial fracture, within which an orthogonal refracture is optimal for the field productivity. For convenience, this region is called as 'orthogonal refracture region' in the following text. In a real field case, a stress reversal around the initial fracture can be induced due to the production from

the initial fracture [6, 26]. Such stress reversal is favorable for creating an orthogonal refracture. Therefore, in the filed application, the operators can utilize the induced stress reversal region to create an orthogonal refracture to optimize the productivity of the refracture. Beyond the orthogonal refracture region, the optimal reorientation azimuth is increased along the counter-clockwise direction. In addition, comparing the orthogonal refracture regions shown through Figures 4-17a to 4-17d, one can see that the area of the orthogonal refracture region is decreased as the refracture's conductivity is increased.

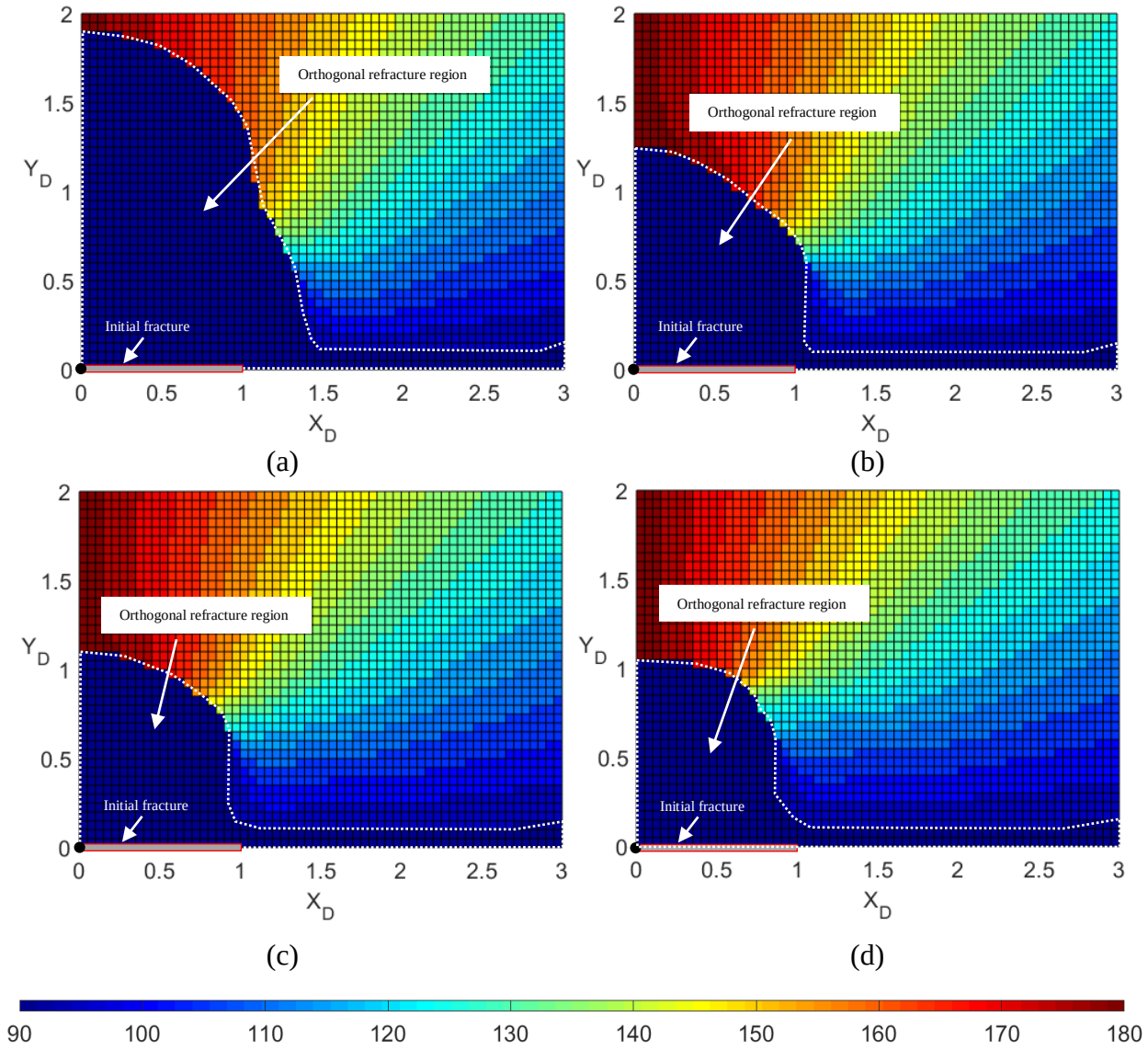

Figure 4-16. Optimal refracture's azimuth with different dimensionless conductivities of the refracture: (a) optimal refracture's azimuth with C_{F_2D} = 0.1; (b) optimal refracture's azimuth with C_{F_2D} = 1; (c) optimal refracture's azimuth with C_{F_2D} = 10; (d) optimal refracture's azimuth with C_{F_2D} = 100.

4.4.4 Suggestions on Industrial Applications

Although only a 2-fracture system is studied in this work, this proposed semi-analytical model can also be used to characterize the fluid transient flow of multiple-fracture systems. In addition, natural fractures can also be incorporated into this proposed model. In order to simulate the fluid transient flow in a naturally fractured reservoir, the natural fractures can be treated as initial fractures that have a constant production rate of 0. **Figure 4-17a** presents the distribution of fractures (including 4 natural fracture, 1 initial fracture, and 1 refracture) in a reservoir from a top view. The dimensionless conductivities of the 4 natural fractures are 1000. Figure 4-17b compares the dimensionless production rates of the scenario without natural fractures against that with natural fractures. From this figure, one can find that the field production rates of the scenario with natural fractures are higher than those without natural fractures.

For the real field applications, one can make minor modifications on this proposed model to account for the specific reservoir conditions. For example, the gas condensate flow can be simulated by applying the concept of pseudo-pressure and pseudo-time, the pressure-dependent fracture conductivity can be taken into consideration with the method introduced by Yu *et al*. (2016) [27].

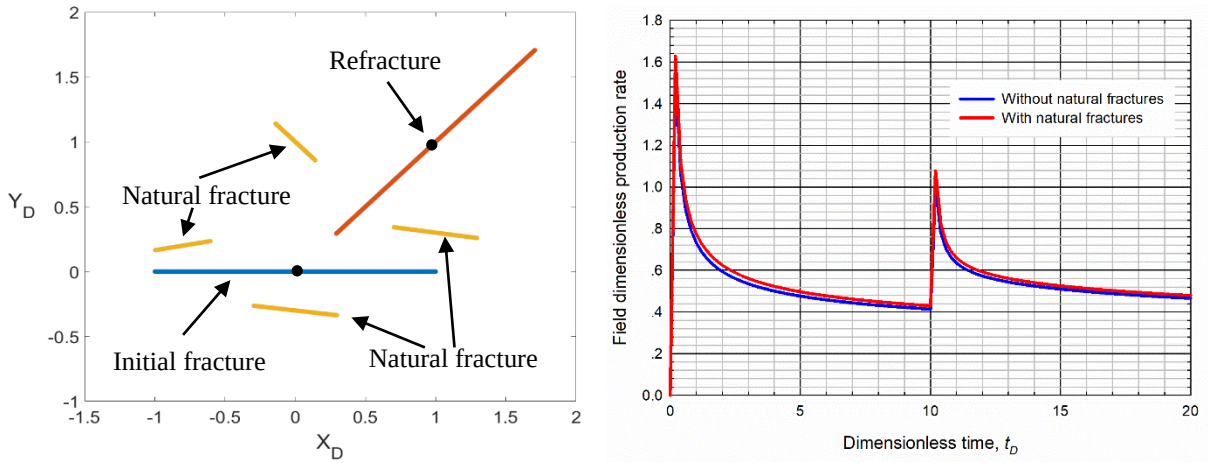

(a) (b)

Figure 4-17. A calculation example of applying the proposed semi-analytical model to a naturally fractured reservoir: (a) top view of the fracture distribution in a reservoir; and (b) comparison between dimensionless productions of the scenario with natural fractures and those without natural fractures.

4.5. Conclusions

In this work, we develop a semi-analytical model to characterize the transient flow behavior of reoriented refractures. This proposed model can be used to evaluate the performance of the refractures with the aid of a geomechanical model, or can be applied to conduct history matching work. On the basis of this proposed model, we carry out a thorough investigation on the flow regimes that can be observed during the production period of the refracture. We also study the influences of refracture's azimuth, permeability anisotropy, and refracture's position on the field productivity. Subsequently, we obtain the optimal reorientation azimuth map of the refractures around an initial fracture. These case studies lead us to draw the following conclusions:

- A new semi-analytical model is developed that can be used to characterize the flow transient flow behavior of reoriented refractures;
- Both the formation linear flow and bilinear flow can be observed during the production period of a refracture with certain refracture conductivities. At the late production period,

two pseudo-radial flow can appear: one is around the refracture and one is around both the initial fracture and refracture;

- In an anisotropic-permeability reservoir, both the refracture's azimuth and refracture's position can significantly influence the productivity of the field and fractures. Their influence on the well performance will be less pronounced if the reservoir permeability is homogeneous;
- In the vicinity of the initial fracture, there is an orthogonal region, within which an orthogonal refracture can lead to the highest field productivity. The area of the orthogonal refracture region is decreased as the refracture's conductivity is increased.

Nomenclature

Δl = the length of a fracture segment, m

B = formation volume factor

C = wellbore storage coefficient, bbl/psi

C_D = dimensionless wellbore storage coefficient

C_F = fracture conductivity in the anisotropic permeability system, mD·m

C_f = fracture conductivity in the equivalent isotropic permeability system, mD·m

C_{F_1D} = dimensionless initial fracture conductivity in the anisotropic permeability system

C_{F_2D} = dimensionless refracture conductivity in the anisotropic permeability system

C_{FD} = dimensionless fracture conductivity in the anisotropic permeability system

C_{fD} = dimensionless fracture conductivity in the equivalent isotropic permeability system

C_s = dimensionless coefficient defined in this work

c_{tf} = fracture's total compressibility, MPa^{-1}

c_{tm} = matrix total compressibility, MPa^{-1}

h = formation thickness, m

k_m = matrix permeability in the equivalent isotropic permeability system, mD

K_{mx}, and K_{my} = matrix permeability in the anisotropic permeability system, mD

l = length along the propagation direction of the fracture in the isotropic-permeability system, m

l_D = dimensionless length along the propagation direction of the fracture in the equivalent isotropic-permeability system

l_f = fracture length in the equivalent isotropic permeability system, m

l_{fD} = dimensionless fracture length in the equivalent isotropic permeability system, m

l_r = reference length, m

L_f = fracture length in the anisotropic permeability system, m

L_{f1D} = dimensionless initial fracture length in the anisotropic permeability system

L_{f2D} = dimensionless refracture length in the anisotropic permeability system

L_{fD} = dimensionless fracture length in the anisotropic permeability system

N_1 = the number of initial fractures

N_2 = the number of refractures

p_D = dimensionless pressure

p_f = fracture pressure, MPa

p_{fD} = dimensionless fracture pressure

$p^n_{f_1D,i}$ = dimensionless fracture pressure of the i^{th} initial fracture segment at the n^{th} timestep

$p^n_{f_2D,j}$ = dimensionless fracture pressure of the j^{th} refracture segment at the n^{th} timestep

p_i = initial reservoir pressure, MPa,

p_r = reference pressure, MPa

p_w = bottomhole pressure, MPa

p_{wD} = dimensionless bottomhole pressure

q = flux per unit length from the matrix to the fracture, m^2/d

q_f = flux rate from the matrix to a fracture segment, m^3/d

q_{f1D} = dimensionless flux rate from the matrix to the initial fracture

$q^k_{f1D,I}$ = dimensionless flux from the matrix to the I^{th} initial fracture segment at the k^{th} timestep

q_{f2D} = dimensionless flux rate from the matrix to the refracture

$q^k_{f2D,J}$ = dimensionless flux from the matrix to the J^{th} refracture segment at the k^{th} timestep

q_{fD} = dimensionless flux rate from the matrix to a fracture segment

q_{fw} = flux from fracture to the wellbore, m^3/d

q_{fwD} = dimensionless flux from fracture to the wellbore

q_r = reference production rate, m^3/d

q_w = well production rate, m^3/d

q_{wD} = dimensionless well production rate

Q_D = dimensionless cumulative production

r_w = radius of the wellbore, m

R_K = permeability ratio in the anisotropic permeability system, K_{my}/K_{mx}

t = time, day

t_D = dimensionless time

w_f = fracture width in the equivalent isotropic permeability system, m

w_{fD} = dimensionless fracture width in the equivalent isotropic permeability system

W_f = fracture width in the anisotropic permeability system, m

W_{f1D} = dimensionless initial fracture width in the anisotropic permeability system

W_{f2D} = dimensionless refracture width in the anisotropic permeability system

W_{fD} = dimensionless fracture width in the anisotropic permeability system

x, y and z = coordinates in the equivalent isotropic permeability system, m

x_0, y_0 = coordinates of a line source in the equivalent isotropic permeability system, m

x_{0D}, y_{0D} = dimensionless coordinates of a line source in the equivalent isotropic permeability system

x_D, y_D and z_D = dimensionless coordinates in the equivalent isotropic permeability system

$x_{f1D,i}$, $y_{f1D,i}$ = dimensionless coordinates of the central position of the i^{th} initial fracture segment in the equivalent isotropic permeability system

$x_{f2D,j}$, $y_{f2D,j}$ = dimensionless coordinates of the central position of the j^{th} refracture segment in the equivalent isotropic permeability system

X, Y, and Z = coordinates in the anisotropic permeability system, m

X_D, Y_D, and Z_D = dimensionless coordinates in the anisotropic permeability system

X_{fw1D}, and Y_{fw1D} = dimensionless coordinates of the wellbore of the initial fracture in the anisotropic permeability system

X_{fw2D}, Y_{fw2D} = dimensionless coordinates of the wellbore of the refracture in the anisotropic permeability system

β = unit conversion factor which has a numerical value of 0.0853

γ = a dimensionless coefficient defined in this work

$\eta_f = \beta k_f / \mu \phi_f c_{tf}$, fracture diffusivity coefficient, m^2/d

$\eta_m = \beta k_m / \mu \phi_m c_{tm}$, matrix diffusivity coefficient, m^2/d

μ = oil viscosity, mPa·s

ϕ_f = effective porosity in the fracture system

ϕ_m = matrix porosity

θ = fracture azimuth with respect to *X-axis* in the anisotropic permeability system

θ_{f1} = initial fracture azimuth with respect to *X-axis* in the anisotropic permeability system

θ_{f2} = refracture azimuth with respect to *X-axis* in the anisotropic permeability system

$\odot$ = Hadamard product operator

Subscripts

f_1^m = the m^{th} initial fracture

f_2^m = the m^{th} refracture

f_1 = initial fracture

f_2 = refracture

m = matrix

t = total

Acknowledgments

The authors would like to acknowledge the financial support provided by the Natural Science and Engineering Research Council of Canada (NSERC) as well as the financial support from China Scholarship Council (CSC). The authors also thank Schlumberger for providing us the academic license of Eclipse.

Appendix 4A – Definition of the Matrices Used to Characterize the Matrix Flow.

The matrices of $\boldsymbol{p}$, $\boldsymbol{q}$, $\boldsymbol{G}$, and $\boldsymbol{RHS}$ are defined as follows:

$$\boldsymbol{p}^n_{f_1D} = \begin{bmatrix} p^n_{f_1D,1} \\ \vdots \\ p^n_{f_1D,n_1} \end{bmatrix},\ \boldsymbol{p}^n_{f_2D} = \begin{bmatrix} p^n_{f_2D,1} \\ \vdots \\ p^n_{f_2D,n_2} \end{bmatrix},\ \boldsymbol{q}^n_{f_1D} = \begin{bmatrix} q^n_{f_1D,1} \\ \vdots \\ q^n_{f_1D,n_1} \end{bmatrix}, \text{ and } \boldsymbol{q}^n_{f_2D} = \begin{bmatrix} q^n_{f_2D,1} \\ \vdots \\ q^n_{f_2D,n_2} \end{bmatrix} \tag{4A-1}$$

$$\boldsymbol{G}^n_{f_1D,\,f_1} = \begin{bmatrix} G^n_{f_1D,1}\left(x_{f_1D,1}, y_{f_1D,1}, t^n_D\right) & \cdots & G^n_{f_1D,n_1}\left(x_{f_1D,1}, y_{f_1D,1}, t^n_D\right) \\ \vdots & \ddots & \vdots \\ G^n_{f_1D,1}\left(x_{f_1D,n_1}, y_{f_1D,n_1}, t^n_D\right) & \cdots & G^n_{f_1D,n_1}\left(x_{f_1D,n_1}, y_{f_1D,n_1}, t^n_D\right) \end{bmatrix} \tag{4A-2}$$

$$\boldsymbol{G}^n_{f_1D,\,f_2} = \begin{bmatrix} G^n_{f_1D,1}\left(x_{f_2D,1}, y_{f_2D,1}, t^n_D\right) & \cdots & G^n_{f_1D,n_1}\left(x_{f_2D,1}, y_{f_2D,1}, t^n_D\right) \\ \vdots & \ddots & \vdots \\ G^n_{f_1D,1}\left(x_{f_2D,n_2}, y_{f_2D,n_2}, t^n_D\right) & \cdots & G^n_{f_1D,n_1}\left(x_{f_2D,n_2}, y_{f_2D,n_2}, t^n_D\right) \end{bmatrix} \tag{4A-3}$$

$$\boldsymbol{G}^n_{f_2D,\,f_1} = \begin{bmatrix} G^n_{f_2D,1}\left(x_{f_1D,1}, y_{f_1D,1}, t^n_D\right) & \cdots & G^n_{f_2D,n_2}\left(x_{f_1D,1}, y_{f_1D,1}, t^n_D\right) \\ \vdots & \ddots & \vdots \\ G^n_{f_2D,1}\left(x_{f_1D,n_1}, y_{f_1D,n_1}, t^n_D\right) & \cdots & G^n_{f_2D,n_2}\left(x_{f_1D,n_1}, y_{f_1D,n_1}, t^n_D\right) \end{bmatrix} \tag{4A-4}$$

$$\boldsymbol{G}^n_{f_2D,\,f_2} = \begin{bmatrix} G^n_{f_2D,1}\left(x_{f_2D,1}, y_{f_2D,1}, t^n_D\right) & \cdots & G^n_{f_2D,n_2}\left(x_{f_2D,1}, y_{f_2D,1}, t^n_D\right) \\ \vdots & \ddots & \vdots \\ G^n_{f_2D,1}\left(x_{f_2D,n_2}, y_{f_2D,n_2}, t^n_D\right) & \cdots & G^n_{f_2D,n_2}\left(x_{f_2D,n_2}, y_{f_2D,n_2}, t^n_D\right) \end{bmatrix} \tag{4A-5}$$

$$\boldsymbol{RHS}_1 = \begin{bmatrix} \sum_{I=1}^{I=n_1} \sum_{k=1}^{k=n\text{-}1} q^k_{f_1D,I} G^k_{f_1D,I}\left(x_{f_1D,1}, y_{f_1D,1}, t^n_D\right) \\ \vdots \\ \sum_{I=1}^{I=n_1} \sum_{k=1}^{k=n\text{-}1} q^k_{f_1D,I} G^k_{f_1D,I}\left(x_{f_1D,n_1}, y_{f_1D,n_1}, t^n_D\right) \end{bmatrix} \tag{4A-6}$$

$$\boldsymbol{RHS}_2 = \begin{bmatrix} \sum_{I=1}^{I=n_1} \sum_{k=1}^{k=n\text{-}1} q^k_{f_1D,I} G^k_{f_1D,I}\left(x_{f_1D,1}, y_{f_1D,1}, t^n_D\right) + \sum_{J=1}^{J=n_2} \sum_{k=K}^{k=n-1} q^k_{f_2D,J} G^k_{f_2D,J}\left(x_{f_1D,1}, y_{f_1D,1}, t^n_D\right) \\ \vdots \\ \sum_{I=1}^{I=n_1} \sum_{k=1}^{k=n\text{-}1} q^k_{f_1D,I} G^k_{f_1D,I}\left(x_{f_1D,n_1}, y_{f_1D,n_1}, t^n_D\right) + \sum_{J=1}^{J=n_2} \sum_{k=K}^{k=n-1} q^k_{f_2D,J} G^k_{f_2D,J}\left(x_{f_1D,n_1}, y_{f_1D,n_1}, t^n_D\right) \end{bmatrix} \tag{4A-7}$$

$$\boldsymbol{RHS}_3 = \begin{bmatrix} \sum_{I=1}^{I=n_1} \sum_{k=1}^{k=n-1} q_{f_1D,I}^{k} G_{f_1D,I}^{k}\left(x_{f_2D,1}, y_{f_2D,1}, t_D^n\right) + \sum_{J=1}^{J=n_2} \sum_{k=K}^{k=n-1} q_{f_2D,J}^{k} G_{f_2D,J}^{k}\left(x_{f_2D,1}, y_{f_2D,1}, t_D^n\right) \\ \vdots \\ \sum_{I=1}^{I=n_1} \sum_{k=1}^{k=n-1} q_{f_1D,I}^{k} G_{f_1D,I}^{k}\left(x_{f_2D,n_2}, y_{f_2D,n_2}, t_D^n\right) + \sum_{J=1}^{J=n_2} \sum_{k=K}^{k=n-1} q_{f_2D,J}^{k} G_{f_2D,J}^{k}\left(x_{f_2D,n_2}, y_{f_2D,n_2}, t_D^n\right) \end{bmatrix} \quad (4A\text{-}8)$$

Appendix 4B – Definition of the Matrices Used to Characterize the Fracture Flow.

$$\boldsymbol{A}_{f_1}^{n} = \begin{bmatrix} \boldsymbol{A}_{f_1^1}^{n} & \boldsymbol{0} & \cdots & \cdots & \boldsymbol{0} \\ \boldsymbol{0} & \ddots & \boldsymbol{0} & \ddots & \vdots \\ \vdots & \boldsymbol{0} & \boldsymbol{A}_{f_1^m}^{n} & \boldsymbol{0} & \vdots \\ \vdots & \ddots & \boldsymbol{0} & \ddots & \boldsymbol{0} \\ \boldsymbol{0} & \cdots & \cdots & \boldsymbol{0} & \boldsymbol{A}_{f_1^{N_1}}^{n} \end{bmatrix} \tag{4B-1}$$

and

$$\boldsymbol{A}_{f_1^m}^{n} = \begin{bmatrix} -\left(1-\frac{\Delta l_{fD}^2 w_{fD} C_s}{C_{fD}\Delta t_D^k}\right)_{f_1^m} & 1 & 0 & \cdots & \cdots & \cdots & 0 & 0 \\ 1 & -\left(2-\frac{\Delta l_{fD}^2 w_{fD} C_s}{C_{fD}\Delta t_D^k}\right)_{f_1^m} & 1 & 0 & \ddots & \ddots & \ddots & 0 \\ 0 & 1 & \ddots & 1 & \ddots & \ddots & \ddots & \vdots \\ \vdots & 0 & 1 & \boxed{-\left(1-\frac{\Delta l_{fD}^2 w_{fD} C_s}{C_{fD}\Delta t_D^k}\right)_{f_1^m}} & 0 & \ddots & \ddots & \vdots \\ \vdots & \ddots & 0 & 0 & \boxed{-\left(1-\frac{\Delta l_{fD}^2 w_{fD} C_s}{C_{fD}\Delta t_D^k}\right)_{f_1^m}} & 1 & 0 & \vdots \\ \vdots & \ddots & \ddots & \ddots & 1 & \ddots & 1 & 0 \\ 0 & \ddots & \ddots & \ddots & 0 & 1 & -\left(2-\frac{\Delta l_{fD}^2 w_{fD} C_s}{C_{fD}\Delta t_D^k}\right)_{f_1^m} & 1 \\ 0 & 0 & \cdots & \cdots & \cdots & 0 & 1 & -\left(1-\frac{\Delta l_{fD}^2 w_{fD} C_s}{C_{fD}\Delta t_D^k}\right)_{f_1^m} \end{bmatrix} \tag{4B-2}$$

where the boxes enclosing the coefficients represent that the corresponding fracture segments are connected to the wellbore.

$$\boldsymbol{B}_{f_1} = \begin{bmatrix} \boldsymbol{B}_{f_1^1} & \cdots & \boldsymbol{B}_{f_1^m} & \cdots & \boldsymbol{B}_{f_1^{N_1}} \end{bmatrix}^T \tag{4B-3}$$

and

$$\boldsymbol{B}_{f_1^m} = \begin{bmatrix} \left(-\frac{2\pi\Delta l_{fD}}{C_{fD}}\right)_{f_1^m} & \cdots & \left(-\frac{2\pi\Delta l_{fD}}{C_{fD}}\right)_{f_1^m} \end{bmatrix}_{1\times n_1^m} \tag{4B-4}$$

where the subscribe 'n_1^m' indicates that there are n_1^m fracture segments in the m^{st} initial fracture.

$$\boldsymbol{C}_{f_1}=\begin{bmatrix}\left(-\dfrac{2\pi\Delta l_{fD}}{C_{fD}}\right)_{f_1^1}\boldsymbol{M}_{f_1^1} & \mathbf{0} & \cdots & \cdots & \mathbf{0}\\ \mathbf{0} & \ddots & \mathbf{0} & \ddots & \vdots\\ \vdots & \mathbf{0} & \left(-\dfrac{2\pi\Delta l_{fD}}{C_{fD}}\right)_{f_1^m}\boldsymbol{M}_{f_1^m} & \mathbf{0} & \vdots\\ \vdots & \ddots & \mathbf{0} & \ddots & \mathbf{0}\\ \mathbf{0} & \cdots & \cdots & \mathbf{0} & \left(-\dfrac{2\pi\Delta l_{fD}}{C_{fD}}\right)_{f_1^{N_1}}\boldsymbol{M}_{f_1^{N_1}}\end{bmatrix} \tag{4B-5}$$

where

$$\boldsymbol{M}_{f_1^m}=\begin{bmatrix}0 & 0\\ \vdots & \vdots\\ \boxed{1} & 0\\ 0 & \boxed{1}\\ \vdots & \vdots\\ 0 & 0\end{bmatrix}_{n_1^m\times 2} \tag{4B-6}$$

$$\boldsymbol{D}_{f_1}^n=\begin{bmatrix}\boldsymbol{D}_{f_1^1}^n & \cdots & \boldsymbol{D}_{f_1^m}^n & \cdots & \boldsymbol{D}_{f_1^{N_1}}^n\end{bmatrix}^T \tag{4B-7}$$

and

$$\boldsymbol{D}_{f_1^m}^n=\begin{bmatrix}\left(-\dfrac{\Delta l_{fD}^2 w_{fD} C_s}{C_{fD}\Delta t_D^n}\right)_{f_1^m} & \cdots & \left(-\dfrac{\Delta l_{fD}^2 w_{fD} C_s}{C_{fD}\Delta t_D^n}\right)_{f_1^m}\end{bmatrix}_{1\times n_1^m} \tag{4B-8}$$

$$\boldsymbol{q}_{fw_1D}^n=\begin{bmatrix}\boldsymbol{q}_{fw_1^1D}^n & \cdots & \boldsymbol{q}_{fw_1^mD}^n & \cdots & \boldsymbol{q}_{fw_1^{N_1}D}^n\end{bmatrix}^T \tag{4B-9}$$

$$\boldsymbol{q}_{fw_1^mD}^n=\begin{bmatrix}q_{fw_1^mD^-}^n & q_{fw_1^mD^+}^n\end{bmatrix} \tag{4B-10}$$

The matrices $\boldsymbol{A}_{f_2}$, $\boldsymbol{B}_{f_2}$, $\boldsymbol{C}_{f_2}$, $\boldsymbol{D}_{f_2}$, and $\boldsymbol{q}_{f_2wD}$ have similar definitions with those of $\boldsymbol{A}_{f_1}$, $\boldsymbol{B}_{f_1}$, $\boldsymbol{C}_{f_1}$, $\boldsymbol{D}_{f_1}$, and $\boldsymbol{q}_{f_1wD}$. The only difference is that the properties of the refracture should be used in the matrices that have the subscript of 'f_2'.

Appendix 4C – Definition of the Matrices Used to Characterize the Production Constraints.

$$\boldsymbol{BHP}_{f_1} = \begin{bmatrix} p_{w_1^1 D} & p_{w_1^1 D} & \cdots & p_{w_1^m D} & p_{w_1^m D} & \cdots & p_{w_1^{N_1} D} & p_{w_1^{N_1} D} \end{bmatrix}^T_{1\times 2N_1} \tag{4C-1}$$

$$\boldsymbol{F}_{f_1} = \begin{bmatrix} \left(\frac{\pi\Delta l_{fD}}{C_{fD}}\right)_{f_1^1} \boldsymbol{M}_{f_1^1} & \mathbf{0} & \cdots & \cdots & \mathbf{0} \\ \mathbf{0} & \ddots & \mathbf{0} & \ddots & \vdots \\ \vdots & \mathbf{0} & \left(\frac{\pi\Delta l_{fD}}{C_{fD}}\right)_{f_1^m} \boldsymbol{M}_{f_1^m} & \mathbf{0} & \vdots \\ \vdots & \ddots & \mathbf{0} & \ddots & \mathbf{0} \\ \mathbf{0} & \cdots & \cdots & \mathbf{0} & \left(\frac{\pi\Delta l_{fD}}{C_{fD}}\right)_{f_1^{N_1}} \boldsymbol{M}_{f_1^{N_1}} \end{bmatrix} \tag{4C-2}$$

$$\boldsymbol{H}_{f_1} = \begin{bmatrix} 1 & 1 & 0 & \cdots & \cdots & 0 \\ 0 & 1 & 1 & 0 & \ddots & \vdots \\ \vdots & 0 & \ddots & \ddots & 0 & \vdots \\ \vdots & \ddots & 0 & 1 & 1 & 0 \\ 0 & \cdots & \cdots & 0 & 1 & 1 \end{bmatrix}_{N_1\times 2N_1} \tag{4C-3}$$

$$\boldsymbol{L}_{f_1} = \begin{bmatrix} \left(\frac{\gamma C_{fD}}{\Delta t_D^n}\right)_{f_1^1} & \cdots & \left(\frac{\gamma C_{fD}}{\Delta t_D^n}\right)_{f_1^m} & \cdots & \left(\frac{\gamma C_{fD}}{\Delta t_D^n}\right)_{f_1^{N_1}} \end{bmatrix}^T \tag{4C-4}$$

$$\boldsymbol{M}_{f_1} = \begin{bmatrix} \boldsymbol{M}_{f_1^1} & \mathbf{0} & \cdots & \cdots & \mathbf{0} \\ \mathbf{0} & \ddots & \mathbf{0} & \ddots & \vdots \\ \vdots & \mathbf{0} & \boldsymbol{M}_{f_1^m} & \mathbf{0} & \vdots \\ \vdots & \ddots & \mathbf{0} & \ddots & \mathbf{0} \\ \mathbf{0} & \cdots & \cdots & \mathbf{0} & \boldsymbol{M}_{f_1^{N_1}} \end{bmatrix} \tag{4C-5}$$

where $M_{f_1^m}$ is defined in Equation (4B-6).

$$\boldsymbol{p}^n_{w_1 D} = \begin{bmatrix} \boldsymbol{p}^n_{w_1^1 D} & \cdots & \boldsymbol{p}^n_{w_1^m D} & \cdots & \boldsymbol{p}^n_{w_1^{N_1} D} \end{bmatrix}^T \tag{4C-6}$$

$$\boldsymbol{q}_{w_1 D}^{n} = \left[\boldsymbol{q}_{w_1^1 D}^{n} \quad \cdots \quad \boldsymbol{q}_{w_1^m D}^{n} \quad \cdots \quad \boldsymbol{q}_{w_1^{N_1} D}^{n} \right]^T \tag{4C-7}$$

The matrices $\boldsymbol{BHP}_{f_2}$, $\boldsymbol{F}_{f_2}$, $\boldsymbol{H}_{f_2}$, $\boldsymbol{L}_{f_2}$, $\boldsymbol{p}_{w_2 D,}$ and $\boldsymbol{q}_{w_2 D}$ have similar definitions with those of $\boldsymbol{BHP}_{f_1}$, $\boldsymbol{F}_{f_1}$, $\boldsymbol{H}_{f_1}$, $\boldsymbol{L}_{f_1}$, $\boldsymbol{p}_{w_1 D}$ and $\boldsymbol{q}_{w_1 D}$. The only difference is that the properties of the refracture should be used in the matrices that have the subscript of 'f_2'.

Appendix 4D – Systems of the Linear Equations that Characterize the Transient Flow Behavior of the Refractures.

Before the refracturing treatment, we have:

for the constant BHP condition,

$$\begin{cases} \boldsymbol{p}_{f_1D}^{n} - \boldsymbol{G}_{f_1D,f_1}^{k} \cdot \boldsymbol{q}_{f_1D}^{k} = \boldsymbol{RHS}_1 \\ \boldsymbol{A}_{f_1}^{n} \cdot \boldsymbol{p}_{f_1D}^{n} + \boldsymbol{B}_{f_1} \odot \boldsymbol{q}_{f_1D}^{n} + \boldsymbol{C}_{f_1} \cdot \boldsymbol{q}_{fw_1D}^{n} = \boldsymbol{D}_{f_1}^{n} \odot \boldsymbol{p}_{f_1D}^{n-1} \\ \boldsymbol{M}_{f_1} \cdot \boldsymbol{p}_{f_1D}^{n} + \boldsymbol{F}_{f_1} \cdot \boldsymbol{q}_{fw_1D}^{n} = \boldsymbol{BHP}_{f_1} \\ \boldsymbol{H}_{f_1} \cdot \boldsymbol{q}_{fw_1D}^{n} - \boldsymbol{q}_{w_1D}^{n} = \boldsymbol{0} \end{cases} \tag{4D-1}$$

and for the constant production rate condition,

$$\begin{cases} \boldsymbol{p}_{f_1D}^{n} - \boldsymbol{G}_{f_1D,f_1}^{k} \cdot \boldsymbol{q}_{f_1D}^{k} = \boldsymbol{RHS}_1 \\ \boldsymbol{A}_{f_1}^{n} \cdot \boldsymbol{p}_{f_1D}^{n} + \boldsymbol{B}_{f_1} \odot \boldsymbol{q}_{f_1D}^{n} + \boldsymbol{C}_{f_1} \cdot \boldsymbol{q}_{fw_1D}^{n} = \boldsymbol{D}_{f_1}^{n} \odot \boldsymbol{p}_{f_1D}^{n-1} \\ \boldsymbol{M}_{f_1} \cdot \boldsymbol{p}_{f_1D}^{n} + \boldsymbol{F}_{f_1} \cdot \boldsymbol{q}_{fw_1D}^{n} - \boldsymbol{BHP}_{f_1}^{n} = \boldsymbol{0} \\ \boldsymbol{H}_{f_1} \cdot \boldsymbol{q}_{fw_1D}^{n} + \boldsymbol{L}_{f_1}^{n} \odot \boldsymbol{p}_{w_1D}^{n} = \boldsymbol{q}_{w_1D} + \boldsymbol{L}_{f_1}^{n} \odot \boldsymbol{p}_{w_1D}^{n-1} \end{cases} \tag{4D-2}$$

After the refracturing treatment, we have:

For the constant BHP condition,

$$\begin{cases} \boldsymbol{p}_{f_1D}^{n} - \boldsymbol{G}_{f_1D,f_1}^{k} \cdot \boldsymbol{q}_{f_1D}^{k} - \boldsymbol{G}_{f_2D,f_1}^{k} \cdot \boldsymbol{q}_{f_2D}^{k} = \boldsymbol{RHS}_2 \\ \boldsymbol{p}_{f_2D}^{n} - \boldsymbol{G}_{f_1D,f_2}^{k} \cdot \boldsymbol{q}_{f_1D}^{k} - \boldsymbol{G}_{f_2D,f_2}^{k} \cdot \boldsymbol{q}_{f_2D}^{k} = \boldsymbol{RHS}_3 \\ \boldsymbol{A}_{f_1}^{n} \cdot \boldsymbol{p}_{f_1D}^{n} + \boldsymbol{B}_{f_1} \odot \boldsymbol{q}_{f_1D}^{n} + \boldsymbol{C}_{f_1} \cdot \boldsymbol{q}_{fw_1D}^{n} = \boldsymbol{D}_{f_1}^{n} \odot \boldsymbol{p}_{f_1D}^{n-1} \\ \boldsymbol{A}_{f_2}^{n} \cdot \boldsymbol{p}_{f_2D}^{n} + \boldsymbol{B}_{f_2} \odot \boldsymbol{q}_{f_2D}^{n} + \boldsymbol{C}_{f_2} \cdot \boldsymbol{q}_{fw_2D}^{n} = \boldsymbol{D}_{f_2}^{n} \odot \boldsymbol{p}_{f_2D}^{n-1} \\ \boldsymbol{M}_{f_1} \cdot \boldsymbol{p}_{f_1D}^{n} + \boldsymbol{F}_{f_1} \cdot \boldsymbol{q}_{fw_1D}^{n} = \boldsymbol{BHP}_{f_1} \\ \boldsymbol{M}_{f_2} \cdot \boldsymbol{p}_{f_2D}^{n} + \boldsymbol{F}_{f_2} \cdot \boldsymbol{q}_{fw_2D}^{n} = \boldsymbol{BHP}_{f_2} \\ \boldsymbol{H}_{f_1} \cdot \boldsymbol{q}_{fw_1D}^{n} - \boldsymbol{q}_{w_1D}^{n} = \boldsymbol{0} \\ \boldsymbol{H}_{f_2} \cdot \boldsymbol{q}_{fw_2D}^{n} - \boldsymbol{q}_{w_2D}^{n} = \boldsymbol{0} \end{cases} \tag{4D-3}$$

and for the constant production rate condition,

$$
\begin{cases}
\boldsymbol{p}^{n}_{f_1D} - \boldsymbol{G}^{k}_{f_1D,f_1} \cdot \boldsymbol{q}^{k}_{f_1D} - \boldsymbol{G}^{k}_{f_2D,f_1} \cdot \boldsymbol{q}^{k}_{f_2D} = \boldsymbol{RHS}_2 \\
\boldsymbol{p}^{n}_{f_2D} - \boldsymbol{G}^{k}_{f_1D,f_2} \cdot \boldsymbol{q}^{k}_{f_1D} - \boldsymbol{G}^{k}_{f_2D,f_2} \cdot \boldsymbol{q}^{k}_{f_2D} = \boldsymbol{RHS}_3 \\
\boldsymbol{A}^{n}_{f_1} \cdot \boldsymbol{p}^{n}_{f_1D} + \boldsymbol{B}_{f_1} \odot \boldsymbol{q}^{n}_{f_1D} + \boldsymbol{C}_{f_1} \cdot \boldsymbol{q}^{n}_{fw_1D} = \boldsymbol{D}^{n}_{f_1} \odot \boldsymbol{p}^{n-1}_{f_1D} \\
\boldsymbol{A}^{n}_{f_2} \cdot \boldsymbol{p}^{n}_{f_2D} + \boldsymbol{B}_{f_2} \odot \boldsymbol{q}^{n}_{f_2D} + \boldsymbol{C}_{f_2} \cdot \boldsymbol{q}^{n}_{fw_2D} = \boldsymbol{D}^{n}_{f_2} \odot \boldsymbol{p}^{n-1}_{f_2D} \\
\boldsymbol{M}_{f_1} \cdot \boldsymbol{p}^{n}_{f_1D} + \boldsymbol{F}_{f_1} \cdot \boldsymbol{q}^{n}_{fw_1D} - \boldsymbol{BHP}^{n}_{f_1} = \boldsymbol{0} \\
\boldsymbol{M}_{f_2} \cdot \boldsymbol{p}^{n}_{f_2D} + \boldsymbol{F}_{f_2} \cdot \boldsymbol{q}^{n}_{fw_2D} - \boldsymbol{BHP}^{n}_{f_2} = \boldsymbol{0} \\
\boldsymbol{H}_{f_1} \cdot \boldsymbol{q}^{n}_{fw_1D} + \boldsymbol{L}^{n}_{f_1} \odot \boldsymbol{p}^{n}_{w_1D} = \boldsymbol{q}_{w_1D} + \boldsymbol{L}^{n}_{f_1} \odot \boldsymbol{p}^{n-1}_{w_1D} \\
\boldsymbol{H}_{f_2} \cdot \boldsymbol{q}^{n}_{fw_2D} + \boldsymbol{L}^{n}_{f_2} \odot \boldsymbol{p}^{n}_{w_2D} = \boldsymbol{q}_{w_2D} + \boldsymbol{L}^{n}_{f_2} \odot \boldsymbol{p}^{n-1}_{w_2D}
\end{cases}
\tag{4D-4}
$$

References

[1] Watts, R.J., Yost, A.B., Farrell, H.H., Kennedy, J., Lowry, P. 1988. Devonian Shale Oil Production Analysis and Evaluation. Paper SPE 18552 presented at SPE Eastern Regional Meeting, Charleston, West Virginia, 1-4 November.

[2] Tran, T., Sinurat, P.D., and Wattenbarger, B.A. 2011. Production Characteristics of the Bakken Shale Oil. Paper SPE 145684 presented at SPE Annual Technical Conference and Exhibition, Denver, Colorado, USA, 30 October-2 November.

[3] Tripathi, D., and Pournik, M. 2014. Effect of Acid on Productivity of Fractured Shale Reservoirs. Paper URTEC-1922960 presented at Unconventional Resources Technology Conference, Denver, Colorado, USA, 25-27 August.

[4] Wright, C.A., Conant, R.A., Stewart, D.W., and Byerly, P.M. 1994. Reorientation of Propped Refracture Treatments. Paper SPE 28078 presented at Rock Mechanics in Petroleum Engineering, Delft, Netherlands, 29-31 August.

[5] Siebrits, E., Elbel, J.L., Detournay, E., Detouray-Piette, C., Christianson, M., Robinson, B.M., and Diyashev, I.R. 1998. Parameters Affecting Azimuth and Length of a Secondary Fracture During a Refracture Treatment. Paper SPE 48928 presented at SPE Annual Technical Conference and Exhibition, New Orleans, Louisiana, 27-30 September.

[6] Roussel, N.P., and Sharma, M.M. 2012. Role of Stress Reorientation in the Success of Refracture Treatments in Tight Gas Sands. *SPE Prod. Oper.* 27 (4): 346-355.

[7] Asalkhuzina, G.F., Davletbaev, A.Ya., Fedorov, A.I., Yuldasheva, A.R., Efremov, A.N., Sergeychev, A.V., and Ishkin, D.Z. 2017. Identification of Refracturing Reorientation using Decline-Analysis and Geomechanical Simulator. Paper SPE 187750 presented at SPE Russian Petroleum Technology Conference, Moscow, Russia, 16-18 October.

[8] Xia, K., Mondal. S., Fonseca, E., and Jones, R. 2017. Understanding Stress Reorientation Process in Shale Gas Play and Its Impact on Refracturing Time Window. Paper ARMA-2017-1012 presented at 51st U.S. Rock Mechanics/Geomechanics Symposium, San Francisco, California, USA, 25-28 June.

[9] Wright, C.A., and Conant, R.A. 1995. Hydraulic Fracture Reorientation in Primary and Secondary Recovery from Low-Permeability Reservoirs. Paper SPE 30484 presented at SPE Annual Technical Conference and Exhibition, Dallas, Texas, 22-25 October.

[10] Wolhart, S.L., and Mclntosh, G.E., Zoll, M.B., and Weijers, L. 2007. Surface Tiltmeter Mapping Shows Hydraulic Fracture Reorientation in the Codell Formation, Wattenberg Field, Colorado. Paper SPE 110034 presented at SPE Annual Technical Conference and Exhibition, Anaheim, California, U.S.A., 11-14 November.

[11] Aghighi, M.A., Rahman, S.S., and Rahman, M.M. 2009. Effect of Formation Stress Distribution on Hydraulic Fracture Reorientation in Tight Gas Sands. Paper SPE 122723 presented at Asia Pacific Oil and Gas Conference & Exhibition, Jakarta, Indonesia, 4-6 August.

[12] Benedict, D., and Miskimins, J.L. 2009. The Effects of Hydraulic Fracture Reorientation. Paper SPE 119355 presented at SPE Hydraulic Fracturing Technology Conference, The Woodlands, Texas, 19-21 January.

[13] Xu, Y., Yu, W., and Sepehrnoori, K. 2017. Modeling Dynamic Behaviors of Complex Fractures in Conventional Reservoir Simulators. Paper URTEC-2670513 presented at SPE/AAPG/SEG Unconventional Resources Technology Conference, Austin, Texas, USA, 24-26 July.

[14] Warpinski, N.R., and Branagan, P.T. 1989. Altered-Stress Fracturing. *J. Pet. Tech.* 41 (9): 990-997.

[15] Elbel, J.L., and Mack, M.G. 1993. Refracturing: Observations and Theories. Paper SPE 25464 presented at SPE Production Operations Symposium, Oklahoma City, Oklahoma, 21-23 March.

[16] Palmer, I.D. 1993. Induced Stresses Due to Propped Hydraulic Fracture in Coalbed Methane Wells. Paper SPE 25861 presented at Low Permeability Reservoirs Symposium, Denver, Colorado, 26-28 April.

[17] Wright, C.A., Stewart, D.W., Emanuele, M.A., and Wright, W.W. 1994. Reorientation of Propped Refracture Treatments in the Lost Hills Field. Paper SPE 27896 presented at SPE Western Regional Meeting, Long Beach, California, 23-25 March.

[18] Cinco-Ley, H., Samaniego-V., F., and Dominguez-A., N. 1978. Transient Pressure Behavior for a Well with a Finite-Conductivity Vertical Fracture. *SPE J.* 18 (04): 253-264.

[19] Valko, P., and Economides, M.J. 1997. Transient Behavior of Finite Conductivity Horizontal Fractures. *SPE J.* 2 (02): 213-222.

[20] Zhou, W., Banerjee, R., Poe, B.D., and Spath, J. 2014. Semianalytical Production Simulation of Complex Hydraulic-Fracture-Networks. *SPE J.* 19 (01): 6-18.

[21] Yang, D., Zhang, F., Styles, J.A., and Gao, J. 2015. Performance Evaluation of a Horizontal Well With Multiple Fractures by Use of a Slab-Source Function. *SPE J.* 20 (03): 652-662.

[22] Luo, W., and Tang, C. 2015. Pressure-Transient Analysis of Multiwing Fractures Connected to a Vertical Wellbore. *SPE J.* 20 (02): 360-367.

[23] Spivey, J.P., and Lee, W.J. 1998. New Solutions for Pressure Transient Response for a Horizontal or a Hydraulically Fractured Well at an Arbitrary Orientation in an Anisotropic Reservoir. Paper SPE 49236 presented at SPE Annual Technical Conference and Exhibition, New Orleans, Louisiana, 27-30 September.

[24] Gringarten, A.C., and Ramey, H.J. 1973. The Use of Source and Green's Functions in Solving Unsteady-Flow Problems in Reservoirs. *SPE J.* 13 (05): 285-296.

[25] van Everdingen, A.F., and Hurst, W. 1949. The Application of the Laplace Transformation to Flow Problems in Reservoirs. *Trans. AIME* 1 (12): 305-324.

[26] Siebrits, E., Elbel, J.L., Hoover, R.S., Diyashev, I.R., Griffin, L.G., Demntrius, S.L., Wright, C.A., Davidson, B.M., Steinsberger, N.P., and Hill, D.G. 2000. Refracture Reorientation Enhances Gas Production in Barnett Shale Tight Gas Wells. Paper SPE 63030 presented at SPE Annual Technical Conference and Exhibition, Dallas, Texas, 1-4 October.

[27] Yu, W., Wu, K., and Sepehrnoori, K. 2016. A Semianalytical Model for Production Simulation from Nonplanar Hydraulic-Fracture Geometry in Tight Oil Reservoirs. *SPE J.* 21 (03): 1028-1040.

CHAPTER 5 A SEMI-ANALYTICAL MODEL FOR EVALUATING THE PERFORMANCE OF A REFRACTURED VERTICAL WELL WITH AN ORTHOGONAL REFRACTURE

A version of this chapter has been published in *SPE Journal.*

Summary

The production from a fractured vertical well will lead to a redistribution of the stress field in the formations. If the induced stress changes are sufficiently large to overcome the effect of the initial horizontal stress deviator, the direction of the minimum horizontal stress can be turned into the direction of the maximum horizontal stress within an elliptical region around the initial fracture, resulting in a stress reversal region near the wellbore. In such cases, a refracturing treatment can create a refracture that propagates orthogonally to the initial fracture due to the stress reversal. As such, the high-pressure area of the formation can be stimulated by the refracture and the productivity of the refractured well can be improved. In this work, we develop a semi-analytical model to evaluate the performance of a refractured vertical well with an orthogonal refracture. In order to simulate the well performance throughout the entire production period, we divide the well production into three stages: the first stage - the well is producing oil with the initial fracture; the second stage - the well is shut down for the refracturing treatment; and the third stage - the well is producing oil with both the initial fracture and the refracture. In addition, by discretizing the initial fracture and the refracture into small segments, the conductivity of the fractures can be taken into account and the geometry of the fracture system can be captured. We use the Green's function method to analytically simulate the reservoir flow while use the finite difference method to numerically simulate the fracture flow; therefore, a semi-analytical model can be constructed by coupling the reservoir flow equations with the fracture flow equations. This proposed model is applied to different wellbore and reservoir conditions. The calculated results show that this proposed model is versatile as it can simulate various wellbore constraints, including the conditions of constant bottomhole pressure, varying bottomhole pressure, constant production rate, and varying production rate. The permeability

anisotropy of the reservoir system, as well as the non-uniform conductivity distribution along the fracture, can also be incorporated into this proposed model. In addition, we demonstrate that this proposed model can be used to simulate other types of refractured vertical well with minor modifications.

5.1. Introduction

The refracturing treatment has been widely used to repair or replace an inadequate initial fracturing treatment (Branch and Drennan, 1991; Lantz *et al*., 2007; Benedict and Miskimins, 2009; Potapenko *et al*., 2009; Ruhle, 2016). The existence of stress reorientation due to the production from a good initial fracture provides another motivation for the refracturing treatment (Wright *et al*., 1994; Siebrits *et al*., 1998; Aghighi *et al*., 2009; Roussel and Sharma, 2010; Zhao *et al*., 2016). Numerical simulations show that, during the production of a fractured vertical well, the stress parallel to the initial fracture will undergo a much faster reduction than that orthogonal to the initial fracture. If the stress changes due to the depletion of the formation pressure can overcome the effect of the initial horizontal stress deviator, the direction of the local minimum horizontal stress will become the direction of the far-field maximum horizontal stress within an elliptical area around the initial fracture. As such, a stress reversal region can be observed in the vicinity of the wellbore (Siebrits *et al*., 2000; Weng and Siebrits, 2007; Wolhart *et al*., 2007; Jiang *et al*., 2016; Gala and Sharma, 2017).

As generally acknowledged, the hydraulic fractures are always perpendicular to the least principal stress (Hubbert and Willis, 1957; Daneshy, 1978; Medlin and Masse, 1984), a refracturing treatment on a fractured well with stress reversal region will result in an orthogonal refracture to the initial fracture. **Figure 5-1a** presents the propagation of a refracture as a function of time, which is interpreted from the field tiltmeter data (Siebrits *et al*., 2000). As one can see,

although this refracture initially orientates along a direction that has a small angle with respect to the initial fracture, it immediately turns towards a direction that is near-orthogonal to the initial fracture. Figure 5-1b exhibits another orthogonal refracture system monitored in Daqing oilfield, China (Liu *et al*., 2008). This orthogonal refracture changes the propagation direction after it reaches a certain position distant from the initial fracture. These two real field cases provide a partial validation of the concept of the orthogonal refracture. **Figure 5-2** illustrates a schematic of a sufficiently large orthogonal refracture with a stress reversal region near the wellbore, where σ_{hmax} is the maximum horizontal stress and σ_{hmin} is the minimum horizontal stress. As is shown in this figure, this refracture propagates orthogonally to the initial fracture until it reaches the isotropic points where the horizontal stresses are equal along different directions. Beyond the isotropic points, the maximum horizontal stress switches back to its original direction, causing the refracture to gradually turn towards the initial fracture orientation (Siebrits *et al*., 1998; Weng and Siebrits, 2007; Roussel and Sharma, 2012). In practice, if the fracture growth is dominantly impacted by toughness, the tendency to curve can be reduced by increasing the fracture toughness. If the fracture toughness is sufficiently large, the orthogonal section of the refracture can be extended to a certain position beyond the isotropic point. As depicted in Figure 5-2, the orthogonal section of the refracture penetrates beyond the stress reversal region (Siebrits *et al*., 1998; Siebrits *et al*., 2000). Overall, an orthogonal refracture is composed of three sections, namely, the orthogonal section (solid red line), the transition section (dash yellow line), and the parallel section (solid green line). It is noted that the transition section and the parallel section can be absent in the real field cases if the stress reversal region is sufficiently large or the refracture has a poor growth, as presented in Figure 5-1a.

The orthogonal refracture can propagate a distance from the initial fracture and penetrate into the high-pressure region in the formations. This is the scenario of the most successful refracturing treatments, especially in the formations with a favorable permeability anisotropy. Since the orthogonal refracture can significantly improve field productivity without requiring new wells, it is economically worthwhile for the industry to take advantage of the stress reversal region to induce an orthogonal refracture. Warpinski and Branagan (1989) introduced the concept of altered-stress fracturing and claimed that a refracture could exhibit a certain azimuth with respect to the initial fracture because of the stress reorientation in the formations. On the basis of the results from numerical simulations, Elbel and Mack (1993) demonstrated that an orthogonal refracture can be created due to the stress reversal near the wellbore. They also suggested that the optimum refracturing time should be taken into account to maximize the orthogonal section of the refracture. Roussel (2013) proposed guidelines for selecting the candidate wells that have potential to induce orthogonal refractures by analyzing production data. Further knowledge about the orthogonal refractures can also be found in Siebrits *et al*. (1998), Weng and Siebrits (2007), and Roussel and Sharma (2010). Even though great efforts have been invested to study the mechanisms of inducing an optimal orthogonal refracture, there still lacks a corresponding model to evaluate the production performance of such a refractured well.

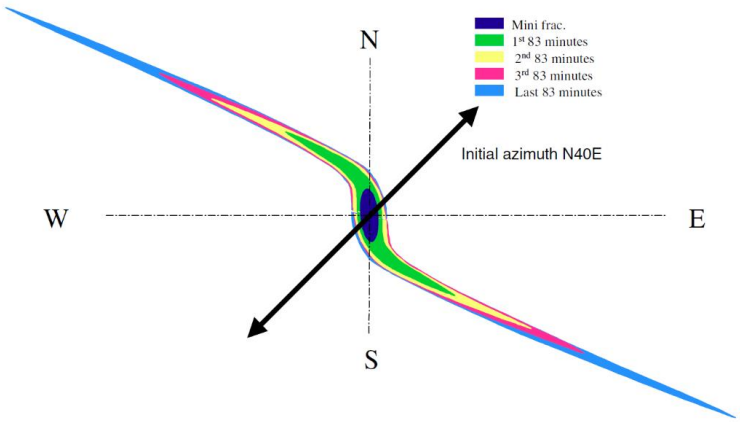

(a)

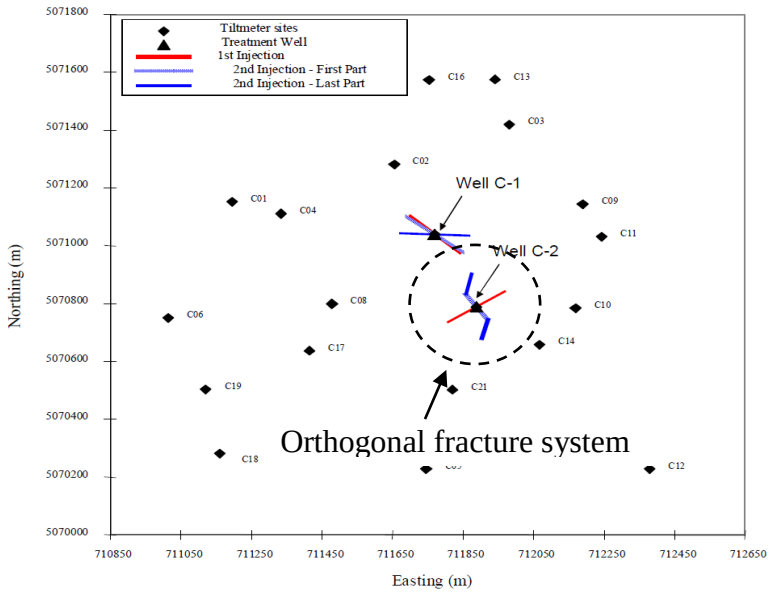

(b)

Figure 5-1. Field examples where an orthogonal refracture is observed: (a) the schematic indicates the propagation of an orthogonal refracture as a function of time, and the black arrow indicates the azimuth of the initial fracture (Siebrits *et al*., 2000); and (b) an orthogonal refracture system monitored in Daqing field (Adapted from Liu *et al*., 2008).

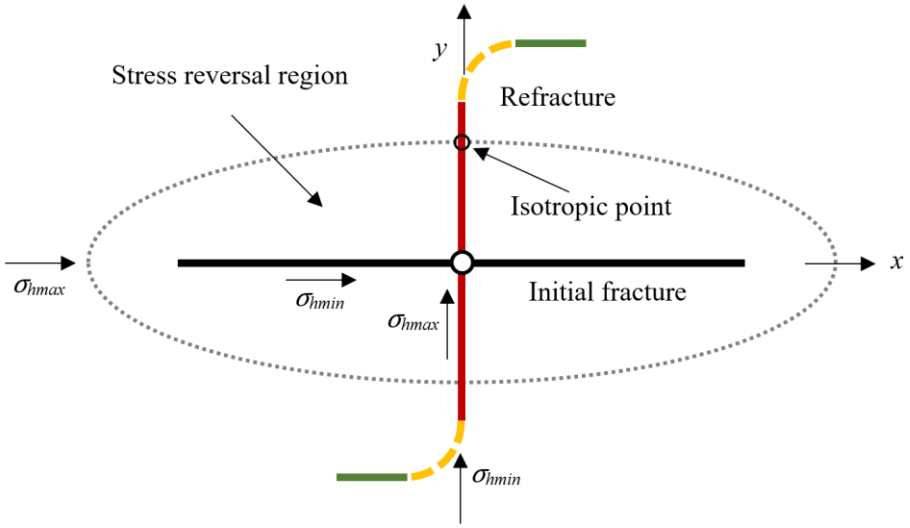

Figure 5-2. Schematic of an orthogonal refracture induced by a stress reversal region (adapted from Siebrits *et al*., 1998).

Numerical simulation is a useful and powerful tool to characterize the transient flow behavior of fractured wells. When one relies on numerical simulations to conduct history matching work or optimize the refracturing treatment, a few hundreds or even thousands of simulations need to be

run. The heavy load of setting up the numerical models and the low computational efficiency make the numerical simulation approach less attractive in this case (Zhou *et al.*, 2014; Yang *et al*., 2015). In recent years, semi-analytical approaches have been extensively used to evaluate the performance of complex fractures. Zhou *et al.* (2014) simulated the production from a complex fracture network on the basis of a plane source function. Luo and Tang (2015) studied the pressure transient behavior of multi-wing fractures connected to a vertical well. Chen *et al.* (2016) investigated the pressure response of a multistage fractured horizontal well that connects with secondary-fracture networks. Yu and Wu (2016) proposed a semi-analytical model to predict the production from nonplanar hydraulic fractures. Although the existing semi-analytical models can be used to model various complex fracture systems, the refracture, which is created after the initial fracture is being put into production, cannot be accommodated by these models. Currently, there are still no semi-analytical models available for characterizing the transient flow behavior of a refractured well.

In this work, we develop a semi-analytical model that can be used to characterize the transient flow behavior of a refractured well with an orthogonal refracture. This proposed model is applied to different wellbore and reservoir conditions. We also show that, in addition to the orthogonal refracture, this proposed model can be extended to model other refracture patterns with minor modifications. Furthermore, in order to briefly introduce how to apply the proposed model to a real field case, we fit the production data of an orthogonally refractured well by using such a proposed model.

5.2. Methodology

This study considers a refractured well with an orthogonal refracture in a box-shaped reservoir. The entire production period, including the first stage (the well is producing oil with the initial

fracture), the second stage (the well is shut down for the refracturing treatment), and the third stage (the well is producing oil with both the initial fracture and the refracture), is simulated in this model. We assume that the fracture system is located at the center of the formation and is symmetrical with respect to the wellbore; thus, a half of the fracture system is sufficient to represent the entire fracture system. **Figure 5-3** shows the schematic of a half fracture system with both the initial fracture and the orthogonal refracture. In this figure, L_{f1} represents the length of the unilateral initial fracture. The real propagation of a refracture in the transition section can be monitored by tiltmeter technique. In this work, we assume that the transition section of the refracture can be approximated with a quarter ellipse for simplicity. This ellipse has a semi-axis of a along y-axis and a semi-axis of b along x-axis. In addition, the length of the orthogonal section of the refracture is represented by L_{f2o}, and the length of the parallel section of the refracture is represented by L_{f2p}. As such, the structure of the refracture can be characterized by L_{f2o}, a, b, and L_{f2p}. We discretize the unilateral initial fracture into n_1 segments and the unilateral refracture into n_2 segments. In order to construct a semi-analytical model to characterize the transient flow from such a refractured well, we make the following assumptions:

- the reservoir is box-shaped and sealed by impermeable boundaries with a length of X_e along the x-axis and a width of Y_e along the y-axis;
- both the initial fracture and the refracture are fully penetrating the reservoir in the vertical direction;
- the reservoir is homogeneous with a constant thickness, porosity, permeability, and initial reservoir pressure;
- the well is producing single-phase oil with constant viscosity and compressibility.
- influence of the fracturing treatment on the reservoir pressure is neglected;

- oil enters the wellbore only through the fractures; and
- effect of gravity is negligible.

Since the anisotropy of the reservoir permeability is considered in the proposed model, we first convert the anisotropic permeability system into an equivalent isotropic permeability system based on the method introduced by Spivey and Lee (1998). **Table 5-1** lists the parameters in the anisotropic permeability system and their counterparts in the equivalent isotropic permeability system. In this table, k_{mx} and k_{my} represent the reservoir permeability along x and y directions in the anisotropic system; k_m represents the reservoir permeability in the equivalent isotropic system; X, Y, and Z represent the coordinates in the anisotropic system; x, y, and z represent the coordinates in the equivalent isotropic system; L_f, W_f, and K_f are fracture length, fracture width and fracture permeability in the anisotropic system, respectively; and l_f, w_f, and k_f are their counterparts in the isotropic system.

Table 5-1. Conversion from an anisotropic permeability system to an equivalent isotropic permeability system.

Anisotropic system	Equivalent isotropic system
k_{mx}, k_{my}	$k_m = \sqrt{k_{mx} k_{my}}$
X	$x = \sqrt{\frac{k_m}{k_{mx}}} X$
Y	$y = \sqrt{\frac{k_m}{k_{my}}} Y$
Z	$z = Z$
L_f	$l_f = L_f \sqrt{\frac{k_m}{k_{mx}} \cos^2\theta + \frac{k_m}{k_{my}} \sin^2\theta}$

$$\theta_1 = \arctan\left(\sqrt{\frac{k_{mx}}{k_{my}}}\tan\theta\right)$$

W_f

$$\theta_2 = \arctan\left(\sqrt{\frac{k_{my}}{k_{mx}}}\tan\theta\right)$$

$$w_f = W_f\sqrt{\frac{k_m}{k_{mx}}\sin^2\theta + \frac{k_m}{k_{my}}\cos^2\theta}\cos(\theta_2 - \theta_1)$$

K_f

$$k_f = K_f\frac{W_f l_f}{w_f L_f}$$

θ is fracture azimuth corresponding to *x-axis*

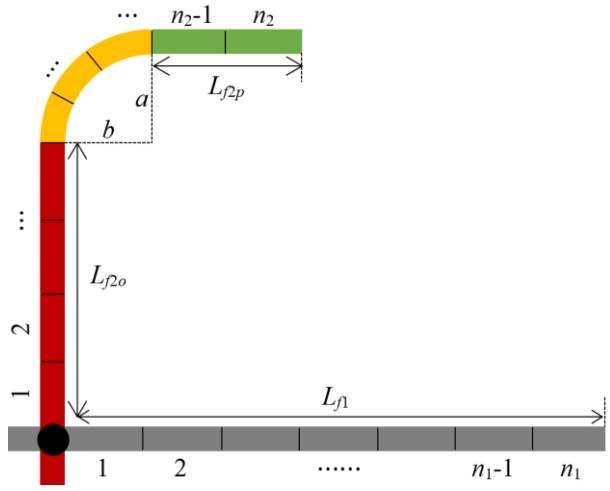

Figure 5-3. Discretization of the unilateral initial fracture and the unilateral refracture.

5.2.1 Transient Flow in the Fracture System

The fracture width is far smaller than the fracture length such that the transient flow in the fracture system can be simplified as a 1D flow. The 1D flow equation, considering the source term, is given as

$$\frac{\partial}{\partial l}\left(w_f\eta_f\frac{\partial p_f}{\partial l}\right) + \frac{q_f B}{h\phi_f c_{tf}} = w_f\frac{\partial p_f}{\partial t}, \tag{5-1}$$

where η_f is diffusivity coefficient defined as $\eta_f = \beta k_f / \mu \phi_f c_{tf}$, β is unit conversion factor whose numerical value is 0.0853, μ is oil viscosity, ϕ_f is effective porosity in the fracture system, c_{tf} is total compressibility of fracture system, p_f is fracture pressure, l is the position along the direction of the fracture propagation, q_f is flux per unit length (m^2/d) from the reservoir to the fracture, B is formation volume factor, h is formation thickness, and t is time. Substituting the properties of the initial fracture and the refracture into Equation (5-1) yields

$$\frac{\partial}{\partial l_{f1}}\left(w_{f1}\eta_{f1}\frac{\partial p_{f1}}{\partial l_{f1}} \right) + \frac{q_{f1}B}{h\phi_{f1}c_{tf1}} = w_{f1}\frac{\partial p_{f1}}{\partial t} \tag{5-2}$$

and

$$\frac{\partial}{\partial l_{f2}}\left(w_{f2}\eta_{f2}\frac{\partial p_{f2}}{\partial l_{f2}} \right) + \frac{q_{f2}B}{h\phi_{f2}c_{tf2}} = w_{f2}\frac{\partial p_{f2}}{\partial t}, \tag{5-3}$$

where the subscripts '*f*1' and '*f*2' represent the initial fracture and the refracture, respectively. The production of the fractured well is divided into three stages and the inner boundary conditions of the initial fracture are

$$\begin{cases} p_{f1}\big|_{l_{f1}=0} = p_w & (0 < t \le T_1) \\ q_w = 0 & (T_1 < t \le T_2), \\ p_{f1}\big|_{l_{f1}=0} = p_w & (t > T_2) \end{cases} \tag{5-4}$$

where $l_{f1} = 0$ indicates the position of the wellbore, p_w is the bottomhole pressure, T_1 is the end of the first production stage, q_w is well production rate, and T_2 is the end of the second production stage. The refracture is created during the second stage and starts producing oil at the start of the third stage; hence, the inner boundary condition of the refracture can be written as

$$p_{f2}\big|_{l_{f2}=0} = p_w \quad (t > T_2). \tag{5-5}$$

Applying the finite difference approximation to Equations (5-2) and (5-3) gives

$$\frac{\partial}{\partial l_{f1}}\left(w_{f1}\eta_{f1}\frac{\partial p_{f1}}{\partial l_{f1}}\right)\approx\frac{1}{\Delta l_{f1,i}}\left[\left(w_{f1}\eta_{f1}\frac{\partial p^k_{f1,i}}{\partial l_1}\right)_{i+1/2}-\left(w_{f1}\eta_{f1}\frac{\partial p^k_{f1,i}}{\partial l_1}\right)_{i-1/2}\right]$$
$$\approx\frac{1}{\Delta l_{f1,i}}\left[\left(\frac{w_{f1}\eta_{f1}}{\Delta l_{f1}}\right)_{i+1/2}\left(p^k_{f1,i+1}-p^k_{f1,i}\right)-\left(\frac{w_{f1}\eta_{f1}}{\Delta l_{f1}}\right)_{i-1/2}\left(p^k_{f1,i+1}-p^k_{f1,i}\right)\right] \tag{5-6}$$

and

$$\left(\frac{B}{h\phi_{f2}c_{tf2}}\right)_j q^k_{f2,j}-\left[\left(\frac{w_{f2}\eta_{f2}}{\Delta l_{f2}}\right)_{j-1/2}+\left(\frac{w_{f2}\eta_{f2}}{\Delta l_{f2}}\right)_{j+1/2}-\frac{\Delta l_{f2,j}w_{f2,j}}{\Delta t^k}\right]p^k_{f2,j}$$
$$+\left(\frac{w_{f2}\eta_{f2}}{\Delta l_{f2}}\right)_{j+1/2}p^k_{f2,j+1}+\left(\frac{w_{f2}\eta_{f2}}{\Delta l_{f2}}\right)_{j-1/2}p^k_{f2,j-1}=-\frac{\Delta l_{f2,j}w_{f2,j}}{\Delta t^k}p^{k-1}_{f2,j} \tag{5-7}$$

where $i = 1, 2\ldots n_1$, $j = 1, 2\ldots n_2$, and $k = 1, 2\ldots n$. It is noteworthy that Equation (5-7), which characterizes the transient flow in the refracture, should not be used if the production time t^k is smaller than T_2. The transient flow equations for the fracture segments can be arranged into a matrix format. Combining these flow equations with the boundary conditions, we can obtain the following systems of equations that characterize the transient flow in the fracture system throughout the entire production period:

for the first stage (i.e., $0 < t^k \le T_1$),

$$\begin{cases}\boldsymbol{c}^k_{f1}\boldsymbol{p}^k_{f1}+\boldsymbol{c}^k_{f1\_q}\boldsymbol{q}^k_{f1}=\boldsymbol{c}^k_{f1\_t}\boldsymbol{p}^{k\text{-}1}_{f1}\\ \dfrac{2k_{f1,1}}{B\mu}w_{f1,1}h\dfrac{p^k_{f1,1}-p^k_w}{\Delta l_{f1,1}}=q^k_{wf1}\\ q^k_w=2q^k_{wf1}\end{cases} \tag{5-8}$$

for the second stage (i.e., $T_1 < t^k \le T_2$),

$$\begin{cases}\boldsymbol{c}^k_{f1}\boldsymbol{p}^k_{f1}+\boldsymbol{c}^k_{f1\_q}\boldsymbol{q}^k_{f1}=\boldsymbol{c}^k_{f1\_t}\boldsymbol{p}^{k\text{-}1}_{f1}\\ p^k_{f1,1}=p^k_w\end{cases} \tag{5-9}$$

and for the third stage (i.e., $t^k > T_2$),

$$\begin{cases} \boldsymbol{c}_{f1}^k \boldsymbol{p}_{f1}^k + \boldsymbol{c}_{f1\_q}^k \boldsymbol{q}_{f1}^k = \boldsymbol{c}_{f1\_t}^k \boldsymbol{p}_{f1}^{k-1} \\ \boldsymbol{c}_{f2}^k \boldsymbol{p}_{f2}^k + \boldsymbol{c}_{f2\_q}^k \boldsymbol{q}_{f2}^k = \boldsymbol{c}_{f2\_t}^k \boldsymbol{p}_{f2}^{k-1} \\ \dfrac{2k_{f1,1}}{B\mu} w_{f1,1} h \dfrac{p_{f1,1}^k - p_w^k}{\Delta l_{f1,1}} = q_{wf1}^k \\ \dfrac{2k_{f2,1}}{B\mu} w_{f2,1} h \dfrac{p_{f2,1}^k - p_w^k}{\Delta l_{f2,1}} = q_{wf2}^k \\ q_w^k = 2q_{wf1}^k + 2q_{wf2}^k \end{cases}, \tag{5-10}$$

where q_{wf1} is flow rate from a unilateral initial fracture to the wellbore, and q_{wf2} is flow rate from a unilateral refracture to the wellbore. The definitions of the matrices $\boldsymbol{c}_{f2}^k$, $\boldsymbol{p}_{f2}^k$, $\boldsymbol{c}_{f2\_q}^k$, $\boldsymbol{q}_{f2}^k$, $\boldsymbol{c}_{f2\_t}^k$, $\boldsymbol{c}_{f1}^k$, $\boldsymbol{p}_{f1}^k$, $\boldsymbol{c}_{f1\_q}^k$, $\boldsymbol{q}_{f1}^k$, and $\boldsymbol{c}_{f1\_t}^k$, and the detailed derivations of the equations presented in Equations (5-8), (5-9) and (5-10) can be found in **Appendix 5A**.

5.2.2 Transient Flow in the Reservoir System

The fracture system is discretized into small segments and each of these fracture segments can be regarded as a plane source. Assuming that the flux rate from the reservoir to a fracture segment during a single timestep can be approximated with an average value q_f, the pressure change at position (x, y) and time t caused by a single fracture segment can be written as

$$\begin{aligned} \Delta p(x,y,t) = q_f \int_{\tau_1}^{\tau_2} \int_0^{\Delta l_f} & \frac{B}{\phi_m c_{tm} \Delta l_f x_e y_e h} \\ & \left\{1 + 2\sum_{m=1}^{\infty} \exp\left[-\frac{m^2\pi^2\eta_m(t-\tau)}{x_e^2}\right] \cos\frac{m\pi x_f}{x_e} \cos\frac{m\pi x}{x_e}\right\} \\ & \left\{1 + 2\sum_{m=1}^{\infty} \exp\left[-\frac{m^2\pi^2\eta_m(t-\tau)}{y_e^2}\right] \cos\frac{m\pi y_f}{y_e} \cos\frac{m\pi y}{y_e}\right\} \mathrm{d}l\mathrm{d}\tau \end{aligned}, \tag{5-11}$$

where Δp is pressure change caused by a fracture segment, (τ_1, τ_2) represents that the flux is continued from τ_1 to τ_2, Δl_f is length of this fracture segment, (x_f, y_f) represents the center position of this fracture segment, ϕ_m is reservoir porosity, c_{tm} is total compressibility of the reservoir, x_e

and y_e represent the reservoir dimensions, and η_m is diffusivity coefficient of the reservoir system which is defined as $\eta_m = \beta k_m / \mu \phi_m c_{tm}$. The detailed derivation of Equation (5-11) can be found in Appendix 5B. On the basis of Equation (5-11), we can calculate the pressure change at the center position of the fracture segments:

for the first stage and the second stage (i.e., $0 < t^k \le T_2$),

$$\Delta p_{f1,I}^k \left(x_{f1,I}, y_{f1,I}, t^k \right) = \sum_{i=1}^{i=n_1} \sum_{s=1}^{s=k} q_{f1,i}^s \left(G_{i,I}^{s,k} + G_{-i,I}^{s,k} \right) \tag{5-12}$$

and for the third stage (i.e., $t^k > T_2$),

$$\begin{aligned} \Delta p_{f1,I}^k \left(x_{f1,I}, y_{f1,I}, t^k \right) &= \sum_{i=1}^{i=n_1} \sum_{s=1}^{s=k} q_{f1,i}^s \left(G_{i,I}^{s,k} + G_{-i,I}^{s,k} \right) + \sum_{j=1}^{j=n_2} \sum_{s=K+1}^{s=k} q_{f2,j}^s \left(G_{j,I}^{s,k} + G_{-j,I}^{s,k} \right) \\ \Delta p_{f2,J}^k \left(x_{f2,J}, y_{f2,J}, t^k \right) &= \sum_{i=1}^{i=n_1} \sum_{s=1}^{s=k} q_{f1,i}^s \left(G_{i,J}^{s,k} + G_{-i,J}^{s,k} \right) + \sum_{j=1}^{j=n_2} \sum_{s=K+1}^{s=k} q_{f2,j}^s \left(G_{j,J}^{s,k} + G_{-j,J}^{s,k} \right) \end{aligned}, \tag{5-13}$$

where $I = 1, 2 \ldots n_1$, $J = 1, 2 \ldots n_2$, Δp^k represents pressure change at time t^k of the initial fracture 'f1' or the refracture 'f2', the subscript 'I' (or 'J') of the Δp term indicates that the pressure change occurs at the central position of the I^{th} segment of the initial fracture (or the J^{th} segment of the refracture). The G term represents the integral term of Equation (5-11) and is defined in detail in Appendix 5B. With the aid of Equations (5-12) and (5-13), we can build the relationship between the flux and the pressure of these fracture segments:

for the first stage and the second stage (i.e., $0 < t^k \le T_2$),

$$\boldsymbol{p}_{f1}^k + \boldsymbol{G}_{f1,f1}^k \boldsymbol{q}_{f1}^k = \boldsymbol{p}_{f1}^{k-1} - \boldsymbol{A}_{f1,f1} \tag{5-14}$$

and for the third stage (i.e., $t^k > T_2$),

$$\begin{cases} \boldsymbol{p}_{f1}^k + \boldsymbol{G}_{f1,f1}^k \boldsymbol{q}_{f1}^k + \boldsymbol{G}_{f1,f2}^k \boldsymbol{q}_{f2}^k = \boldsymbol{p}_{f1}^{k-1} - \boldsymbol{A}_{f1,f1} - \boldsymbol{A}_{f1,f2} \\ \boldsymbol{p}_{f2}^k + \boldsymbol{G}_{f2,f1}^k \boldsymbol{q}_{f1}^k + \boldsymbol{G}_{f2,f2}^k \boldsymbol{q}_{f2}^k = \boldsymbol{p}_{f2}^{k-1} - \boldsymbol{A}_{f2,f1} - \boldsymbol{A}_{f2,f2} \end{cases}, \tag{5-15}$$

where the matrices of $\boldsymbol{G}$ and $\boldsymbol{A}$ are defined in Appendix 5B.

5.2.3 Solution Methodology

Based on the continuity of the flux and pressure, we can couple the transient flow equations of the fracture system with those of the reservoir system. As such, we can construct the following semi-analytical model to characterize the transient flow behavior of a refractured well throughout the entire production period:

for the first stage (i.e., $0 < t^k \le T_1$),

$$\begin{cases} \boldsymbol{c}_{f1}^k \boldsymbol{p}_{f1}^k + \boldsymbol{c}_{f1\_q}^k \boldsymbol{q}_{f1}^k = \boldsymbol{c}_{f1\_t}^k \boldsymbol{p}_{f1}^{k\text{-}1} \\ \boldsymbol{p}_{f1}^k + \boldsymbol{G}_{f1,f1}^k \boldsymbol{q}_{f1}^k = \boldsymbol{p}_{f1}^{k\text{-}1} - \boldsymbol{A}_{f1,f1} \\ \dfrac{2k_{f1,1}}{B\mu} w_{f1,1} h \dfrac{p_{f1,1}^k - p_w^k}{\Delta l_{f1,1}} = q_{wf1}^k \\ q_w^k = 2q_{wf1}^k \end{cases} \tag{5-16}$$

for the second stage (i.e., $T_1 < t^k \le T_2$),

$$\begin{cases} \boldsymbol{c}_{f1}^k \boldsymbol{p}_{f1}^k + \boldsymbol{c}_{f1\_q}^k \boldsymbol{q}_{f1}^k = \boldsymbol{c}_{f1\_t}^k \boldsymbol{p}_{f1}^{k\text{-}1} \\ \boldsymbol{p}_{f1}^k + \boldsymbol{G}_{f1,f1}^k \boldsymbol{q}_{f1}^k = \boldsymbol{p}_{f1}^{k\text{-}1} - \boldsymbol{A}_{f1,f1} \\ p_{f1,1}^k = p_w^k \end{cases} \tag{5-17}$$

and for the third stage (i.e., $t^k > T_2$),

$$\begin{cases} \boldsymbol{c}_{f1}^k \boldsymbol{p}_{f1}^k + \boldsymbol{c}_{f1\_q}^k \boldsymbol{q}_{f1}^k = \boldsymbol{c}_{f1\_t}^k \boldsymbol{p}_{f1}^{k\text{-}1} \\ \boldsymbol{c}_{f2}^k \boldsymbol{p}_{f2}^k + \boldsymbol{c}_{f2\_q}^k \boldsymbol{q}_{f2}^k = \boldsymbol{c}_{f2\_t}^k \boldsymbol{p}_{f2}^{k\text{-}1} \\ \boldsymbol{p}_{f1}^k + \boldsymbol{G}_{f1,f1}^k \boldsymbol{q}_{f1}^k + \boldsymbol{G}_{f1,f2}^k \boldsymbol{q}_{f2}^k = \boldsymbol{p}_{f1}^{k\text{-}1} - \boldsymbol{A}_{f1,f1} - \boldsymbol{A}_{f1,f2} \\ \boldsymbol{p}_{f2}^k + \boldsymbol{G}_{f2,f1}^k \boldsymbol{q}_{f1}^k + \boldsymbol{G}_{f2,f2}^k \boldsymbol{q}_{f2}^k = \boldsymbol{p}_{f2}^{k\text{-}1} - \boldsymbol{A}_{f2,f1} - \boldsymbol{A}_{f2,f2} \\ \dfrac{2k_{f1,1}}{B\mu} w_{f1,1} h \dfrac{p_{f1,1}^k - p_w^k}{\Delta l_{f1,1}} = q_{wf1}^k \\ \dfrac{2k_{f2,1}}{B\mu} w_{f2,1} h \dfrac{p_{f2,1}^k - p_w^k}{\Delta l_{f2,1}} = q_{wf2}^k \\ q_w^k = 2q_{wf1}^k + 2q_{wf2}^k \end{cases} . \tag{5-18}$$

These above systems of equations are closed and can be solved using Gaussian elimination method. It should be noted that this proposed model can be readily used to simulate different wellbore conditions, including constant bottomhole pressure, constant production rate, varying bottomhole pressure, and varying production rate. For example, for the varying bottomhole pressure case, p_w^k is known but varied at each timestep and one can obtain the production rate q_w^k by solving this proposed model.

5.3. Validation of the Proposed Model

Before we validate the new developed model, the impact of the number of fracture segments on the simulation outputs is examined. We discretize the unilateral initial fracture and the unilateral refracture into 5 and 5, 10 and 10, 15 and 15, and 20 and 20 segments, respectively, and calculate the performance of the refractured well with the proposed model. The parameter values used in this section are: p_i = 30 MPa, X_e = 500 m, Y_e = 400 m, h = 15 m, k_{mx} = 0.02 mD, k_{my} = 0.01 mD, ϕ_m = 0.2, ϕ_{f1} = 0.2, ϕ_{f2} = 0.2, c_{tm} = 0.0012 MPa^{-1}, c_{tf1} = 0.0012 MPa^{-1}, c_{tf2} = 0.0012 MPa^{-1}, L_{f1} = 100 m, L_{f2o} = 50 m, a = 10, b = 10 m, L_{f2p} = 30 m, C_{f1} = 10 mD·m, C_{f2} = 10 mD·m, W_{f1} = 0.1 m, W_{f2} = 0.1 m, μ = 1 mPa·s, B = 0.985 (dead oil), p_w = 5 MPa during the first and third stages, T_1 = 980 d, and T_2 = 1000 d. **Figure 5-4** presents the production rates and cumulative productions of the refractured well which are calculated with the proposed model with different numbers of fracture segments. This figure shows that the production rates and cumulative productions undergo negligible difference when the number of the unilateral initial fracture segments and the unilateral refracture segments are larger than 15; therefore, we discretize the unilateral initial fracture and the unilateral refracture into 15 segments in the following studies.

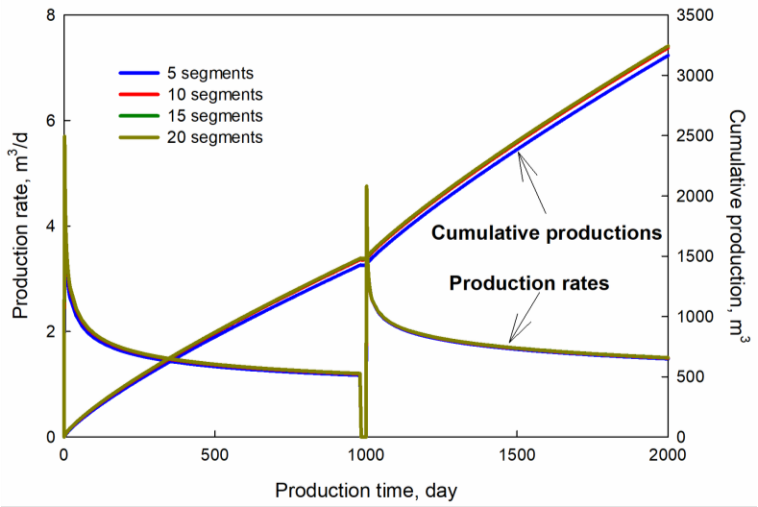

Figure 5-4. Impact of the number of fracture segments on the outputs of the semi-analytical model.

Afterward, we validate the proposed semi-analytical model against a numerical simulator (Eclipse). **Figure 5-5a** gives a top view of the global grid system used to simulate the initial fracture and the refracture in Eclipse. Figures 5-5b to 5-5d present an enlarged view of the local grid system where the red cells represent the fracture system. As shown in these figures, we use refined grids to capture the structure of the fractures and both the fracture width and the fracture conductivity used in Eclipse are consistent with those used in the semi-analytical model. **Figure 5-6** compares the production rates and cumulative productions which are calculated with the proposed model against those calculated with Eclipse. One can observe that the results obtained with the proposed model agree well with the results obtained with Eclipse, indicating that the proposed model is reliable in evaluating the performance of a refractured well. It should be noted that the computational time of the semi-analytical model is highly dependent on the programming language and the skill of the programmer. Since the code used for solving the semi-analytical model has not been optimized for achieving a high-level computational efficiency, we do not compare the computational time of the semi-analytical model to that of the professional reservoir simulator (i.e., Eclipse).

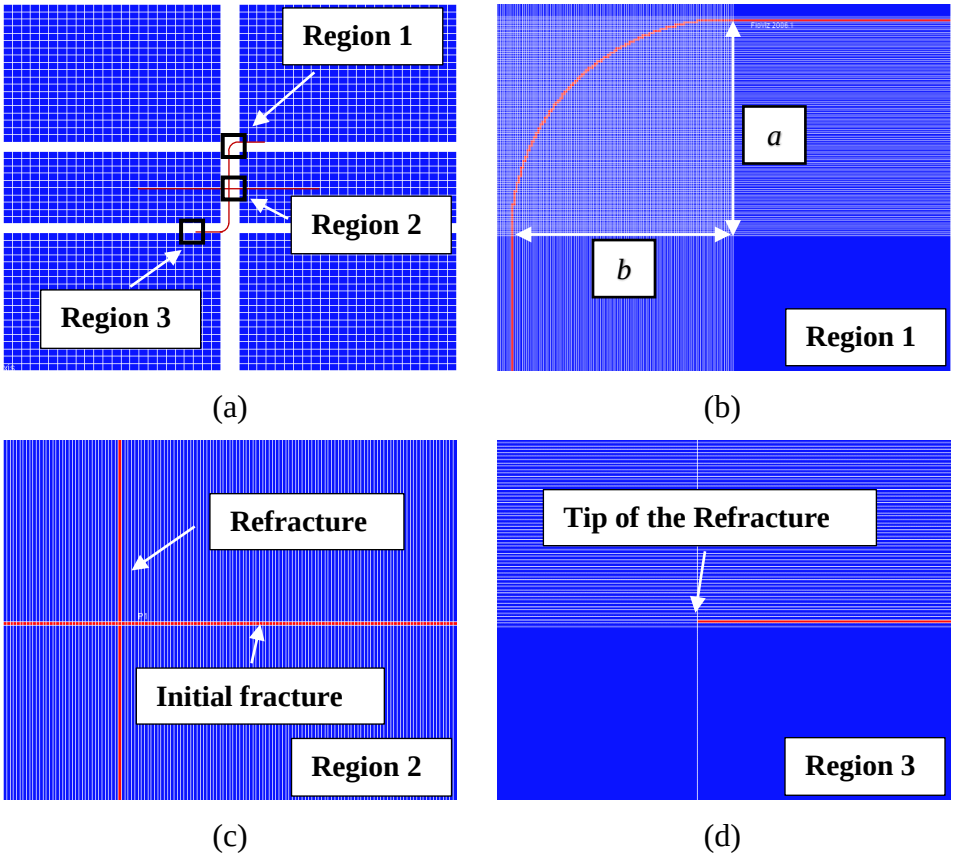

Figure 5-5. Top views of the grid system used in the Eclipse: (a) the global grid system; (b) an enlarged view of the transition section in the grid system; (c) an enlarged view of the intersection of the initial fracture and refracture in the grid system; (d) an enlarged view of the tip of the refracture in the grid system.

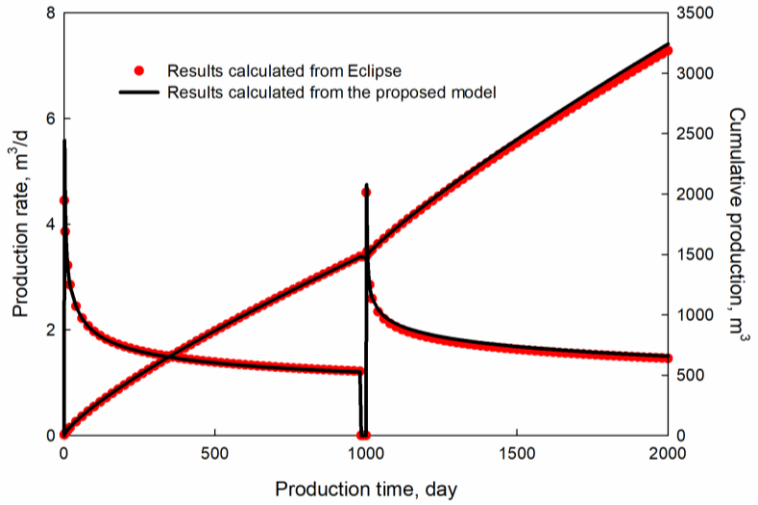

Figure 5-6. Comparison between the production rates and cumulative productions calculated with the proposed model and those by Eclipse.

5.4. Results and Discussion

In this work, we apply this proposed model to an orthogonally refractured well under different wellbore and reservoir conditions. Furthermore, we fit the production data of an orthogonally refractured well in order to demonstrate how to apply the proposed model to a real field case.

5.4.1 Case Studies

Using the proposed semi-analytical model, we calculate the performance of a refractured well with different wellbore conditions, different permeability anisotropy, and different non-uniform fracture conductivity. Since the geometry of the orthogonal refracture is highly dependent on the production-induced pressure distribution, it is necessary to consider the change of the refracture's geometry due to the change in the influencing parameters. In this work, we use the method introduced by Roussel and Sharma (2012) to estimate the geometry of the orthogonal refracture. As such, the geometry of the orthogonal refracture can be estimated with the following equations (Roussel and Sharma, 2012):

$$\begin{cases} \left(L_{f2o}+a\right)=1.5d \\ a=0.5L_{f2o} \\ \left(L_{f2o}+a\right)+\left(L_{f2p}+b\right)=0.8L_{f1} \end{cases}, \tag{5-19}$$

where d is the distance from the isotropic point to the wellbore. It is noted that Roussel and Sharma (2012) assumed that the orthogonal refracture is composed of two straight fractures whose lengths are $L_{f2o}+a$ and $L_{f2p}+b$, whereas in this work we assume that there is a transition section between the orthogonal section and the parallel section. In order to estimate the geometry of the transition section, we further assume that

$$b=0.5L_{f2p}, \tag{5-20}$$

which is similar to the equation $a = 0.5L_{f2o}$ that is presented in Equation (5-19). Combining Equation (5-19) with Equation (5-20) yields a system of linear equations. Since the value of L_{f1} is given, this system of equations can be solved if the value of d is known.

In practice, the value of d is impacted by multiple reservoir and fracture parameters, such as the reservoir boundary conditions, horizontal stress deviator, production-induced pressure gradients, and the deformation of the rock caused by the fracturing treatment (Roussel and Sharma, 2012). However, considering all these influencing factors to accurately calculate d is much beyond the scope of this work. Roussel and Sharma (2012) demonstrated that the value of d tends to grow at the early production period as the pressure front moves further into the reservoir, whereas the value of d will decrease during the late production period as the pressure gradient goes down throughout the reservoir; therefore, in the benchmark reservoir model, we assume that the isotropic point can be observed at the position represented by

$$\frac{\partial p}{\partial y} = \gamma , \tag{5-21}$$

where γ is a constant. With such an assumption, in the benchmark reservoir model, the isotropic point will move further from the wellbore during the early production period, whereas it will move closer to the wellbore during the late production period. As such, the tendency of the change of the isotropic point is consistent with that shown in Roussel and Sharma (2012). It should be noted that this assumption is only applied for simplification purposes, and the cases studies presented in this work are only aimed to show that this proposed model is applicable to simulate various scenarios. In practical applications, one should incorporate a proper geomechanical model to predict the geometry of the refracture and the position of the isotropic point for a specific reservoir.

On the basis of the proposed semi-analytical model, one can also obtain the pressure distribution within the reservoir, such that the position of the isotropic point in the reservoir can be approximately determined. Afterward, the geometry of the orthogonal refracture can be estimated with Equation (5-19) together with Equation (5-20). The following benchmark values of parameters are used in this section: γ = -0.05 MPa/m, X_e = 500 m, Y_e = 400 m, h = 15 m, k_{mx} = 3×10^{-3} mD, k_{my} = 3×10^{-3} mD, ϕ_m = 0.2, ϕ_{f1} = 0.2, ϕ_{f2} = 0.2, c_{tm} = 0.0012 MPa^{-1}, c_{tf1} = 0.0012 MPa^{-1}, c_{tf2} = 0.0012 MPa^{-1}, L_{f1} = 100 m, C_{f1} = 10 mD·m, C_{f2} = 10 mD·m, W_{f1} = 0.001 m, W_{f2} = 0.001 m, μ = 1 mPa·s, B = 0.985 (dead oil), p_i = 30 MPa, p_w = 5 MPa during the first and third stages under constant bottomhole pressure condition, q_w = 1 m^3/d during the first and third stages under constant production rate condition, T_1 = 980 d, and T_2 = 1000 d. **Table 5-2** lists the values of the parameters that are varied for the case studies and the corresponding values of d, L_{f2o}, a, b, and L_{f2p} that are obtained by identifying the pressure gradient in the reservoir.

Table 5-2. Varied values of the parameters used in the case studies and the corresponding values of d, L_{f2o}, a, b, and L_{f2p}.

parameters	values	d	L_{f2o}	a	b	L_{f2p}
Wellbore constraints	Constant p_w	47.4	47.4	23.7	3.0	5.9
	Varying p_w	47.1	47.1	23.6	3.1	6.2
	Constant q_w	37.0	37.0	18.5	8.2	16.4
	Varying q_w	37.0	37.0	18.5	8.2	16.4
R_k	0.1	19.4	19.4	9.7	17.0	34.0
	1	47.4	47.4	23.7	3.0	5.9
	10	38.0	38.0	19.0	7.6	15.3
Non-uniform C_{f1} and C_{f2}	Uniform	40.8	40.8	20.4	6.2	12.5
	Linear decrease	41.3	41.3	20.7	6.0	12.0
	Quadratic decrease	41.4	41.4	20.7	5.9	11.9

5.4.1.1 Wellbore Condition

Figure 5-7a illustrates the bottomhole pressure profiles under constant bottomhole pressure condition and varying bottomhole pressure condition. Figure 5-7b presents the production rates profiles and cumulative production profiles that are calculated with the bottomhole pressure profiles shown in Figure 5-7a. **Figure 5-8a** shows the production rate profiles under constant production rate condition and varying production rate condition. Figure 5-8b exhibits the bottomhole pressure profiles that are calculated with the production rate profiles presented in Figure 5-8a. The results shown in Figure 5-7b and Figure 5-8b imply that this proposed model can be used to simulate different wellbore constraints, including constant bottomhole pressure, varying bottomhole pressure, constant production rate, and varying production rate. The constant bottomhole pressure condition is used in all the following case studies.

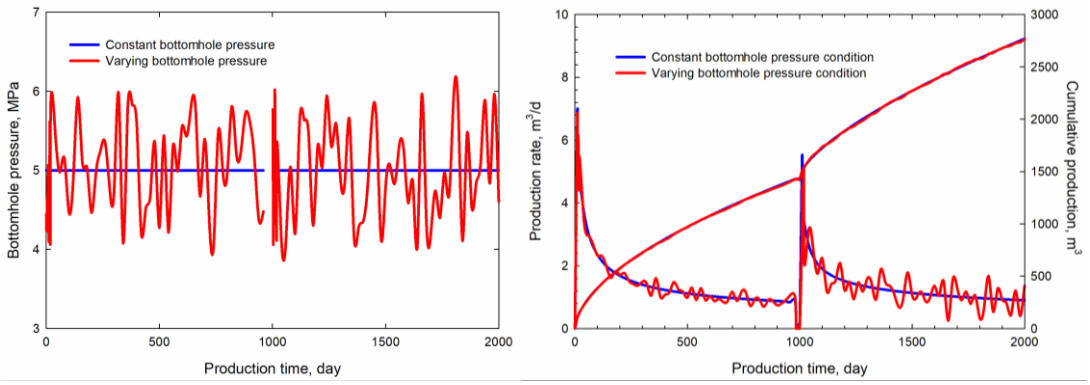

(a) (b)

Figure 5-7. Bottomhole pressure profiles and production profiles under constant bottomhole pressure condition and varying bottomhole pressure condition: (a) bottomhole pressure profiles; and (b) production rate and cumulative production profiles.

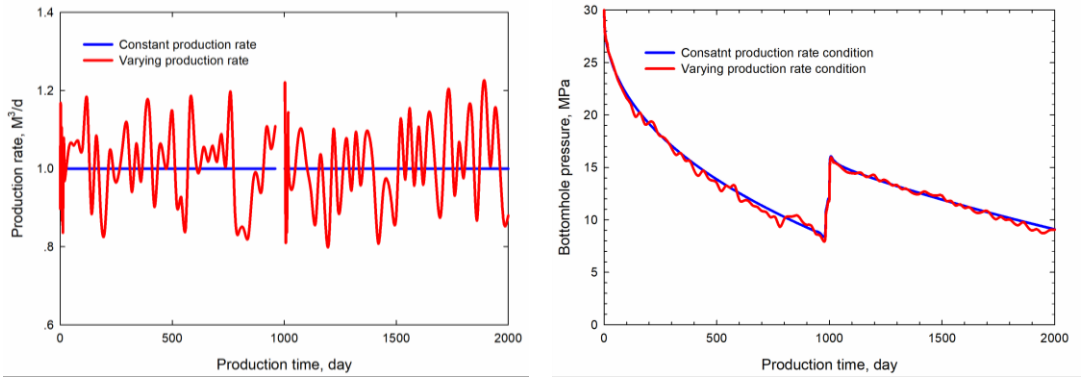

(a) (b)

Figure 5-8. Production rate profiles and bottomhole pressure profiles under constant production rate condition and varying production rate condition: (a) production rate profiles; and (b) bottomhole pressure profiles.

5.4.1.2 Permeability Anisotropy

Figure 5-9 shows the production rates and cumulative productions that are calculated with the proposed model at different permeability anisotropies. The dotted lines represent the cumulative productions and production rates without refracturing treatments. Different permeability ratios R_k (k_{mx}/k_{my}) = 0.1, 1 and 10 are used in the calculations to explore the influence of permeability anisotropies on the well performance. Since $k_m = (k_{mx}k_{my})^{1/2}$, the equivalent isotropic permeability remains unchanged in these three cases. As seen in Figure 5-9, the cumulative production of a refractured well at the highest R_k undergoes a maximum increase (from 1457 m^3 to 2450 m^3), while the cumulative production of a refractured well at the lowest R_k undergoes a minimum increase (from 3390 m^3 to 3666 m^3). This is because the initial fracture propagates along the *x*-axis while the refracture propagates mainly along the *y*-axis; therefore, a higher R_k (higher k_{mx} but lower k_{my}) is more favorable for enhancing the productivity of the refracture. **Figure 5-10** compares the pressure maps on the 1600th day with and without refracturing treatment with different values of R_k. It is interesting to note that, the value of *d* has the maximum value with R_k = 1 (see Table 5-2). This is because we assume that the isotropic point can be observed at the position with a certain pressure gradient (see Equation(5-21)) in the benchmark reservoir model.

Under the constant bottomhole pressure condition, the pressure gradient in the reservoir will increase during the early production period but decrease during the late production period. With R_k = 0.1, the pressure along the *y*-axis decreases rapidly over the entire production period and the pressure gradient exhibits a decreasing trend at the fracturing time 980th day. As such, the value of *d* with R_k = 0.1 has the smallest value among these three scenarios. Since the reservoir permeability component k_{my} with R_k = 1 and 10 is smaller than that with R_k = 0.1, the pressure along the *y*-axis decreases in a slower manner while the pressure gradient still keeps an increasing trend. Therefore, the smallest value of *d* can be observed with R_k = 0.1, whereas the largest value of *d* can be observed with R_k = 1. In practice, since the stress change is highly dependent of the pressure gradient, the stress reversal region will also shrink after it reaches a maximum value (Roussel and Sharma, 2012).

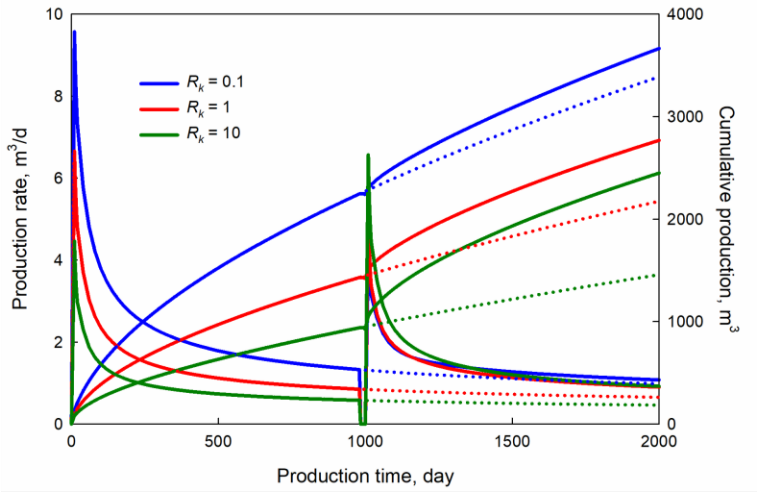

Figure 5-9. Impact of the permeability anisotropy on the production rates and cumulative productions.

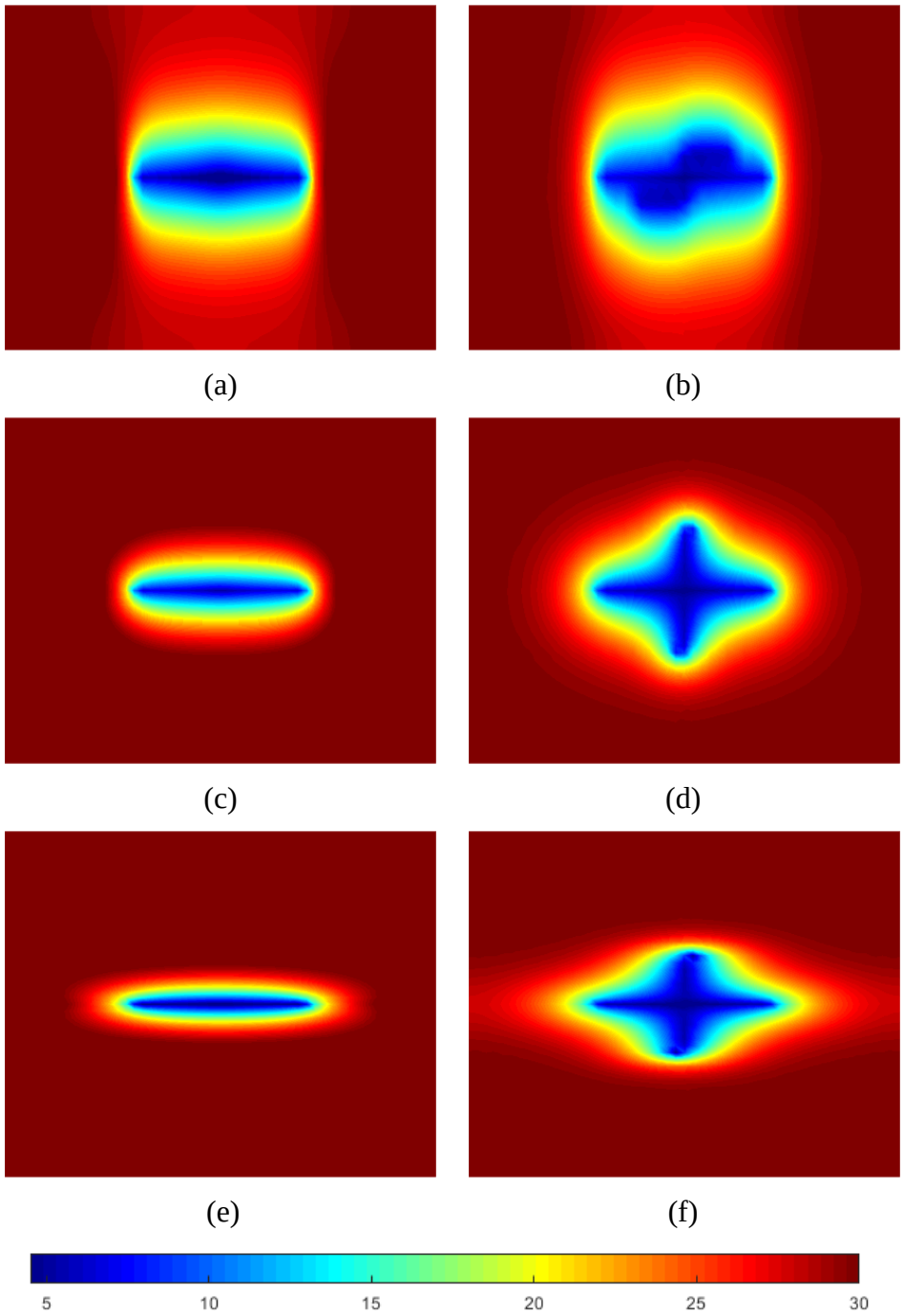

Figure 5-10. Comparison of the pressure maps (MPa) on the 1600th day with and without refracturing treatment with different permeability anisotropies: (a) pressure map without refracturing treatment with R_k = 0.1; (b) pressure map with refracturing treatment with R_k = 0.1; (c) pressure map without refracturing treatment with R_k = 1; (d) pressure map with refracturing treatment with R_k = 1; (e) pressure map without refracturing treatment with R_k = 10; and (f) pressure map with refracturing treatment with R_k = 10.

5.4.1.3 Non-Uniform Fracture Conductivity

In a real field case, the conductivity distribution along the fractures can be non-uniform; therefore, we compare the well performance of three scenarios: 1) the conductivity is uniform along the initial fracture and the refracture; 2) the conductivity is linearly decreased along the initial fracture and the refracture; and 3) the conductivity is quadratically decreased along the initial fracture and the refracture. In scenarios 2 and 3, the minimum fracture conductivity with a value of 0 can be observed at the fracture tips, whereas the maximum fracture conductivity can be observed at the wellbore. Among these three scenarios, the average conductivity remains unchanged. **Figure 5-11** shows the production rates and cumulative productions that are calculated for these three scenarios. It can be seen from Figure 5-11 that both the production rates and the cumulative productions show slight differences among the three scenarios.

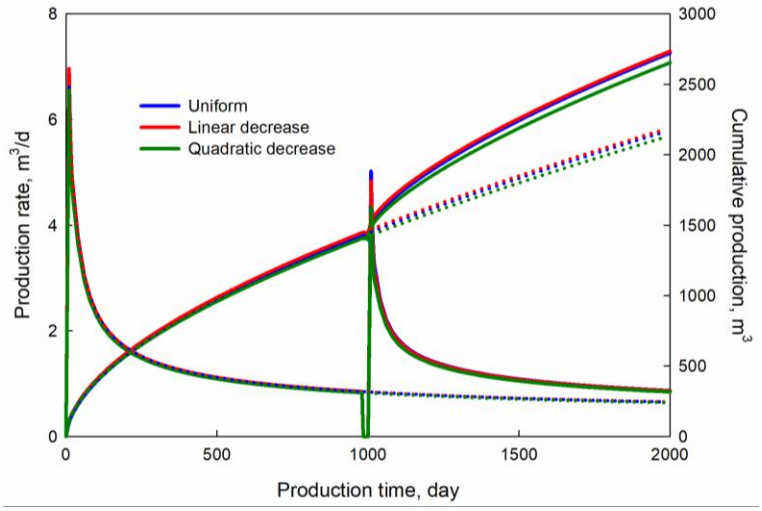

Figure 5-11. Impact of the conductivity distribution on the production rates and cumulative production.

5.4.2 Comparison with Other Refracture Patterns

In practice, the production of a fractured well does not always induce a stress reversal region near the wellbore. The real propagation of a refracture can be very different from what is shown in Figure 5-2. **Figure 5-12** presents the structure of another four refracture patterns: refracture

pattern #1 (Figure 5-12a), a refracture that is not exactly orthogonal to the initial fracture; refracture pattern #2 (Figure 5-12b), a refracture that is initiated at the tip of the initial fracture; refracture pattern #3 (Figure 5-12c), a refracture propagates orthogonally to the initial fracture from the wellbore and a refracture propagates parallel to the initial fracture from the tip of the initial fracture; refracture pattern #4 (Figure 5-12d), a refracture propagates non-orthogonally to the initial fracture from the wellbore and a refracture propagates non-parallel to the initial fracture from the tip of the initial fracture. By applying minor modifications, one can use the proposed model to simulate the productions of these four refracture patterns. In order to make a proper comparison between the well performance of an orthogonal refracture and those of the other four refracture patterns, we neglect the impact of the stress field on the geometry of the refracture. In addition, the transition section and the parallel section are absent in the orthogonal refracture. The comparison is conducted with the same total unilateral refracture length of 50 m. The azimuth angle θ is assumed to be 45^{o} for the refracture patterns (a), (b) and (d).

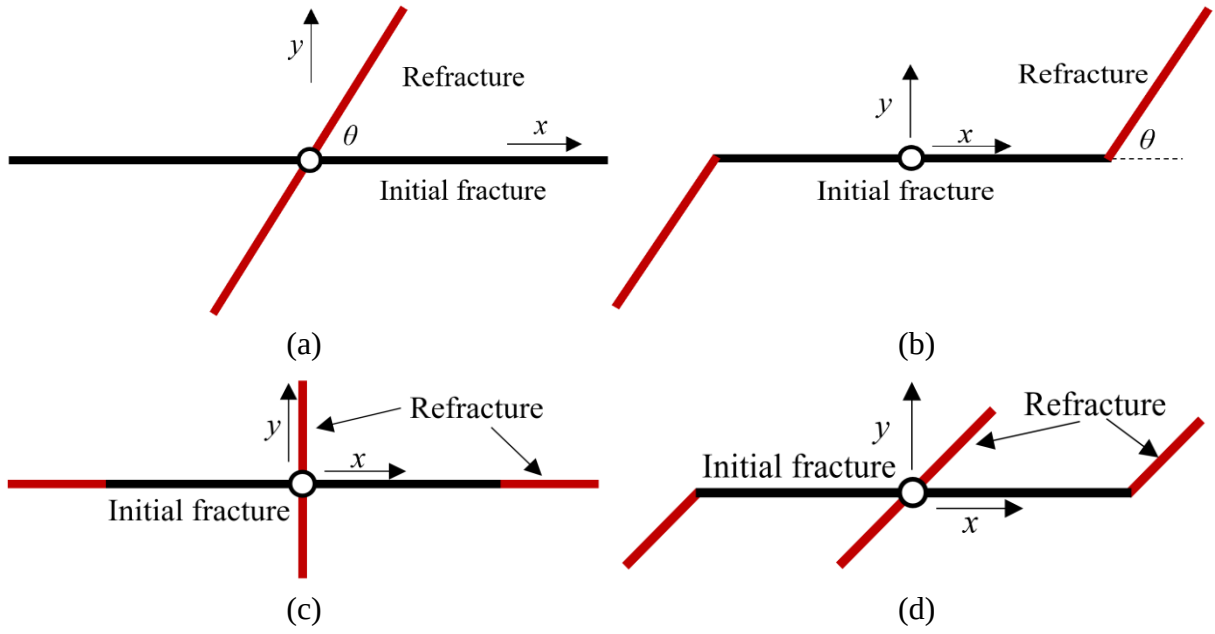

Figure 5-12. Schematics of other refracture patterns that are different from the orthogonal refracture (θ is azimuth of the refracture with respect to the initial fracture): (a) refracture pattern

#1, a refracture that is not exactly orthogonal to the initial fracture; (b) refracture pattern #2, a refracture that is initiated at the tip of the initial fracture; (c) refracture pattern #3, a refracture propagates orthogonally to the initial fracture from the wellbore, and a refracture propagates parallel to the initial fracture from the tip of the initial fracture; and (d) refracture pattern #4, a refracture propagates non-orthogonally to the initial fracture from the wellbore, and a refracture propagates non-parallel to the initial fracture from the tip of the initial fracture.

Figure 5-13 compares the production rates and cumulative productions of these five refracture patterns. As shown in Figure 5-13, the orthogonal refracture and refracture pattern #2 lead to higher increases in the productivity of the refractured well. The cumulative production of the orthogonal refracture is higher than that of refracture patterns #2 at the early production period after the refracturing treatment, while it is lower than that when the production time is beyond the 1950^{th} day. This is attributed to the following: at the early production period after the refracturing treatment, the produced fluid is mainly from the reservoir area that is near the wellbore; thus, the orthogonal refracture that is initiated from the wellbore is favorable for the well production and yields a higher productivity at the early period after the refracturing treatment. However, if the production time is sufficiently long, the reservoir pressure near the wellbore will be significantly depleted and the fracture pattern #2 (that can penetrate into a deeper part of the reservoir) can give a higher well productivity. **Figure 5-14** illustrates the pressure maps of the production well on the 1600^{th} day with and without refracturing treatment under different refracture patterns. Figure 5-14 shows that the orthogonal refracture and the fracture pattern #2 can stimulate the high-pressure area of the reservoir more effectively compared to the other refracture patterns. However, note that the results shown in Figures 5-13 and 5-14 do not indicate that the fracture pattern #2 is more effective than an orthogonal refracture in improving the well productivity. In the real field cases, the effectiveness of a specific refracture pattern is highly dependent of the reservoir properties and the geomechanical conditions.

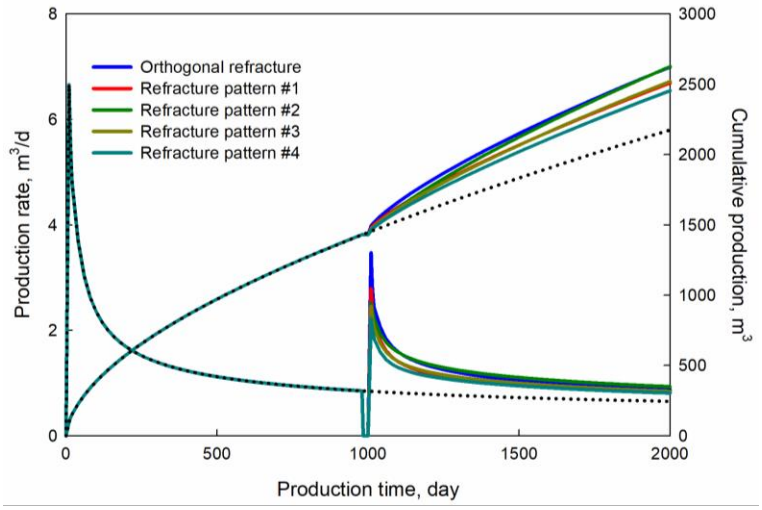

Figure 5-13. Impact of the refracture patterns on the production rates and cumulative production.

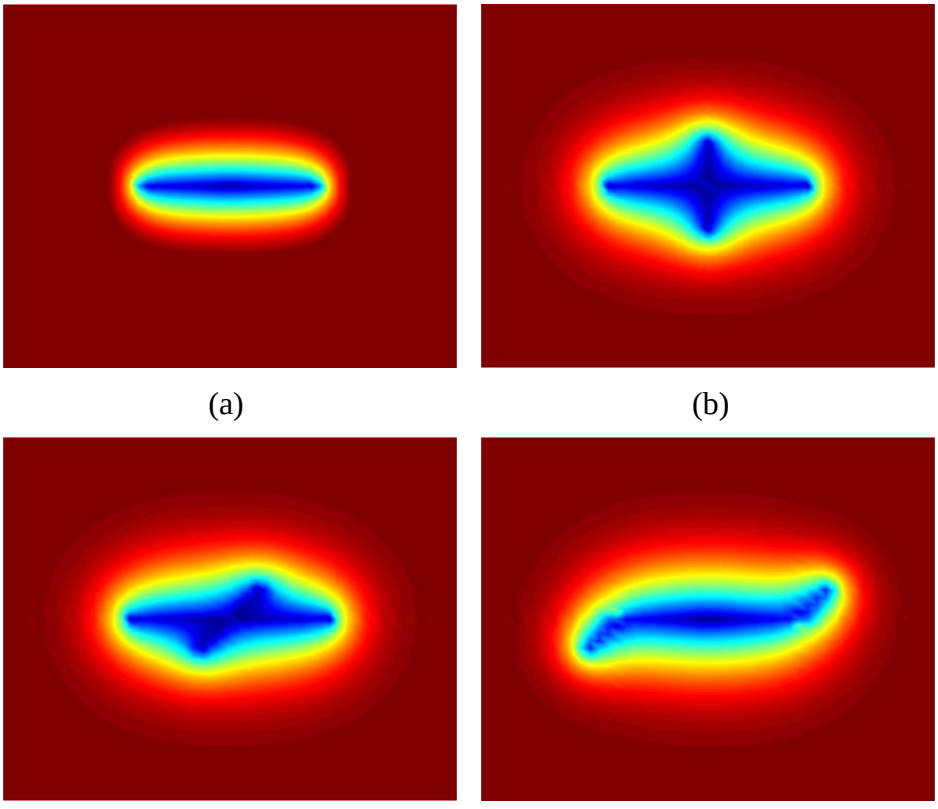

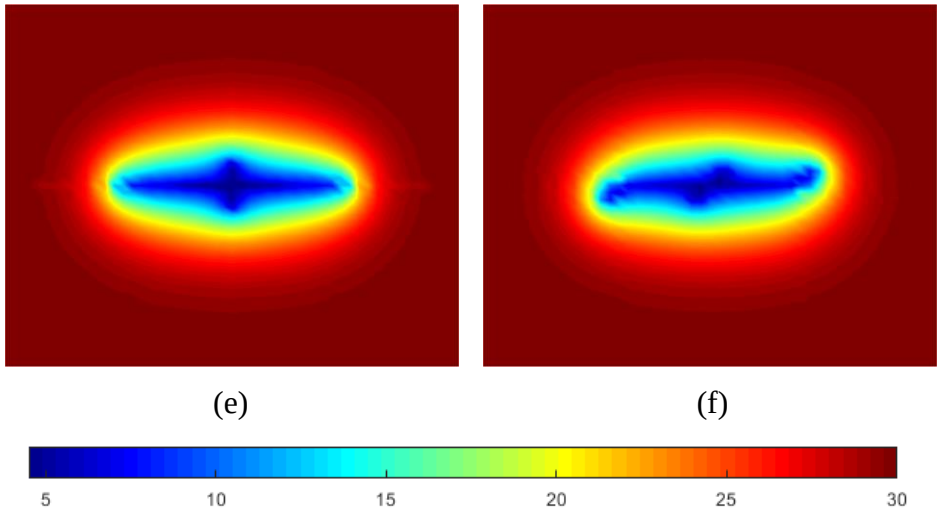

Figure 5-14. Comparison of the pressure maps (MPa) on the 1600th day with and without refracturing treatment at different refracture patterns: (a) pressure map without refracturing treatment; (b) pressure map with an orthogonal refracture; (c) pressure map with refracture pattern #1; (d) pressure map with refracture pattern #2; (e) pressure map with refracture pattern #3; and (f) pressure map with refracture pattern #4.

5.4.3 Field Case Application

Figure 5-15 shows the production profile of a refractured well in Wattenberg field (Roussel and Sharma, 2013). By analyzing the production data, Roussel and Sharma (2013) claimed that a stress reorientation highly likely appeared in the vicinity of the wellbore. In order to obtain the properties of the fluid and fractures, we perform history matching on this refractured well by using the proposed semi-analytical model. Unfortunately, there is no more available information about this refractured well or the reservoir properties. In order to briefly introduce how to apply the proposed model to a real field case, we use the parameters of a production well which is also located in Wattenberg field to help fit the production data. The parameters values are as follows: k_m = 0.05 mD, ϕ_m = 0.14, p_i = 31 MPa, and h = 6.1 m (Roussel and Sharma, 2013). In addition, we assume that the refractured well is located at the center of a square-shaped drainage area and produces oil with a constant bottomhole pressure both before and after the refracturing treatment. The constant bottomhole pressure before the refracturing treatment is 10 MPa, while the constant

bottomhole pressure after the refracturing treatment is 3 MPa, both of which are randomly but properly assigned. It is noted that the production rates shown in Figure 5-15 exhibit an increasing tendency after the 4000th day, which should not occur at a constant bottomhole pressure constraint; thus, the fitting of the production data is only conducted from the beginning to the 4000th day.

The fitting of the production data is carried out with assumed formation properties and bottomhole pressures, which aims to demonstrate how to apply the proposed model to a real field case. In practical applications, the real formation properties and bottomhole pressures should be used for the fitting of production data. In addition to the assumed parameter values, the following parameter values remain unknown: the length of the square-shaped drainage area X_e, oil viscosity μ, total compressibility c_{tm}, unilateral initial fracture length L_{f1}, initial fracture conductivity C_{f1}, the four parameters that characterize the structure of the refracture (L_{f2o}, a, b, and L_{f2p}), and refracture conductivity $C_{f2.}$

With the assumed constant bottomhole pressures and formation properties, we firstly fit the production data for the time period before the refracturing treatment. The values of X_e, μ, c_{tm}, L_{f1}, and C_{f1} are varied until a good agreement between the results calculated with the proposed model and the production data is achieved. Subsequently, we proceed to fit the production data after the refracturing treatment with the assumed parameter values and the previously obtained X_e, μ, c_{tm}, L_{f1}, and C_{f1}. **Figures 5-16** and **5-17** compare the fitted production rates against the real production rates in linear and log-log plots. As observed in these two figures, the stimulated production rates and the real production rates agree well with each other. **Table 5-3** lists the parameter values that are obtained by fitting the production data. One can also distinguish a half-unit slope period on the log-log plot before the refracturing treatment, which indicates that the flow regime is

formation linear flow (Bello and Wattenbarger, 2008). Additionally, the rapid decline period in the log-log plot implies that the production rate is influenced by the drainage boundary.

Table 5-3. Values of the various parameters obtained by fitting the production data

Parameter	Value
Length of the square drainage area X_e, m	600
Total compressibility c_{tm}, MPa^{-1}	0.0022
Oil viscosity, mPa·s	0.4
Half-length of the initial fracture L_{f1}, m	250
Length of the orthogonal section of the refracture L_{f2o}, m	100
Length of the parallel section of the refracture L_{f2p}, m	33
Length of the semi-axis along the *y*-axis *a*, m	50
Length of the semi-axis along the *x*-axis *b*, m	17
Initially fracture conductivity C_{f1}, mD·m	8000
Refracture conductivity C_{f2}, mD·m	5000

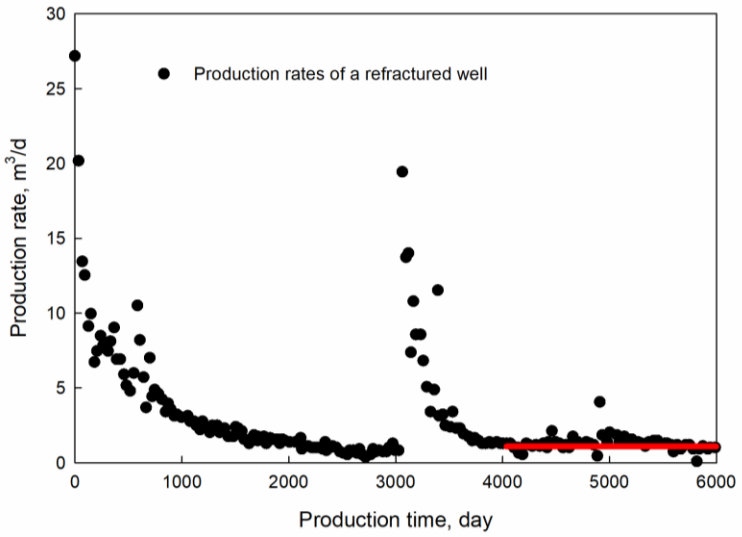

Figure 5-15. Production rates of an orthogonally refractured well (Roussel and Sharma, 2013).

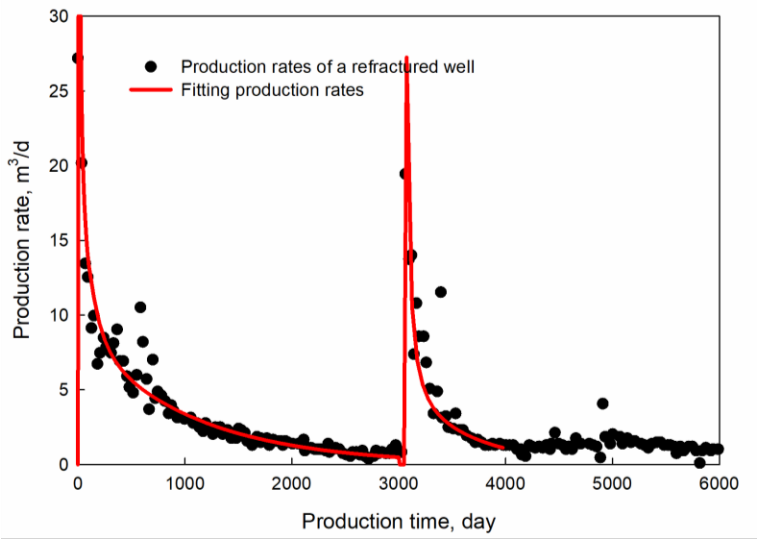

Figure 5-16. Comparison of the real production rates against the fitting production rates in linear plot.

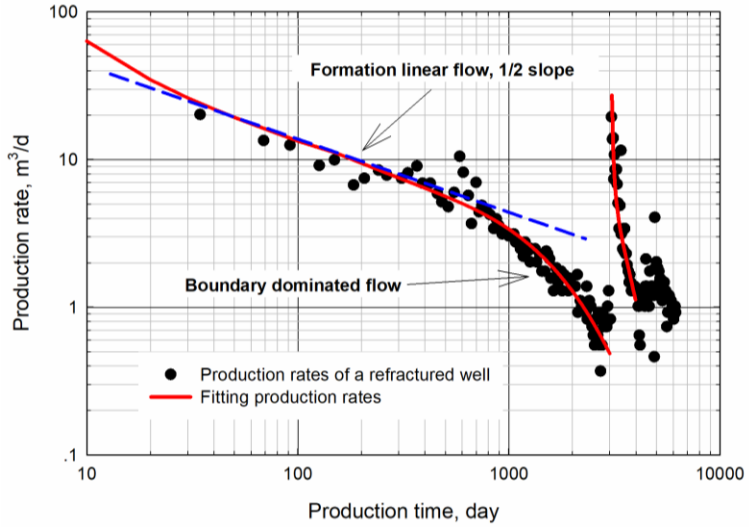

Figure 5-17. Comparison of the real production rates against the fitting production rates in log-log plot.

5.5. Conclusions

In this work, we develop a novel semi-analytical model to evaluate the performance of a refractured well with an orthogonal refracture. With the aid of the proposed model, we investigate the performance of a refractured well with different fracture conductivity, permeability anisotropy, and non-uniform fracture conductivity. We also compare the productivity of an orthogonal refracture against that of other refracture patterns. Subsequently,

we fit the production data of an orthogonally refractured well to demonstrate how to apply the proposed model to a real field case. The calculated results lead us to draw the following conclusions:

- this proposed semi-analytical model is versatile as it can simulate various wellbore constraints, such as the conditions of constant bottomhole pressure, varying bottomhole pressure, constant production rate, and varying production rate;
- the anisotropy of reservoir permeability and non-uniform conductivity distribution along the fracture can be incorporated into this model;
- in addition to an orthogonal refracture, one can also apply this proposed model to characterize the fluid transient flow of other types of refractured vertical wells with minor modifications;
- for practical applications, one can couple this proposed model with geomechanical models to predict the production of orthogonally refractured wells; and
- since the semi-analytical method has a natural advantage over the numerical method in terms of computational speed, this model can be used to carry out simulations involving numerous runs (e.g., optimizing the refracturing treatment and conducting history matching work).

Nomenclature

a = semi-axis of the ellipse along the y-axis used to approximate the transition section of the refracture, m

b = semi-axis of the ellipse along the x-axis used to approximate the transition section of the refracture, m

B = formation volume factor

c_{tf1} = initial fracture total compressibility, MPa^{-1}

c_{tf2} = refracture total compressibility, MPa^{-1}

c_{tm} = reservoir total compressibility, MPa^{-1}

C_{f1} = initial fracture conductivity, mD·m

C_{f2} = refracture conductivity, mD·m

C_s = dimensionless coefficient defined in this work

d = distance from the isotropic point to the wellbore, m

h = formation thickness, m

k_{f2}= refracture permeability in the equivalent isotropic permeability system, mD

k_m = reservoir permeability in the equivalent isotropic permeability system, mD

k_{mx} = reservoir permeability along the x-axis in the anisotropic permeability system, mD

k_{my} = reservoir permeability along the y-axis in the anisotropic permeability system, mD

k_{f1}= initial fracture permeability in the equivalent isotropic permeability system, mD

K_{f1} = initial fracture permeability in the anisotropic permeability system, mD

K_{f2} = refracture permeability in the anisotropic permeability system, mD

l_{f1} = position along the initial fracture, m

l_{f2} = position along the refracture, m

L_{f1} = half length of the initial fracture, m

L_{f2o} = length of the orthogonal section of the refracture, m

L_{f2p} = length of the parallel section of the refracture, m

p_{f1} = pressure of the initial fracture, MPa

p_{f2} = pressure of the refracture, MPa

p_i = initial reservoir pressure, MPa

p_w = bottomhole pressure, MPa

q_{f1} = flux rate per unit length from the reservoir to the initial fracture, m^2/d

q_{f2} = flux rate per unit length from the reservoir to the refracture, m^2/d

$q_{f1,i}^k$ = average flux rate from the reservoir to the *i*th segment of the initial fracture during the k^{th} timestep, m^3/d

$q_{f2,j}^k$ = average flux rate from the reservoir to the *j*th segment of the refracture during the k^{th} timestep, m^3/d

q_w = well production rate, m^3/d

q_{wf1} = flow rate from a unilateral initial fracture to the wellbore, m^3/d

q_{wf2} = flow rate from a unilateral refracture to the wellbore, m^3/d

$R_k = k_{mx}/k_{my}$, permeability ratio

t = time, d

T_1 = the end of the first production stage, d

T_2 = the end of the second production stage, d

w_{f1} = initial fracture width in the equivalent isotropic permeability system, m

w_{f2} = refracture width in the equivalent isotropic permeability system, m

W_{f1} = initial fracture width in the anisotropic permeability system, m

W_{f2} = refracture width in the anisotropic permeability system, m

x, *y* and *z* = *x-, y-,* and *z*-coordinate in the equivalent isotropic permeability system

X, *Y* and *Z* = *X-, Y-,* and *Z*-coordinate in the anisotropic permeability system

β = unit conversion factor which equals to 0.0853

γ =pressure gradient, MPa/m

δ = flux rate per unit length, area, or volume, m^2/d, m/d, or 1/d

η_{f1} = diffusivity in the initial fracture, m^2/d

η_{f2} = diffusivity in the refracture, m^2/d

η_m = diffusivity in the reservoir system, m^2/d

θ = refracture azimuth corresponding to the initial fracture

μ = oil viscosity, mPa·s

ξ = x or y

σ_{hmax} = maximum horizontal stress, MPa

σ_{hmin} = minimum horizontal stress, MPa

τ = the time that the flux happens, d

ϕ_{f1} = effective porosity in the initial fracture

ϕ_{f2} = effective porosity in the refracture

ϕ_m = reservoir porosity

Acknowledgements

The authors would like to acknowledge the financial support provided by the Natural Science and Engineering Research Council of Canada (NSERC) as well as the financial support from China Scholarship Council (CSC). The authors also thank Schlumberger for providing us the academic license of Eclipse.

Appendix 5A - Numerical Formulation of the Oil Flow in the Fracture System

In the fracture system, the transient flow equation for the oil flow in the initial fracture and the refracture can be written as (Ertekin *et al*., 2001)

$$\frac{\partial}{\partial l_{f1}}\left(w_{f1}\eta_{f1}\frac{\partial p_{f1}}{\partial l_{f1}}\right)+\frac{q_{f1}B}{h\phi_{f1}c_{tf1}}=w_{f1}\frac{\partial p_{f1}}{\partial t} \tag{5A-1}$$

and

$$\frac{\partial}{\partial l_{f2}}\left(w_{f2}\eta_{f2}\frac{\partial p_{f2}}{\partial l_{f2}}\right)+\frac{q_{f2}B}{h\phi_{f2}c_{tf2}}=w_{f2}\frac{\partial p_{f2}}{\partial t}. \tag{5A-2}$$

At the k^{th} (k = 1, 2…n) timestep, applying finite difference approximation to the first term on the left-hand side of Equation (5A-1) yields

$$\begin{aligned}\frac{\partial}{\partial l_{f1}}\left(w_{f1}\eta_{f1}\frac{\partial p_{f1}}{\partial l_{f1}}\right)&\approx\frac{1}{\Delta l_{f1,i}}\left[\left(w_{f1}\eta_{f1}\frac{\partial p^{k}_{f1,i}}{\partial l_1}\right)_{i+\frac{1}{2}}-\left(w_{f1}\eta_{f1}\frac{\partial p^{k}_{f1,i}}{\partial l_1}\right)_{i-\frac{1}{2}}\right],\\ &\approx\frac{1}{\Delta l_{f1,i}}\left[\left(\frac{w_{f1}\eta_{f1}}{\Delta l_{f1}}\right)_{i+\frac{1}{2}}\left(p^{k}_{f1,i+1}-p^{k}_{f1,i}\right)-\left(\frac{w_{f1}\eta_{f1}}{\Delta l_{f1}}\right)_{i-\frac{1}{2}}\left(p^{k}_{f1,i+1}-p^{k}_{f1,i}\right)\right]\end{aligned} \tag{5A-3}$$

where i = 1, 2…n_1, and

$$\begin{aligned}\left(\frac{w_{f1}\eta_{f1}}{\Delta l_{f1}}\right)_{i+\frac{1}{2}}&=2\left[\left(\frac{\Delta l_{f1}}{w_{f1}\eta_{f1}}\right)_i+\left(\frac{\Delta l_{f1}}{w_{f1}\eta_{f1}}\right)_{i+1}\right]^{-1}\\ \left(\frac{w_{f1}\eta_{f1}}{\Delta l_{f1}}\right)_{i-\frac{1}{2}}&=2\left[\left(\frac{\Delta l_{f1}}{w_{f1}\eta_{f1}}\right)_i+\left(\frac{\Delta l_{f1}}{w_{f1}\eta_{f1}}\right)_{i-1}\right]^{-1}\end{aligned}. \tag{5A-4}$$

The source term in Equation (5A-1) can be rewritten as

$$\frac{q_{f1}B}{h\phi_{f1}c_{tf1}}=\left(\frac{B}{\Delta l_{f1}h\phi_{f1}c_{tf1}}\right)_i q^{k}_{f1,i}, \tag{5A-5}$$

where $q_{f1,i}^{k}$ is average flux rate from the reservoir to the i^{th} segment of the initial fracture during the k^{th} timestep. Applying backward-difference approximation on the time derivative term in Equation (5A-1), we can have

$$w_{f1}\frac{\partial p_{f1}}{\partial t}=\frac{w_{f1,i}}{\Delta t^{k}}\left(p_{f1,i}^{k}-p_{f1,i}^{k-1}\right), \tag{5A-6}$$

where,

$$\Delta t^{k}=t^{k}-t^{k-1}. \tag{5A-7}$$

Inserting Equations (5A-3), (5A-5) and (5A-6) into Equation (5A-1) and rearranging this equation gives

$$\begin{aligned}&\left(\frac{B}{h\phi_{f1}c_{tf1}}\right)_{i}q_{f1,i}^{k}-\left[\left(\frac{w_{f1}\eta_{f1}}{\Delta l_{f1}}\right)_{i-1/2}+\left(\frac{w_{f1}\eta_{f1}}{\Delta l_{f1}}\right)_{i+1/2}-\frac{\Delta l_{f1,i}w_{f1,i}}{\Delta t^{k}}\right]p_{f1,i}^{k}\\&+\left(\frac{w_{f1}\eta_{f1}}{\Delta l_{f1}}\right)_{i+1/2}p_{f1,i+1}^{k}+\left(\frac{w_{f1}\eta_{f1}}{\Delta l_{f1}}\right)_{i-1/2}p_{f1,i-1}^{k}=-\frac{\Delta l_{f1,i}w_{f1,i}}{\Delta t^{k}}p_{f1,i}^{k-1}\end{aligned}. \tag{5A-8}$$

For convenience, we define the following parameters:

$$c_{f1,i-1/2}^{k}=\left(\frac{w_{f1}\eta_{f1}}{\Delta l_{f1}}\right)_{i-1/2}, \tag{5A-9}$$

$$c_{f1,i}^{k}=-\left[\left(\frac{w_{f1}\eta_{f1}}{\Delta l_{f1}}\right)_{i-1/2}+\left(\frac{w_{f1}\eta_{f1}}{\Delta l_{f1}}\right)_{i+1/2}-\frac{\Delta l_{f1,i}w_{f1,i}}{\Delta t^{k}}\right], \tag{5A-10}$$

$$c_{f1,i+1/2}^{k}=\left(\frac{w_{f1}\eta_{f1}}{\Delta l_{f1}}\right)_{i+1/2}, \tag{5A-11}$$

$$c_{f1\_q,i}^{k}=\left(\frac{B}{h\phi_{f1}c_{tf1}}\right)_{i}, \tag{5A-12}$$

and

$$c_{f1\_t,i}^{k} = -\frac{\Delta l_{f1,i} w_{f1,i}}{\Delta t^{k}} . \tag{5A-13}$$

In particular,

$$\begin{cases} \text{if } i = 0,\ c_{f1,i-1/2}^{k} = 0 \text{ and } c_{f1,i}^{k} = -\left[\left(\dfrac{w_{f1}\eta_{f1}}{\Delta l_{f1}} \right)_{i+1/2} - \dfrac{\Delta l_{f1,i} w_{f1,i}}{\Delta t^{k}} \right] \\ \text{if } i = n_1,\ c_{f1,i+1/2}^{k} = 0 \text{ and } c_{f1,i}^{k} = -\left[\left(\dfrac{w_{f1}\eta_{f1}}{\Delta l_{f1}} \right)_{i-1/2} - \dfrac{\Delta l_{f1,i} w_{f1,i}}{\Delta t^{k}} \right] \end{cases} . \tag{5A-14}$$

As such, Equation (5A-8) can be rewritten as

$$c_{f1,i-1/2}^{k} p_{f1,i-1}^{k} + c_{f1,i}^{k} p_{f1,i}^{k} + c_{f1,i+1/2}^{k} p_{f1,i+1}^{k} + c_{f1\_q,i}^{k} q_{f1,i}^{k} = c_{f1\_t,i}^{k} p_{f1,i}^{k-1} . \tag{5A-15}$$

Applying Equation (5A-15) to the n_1 segments of the initial fracture and arranging these equations into a matrix format gives

$$\boldsymbol{c}_{f1}^{k} \boldsymbol{p}_{f1}^{k} + \boldsymbol{c}_{f1\_q}^{k} \boldsymbol{q}_{f1}^{k} = \boldsymbol{c}_{f1\_t}^{k} \boldsymbol{p}_{f1}^{k-1} , \tag{5A-16}$$

where

$$\boldsymbol{c}_{f1}^{k} = \begin{bmatrix} c_{f1,1}^{k} & c_{f1,1+1/2}^{k} & 0 & \cdots & 0 \\ c_{f1,2-1/2}^{k} & c_{f1,2}^{k} & c_{f1,2+1/2}^{k} & & \vdots \\ 0 & & \ddots & & 0 \\ \vdots & & c_{f1,n_1-1-1/2}^{k} & c_{f1,n_1-1}^{k} & c_{f1,n_1-1+1/2}^{k} \\ 0 & \cdots & 0 & c_{f1,n_1-1-1/2}^{k} & c_{f1,n_1}^{k} \end{bmatrix} , \quad \boldsymbol{p}_{f1}^{k} = \begin{bmatrix} p_{f1,1}^{k} \\ \vdots \\ p_{f1,n_1}^{k} \end{bmatrix} , \quad \boldsymbol{c}_{f1\_q}^{k} = \begin{bmatrix} c_{f1\_q,1}^{k} \\ \vdots \\ c_{f1\_q,n1}^{k} \end{bmatrix} ,$$

$$\boldsymbol{q}_{f1}^{k} = \begin{bmatrix} q_{f1,1}^{k} \\ \vdots \\ q_{f1,n_1}^{k} \end{bmatrix}, \text{ and } \boldsymbol{c}_{f1\_t}^{k} = \begin{bmatrix} c_{f1\_t,1}^{k} \\ \vdots \\ c_{f1\_t,n1}^{k} \end{bmatrix} .$$

Applying the same procedures introduced above to Equation (5A-2), we can obtain the approximated flow equation that characterizes the transient flow in the refracture:

$$\left(\frac{B}{h\phi_{f2}c_{tf2}}\right)_j q_{f2,j}^k - \left[\left(\frac{w_{f2}\eta_{f2}}{\Delta l_{f2}}\right)_{j-1/2} + \left(\frac{w_{f2}\eta_{f2}}{\Delta l_{f2}}\right)_{j+1/2} - \frac{\Delta l_{f2,j} w_{f2,j}}{\Delta t^k}\right] p_{f2,j}^k + \left(\frac{w_{f2}\eta_{f2}}{\Delta l_{f2}}\right)_{j+1/2} p_{f2,j+1}^k + \left(\frac{w_{f2}\eta_{f2}}{\Delta l_{f2}}\right)_{j-1/2} p_{f2,j-1}^k = -\frac{\Delta l_{f2,j} w_{f2,j}}{\Delta t^k} p_{f2,j}^{k-1}, \quad \text{(5A-17)}$$

and the system of flow equations that is written in a matrix format:

$$\boldsymbol{c}_{f2}^k \boldsymbol{p}_{f2}^k + \boldsymbol{c}_{f2\_q}^k \boldsymbol{q}_{f2}^k = \boldsymbol{c}_{f2\_t}^k \boldsymbol{p}_{f2}^{k-1}, \quad \text{(5A-18)}$$

where $j = 1, 2 \ldots n_2$, $q_{f2,j}$ is the flux from the reservoir to the j^{th} segment of the refracture, the matrices of $\boldsymbol{c}_{f2}^k$, $\boldsymbol{p}_{f2}^k$, $\boldsymbol{c}_{f2\_q}^k$, $\boldsymbol{q}_{f2}^k$, and $\boldsymbol{c}_{f2\_t}^k$ have similar definitions to $\boldsymbol{c}_{f1}^k$, $\boldsymbol{p}_{f1}^k$, $\boldsymbol{c}_{f1\_q}^k$, $\boldsymbol{q}_{f1}^k$, and $\boldsymbol{c}_{f1\_t}^k$. The only difference is that the subscript '*f*2' indicates the properties of the refracture should be used in these matrices.

Based on the Darcy equation, the inner boundary conditions (i.e., Equations (5-4) and (5-5)) can be rewritten as

$$\begin{cases} \dfrac{2k_{f1,1}}{B\mu} w_{f1,1} h \dfrac{p_{f1,1}^k - p_w^k}{\Delta l_{f1,1}} = q_{wf1}^k & \left(0 < t^k \le T_1\right) \\ p_{f1,1}^k = p_w^k & \left(T_1 < t^k \le T_2\right) \\ \dfrac{2k_{f1,1}}{B\mu} w_{f1,1} h \dfrac{p_{f1,1}^k - p_w^k}{\Delta l_{f1,1}} = q_{wf1}^k & \left(t^k > T_2\right) \end{cases} \quad \text{(5A-19)}$$

and

$$\frac{2k_{f2,1}}{B\mu} w_{f2,1} h \frac{p_{f2,1}^k - p_w^k}{\Delta l_{f2,1}} = q_{wf2}^k \quad \left(t^k > T_2\right), \quad \text{(5A-20)}$$

where q_{wf1} is flow rate from a unilateral initial fracture to the wellbore, p_w is bottomhole pressure and q_{wf2} is flow rate from a unilateral refracture to the wellbore.

In addition, as we assume that the oil enters the wellbore only through the fractures, we can have the following relationship between the well production rate (q_w) and the flux rate from the unilateral initial fracture (q_{wf1}) and the unilateral refracture (q_{wf2}):

$$\begin{cases} q_w^k = 2q_{wf1}^k & \left(0 < t^k \le T_1\right) \\ q_w^k = 0 & \left(T_1 < t^k \le T_2\right) \\ q_w^k = 2q_{wf1}^k + 2q_{wf2}^k & \left(t^k > T_2\right) \end{cases} \tag{5A-21}$$

Appendix 5B – Analytical Solution for the Oil Flow in the Reservoir System

The Green's function of an instantaneous line source in a 1-dimension bounded reservoir is given as (Gringarten and Ramey; 1973)

$$\frac{\phi_m c_{tm}}{\delta B}\Delta p\left(\xi, t\right)=\frac{1}{\xi_e}\left\{1+2\sum_{m=1}^{\infty}\exp\left[-\frac{m^2\pi^2\eta_m\left(t-\tau\right)}{\xi_e^2}\right]\cos\frac{m\pi\xi_f}{\xi_e}\cos\frac{m\pi\xi}{\xi_e}\right\}, \qquad (5B\text{-}1)$$

where δ represents flux rate per unit length, area, or volume, $\xi = x$ or y, τ indicates that the instantaneous flux happens at time τ. Based on the Newman product method, the pressure change of the point source in a 2-dimension bounded reservoir can be obtained by multiplying a line source function along x-direction with a line source function along y-direction. As such, we can have the instantaneous point source function in a 2-dimension reservoir, which is written as

$$\begin{aligned}&\frac{\phi_m c_{tm}}{\delta B}\Delta p\left(x, y, t\right)=\\&\frac{1}{x_e}\left\{1+2\sum_{m=1}^{\infty}\exp\left[-\frac{m^2\pi^2\eta_m\left(t-\tau\right)}{x_e^2}\right]\cos\frac{m\pi x_f}{x_e}\cos\frac{m\pi x}{x_e}\right\}.\\&\frac{1}{y_e}\left\{1+2\sum_{m=1}^{\infty}\exp\left[-\frac{m^2\pi^2\eta_m\left(t-\tau\right)}{y_e^2}\right]\cos\frac{m\pi y_f}{y_e}\cos\frac{m\pi y}{y_e}\right\}\end{aligned} \qquad (5B\text{-}2)$$

The fractures are discretized into small segments. The pressure change at position (x, y) caused by a single fracture segment with an average flux rate of q_f can be readily calculated by integrating Equation (5B-2) along the direction of the fracture segment from $t = \tau_1$ to $t = \tau_2$ ((τ_1, τ_2) indicates that the flux is continued from $t = \tau_1$ to $t = \tau_2$):

$$\begin{aligned}&\Delta p\left(x, y, t\right)=q_f\int_{\tau_1}^{\tau_2}\int_0^{\Delta l_f}\frac{B}{\phi_m c_{tm}\Delta l_f x_e y_e h}\\&\left\{1+2\sum_{m=1}^{\infty}\exp\left[-\frac{m^2\pi^2\eta_m\left(t-\tau\right)}{x_e^2}\right]\cos\frac{m\pi x_f}{x_e}\cos\frac{m\pi x}{x_e}\right\}\\&\left\{1+2\sum_{m=1}^{\infty}\exp\left[-\frac{m^2\pi^2\eta_m\left(t-\tau\right)}{y_e^2}\right]\cos\frac{m\pi y_f}{y_e}\cos\frac{m\pi y}{y_e}\right\}\mathrm{d}l\,\mathrm{d}\tau\end{aligned} \qquad (5B\text{-}3)$$

In particular, if the fracture segment is parallel to the *x*-axis, Equation (5B-3) can be written as

$$\Delta p\left(x,y,t\right)=q_f\int_{\tau_1}^{\tau_2}\frac{B}{\phi_m c_{tm}x_e y_e h}$$
$$\left\{1+\frac{4x_e}{\pi\Delta l_f}\sum_{m=1}^{\infty}\frac{1}{m}\exp\left[-\frac{m^2\pi^2\eta_m\left(t-\tau\right)}{x_e^2}\right]\sin\frac{m\pi\Delta l_f}{2x_e}\cos\frac{m\pi x_f}{x_e}\cos\frac{m\pi x}{x_e}\right\}. \tag{5B-4}$$
$$\left\{1+2\sum_{m=1}^{\infty}\exp\left[-\frac{m^2\pi^2\eta_m\left(t-\tau\right)}{y_e^2}\right]\cos\frac{m\pi y_f}{y_e}\cos\frac{m\pi y}{y_e}\right\}\mathrm{d}\tau$$

If the fracture segment is parallel to the *y*-axis, Equation (5B-3) can be written as

$$\Delta p\left(x,y,t\right)=q_f\int_{\tau_1}^{\tau_2}\frac{B}{\phi_m c_{tm}x_e y_e h}$$
$$\left\{1+2\sum_{m=1}^{\infty}\exp\left[-\frac{m^2\pi^2\eta_m\left(t-\tau\right)}{x_e^2}\right]\cos\frac{m\pi x_f}{x_e}\cos\frac{m\pi x}{x_e}\right\} \tag{5B-5}$$
$$\left\{1+\frac{4y_e}{\pi\Delta l_f}\sum_{m=1}^{\infty}\frac{1}{m}\exp\left[-\frac{m^2\pi^2\eta_m\left(t-\tau\right)}{y_e^2}\right]\sin\frac{m\pi\Delta l_f}{2y_e}\cos\frac{m\pi y_f}{y_e}\cos\frac{m\pi y}{y_e}\right\}\mathrm{d}\tau$$

For convenience, the pressure change is written in a uniform format as

$$\Delta p\left(x,y,t\right)=q_f G\,, \tag{5B-6}$$

where G denotes the integral terms on the right-hand side of Equations (5B-3), (5B-4), and (5B-5). As such, at the k^{th} timestep, the pressure change at the center position of the I^{th} ($I = 1, 2\ldots n_1$) segment of the initial fracture before the refracture is put into production can be expressed as

$$\Delta p_{f1,I}^{k}\left(x_{f1,I},y_{f1,I},t^k\right)=\sum_{i=1}^{i=n_1}\sum_{s=1}^{s=k}q_{f1,i}^{s}G_{i,I}^{s,k}+\sum_{i=1}^{i=n_1}\sum_{s=1}^{s=k}q_{f1,-i}^{s}G_{-i,I}^{s,k}\,, \tag{5B-7}$$

where $\Delta p_{f1,I}^{k}$ represents the pressure change at the position ($x_{f1,I}$, $y_{f1,I}$) at the k^{th} timestep; the subscripts 'i' and 'I' of the G term in Equation (5B-7) indicates that the flux of the i^{th} fracture segment ($x_{f1,i}$, $y_{f1,i}$) should be used to calculate the pressure change at position ($x_{f1,I}$, $y_{f1,I}$); the superscript 's' and 'k' of the G term indicates that the time integral is from t^{s-1} to t^{s} and the

investigated time is t^k; the second summation term on the right-hand side of Equation (5B-7) represents the pressure change caused by the other unilateral initial fracture; and '-*i*' indicates the i^{th} fracture segment of the other unilateral initial fracture. Since the well is located at the center of the reservoir and the fracture system is symmetrical with respect to the wellbore, the flux and pressure of the i^{th} fracture segment should be equivalent to those of the $-i^{\text{th}}$ fracture segment; thus, Equation (5B-7) can be simplified as

$$\Delta p_{f1,I}^{k}\left(x_{f1,I}, y_{f1,I}, t^{k}\right)=\sum_{i=1}^{i=n_1}\sum_{s=1}^{s=k} q_{f1,i}^{s}\left(G_{i,I}^{s,k}+G_{-i,I}^{s,k}\right). \tag{5B-8}$$

The pressure change at the center position of the I^{th} ($I = 1, 2\ldots n_1$) segment of the initial fracture after the refracturing treatment can be expressed as

$$\Delta p_{f1,I}^{k}\left(x_{f1,I}, y_{f1,I}, t^{k}\right)=\sum_{i=1}^{i=n_1}\sum_{s=1}^{s=k} q_{f1,i}^{s}\left(G_{i,I}^{s,k}+G_{-i,I}^{s,k}\right)+\sum_{j=1}^{j=n_2}\sum_{s=K+1}^{s=k} q_{f2,j}^{s}\left(G_{j,I}^{s,k}+G_{-j,I}^{s,k}\right), \tag{5B-9}$$

and the pressure change at the center position of the J^{th} ($I = 1, 2\ldots n_2$) segment of the refracture can be expressed as

$$\Delta p_{f2,J}^{k}\left(x_{f2,J}, y_{f2,J}, t^{k}\right)=\sum_{i=1}^{i=n_1}\sum_{s=1}^{s=k} q_{f1,i}^{s}\left(G_{i,J}^{s,k}+G_{-i,J}^{s,k}\right)+\sum_{j=1}^{j=n_2}\sum_{s=K+1}^{s=k} q_{f2,j}^{s}\left(G_{j,J}^{s,k}+G_{-j,J}^{s,k}\right), \tag{5B-10}$$

where in Equations (5B-9) and (5B-10), K represents the K^{th} timestep at the end of which the second stage is terminated. The pressure change can also be expressed as

$$\Delta p_f^k = p_i - p_f^k, \tag{5B-11}$$

where p_i is reservoir initial pressure. Combing Equation (5B-11) with Equations (5B-8) to (5B-10), we can construct the following systems of equations to characterize the relationship between the flux and the pressure in the fracture system:

$$\begin{cases} \boldsymbol{p}_{f1}^{k}+\boldsymbol{G}_{f1,f1}^{k}\boldsymbol{q}_{f1}^{k}=p_i-\boldsymbol{A}_{f1,f1} & \left(t^k\le T_2\right) \\ \boldsymbol{p}_{f1}^{k}+\boldsymbol{G}_{f1,f1}^{k}\boldsymbol{q}_{f1}^{k}+\boldsymbol{G}_{f1,f2}^{k}\boldsymbol{q}_{f2}^{k}=p_i-\boldsymbol{A}_{f1,f1}-\boldsymbol{A}_{f1,f2} & \left(t^k>T_2\right) \end{cases} \tag{5B-12}$$

and

$$\begin{cases} \boldsymbol{p}_{f2}^{k}+\boldsymbol{G}_{f2,f1}^{k}\boldsymbol{q}_{f1}^{k}=p_i-\boldsymbol{A}_{f2,f1} & \left(t^k\le T_2\right) \\ \boldsymbol{p}_{f2}^{k}+\boldsymbol{G}_{f2,f1}^{k}\boldsymbol{q}_{f1}^{k}+\boldsymbol{G}_{f2,f2}^{k}\boldsymbol{q}_{f2}^{k}=p_i-\boldsymbol{A}_{f2,f1}-\boldsymbol{A}_{f2,f2} & \left(t^k>T_2\right) \end{cases}, \tag{5B-13}$$

where,

$$\boldsymbol{G}_{f1,f1}^{k}=\begin{bmatrix} G_{1,1}^{k,k}+G_{-1,1}^{k,k} & \cdots & G_{1,n_1}^{k,k}+G_{-1,n_1}^{k,k} \\ \vdots & \ddots & \vdots \\ G_{n_1,1}^{k,k}+G_{-n_1,1}^{k,k} & \cdots & G_{n_1,n_1}^{k,k}+G_{-n_1,n_1}^{k,k} \end{bmatrix},\ \boldsymbol{G}_{f1,f2}^{k}=\begin{bmatrix} G_{1,1}^{k,k}+G_{-1,1}^{k,k} & \cdots & G_{1,n_2}^{k,k}+G_{-1,n_2}^{k,k} \\ \vdots & \ddots & \vdots \\ G_{n_1,1}^{k,k}+G_{-n_1,1}^{k,k} & \cdots & G_{n_1,n_2}^{k,k}+G_{-n_1,n_2}^{k,k} \end{bmatrix},$$

$$\boldsymbol{G}_{f2,f1}^{k}=\begin{bmatrix} G_{1,1}^{k,k}+G_{-1,1}^{k,k} & \cdots & G_{1,n_1}^{k,k}+G_{-1,n_1}^{k,k} \\ \vdots & \ddots & \vdots \\ G_{n_2,1}^{k,k}+G_{-n_2,1}^{k,k} & \cdots & G_{n_2,n_1}^{k,k}+G_{-n_2,n_1}^{k,k} \end{bmatrix},\ \boldsymbol{G}_{f2,f2}^{k}=\begin{bmatrix} G_{1,1}^{k,k}+G_{-1,1}^{k,k} & \cdots & G_{1,n_2}^{k,k}+G_{-1,n_2}^{k,k} \\ \vdots & \ddots & \vdots \\ G_{n_2,1}^{k,k}+G_{-n_2,1}^{k,k} & \cdots & G_{n_2,n_2}^{k,k}+G_{-n_2,n_2}^{k,k} \end{bmatrix},$$

$$\boldsymbol{A}_{f1,f1}=\begin{bmatrix} \sum_{i=1}^{i=n_1}\sum_{s=1}^{s=k-1} q_{f1,i}^{s}\left(G_{i,1}^{s,k}+G_{-i,1}^{s,k}\right) \\ \vdots \\ \sum_{i=1}^{i=n_1}\sum_{s=1}^{s=k-1} q_{f1,i}^{s}\left(G_{i,n_1}^{s,k}+G_{-i,n_1}^{s,k}\right) \end{bmatrix},\ \boldsymbol{A}_{f1,f2}=\begin{bmatrix} \sum_{j=1}^{j=n_2}\sum_{s=1}^{s=k-1} q_{f2,i}^{s}\left(G_{j,1}^{s,k}+G_{-j,1}^{s,k}\right) \\ \vdots \\ \sum_{j=1}^{j=n_2}\sum_{s=1}^{s=k-1} q_{f2,i}^{s}\left(G_{j,n_1}^{s,k}+G_{-j,n_1}^{s,k}\right) \end{bmatrix},$$

$$\boldsymbol{A}_{f2,f1}=\begin{bmatrix} \sum_{i=1}^{i=n_1}\sum_{s=1}^{s=k-1} q_{f1,i}^{s}\left(G_{i,1}^{s,k}+G_{-i,1}^{s,k}\right) \\ \vdots \\ \sum_{i=1}^{i=n_1}\sum_{s=1}^{s=k-1} q_{f1,i}^{s}\left(G_{i,n_2}^{s,k}+G_{-i,n_2}^{s,k}\right) \end{bmatrix},\ \text{and}\ \boldsymbol{A}_{f2,f2}=\begin{bmatrix} \sum_{j=1}^{j=n_2}\sum_{s=1}^{s=k-1} q_{f2,i}^{s}\left(G_{j,1}^{s,k}+G_{-j,1}^{s,k}\right) \\ \vdots \\ \sum_{j=1}^{j=n_2}\sum_{s=1}^{s=k-1} q_{f2,i}^{s}\left(G_{j,n_2}^{s,k}+G_{-j,n_2}^{s,k}\right) \end{bmatrix}.$$

SI Metric Conversion Factors	
day × 8.640	E+04 = s
m^2/day × 1.157*	E-05 = m^2/s
m^3/day × 1.157*	E-05 = m^3/s
m^3/MPa × 1.000	E-06 = m^3/Pa
MPa × 1.000	E-06 = Pa
mPa·s × 1.000	E-03 = Pa·s

* Conversion factor is exact

References

Aghighi, M.A., Rahman, S.S., and Rahman, M.M. 2009. Effect of Formation Stress Distribution on Hydraulic Fracture Reorientation in Tight Gas Sands. Paper SPE 122723 presented at Asia Pacific Oil and Gas Conference & Exhibition, Jakarta, Indonesia, 4-6 August.

Bello, R.O., and Wattenbarger, R.A. 2008. Rate Transient Analysis in Naturally Fractured Shale Gas Reservoirs. Paper SPE 114591 presented at CIPC/SPE Gas Technology Symposium 2008 Joint Conference, Calgary, Alberta, Canada, 16-19 June.

Benedict, D.S., and Miskimins, J.L. 2009. The Effects of Hydraulic Fracture Reorientation. Paper SPE 119355 presented at SPE Hydraulic Fracturing Technology Conference, the Woodlands, Texas, 19-21 January.

Branch, G.A., and Drennan, K.M. 1991. Refracture Stimulations in the Norge Marchand Unit: A Case Study. Paper SPE 21642 presented at SPE Production Operations Symposium, Oklahoma City, Oklahoma, 7-9 April.

Chen, Z., Liao, X., Zhao, X., Lv, S., and Zhu, L. 2016. A Semianalytical Approach for Obtaining Type Curves of Multiple-Fractured Horizontal Wells with Secondary-Fracture Networks. *SPE J*. 21 (02): 538-549.

Daneshy, A.A. 1978. Hydraulic Fracture Propagation in Layered Formations. *SPE J.* 18 (01) 33-41.

Elbel, J.L., and Mack, M.G. 1993. Refracturing: Observations and Theories. Paper SPE 25464 presented at SPE Production Operations Symposium, Oklahoma City, Oklahoma, 21-23 March.

Ertekin, T., Abou-Kassem, J.H., and King, G.R. 2001. *Basic Applied Reservoir Simulation*. SPE Textbook Series.

Gala, D.P., and Sharma, M.M. 2017. Effect of Fluid Type and Composition on Changes in Reservoir Stresses Due to Production: Implications for Refracturing. Paper ARMA-2017-0042 presented at 51st U.S. Rock Mechanics/Geomechanics Symposium, San Francisco, California, USA, 25-28 June.

Gringarten, A.C., and Ramey, H.J. 1973. The Use of Source and Green's Functions in Solving Unsteady-Flow Problems in Reservoirs. *SPE J*. 13 (05): 285-296.

Hubbert, M.K., and Willis, D.G. 1957. Mechanics of Hydraulic Fracturing. *Trans. AIME* 210: 153-168.

Jiang, W., Cai, B., Li, Y., He, C., Yan, X., and Xu, Z. 2016. Optimum Time and Critical Re-Orientation Pressure of Re-Fracturing. Paper SPE 181837 presented at SPE Asia Pacific Hydraulic Fracturing Conference, Beijing, China, 24-26 August.

Lantz, T.G., Greene, D., Eberhard, M., Norrid, S., and Pershall, R. 2007. Refracture Treatments Proving Successful In Horizontal Bakken Wells: Richland Count, Montana. Paper SPE 108117 presented at Rocky Mountain Oil & Gas Technology Symposium, Denver, Colorado, U.S.A., 16-18 April.

Liu, H., Lan, Z., Zhang, G., Hou, F., He, X., and Liu, X. 2008. Evaluation of Refracture Reorientation in Both Laboratory and Field Scales. Paper SPE 112445 presented at SPE International Symposium and Exhibition on Formation Damage Control, Lafayette, Louisiana, USA, 13-15 February.

Luo, W., and Tang, C. 2015. Pressure-Transient Analysis of Multiwing Fractures Connected to a Vertical Wellbore. *SPE J*. 20 (02) 360-367.

Medlin, W.L., and Masse, L. 1984. Laboratory Experiments in Fracture Propagation. *SPE J.* 24 (03): 256-268.

Potapenko, D.I., Tinkham, S.K., Lecerf, B., Fredd, C.N., Samuelson, M.L., Gillard, M.R., Le Calvez, J.H., and Daniels, J.L. 2009. Barnett Shale Refracture Stimulations Using a Novel Diversion Technique. Paper SPE 119636 presented at SPE Hydraulic Fracturing Technology Conference, The Woodlands, Texas, 19-21 January.

Roussel, N.P., and Sharma, M.M. 2012. Role of Stress Reorientation in the Success of Refracture Treatments in Tight Gas Sands. *SPE Prod. Oper.* 27 (4): 346-355.

Roussel, N.P., and Sharma, M.M. 2010. Quantifying Transient Effects in Altered-Stress Refracturing of Vertical Wells. *SPE J*. 15 (3): 770-782.

Roussel, N.P., and Sharma, M.M. 2013. Selecting Candidate Wells for Refracturing Using Production Data. *SPE Prod. Oper.* 28 (1): 36-45.

Ruhle, W. 2016. Refracturing: Empirical Results in the Bakken Formation. Paper URTEC 2461740 presented at Unconventional Resources Technology Conference, San Antonio, Texas, USA, 1-3 August.

Siebrits, E., Elbel, J.L., Detournay, E., Detouray-Piette, C., Christianson, M., Robinson, B.M., and Diyashev, I.R. 1998. Parameters Affecting Azimuth and Length of a Secondary

Fracture During a Refracture Treatment. Paper SPE 48928 presented at SPE Annual Technical Conference and Exhibition, New Orleans, Louisiana, 27-30 September.

Siebrits, E., Elbel, J.L., Hoover, R.S., Diyashev, I.R., Griffin, L.G., Demntrius, S.L., Wright, C.A., Davidson, B.M., Steinsberger, N.P., and Hill, D.G. 2000. Refracture Reorientation Enhances Gas Production in Barnett Shale Tight Gas Wells. Paper SPE 63030 presented at SPE Annual Technical Conference and Exhibition, Dallas, Texas, 1-4 October.

Spivey, J.P. and Lee, W.J. 1998. New Solutions for Pressure Transient Response for a Horizontal or a Hydraulically Fractured Well at an Arbitrary Orientation in an Anisotropic Reservoir. Paper SPE 49236 presented at SPE Annual Technical Conference and Exhibition, New Orleans, Louisiana, 27-30 September.

Warpinski, N.R., and Branagan, P.T. 1989. Altered-Stress Fracturing. *J. Pet. Tech.* 41 (9): 990-997.

Weng, X., and Siebrits, E. 2007. Effect of Production-Induced Stress Field on Refracture Propagation and Pressure Response. Paper SPE 106043 presented at SPE Hydraulic Fracturing Technology Conference, College Station, Texas, U.S.A., 29-31 January.

Wolhart, S.L., Mclntosh, G.E., Zoll, M.B., and Weijers, L. 2007. Surface Tiltmeter Mapping Shows Hydraulic Fracture Reorientation in the Codell Formation, Wattenberg Field, Colorado. Paper SPE 106043 presented at SPE Hydraulic Fracturing Technology Conference, College Station, Texas, U.S.A., 29-31 January.

Wright, C.A., Conant, R.A., Stewart, D.W., and Byerly, P.M. 1994. Reorientation of Propped Refracture Treatments. Paper SPE 28078 presented at Rock Mechanics in Petroleum Engineering, Delft, Netherlands, 29-31 August.

Yang, D., Zhang, F., Styles, J.A., and Gao, J. 2015. Performance Evaluation of a Horizontal Well With Multiple Fractures by Use of a Slab-Source Function. *SPE J.* 20 (03): 652-662.

Yu, W., Wu, K., and Sepehrnoori, K. 2016. A Semianalytical Model for Production Simulation From Nonplanar Hydraulic-Fracture Geometry in Tight Oil Reservoirs. *SPE J.* 21 (3) 1028-1040.

Zhao, B., Zhang, G., and Lin, Q. 2016. The Application of Cryogenic Treatment during Refracture Process - Laboratory Studies. Paper ARMA-2016-552 presented at 50th U.S. Rock Mechanics/Geomechanics Symposium, Houston, Texas, 26-29 June.

Zhou, W., Banerjee, R., Poe, B.D., and Spath, J. 2014. Semianalytical Production Simulation of Complex Hydraulic-Fracture-Networks. *SPE J.* 19 (01): 6-18.

CHAPTER 6 A NOVEL ANALYTICAL FRACTURE PERMEABILITY MODEL DEPENDENT ON BOTH FRACTURE WIDTH AND PROPPANT-PACK PROPERTIES

A version of this chapter has been submitted for peer review

Summary

For an empty fracture, the fracture permeability (k_f) is mainly influenced by the effect of viscous shear and can be analytically estimated if the fracture width (w_f) is known a priori (i.e., $k_f = \beta_2 w_f^2 / 12$, where β_2 is unit conversion factor). For an adequately propped fracture, the fracture permeability is mainly influenced by the proppant-pack properties and can be approximated with the proppant-pack permeability ($k_f = k_p$, where k_p is proppant-pack permeability). It can be readily inferred that as the effect of viscous shear fades (or the effect of proppant-pack becomes pronounced), there should be a regime within which both the fracture width and the proppant-pack properties exert significant influences on the fracture permeability. However, the functional relationship between fracture permeability, fracture width, and proppant-pack properties is still elusive. In this work, we propose a new fracture permeability model to account for the influences of the proppant-pack permeability, proppant-pack porosity (ϕ_p), and fracture width on the fracture permeability. This new fracture permeability model is derived from a modified Brinkman equation. The results calculated with the fracture permeability model show that with different values of Darcy parameter the fluid flow can be divided into viscous-shear dominated (VSD) regime, transition regime, and Darcy-flow dominated (DFD) regime. If Darcy parameter is sufficiently large, the effect of proppant-pack permeability on fracture permeability can be neglected and the fracture permeability can be calculated with viscous-shear-dominated fracture-permeability (VSD-FP) equation (i.e., $k_f = \beta_2 \phi_p w_f^2 / 12$), whereas, if Darcy parameter is sufficiently small, the effect of viscous shear on fracture permeability can be neglected and the fracture permeability can be calculated with Darcy-flow-dominated fracture-permeability (DFD-FP) equation (i.e. $k_f = k_p$). Both the VSD-FP equation and DFD-FP equation are special forms of

the proposed fracture permeability model. For the existing empirical/analytical fracture conductivity models that neglect the effect of viscous shear, one can multiply these models by the coefficient of viscous shear in order to make these models capable of estimating the fracture conductivity with large values of Darcy parameter.

6.1. Introduction

If the fluid flow velocity is sufficiently high in a porous media, the effect of viscous shear cannot be neglected and the fluid flow will be in a transition regime between Darcy flow and Navier-Stokes (N-S) flow. In practice, such flow is normally characterized by the Brinkman equation (Brinkman, 1949). In a hydraulically fractured reservoir, a high flow velocity can be observed in the propped fracture. In such cases, the Brinkman equation is preferred to characterize fracture flow than Darcy's law. However, solving the Brinkman equation is far more computationally demanding than solving Darcy's equation. In addition, it is normally not convenient to find out whether Darcy's law or the Brinkman equation is optimal for a specific case before performing the simulation. Therefore, it is highly necessary to account for the influence of viscous shear on the effective permeability of a propped fracture, such that the fracture flow can be simply characterized by inserting the effective fracture permeability into Darcy's law.

A propped fracture can be divided into two sub-systems, including the proppant pack and the fracture walls. The proppant pack provides the fluid with a pathway to flow through the fractures, and the ability of the proppant pack to transmit the fluid can be characterized by proppant-pack permeability. The fracture walls influence the flow velocity via the effect of viscous shear, and such an effect can be quantified if the fracture width is determined a priori. Although it is widely known that the fracture permeability is a function of the proppant-pack properties together with the fracture width, such a functional relationship is still elusive.

For an unpropped vertical fracture, the fluid flow in the fracture can be regarded as plane Poiseuille flow, and the flux rate can be calculated with (Sutera and Skalak, 1993):

$$q = \beta_1 \beta_2 \frac{w_f^3}{12\mu} h_f \frac{\mathrm{d}p}{\mathrm{d}L} \tag{6-1}$$

Based on Darcy's law the flux rate can also be calculated with (Darcy, 1856):

$$q = \beta_1 \frac{k_f}{\mu} w_f h_f \frac{\mathrm{d}p}{\mathrm{d}L} \tag{6-2}$$

Substituting Equation (6-1) into Equation (6-2) yields the permeability of an unpropped fracture, which is written as:

$$k_f = \frac{\beta_2 w_f^2}{12} \tag{6-3}$$

If a fracture is propped and the fracture permeability is mainly affected by the viscous shear from the fracture walls, the porosity of the proppant pack should be added to Equation (6-3), and we will have:

$$k_f = \frac{\beta_2 \phi_p w_f^2}{12} \tag{6-4}$$

In particular, for an empty fracture ϕ_p = 1, Equation (6-4) can be reduced to Equation (6-3). For convenience, if the fracture permeability can be calculated with Equation (6-4), we consider that the fluid flow is in a viscous-shear-dominated (VSD) regime and Equation (6-4) is called viscous-shear-dominated fracture-permeability (VSD-FP) equation in this study. On the other hand, if the fracture width is sufficiently large, the viscous shear from the fracture walls can be neglected and the fracture permeability can be approximated with the proppant-pack permeability, which is expressed as follows:

$$k_f = k_p \tag{6-5}$$

Hence, estimating the fracture permeability can be simplified to estimating the proppant-pack permeability. For the sake of convenience, the flow regime in such scenarios is named as Darcy-flow-dominated (DFD) regime and Equation (6-5) is called Darcy-flow-dominated fracture-permeability (DFD-FP) equation in this study. **Table 6-1** summaries some of the equations that have been widely used to calculate the proppant-pack permeability (Krumbein and Monk, 1943; Carman, 1956; Berg, 1970; van Baaren, 1979; Carman, 1997; Glover *et al.*, 2006). At present, although both VSD-FP equation and the DFD-FP equation have been widely used to estimate the fracture permeability, it is difficult to determine which equation is optimal for a specific scenario. In other words, as the fracture width is increased, the influence of the viscous shear from the fracture walls on the fluid flow becomes less pronounced, and the method of calculating the fracture permeability is transitioned from VSD-FP equation to DFD-FP equation. **Figure 6-1** presents the results of a calculation example in a log-log plot to compare the fracture permeability that is calculated with VSD-FP equation against the fracture permeability that is calculated with the DFD-FP equation. The fracture permeability is calculated with different fracture width and a constant proppant-pack permeability. Based on Figure 6-1, one can readily put forward the following questions: does there exists a smooth transition (see the black dashed line in Figure 6-1) between the results of VSD-FP equation and those of the DFD-FP equation? If there exists, how to describe such a transition?

Table 6-1. Equations that can be used to calculate the proppant-pack permeability.

Name	Equation	Notes (the meanings and the units of the symbols are only used for the equations shown in this table)
Krumbein and Monk equation (Krumbein and Monk, 1943)	$k_p = 760D^2 \exp\left(-1.31\sigma_D\right)$	k_p = permeability, D D = geometric mean grain diameter, mm σ_D = standard deviation of grain size in phi units

Kozeny-Carman equation (Carman, 1937; Carman, 1956)	$k_p = \frac{cD^2\phi_p^3}{\left(1-\phi_p\right)^2}$	k_p = permeability, mD c = proportionality and unit factor, mD/mm^2 D = geometric mean grain diameter, mm ϕ_p = porosity
Berg equation (Berg, 1970)	$k_p = 80.8\times10^{-1.385\gamma}\times D^2\phi_p^{5.1}$	k_p = permeability, D γ = sorting term in phi units D = geometric mean grain diameter, mm ϕ_p = porosity
van Baaren equation (van Baaren, 1979)	$k_p = 10D_d^2\phi_p^{(3.64+m)}C^{-3.64}$	k_p = permeability, mD D_d = dominant grain size, μm ϕ_p = porosity m = cementation exponent C = sorting index which ranges from 0.7 to 1.0
RGPZ equation (Glover *et al*., 2006)	$k_p = \frac{D^2\phi_p^{3m}}{4am^2}$	k_p = permeability, m^2 D = geometric mean grain diameter, m ϕ_p = porosity a = parameter that equals to 8/3 for three dimensional samples composed of quasi-spherical grains m = cementation exponent

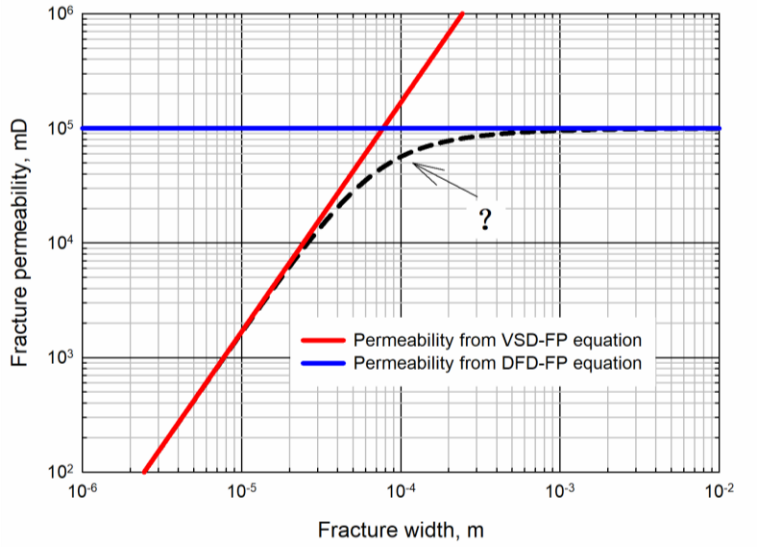

Figure 6-1. A calculation example showing the fracture permeability that is calculated with VSD-FP equation and DFD-FP equation.

In practice, the industry prefers to refer directly to the fracture conductivity for describing the fracture transmitting capability. Lacy *et al*. (1998) experimentally investigated the proppant embedment and fracture conductivity in soft formations. In their work, the embedment is studied as a function of proppant size, carrier fluid type, closure pressure, and leak-off rate. Fredd *et al*. (2001) explored the mechanisms by which the water-fracturing treatment provides sufficient fracture conductivity. The results of their work demonstrate that the fracture conductivity can be significantly influenced by the degree of fracture displacement, the size and distribution of asperities, and rock mechanical properties. More experimental works about the propped fracture conductivity can be found in Pope *et al*. (1996), David (2000), Nguyen *et al*. (2000), Weaver *et al*. (2010), Alramahi and Sundberg (2012), Zhang *et al*. (2014), and Awoleke *et al*. (2016). On the basis of the experimental results, various empirical formulations have been proposed to calculate the fracture conductivity. However, such empirical formulations bear two major deficiencies: firstly, the regressed coefficients are highly dependent on the input experimental data. This implies that the accuracy of such empirical models might not be satisfactory in certain field cases, and it can be a heavy load if one wants to update the coefficients by conducting new experiments; and secondly, the empirical models normally lack clear explanation on the mechanism by which the influencing factors exert their effects on the fracture conductivity. In addition, it should be noted that some of these conductivity-test experiments were conducted with a relatively large fracture width, which indicates that the viscous shear from the fracture walls may not show its effect during these tests. Hence, for a fracture that has a sufficiently small width, it can be inappropriate to infer its conductivity on the basis of such test results.

In order to avoid the deficiencies of the empirical models, researchers also derive analytical models to estimate the fracture conductivity on the basis of theoretical studies. Darin and Huitt (1960) developed an analytical model to consider the effect of partial-monolayer proppant pack on the fracture conductivity. Their model was derived from the Kozeny-Carman equation (1937) and was further validated against experimental methods. Li *et al*. (2015) proposed mathematical models for calculating the proppant embedment and fracture conductivity. In their models, the proppant deformation and the change in fracture aperture can also be considered. Zhang *et al*. (2016) derived a theoretical model from Berg's correlation (1970) to calculate fracture conductivity in shale. This model relates the fracture conductivity to proppant size, packing, sorting, crushing, grain rearrangement, proppant embedment, and water-induced damage. However, in all these theoretical models, the fracture permeability is approximated with proppant-pack permeability, which is reasonable only if the effect of viscous shear from the fracture walls can be neglected. Under such a restriction, these developed models can be inapplicable to the scenario where the effect of viscous shear cannot be neglected.

Based on the aforementioned arguments, we can conclude that: firstly, the fracture permeability is a function of proppant-pack properties as well as fracture width, but such a functional relationship has not been well elucidated; secondly, if the conductivity test is conducted with a large fracture width, it can be inappropriate to use such test results to infer the conductivity of a fracture that has a small width; and lastly, the theoretical fracture-conductivity models are normally developed by approximating the fracture permeability with the proppant-pack permeability, implying that such models are not applicable if the effect of viscous shear cannot be neglected. It is thus highly necessary to develop a more versatile fracture permeability model that is applicable to a wide range of field conditions.

In this study, we derive a new fracture permeability model by considering the effect of viscous shear and the effect of proppant-pack properties on the fracture permeability. This new fracture permeability model is derived from a modified Brinkman equation, and it is validated against an analytical method and a numerical method. With the aid of this model, we can identify the flow regimes that can be observed in a fracture.

6.2. Methodology

At the start of this section, we first review the derivation of the Brinkman equation. Darcy's law describing the fluid flow velocity through porous media is given as:

$$\boldsymbol{v} = -\frac{\beta_1 k}{\mu}\nabla p \tag{6-6}$$

In an empty space, neglecting the inertial terms, the N-S equation for incompressible fluid is simplified to:

$$\Delta p = \frac{\mu}{\beta_2}\nabla^2 \boldsymbol{v} \tag{6-7}$$

The Brinkman equation (Brinkman, 1949) is obtained by combining Equation (6-6) and Equation (6-7):

$$\frac{\mu}{\beta_2}\nabla^2 \boldsymbol{v} - \frac{\mu}{\beta_1 k}\boldsymbol{v} - \nabla p = 0, \;\; \nabla \cdot \boldsymbol{v} = 0 \tag{6-8}$$

As shown in Equation (6-8), the Brinkman equation is a mix of Darcy's law and the N-S equation. The fundamental difference between the Brinkman equation and the N-S equation is that the Brinkman equation characterizes the fluid flow at a macroscopic scale as in Darcy's law, while the N-S equation describes the fluid flow at a microscopic scale. In addition, the Brinkman equation can extend Darcy's law to account for the dissipation of kinetic energy which is caused by viscous shear as in the N-S equation. However, it should be noted that the flow velocity ($\boldsymbol{v}$) in

Equation (6-6) represents the superficial velocity which is the rate of flow through the surface element of a unit area, whereas the flow velocity ($\boldsymbol{v}$) in Equation (6-7) represents the real flow velocity at the microscopic level. This indicates that the combination of Equation (6-6) and Equation (6-7) is reasonable only if the superficial flow velocity is very close to the real flow velocity. The subsequent discussion also demonstrates that the results from the Brinkman equation are only applicable to the scenarios where the volume fraction of the solid in the porous media is sufficiently small (Durlofsky and Brady, 1987; and Belhaj, *et al*., 2003). This is because the superficial flow velocity is closer to the real flow velocity at a smaller volume fraction of the solid.

At present, scholars have made various modifications on the Brinkman equations to expand its application scope. For example, the Brinkman equation used in Comsol is very powerful and versatile (Comsol, 2019). In this work, since we aim to investigate the influence of viscous shear on the permeability of a propped fracture, only minor modification is applied to the original Brinkman equation. In a porous media, the real flow velocity ($\boldsymbol{v}_r$) has the following relationship with the superficial flow velocity ($\boldsymbol{v}_s$):

$$\boldsymbol{v}_r = \frac{\boldsymbol{v}_s}{\phi_p} \tag{6-9}$$

Thus, in this work, the Equation (6-7) is modified to:

$$\Delta p = \frac{\mu}{\beta_2 \phi_p} \nabla^2 \boldsymbol{v} \tag{6-10}$$

and the original Brinkman equation can be modified as:

$$\frac{\mu}{\beta_2 \phi_p} \nabla^2 \boldsymbol{v} - \frac{\mu}{\beta_1 k} \boldsymbol{v} - \nabla p = 0, \quad \nabla \cdot \boldsymbol{v} = 0 \tag{6-11}$$

As such, the flow velocities (***v***) in Equations (6-6), (6-10) and (6-11) have the same meaning and all denote the superficial flow velocity. In order to account for the impact of viscous shear on the fracture permeability, we make the following assumptions:

- The fluid is incompressible and the viscosity of the fluid is constant;
- The fluid flow is a laminar flow and is in a steady state; and
- The effect of gravity is neglected.

It is worth noting that the above assumptions have also be made for deriving the VSD-FP equation. On the basis of the assumptions, Equation (6-8) can be reduced to:

$$\frac{\mu}{\beta_2 \phi_p}\left(\frac{\mathrm{d}^2 v}{\mathrm{d}l_2^2}\right) - \frac{\mu}{\beta_1 k_p} v - \frac{\partial p}{\partial l_1} = 0 \tag{6-12}$$

where l_1 indicates the direction parallel to the fracture wall and l_2 indicates the direction orthogonal to the fracture wall (see **Figure 6-2**). In addition, we have the following boundary conditions:

$$\begin{cases} v = v_0, & l_2 = 0 \\ v = v_0, & l_2 = w_f \end{cases} \tag{6-13}$$

The general solution of Equation (6-12) is:

$$v = A_1 \exp\left(\sqrt{\frac{\beta_2 \phi_p}{k_p}} l_2\right) + A_2 \exp\left(-\sqrt{\frac{\beta_2 \phi_p}{k_p}} l_2\right) - \frac{\beta_1 k_p}{\mu} \frac{\partial p}{\partial l_1} \tag{6-14}$$

where A_1 and A_2 are constants that need to be determined. Inserting the boundary conditions (Equation (6-13)) into Equation (6-14) gives:

$$\begin{cases} A_1 = \dfrac{\left(v_0 + \dfrac{\beta_1 k_p}{\mu}\dfrac{\partial p}{\partial l_1}\right)\left[1-\exp\left(-\sqrt{\dfrac{\beta_2\phi_p}{k_p}}w_f\right)\right]}{2\sinh\left(\sqrt{\dfrac{\beta_2\phi_p}{k_p}}w_f\right)} \\ A_2 = \dfrac{\left(v_0 + \dfrac{\beta_1 k_p}{\mu}\dfrac{\partial p}{\partial l_1}\right)\left[\exp\left(\sqrt{\dfrac{\beta_2\phi_p}{k_p}}w_f\right)-1\right]}{2\sinh\left(\sqrt{\dfrac{\beta_2\phi_p}{k_p}}w_f\right)} \end{cases} \tag{6-15}$$

Inserting Equation (6-15) into Equation (6-14) yields:

$$v = -\frac{\beta_1 k_p}{\mu}\frac{\partial p}{\partial l_1}\left\{1-\frac{\left(\dfrac{v_0}{\dfrac{\beta_1 k_p}{\mu}\dfrac{\partial p}{\partial l_1}}+1\right)\left\{\sinh\left(\sqrt{\dfrac{\beta_2\phi_p}{k_p}}l_2\right)+\sinh\left[\sqrt{\dfrac{\beta_2\phi_p}{k_p}}\left(w_f-l_2\right)\right]\right\}}{\sinh\left(\sqrt{\dfrac{\beta_2\phi_p}{k_p}}w_f\right)}\right\} \tag{6-16}$$

The flux rate q through the cross-section of the fracture can be obtained by integrating Equation (6-16) from $l_2 = 0$ to $l_2 = w_f$, which results in:

$$\begin{aligned} q &= h_f\int_0^{w_f} v\,\mathrm{d}l_2 \\ &= -\frac{\beta_1 h_f w_f k_p}{\mu}\frac{\partial p}{\partial l_1}\left\{1+\frac{2}{w_f}\left(\frac{v_0}{\dfrac{\beta_1 k_p}{\mu}\dfrac{\partial p}{\partial l_1}}+1\right)\sqrt{\frac{k_p}{\beta_2\phi_p}}\left[\operatorname{csch}\left(\sqrt{\frac{\beta_2\phi_p}{k_p}}w_f\right)-\coth\left(\sqrt{\frac{\beta_2\phi_p}{k_p}}w_f\right)\right]\right\} \end{aligned} \tag{6-17}$$

Combination of Equation (6-17) and Equation (6-2) leads to the following fracture permeability model:

$$k_f = k_p \left\{ 1 + \frac{2}{w_f} \left(\frac{v_0}{\frac{\beta_1 k_p}{\mu} \frac{\partial p}{\partial l_1}} + 1 \right) \sqrt{\frac{k_p}{\beta_2 \phi_p}} \left[\operatorname{csch}\left(\sqrt{\frac{\beta_2 \phi_p}{k_p}} w_f \right) - \coth\left(\sqrt{\frac{\beta_2 \phi_p}{k_p}} w_f \right) \right] \right\} \tag{6-18}$$

If the viscous shear from the fracture walls can be neglected, we will have

$$v_0 = -\frac{\beta_1 k_p}{\mu} \frac{\partial p}{\partial l_1} \tag{6-19}$$

Inserting Equation (6-19) into Equation (6-18) gives

$$k_f = k_p \tag{6-20}$$

This implies that the fracture permeability equals to the proppant-pack permeability if the effect of viscous shear from the fracture walls can be neglected. Such a result is consistent with the real observations. In addition, if there is no slippage at the fracture walls due to the effect of viscous shear, we will have v_0 = 0 m/d and Equations (6-16) and (6-18) can be reduced to:

$$v = -\frac{\beta_1 k_p}{\mu} \frac{\partial p}{\partial l_1} \left\{ 1 - \frac{\left\{ \sinh\left(\sqrt{\frac{\beta_2 \phi_p}{k_p}} l_2 \right) + \sinh\left[\sqrt{\frac{\beta_2 \phi_p}{k_p}} \left(w_f - l_2 \right) \right] \right\}}{\sinh\left(\sqrt{\frac{\beta_2 \phi_p}{k_p}} w_f \right)} \right\} \tag{6-21}$$

and

$$k_f = k_p \left\{ 1 + \frac{2}{w_f} \sqrt{\frac{k_p}{\beta_2 \phi_p}} \left[\operatorname{csch}\left(\sqrt{\frac{\beta_2 \phi_p}{k_p}} w_f \right) - \coth\left(\sqrt{\frac{\beta_2 \phi_p}{k_p}} w_f \right) \right] \right\} \tag{6-22}$$

Equation (6-22) characterizes the relationship between the fracture permeability, proppant-pack permeability, proppant-pack porosity, and fracture width. In this work, since the effect of the viscous shear from the fracture walls is considered, the investigations in the following sections are conducted on the basis of Equations (6-21) and (6-22). It should be noted that, in practice, the

proppant-pack permeability, proppant-pack porosity, and fracture width are highly dependent of proppant concentration, proppant sorting, proppant diameter, closure pressure, and rock softness, etc. Therefore, the influencing factors, including but not limited to these properties, have not been directly considered in this work. For practical application, such factors can be readily accommodated into our proposed model if the empirical/analytical relationship between these factors and fracture properties (including proppant-pack permeability, proppant-pack porosity, and fracture width) is constructed beforehand.

For an unpropped fracture, there is no proppant in the fracture and k_p can be regarded as infinite. Based on Taylor series expansion, Equation (6-22) can be rewritten as:

$$\begin{aligned} k_f &\approx k_p \left\{ 1+\frac{2}{w_f}\sqrt{\frac{k_p}{b_2 f}} \left[\begin{array}{l} \left(\sqrt{\frac{b_2 f_p}{k_p}} w_f \right)^{-1} - \frac{1}{6}\sqrt{\frac{b_2 f_p}{k_p}} w_f + \frac{7}{360}\left(\sqrt{\frac{b_2 f_p}{k_p}} w_f \right)^3 \\ -\left(\sqrt{\frac{b_2 f_p}{k_p}} w_f \right)^{-1} - \frac{1}{3}\sqrt{\frac{b_2 f_p}{k_p}} w_f + \frac{1}{45}\left(\sqrt{\frac{b_2 f_p}{k_p}} w_f \right)^3 \end{array} \right] \right\} \\ &= k_p \left\{ 1+\frac{2}{w_f}\sqrt{\frac{k_p}{b_2 f_p}} \left[-\frac{1}{2}\sqrt{\frac{b_2 f_p}{k_p}} w_f + \frac{1}{24}\left(\sqrt{\frac{b_2 f_p}{k_p}} w_f \right)^3 \right] \right\} \\ &= \frac{b_2 f_p w_f^2}{12} \end{aligned} \tag{6-23}$$

In addition, if the fracture width is sufficiently large (or the value of $\sqrt{k_p/\beta_2\phi}\Big/w_f$ is sufficiently small), the term $\frac{2}{w_f}\sqrt{\frac{k_p}{\beta_2\phi_p}}\left[\operatorname{csch}\left(\sqrt{\frac{\beta_2\phi_p}{k_p}} w_f \right) - \coth\left(\sqrt{\frac{\beta_2\phi_p}{k_p}} w_f \right) \right]$ in Equation (6-22) approaches 0. Thus we can have:

$$k_f = k_p \times \left\{ 1 + \frac{2}{w_f} \sqrt{\frac{k_p}{\beta_2 \phi_p}} \left[\operatorname{csch}\left(\sqrt{\frac{\beta_2 \phi_p}{k_p}} w_f \right) - \coth\left(\sqrt{\frac{\beta_2 \phi_p}{k_p}} w_f \right) \right] \right\}$$
$$\approx k_p \times \{1 + 0\} \quad (6\text{-}24)$$
$$= k_p$$

This indicates that the VSD-FP equation and the DFD-FP equation are both special forms of the proposed fracture permeability model.

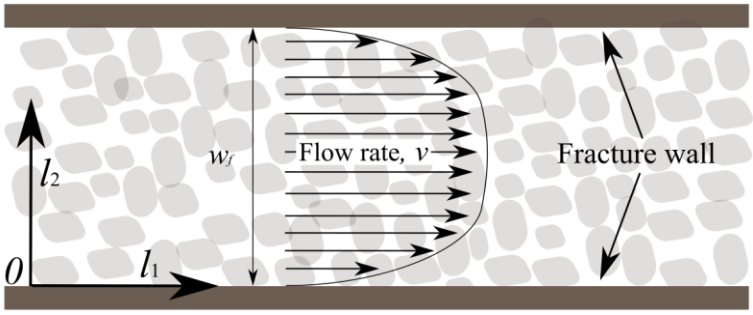

Figure 6-2. Schematic of fluid flow in the proppant pack between the fracture walls.

6.3. Model Validation

Due to the fact that there is no available experiment data or proposed method in the previous studies that can be used to validate the proposed fracture permeability model, the validation of the proposed fracture permeability model is conducted on two assumed propped fracture models. Fracture model #1 is shown in **Figure 6-3**. In Figure 6-3, the fracture is propped with impermeable slabs, and the fluid can flow in the channels between the slabs. Since the fracture permeability of such a propped fracture can be analytically calculated with the method introduced by Spiga and Morini (1994), we can validate the proposed fracture permeability model by comparing the results calculated with the proposed model against those calculated with the method of Spiga and Morini (1994). One of the major reasons for using such a fracture to validate the fracture permeability model is that, for this specific scenario, both the proppant-pack permeability and the fracture permeability can be analytically calculated.

Spiga and Morini (1994) derived the following equation to calculate the average flux velocity along a single rectangle channel (see Figure 6-3):

$$v_{ave} = \frac{64\beta_2 a^2}{\pi^6} \sum_{n-\text{odd}}^{\infty} \sum_{m-\text{odd}}^{\infty} \frac{1}{n^2 m^2 \left(n^2 + \frac{m^2}{b^2} \right)} \left(-\frac{1}{\mu} \frac{\mathrm{d}p}{\mathrm{d}l_1} \right) \tag{6-25}$$

where,

$$\begin{cases} a = \max\left\{ w_c, w_f \right\} \\ b = \dfrac{\min\left\{ w_c, w_f \right\}}{\max\left\{ w_c, w_f \right\}} \end{cases} \tag{6-26}$$

As such, the total flux rate q through a fracture, whose cross area is $w_f \times h_f$, can be obtained by:

$$q = v_{ave} w_f h_f \phi_p = \frac{64\phi_p \beta_2 a^2}{\pi^6} \sum_{n-\text{odd}}^{\infty} \sum_{m-\text{odd}}^{\infty} \frac{1}{n^2 m^2 \left(n^2 + \frac{m^2}{b^2} \right)} \left(-\frac{w_f h_f}{\mu} \frac{\mathrm{d}p}{\mathrm{d}L} \right) \tag{6-27}$$

Comparing Equation (6-27) to Darcy's Equation (6-2), we can have the fracture permeability written as:

$$k_f = \frac{64\phi_p \beta_2 a^2}{\pi^6} \sum_{n-\text{odd}}^{\infty} \sum_{m-\text{odd}}^{\infty} \frac{1}{n^2 m^2 \left(n^2 + \frac{m^2}{b^2} \right)} \tag{6-28}$$

With the aid of Equation (6-28), one can obtain the fracture permeability based on the method of Spiga and Morini (1994). In addition, the proppant-pack permeability should be independent of the fracture width. Neglecting the impact of the fracture wall, the permeability of a single channel between the slabs can be calculated with Equation (6-3), leading to:

$$k_c = \frac{\beta_2 w_c^2}{12} \tag{6-29}$$

whereas the permeability of the entire proppant-pack can be obtained by:

$$k_p = \phi_p k_c = \frac{\beta_2 \phi_p w_c^2}{12} \tag{6-30}$$

Inserting Equation (6-30) into Equation (6-22), one can also calculate the fracture permeability with the proposed fracture permeability model. As such, we can validate the proposed fracture permeability model by comparing the results of the proposed model to those obtained from the method of Spiga and Morini (1994). The values of the parameters used for validating the fracture permeability model are as follows: w_c = 1×10^{-3} m, ϕ = 0.2, β_2 is a unit conversion factor whose numerical value is 1.01×10^{15}, and w_f is varied from 1×10^{-5} m to 1×10^{-1} m. **Figure 6-4** compares the fracture permeability that is calculated with the proposed model against the fracture permeability that is calculated with the method of Spiga and Morini (1994). From Figure 6-4, one can find that the fracture permeability calculated with the proposed fracture permeability model has an excellent agreement with that calculated with the method of Spiga and Morini (1994), which partly verifies the correctness of the newly proposed fracture permeability model.

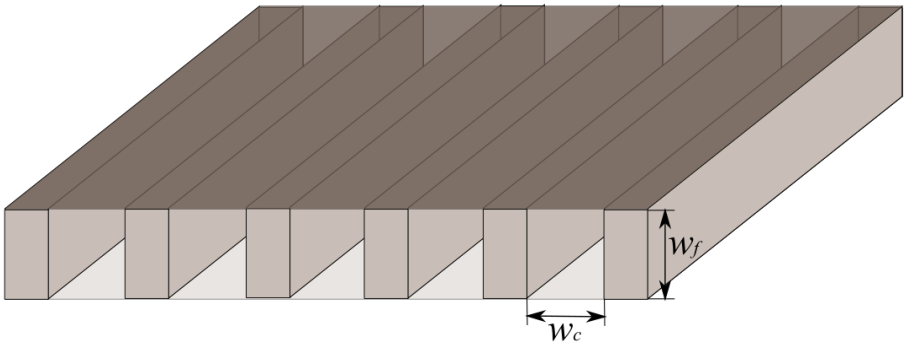

Figure 6-3. Schematic of an assumed propped fracture (w_c is width of the channel, and w_f is fracture width).

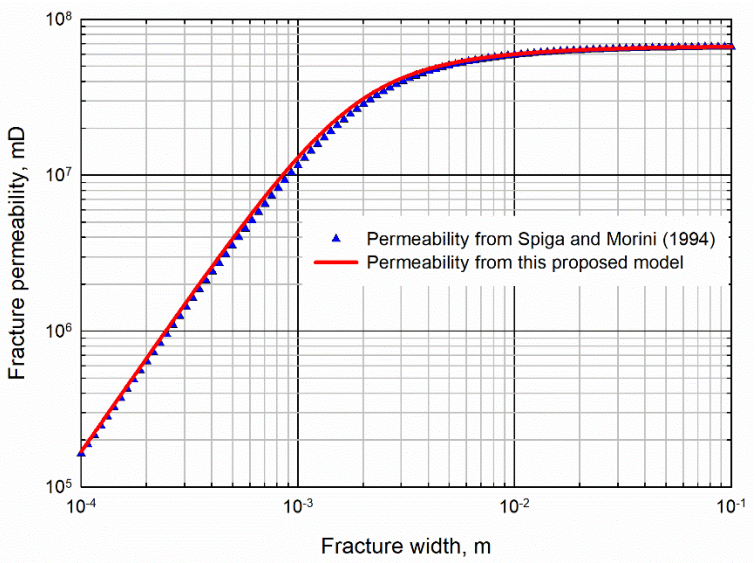

Figure 6-4. Comparison between the fracture permeability of the fracture shown in Figure 6-3 that is calculated with the proposed model and the fracture permeability that is calculated with the method of Spiga and Morini (1994).

Moreover, the validation is also conducted on a numerical fracture model (i.e. model #2) which is shown in **Figure 6-5**. This model is constructed with Comsol. In this figure, the cylinder holes represent proppants, the upper and lower surfaces (surfaces orthogonal to the z-axis) represent fracture walls, and the front and back surfaces (surfaces orthogonal to the y-axis) are impermeable walls. The fluid flows into the fracture model through the inlet surface and flows out of the fracture model through the outlet surface. The radius of the cylinder along *x*-*y* plane is 5×10^{-4} m, the length of model #2 along *x*-axis (L_x) is 1.15×10^{-2} m, the length of model #2 along *y*-axis (L_y) is 4×10^{-3} m, the aperture between the upper and lower surfaces (this aperture is equivalent to fracture width w_f) is varied from 1×10^{-5} m to 1×10^{-2} m, the flow rate is 864 m/d, and the viscosity of the fluid is 1 mP·s. The pressure distribution in this model is calculated with the N-S equation in Comsol. Therefore, the permeability of the porous media can be calculated based on Darcy's law if the average pressures at the surfaces of the inlet and outlet are measured. The proppant-pack permeability is calculated by neglecting the slippage at the upper, lower, front, and back surfaces, whereas the fracture permeability is calculated by neglecting the slippage at front

and back surfaces while considering the slippage at upper and lower surfaces. Since the proppant-pack permeability is independent of aperture, the proppant-pack permeability is only calculated with an aperture of 1×10^{-3} m. **Table 6-2** lists the measured average pressures at the inlet and outlet surfaces as well as the corresponding apertures between the upper and lower surfaces.

On the basis of the measured data in Table 6-2, the proppant-pack permeability can be calculated as follows:

$$k_p = \frac{v\mu L}{\beta_1\left(p_{in} - p_{out}\right)} = \frac{864\times1\times1.15\times10^{-2}}{0.0853\times\left(14.38\times10^{-6} - 0.00\times10^{-6}\right)} = 8.10\times10^{6}\,\text{mD} \tag{6-31}$$

The porosity of the proppant-pack can be obtained by:

$$\phi_p = \frac{\pi r_p^2 w_f}{L_x L_y w_f} = \frac{\pi r_p^2}{L_x L_y} \approx \frac{3.14\times\left(5\times10^{-4}\right)^2}{1.15\times10^{-2}\times4\times10^{-3}} = 0.4437 \tag{6-32}$$

Hence, the fracture permeability can be calculated with the proposed fracture permeability model by inserting the results of Equations (6-31) and (6-32) and the corresponding aperture into Equation (6-22). In addition, the fracture permeability can be calculated with the same method as Equation (6-31) based on the measured data in **Table 6-2**. **Figure 6-6** compares the results from the proposed fracture permeability model against those calculated from the Comsol simulation outputs. It is found that the results from the proposed model agree well with the results from the Comsol outputs. The results shown in Figures 6-4 and 6-6 imply that the proposed fracture permeability model is capable of characterizing the effects of viscous shear and proppant-pack on the fracture permeability.

Table 6-2. Data used in the model built by Comsol for validating the proposed fracture permeability model.

Porous media	Aperture, 10^{-3} m	Average pressure at the inlet surface, 10^{-6} MPa	Average pressure at the outlet surface, 10^{-6} MPa
Proppant pack	1.00	14.38	0.00

Fracture	0.01	31416.00	1.86
	0.02	7969.80	0.88
	0.04	2052.20	0.39
	0.06	959.59	0.29
	0.08	554.60	0.21
	0.10	380.64	0.19
	0.50	34.07	0.03
	1.00	21.21	0.01
	5.00	15.06	0.01
	10.00	14.61	0.01

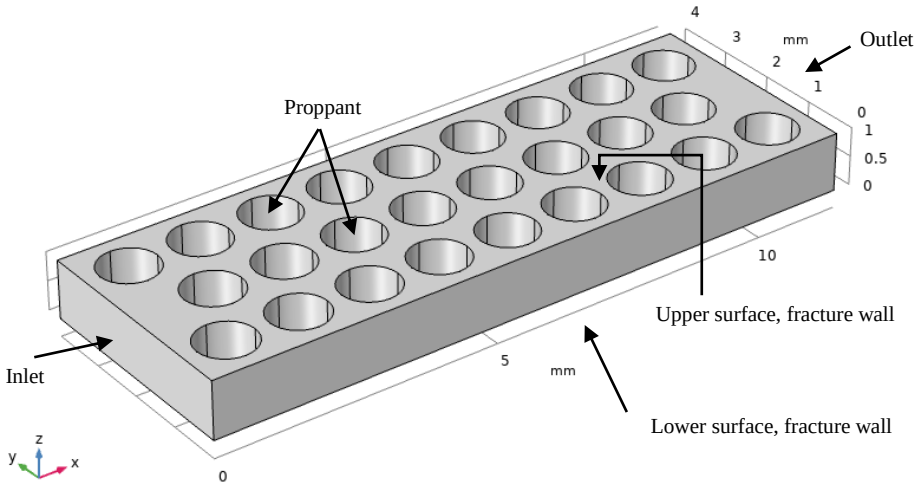

Figure 6-5. A propped fracture model constructed in Comsol for validation purpose.

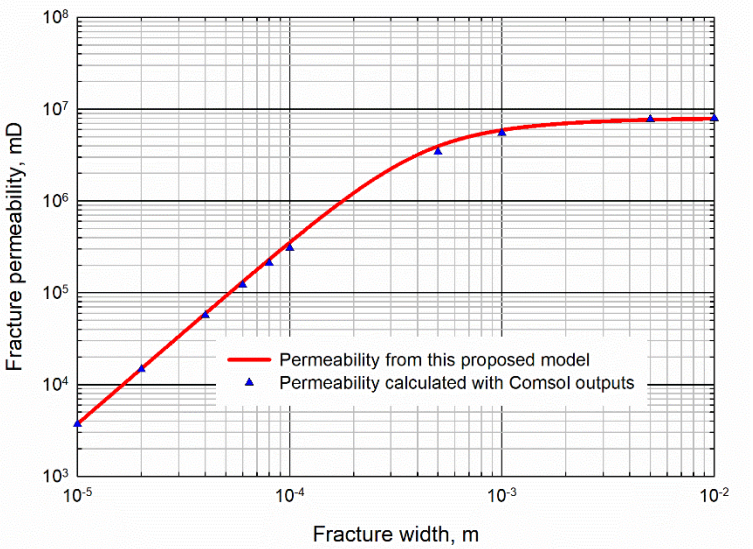

Figure 6-6. Comparison between the fracture permeability that is calculated with the proposed model and the fracture permeability that is calculated with the results of Comsol.

6.4. Results and Discussion

For the sake of convenience, we define the following dimensionless parameters in this section:

$$l_{2D} = \frac{l_2}{w_f}, w_{fD} = \frac{w_f}{w_f} = 1 \tag{6-33}$$

and

$$v_D = -\frac{v\mu}{\beta_1 k_p \dfrac{\partial p}{\partial l_1}} \tag{6-34}$$

The Darcy parameter is defined as (Parvazinia *et al.*, 2005):

$$D_a = \frac{k_p}{\beta_2 \phi_p w_f^2} \tag{6-35}$$

Inserting Equations (6-33) through (6-35) into Equations (6-21) and (6-22) yields:

$$v_D = 1 + \frac{\sinh\left[\sqrt{\dfrac{1}{D_a}}\left(l_{2D} - 1\right)\right] - \sinh\left(\sqrt{\dfrac{1}{D_a}} l_{2D}\right)}{\sinh\left(\sqrt{\dfrac{1}{D_a}}\right)} \tag{6-36}$$

and

$$k_f = k_p \left\{1 + 2\sqrt{D_a}\left[\operatorname{csch}\left(\sqrt{\frac{1}{D_a}}\right) - \coth\left(\sqrt{\frac{1}{D_a}}\right)\right]\right\} \tag{6-37}$$

In Equation (6-36), the second term on the right-hand side indicates the impact of viscous shear on the flow velocity. $v_D = 1$ indicates that the fluid flow is totally governed by Darcy's law. With the aid of the proposed fracture permeability model, we carry out a comprehensive study on the influences of proppant-pack permeability and fracture width on the fracture permeability. We also investigate the velocity profiles in propped fractures with different values of Darcy

parameter. Furthermore, we apply this proposed fracture permeability model together with a semi-analytical model to conduct a post-fracture analysis on a field case.

6.4.1 Sensitivity Analysis

Figure 6-7 presents the fracture permeability (blue solid line) that is calculated by use of the proposed fracture permeability model with a constant proppant-pack permeability (k_p = 1×10^5 mD), constant proppant-pack porosity (ϕ_p =0.2), and different fracture widths (w_f is varied from 1×10^{-6} m to 1×10^{-2} m). In Figure 6-7, the red dashed line shows the fracture permeability that is calculated with VSD-FP equation and the yellow dashed line illustrates the fracture permeability that is calculated with DFD-FP equation. From Figure 6-7 one can find that the change of the fracture permeability can be divided into three regimes:

- VSD regime: this regime can be observed if the fracture width is sufficiently small. During this regime, the results of the proposed fracture-permeability model have a good agreement with those of VSD-FP equation, and the influence of proppant-pack permeability on the fracture permeability can be neglected;
- Transition regime: this regime bridges the VSD regime with the DFD regime. During this regime, both the viscous shear and proppant-pack exert significant influences on the fracture permeability;
- DFD regime: if the fracture width is sufficiently large, the fracture permeability approaches the proppant pack permeability and the results from the proposed fracture permeability model agree well with those from DFD-FP equation. The effect of viscous shear on the fracture permeability can be neglected during this regime.

Figure 6-8 shows the fracture permeability (blue solid line) that is calculated based on the proposed fracture permeability model with a constant fracture width (w_f = 1×10^{-4} m), constant

proppant-pack porosity (ϕ_p =0.2), and different proppant-pack permeability (k_p is varied from 1×10^3 mD to 1×10^9 mD). In this figure, the red dashed line indicates the fracture permeability that is calculated with VSD-FP equation and the yellow dashed line implies the fracture permeability that is calculated with DFD-FP equation. In Figure 6-8, one can also identify three regimes, including the DFD regime, the transition regime, and the VSD regime.

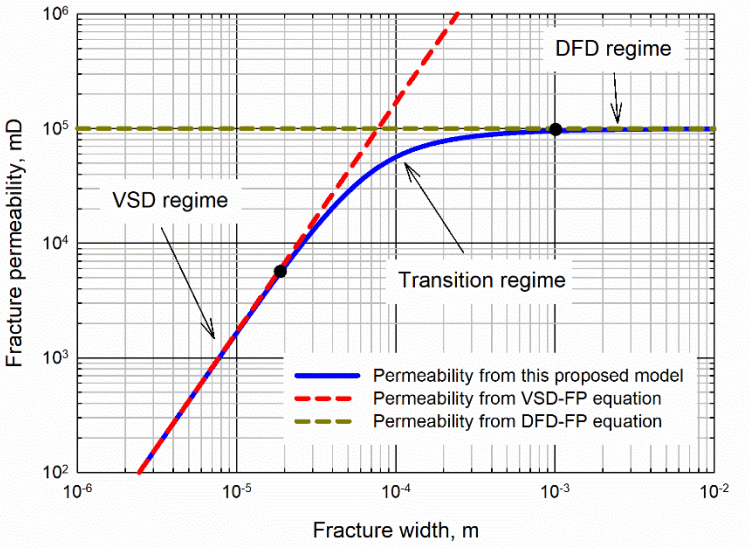

Figure 6-7. Fracture permeability that is calculated with constant proppant-pack permeability, constant proppant-pack porosity, but different fracture widths.

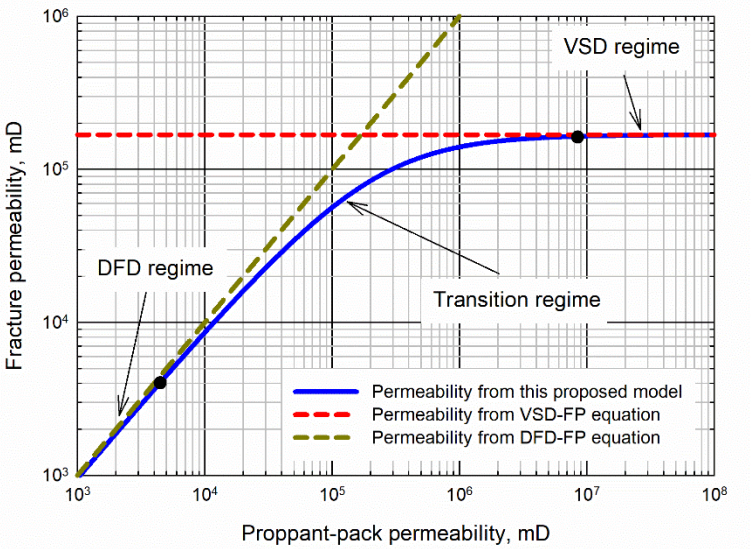

Figure 6-8. Fracture permeability that is calculated with constant fracture width, constant proppant-pack porosity, but different proppant-pack permeability.

The relative absolute deviation between the results of the proposed model and those of VSD-FP/DFD-FP equation can be calculated by:

$$\varepsilon = \left| \frac{K_1 - K_2}{K_2} \right| \times 100\% \tag{6-38}$$

where ε is relative absolute deviation, K_1 is fracture permeability that is calculated with VSD-FP equation or DFD-FP equation, and K_2 is fracture permeability that is calculated with the proposed model. Inserting Equations (6-4), (6-5), (6-35), and (6-37) into Equation (6-38) yields:

if K_1 is calculated with VSD-FP equation (i.e., Equation (6-4)),

$$\varepsilon = \left| \frac{1}{12D_a \left\{ 1 + 2\sqrt{D_a} \left[\operatorname{csch}\left(\sqrt{\frac{1}{D_a}} \right) - \coth\left(\sqrt{\frac{1}{D_a}} \right) \right] \right\}} - 1 \right| \times 100\% \tag{6-39}$$

and if K_1 is calculated with DFD-FP equation (i.e., Equation (6-5)),

$$\varepsilon = \left| \frac{1}{\left\{ 1 + 2\sqrt{D_a} \left[\operatorname{csch}\left(\sqrt{\frac{1}{D_a}} \right) - \coth\left(\sqrt{\frac{1}{D_a}} \right) \right] \right\}} - 1 \right| \times 100\% \tag{6-40}$$

Taking 5% as the threshold value, if ε is less than 5%, one can think that the fracture permeability can be calculated with VSD-F equation or DFD-FP equation. Setting

$$\varepsilon \le 5\% \tag{6-41}$$

and inserting Equations (6-39) and (6-40) into Equation (6-41), one can obtain:

if K_1 is calculated with VSD-FP equation (i.e., Equation (6-4)),

$$\left| \frac{1}{12D_a\left\{1+2\sqrt{D_a}\left[\operatorname{csch}\left(\sqrt{\frac{1}{D_a}}\right)-\coth\left(\sqrt{\frac{1}{D_a}}\right)\right]\right\}}-1 \right| \times 100\% \le 5\% \qquad (6\text{-}42)$$

and if K_1 is calculated with DFD-FP equation (i.e., Equation (6-5)),

$$\left| \frac{1}{1+2\sqrt{D_a}\left[\operatorname{csch}\left(\sqrt{\frac{1}{D_a}}\right)-\coth\left(\sqrt{\frac{1}{D_a}}\right)\right]}-1 \right| \times 100\% \le 5\% \qquad (6\text{-}43)$$

The solutions of Equations (6-42) and (6-43) are $D_a \ge 2.00$ and $D_a \le 5.67\times10^{-4}$, respectively. This indicates that, taking 5% as the threshold value for the relative absolute deviation, if $D_a \ge 2.00$, the effect of proppant-pack permeability on the fracture permeability can be neglected and the fracture permeability can be calculated with VSD-FP equation, whereas, if $D_a \le 5.67\times10^{-4}$, the effect of viscous shear on the fracture permeability can be neglected and the fracture permeability can be calculated with DFD-FP equation.

6.4.2 Velocity Profiles

With the aid of Equation (6-36), we calculate the dimensionless superficial flow velocity along the cross-section of a fracture with different values of D_a (D_a = 1×10^{-5}, 1×10^{-4}, 1×10^{-3}, 1×10^{-2}, and 1×10^{-1}); the calculated results are shown in **Figure 6-9**. As defined in Equation (6-34), $v_D = 1$ represents that the fluid flow is Darcy flow. As one can see from Figure 6-9, with a small value of D_a (e.g., $D_a = 1\times10^{-5}$), the viscous shear exerts a small impact on the fluid flow, and the flow velocities approach a constant value of 1. In addition, with a large value of D_a (e.g., $D_a = 1\times10^{-1}$), the flow velocity is significantly jeopardized due to the impact of viscous shear. This indicates that with small values of D_a the fluid flow in fractures is dominated by Darcy flow, whereas with

large values of D_a the fluid flow is significantly influenced by viscous shear. As the Darcy parameter is increased, the regime of the fluid flow in the fractures is varied from DFD regime to VSD regime. At present, the fracture permeability has been commonly approximated with the proppant-pack permeability for conducting the post-fracture analysis and developing analytical fracture conductivity models (Li *et al.*, 2015; Zhang *et al.*, 2016). Such an approximation is reasonable only if the value of D_a is sufficiently small and the fluid flow in the fracture is in DFD regime. However, in real filed cases, the fluid flow in the fractures can be in the transition regime or even VSD regime, and neither the effect of viscous shear nor the effect of proppant-pack on the fracture permeability can be neglected. A large value of D_a can be observed in the following scenarios: firstly, if the rock is sufficiently soft, the fracture width can be very small because of the embedment of the proppants; and secondly, if the proppant concentration is sufficiently small, the proppant-pack permeability can be very large (e.g., a natural fracture, in which the proppant concentration is 0 and the proppant-pack permeability is infinite, can be regarded as an extreme case).

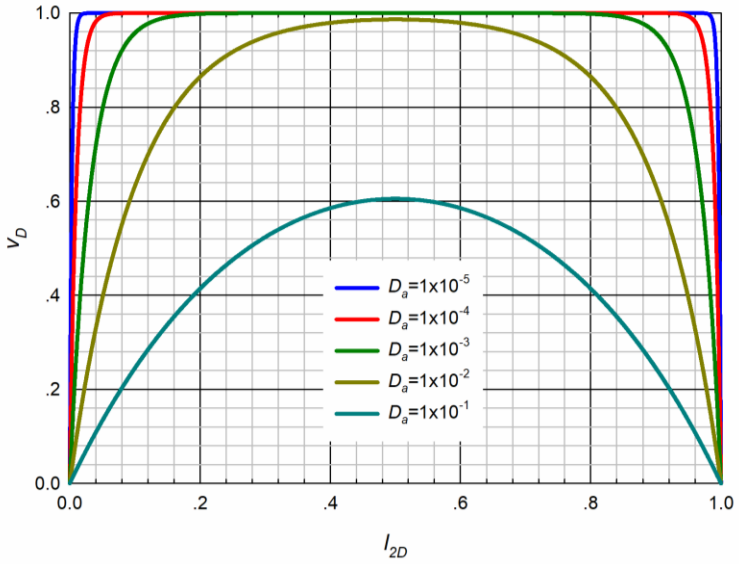

Figure 6-9. Dimensionless flow velocities that are calculated with different values of Darcy parameter along the cross-section of a fracture.

6.4.3. Applications of the Proposed Fracture Permeability Model

In this section, we investigate the effect of viscous shear from fractures walls on the well performance. We also apply the proposed fracture permeability model to conduct history matching work on a fractured well. The simulation work in this section is conducted with a semi-analytical model which is modified from the model introduced by Teng and Li (2019). Compared with the numerical method, the semi-analytical models tend to be more conveniently used for constructing the fractures models and also more computationally efficient. The details of constructing the semi-analytical model are introduced in **Appendices 6A**, **6B**, and **6C**.

Field studies and simulation results show that the width of a hydraulic fracture is normally not uniform along both the vertical and horizontal directions (Morita *et al*., 1988; Gu and Leung, 1993; Swaby and Rawnsley, 1997; Wright *et al*., 1998). Therefore, the fracture model used in this section has a non-uniform width distribution, as shown in **Figure 6-10**. In Figure 6-10, X_f is half fracture length, W_f is fracture width at the wellbore location, and H_f is fracture height at the wellbore location. For the purpose of simplification, we assume that the cross-sections of the fracture along the *x*-*y*, *x*-*z*, and *y*-*z* planes are all ellipses, such that the fracture width distribution can be readily calculated if the values of X_f, W_f, and H_f are given. The fluid in the reservoir is single-phase oil and the properties of the fluid and rock are maintained as constant. The benchmark values of the parameters used in the simulations are as follows: $k_p = 1\times10^5$ mD, X_f = 100 m, $W_f = 2.5\times10^{-4}$ m, H_f = 50 m, ϕ_p = 0.1, c_{tf} = 0.0012 MPa^{-1}, z_e = 60 m, k_m = 2 mD, c_{tm} = 0.0012 MPa^{-1}, ϕ_m = 0.1, C_w = 0.1 m^3/MPa, B = 1.2, r_w = 0.05 m, μ = 5 mPa·s, q_w = 10 m^3/d for the constant production rate case, and p_w = 10 MPa for the constant bottomhole pressure case. At the late production period or in the scenario of sufficiently soft rock, the embedment of the proppant can be significant and the fracture width can be very small (Alramahi and Sundberg, 2012).

When the fracture width is sufficiently small, the effect of the viscous shear from the fracture walls cannot be neglected. In order to investigate the effect of viscous shear on the well performance, W_f in the benchmark model is assigned with a small value. For comparison purpose, the well performance is also studied by neglecting the effect of the viscous shear. In the cases where the effect of viscous shear is neglected, the fracture permeability is approximated with the proppant-pack permeability (i.e., $k_f = k_p$).

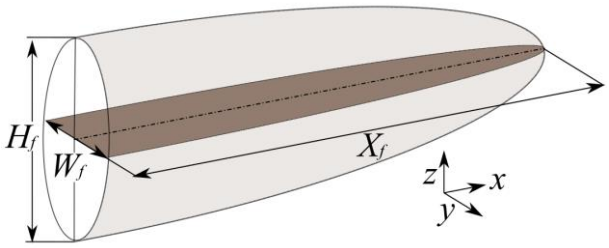

Figure 6-10. Schematic of a half of non-uniform width fracture.

Figure 6-11 compares the fracture conductivity ($C_f = k_f \times w_f$) calculated by neglecting the effect of viscous shear against that calculated by considering the effect of viscous shear. As seen from Figure 6-11, the fracture conductivity that considers the effect of the viscous shear (Figure 6-11b) is overall smaller than the fracture conductivity that neglects the effect of viscous shear (Figure 6-11a). Their difference is particularly noticeable at the edges of the fracture. This is because the fracture width is smaller at the fracture edge than that at the wellbore, which leads to a more significant effect of viscous shear at the fracture edge. **Figure 6-12a** compares the well production rate calculated by considering the effect of viscous shear against the well production rate calculated by considering the effect of viscous shear under constant bottomhole pressure condition, while **Figure 6-12b** compares the well bottomhole pressure calculated by considering the effect of viscous shear against the well bottomhole pressure calculated by considering the effect of viscous shear under constant production rate condition. Figure 6-12 shows that both the production rate plots and the bottomhole pressure drop plots exhibit significant differences

between the cases under comparison. This implies that the effect of viscous shear from the fracture walls on the well performance cannot be neglected if the fracture width is sufficiently small (or the Darcy parameter is sufficiently large).

Furthermore, we apply the semi-analytical model together with the fracture permeability model to fit the pressure buildup data of a partially-penetrating fractured well. The fitting work is conducted with a non-uniform width fracture which is shown in Figure 6-10. The parameter values known in this case are given as follows (Rodriguez *et al*., 1984): q_w = 31.8 m^3/d, z_e = 78.6 m, B = 1.4, μ = 3 mPa·s, c_{tm} = 7.25 × 10^{-4} MPa^{-1}, ϕ_m = 0.3, and r_w = 0.076 m. The matrix permeability of k_m = 4.59 mD is determined by radial flow analysis (Rodriguez *et al*., 1984). For simplification, we assume that the proppant-pack permeability is uniform along this fracture; as such, the unknown parameters include W_f, X_f, H_f, k_p, and ϕ_p. **Figure 6-13** compares the filed production data against the simulated production data using the semi-analytical model together with the proposed fracture permeability model. As one can see from this figure, the simulated pressure transient data exhibit excellent agreements with the field production data. **Table 6-3** summaries the values of the unknowns that are obtained by fitting the history production data. It should be noted that identifying the best fit between the simulated data and the field case can be very subjective, and the fitting results are highly dependent of the assumed fracture geometry. By fitting the field data, the authors only aim to show that the proposed fracture permeability model can be utilized to conduct post-fracture analysis.

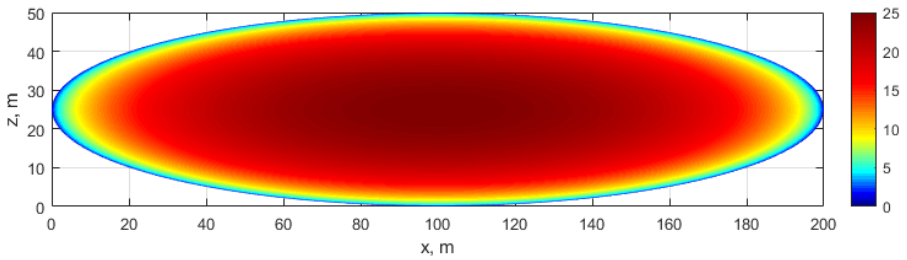

(a)

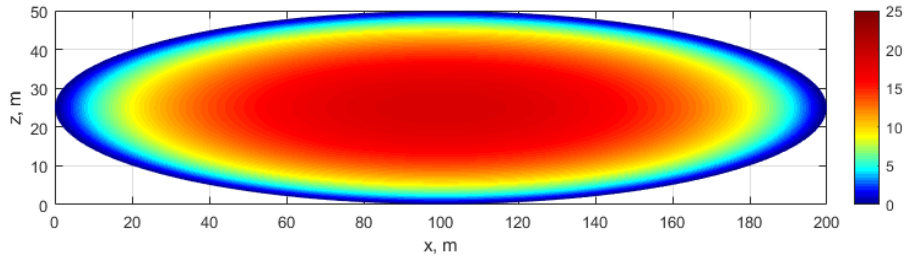

(b)

Figure 6-11. Comparison between the fracture conductivity (mD·m) that neglects the effect of viscous shear and the fracture conductivity that considers the effect of viscous shear: (a) fracture conductivity distribution neglecting the effect of viscous shear; and (b) fracture conductivity distribution considering the effect of viscous shear.

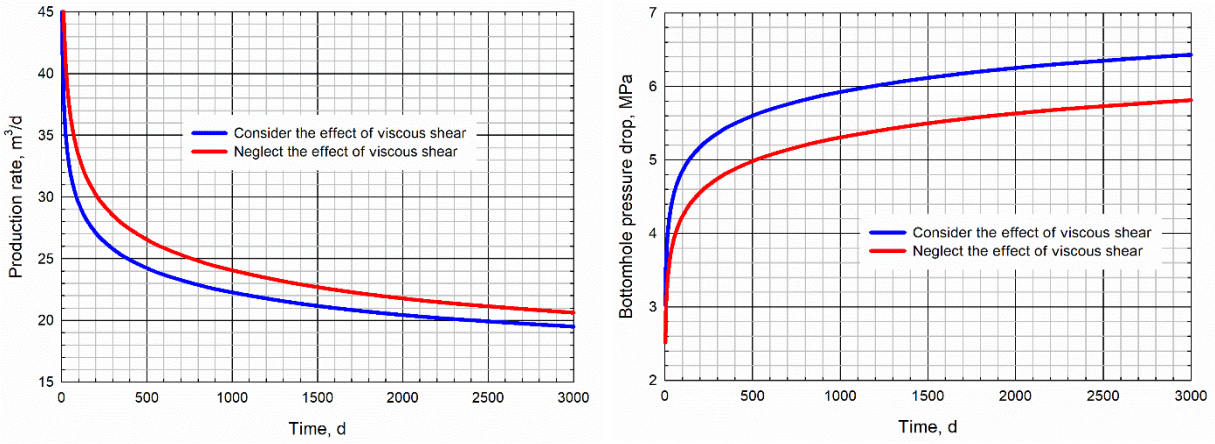

(a) (b)

Figure 6-12. Comparison between the well performance that neglects the effect of viscous shear and the well performance that considers the effect of viscous shear: (a) comparison of production rate under constant bottomhole pressure condition; and (b) comparison of bottomhole pressure drop under constant production rate condition.

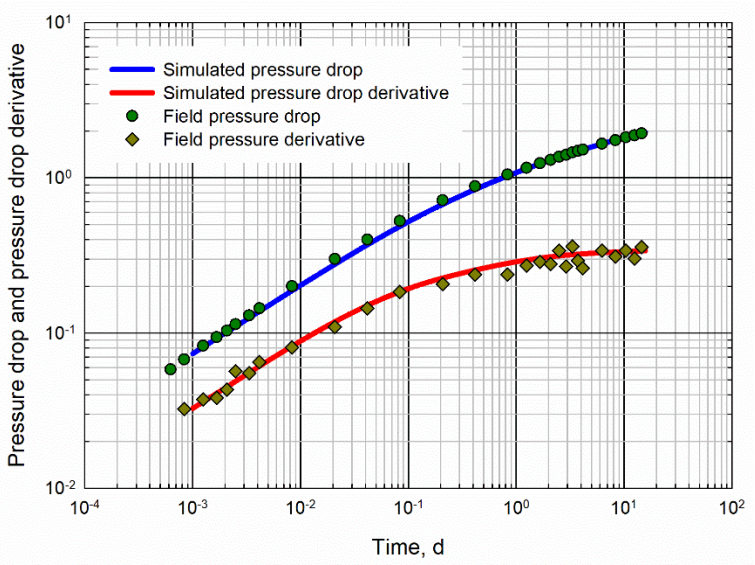

Figure 6-13. Comparison of the pressure transient data from Rodriguez *et al*. (1984) against the fitted one using the semi-analytical model together with the proposed fracture permeability model.

Table 6-3. Values of the parameters that are obtained by fitting the pressure buildup data.

Parameters	Value
W_f	1.00×10^{-2}
X_f	25.67
H_f	62.17
k_p	5.50×10^{5}
ϕ_p	0.35

6.4.4. Recommendation on Real-World Applications of the Proposed Fracture Permeability Model

The term in the bracket of Equation (6-37) reflects the effect of viscous shear on the effective fracture permeability. Hence, the coefficient of viscous shear λ can be defined as follows:

$$\lambda=1+2\sqrt{D_a}\left[\operatorname{csch}\left(\sqrt{\frac{1}{D_a}}\right)-\coth\left(\sqrt{\frac{1}{D_a}}\right)\right] \tag{6-44}$$

As such, the fracture permeability can be obtained by multiplying the proppant-pack permeability by the coefficient of viscous shear, which can be expressed as:

$$k_f = \lambda k_p \tag{6-45}$$

The following recommendations can be made to guide how to apply the proposed fracture permeability model to the following real-world scenarios:

1. If the fracture conductivity tests are conducted with a relatively large fracture width (i.e., the viscous shear on the fracture permeability/conductivity is negligible), the empirical fracture conductivity equation obtained by these tests can be inapplicable to the scenarios of small fracture width (or large Darcy parameter). In such cases, one can multiply the empirical fracture-conductivity equation by the coefficient of viscous shear to make it applicable to small-width fractures;
2. The assumption of approximating the fracture permeability with the proppant-pack permeability restricts the application scope of some analytical fracture-permeability models (e.g., the models proposed in Li *et al*. (2015) and Zhang *et al*. (2016)). The application scope of such models can be expanded by multiplying these models by the coefficient of viscous shear;
3. Although the proposed fracture permeability model only relates the fracture permeability to proppant-pack permeability, proppant-pack porosity, and fracture width, other effects (including but not limited to closure stress, embedment, proppant sorting, and proppant size) can be readily incorporated into this model. For example, the effects of sorting and proppant size on the fracture permeability can be considered by inserting the Berg equation (see Berg equation (1970) in Table 6-1) into the proposed fracture permeability equation (i.e., Equation (6-22)).

6.5. Conclusions

In this work, we derive a new analytical fracture permeability model which can take into account the effect of viscous shear from fracture walls on the effective permeability of a propped fracture. Such fracture permeability model characterizes the relationship between the fracture permeability, proppant-pack permeability, proppant-pack porosity, and fracture width. We first validate the correctness of the new fracture permeability model and then apply such model to history match the measured production data of a fractured well. The following conclusions can be drawn based on the results obtained:

1. The fluid flow in a fracture can be divided into three regimes, including DFD regime, transition regime, and VSD regime. As the Darcy parameter is increased, the flow regime is transitioned from DFD regime to VSD regime;
2. The proposed analytical model fills the gap between the VSD-FP equation and the DFD-FP equation. Both the VSD-FP equation and the DFD-FP equation are special forms of the proposed fracture permeability model; taking 5% as the threshold value of relative absolute difference, if $D_a \geq 2.00$, the effect of proppant-pack permeability on the fracture permeability can be neglected and the fracture permeability can be calculated with VSD equation, whereas, if $D_a \leq 5.67\times10^{-4}$, the effect of viscous shear on the fracture permeability can be neglected and the fracture permeability can be calculated with DFD equation;
3. For the empirical and analytical fracture permeability/conductivity models that neglect the effect of viscous shears, one can multiply these models by the coefficient of viscous shear. By doing so, these model can be applied to estimate the fracture permeability/conductivity even if the Darcy parameter in the fracture is sufficiently large.

Nomenclature

a, b = parameters defined in Equation (6-26)

A_1 and A_2 = constant

B = formation volume factor

c_{tf} = total compressibility of the fracture system, MPa^{-1}

c_{tm} = total compressibility of the matrix system, MPa^{-1}

C_f = fracture conductivity, mD·m

C_w = wellbore storage coefficient, m^3/MPa

D_a = Darcy parameter defined in Equation (6-35)

G = a term defined in this work

h_f = fracture height, m

H_f = fracture height at wellbore, m

k = permeability, mD

k_c = channel permeability, mD

k_f = fracture permeability, mD

k_m = matrix permeability, mD

k_p = proppant-pack permeability, mD

l_1 = direction that is parallel to the fracture wall, m

l_2 = direction that is orthogonal to the fracture wall, m

l_{2D} = dimensionless position along the direction that is orthogonal to the fracture wall

L = length, m

L_x = length of model #2 along x-axis

L_y = length of model #2 along y-axis

n_w = number of fracture segments that are connected to the wellbore

N_f = total number of the fracture segments

Δp = pressure difference, MPa

p = pressure, MPa

p_f = fracture pressure, MPa

p_{in} = pressure at the inlet surface, MPa

p_{out} = pressure at the outlet surface, MPa

p_w = bottomhole pressure, MPa

q = volume flux rate, m^3/d

q_f = flux rate from matrix to the fracture, m^3/d

$q_{f\text{-}w}$ = flux rate from the fracture to the wellbore, m^3/d

q_w = well production rate, m^3/d

r_p = radius of the cylinder, m

r_w = wellbore radius, m

Δt = time interval, d

t = time, d

T = transmissibility, $m^3/(d \cdot MPa)$

v = flow velocity, m/d

v_0 = flow velocity at fracture walls, m/d

v_{ave} = average flow velocity, m/d

v_D = dimensionless Darcy velocity

w_c = width of the channel, m

w_f = fracture width, m

w_{fD} = dimensionless fracture width

W_f = fracture width at wellbore, m

Δx = length of the fracture segment along x-axis, m

Δz = length of the fracture segment along z-axis, m

x_0, y_0, z_0 = central position of a fracture segment, m

X_f = half fracture length, m

z_e = formation thickness, m

β_1 = 0.0853, unit conversion factor

β_2 = 1.01×10^{15}, unit conversion factor

δ = flux per unit length or area

ε = relative difference

$\eta_m = \beta_1 k_m / (\mu \phi_m c_{tm})$, diffusivity, m^2/d

λ = coefficient of viscous shear

μ = viscosity, mPa·s

τ = time the instantaneous source occurs, d

ϕ_m = matrix porosity

ϕ_p = proppant-pack porosity

Acknowledgments

The authors would like to acknowledge the financial support provided by the Natural Science and Engineering Research Council of Canada (NSERC) as well as the financial supports provided by the China Scholarship Council (CSC).

Appendix 6A – Formulations of the Fracture Flow

The fracture flow is characterized with a numerical method; hence, we discretize a unilateral non-uniform-width fracture into N_f small segments, as shown in **Figure 6A-1**. Since we assume that the fracture is symmetrical with respect to the wellbore, a unilateral fracture is sufficient to represent the entire fracture.

In this work, we set that the *x*-axis is parallel to the horizontal propagation direction of the fracture, and the *z*-axis is parallel to the vertical propagation direction of the fracture. An arbitrary fracture segment (*i*, *j*) has a dimension of ($\Delta x_{i,j} \times \Delta z_{i,j} \times w_{f,i,j}$). Due to the fact that the fracture width is much smaller than the fracture length and the fracture height, only 2D flow is considered in the fracture. For the fracture segment (*i*, *j*), the finite difference equation of the 2D flow is given as (Ertekin *et al*., 2001):

$$\begin{aligned} &T_{i+\frac{1}{2},j}\left(p^n_{f,i+1,j}-p^n_{f,i,j}\right)-T_{i-\frac{1}{2},j}\left(p^n_{f,i,j}-p^n_{f,i-1,j}\right)\\ &+T_{i,j+\frac{1}{2}}\left(p^n_{f,i,j+1}-p^n_{f,i,j}\right)-T_{i,j-\frac{1}{2}}\left(p^n_{f,i,j}-p^n_{f,i,j-1}\right)\\ &+q^n_{f,i,j}=\left(\frac{\Delta x\Delta z w_f \phi_p c_{tf}}{B\Delta t}\right)_{i,j}\left(p^n_{f,i,j}-p^{n-1}_{f,i,j}\right) \end{aligned} \tag{6A-1}$$

where *T* is transmissibility which can be obtained by,

$$T_{i+\frac{1}{2},j}=2\left[\left(\frac{w_f\Delta z\beta_1 k_f}{\mu B\Delta x}\right)^{-1}_{i,j}+\left(\frac{w_f\Delta z\beta_1 k_f}{\mu B\Delta x}\right)^{-1}_{i+1,j}\right]^{-1} \tag{6A-2}$$

and the other terms $T_{i-½,j}$, $T_{i,j+½}$, and $T_{i,j-½}$ can also be obtained with equations similar to Equation (6A-2). In particular, if the fracture segment (*i*, *j*) is connected to the wellbore (e.g., the wellbore is located at the position of fracture segment (*i*-1, *j*)), Equation (6A-1) can be rewritten as:

$$\begin{aligned} &T_{i+\frac{1}{2},j}\left(p^n_{f,i+1,j}-p^n_{f,i,j}\right)+T_{i,j+\frac{1}{2}}\left(p^n_{f,i,j+1}-p^n_{f,i,j}\right)-T_{i,j-\frac{1}{2}}\left(p^n_{f,i,j}-p^n_{f,i,j-1}\right)\\ &+q^n_{f,i,j}-q^n_{f-w,i,j}=\left(\frac{\Delta x\Delta z w_f \phi_p c_{tf}}{B\Delta t}\right)_{i,j}\left(p^n_{f,i,j}-p^{n-1}_{f,i,j}\right) \end{aligned} \tag{6A-3}$$

Whereas, if the fracture segment (i, j) is at the boundary of the fracture (e.g., fracture segment (i+1, j) is non-existing), Equation (6A-1) can be rewritten as:

$$-T_{i-\frac{1}{2},j}\left(p^n_{f,i,j}-p^n_{f,i-1,j}\right)+T_{i,j+\frac{1}{2}}\left(p^n_{f,i,j+1}-p^n_{f,i,j}\right)-T_{i,j-\frac{1}{2}}\left(p^n_{f,i,j}-p^n_{f,i,j-1}\right)$$
$$+q^n_{f,i,j}=\left(\frac{\Delta x\Delta z w_f \phi_p c_{tf}}{B\Delta t}\right)_{i,j}\left(p^n_{f,i,j}-p^{n-1}_{f,i,j}\right) \quad \text{(6A-4)}$$

Applying Equations (6A-1), (6A-3), or (6A-4) to all of the fracture segments, we will have N_f linear equations at each timestep.

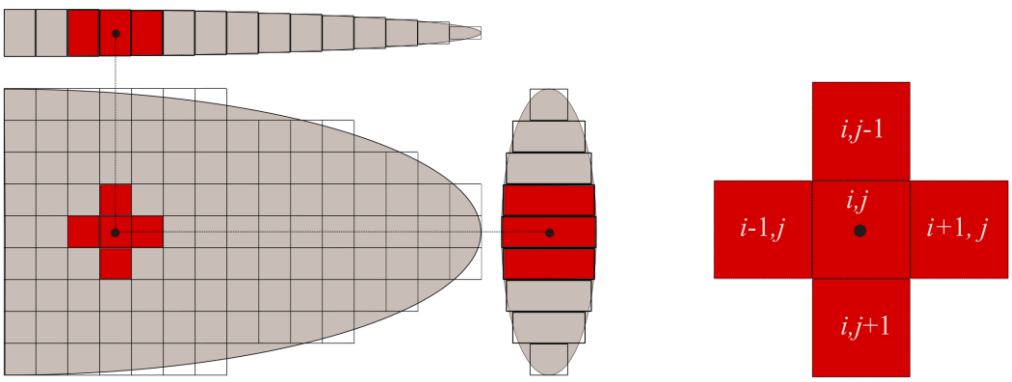

(a) (b)

Figure 6A-1. Schematic of a discretized unilateral non-uniform-width fracture: (a) side view, top view and cross view of the discretized unilateral non-uniform-width fracture; and (b) zoom-in view of the small fracture segments.

Appendix 6B – Formulations of the Matrix Flow

The non-unform-width fracture is discretized into small segments, and each fracture segment can be regarded as a plane source. On the basis of the Newman product method, the instantaneous plane source function of such a fracture segment can be obtained by:

An instantaneous plane source function in a 3D reservoir
(infinite along *x*-/*y*-axis and bounded along *z*-axis) =
An instantaneous plane source function in a 1D infinite reservoir along *x*-axis (6B-1)
× An instantaneous line source function in a 1D infinite reservoir along *y*-axis
× An instantaneous plane source function in a 1D bounded reservoir along *z*-axis

Gringarten and Ramey (1973) derived different source functions under different boundary conditions. The instantaneous plane source function in a 1D infinite reservoir along the *x*-axis is given as (Gringarten and Ramey, 1973):

$$\frac{\phi_m c_{tm}}{\delta}\Delta p\left(x,t\right)=\frac{1}{2}\left\{\operatorname{erf}\left[\frac{0.5\Delta x+\left(x-x_0\right)}{\sqrt{4\eta_m\left(t-\tau\right)}}\right]+\operatorname{erf}\left[\frac{0.5\Delta x-\left(x-x_0\right)}{\sqrt{4\eta_m\left(t-\tau\right)}}\right]\right\} \tag{6B-2}$$

The instantaneous line source function in a 1D infinite reservoir along the *y*-axis is given as (Gringarten and Ramey, 1973):

$$\frac{\phi_m c_{tm}}{\delta}\Delta p\left(y,t\right)=\exp\left[-\frac{\left(y-y_0\right)^2}{4\eta_m\left(t-\tau\right)}\right]\Bigg/\sqrt{4\pi\eta_m\left(t-\tau\right)} \tag{6B-3}$$

And the instantaneous plane source function in a 1D bounded reservoir along the *z*-axis is given as (Gringarten and Ramey, 1973):

$$\frac{\phi_m c_{tm}}{\delta}\Delta p\left(z,t\right)=\frac{\Delta z}{z_e}\left\{1+\frac{4z_e}{\pi\Delta z}\sum_{m=1}^{\infty}\frac{1}{m}\exp\left[-\frac{m^2\pi^2\eta_m\left(t-\tau\right)}{z_e^2}\right]\sin\frac{m\pi\Delta z}{2z_e}\cos\frac{m\pi z_0}{z_e}\cos\frac{m\pi z}{z_e}\right\} \tag{6B-4}$$

Inserting Equations (6B-2) through (6B-4) into Equation (6B-1) gives:

$$\frac{\phi_m c_{tm}}{\delta}\Delta p(x,y,z,t)=$$
$$\frac{1}{2}\left\{\operatorname{erf}\left[\frac{0.5\Delta x+(x-x_0)}{\sqrt{4\eta_m(t-\tau)}}\right]+\operatorname{erf}\left[\frac{0.5\Delta x-(x-x_0)}{\sqrt{4\eta_m(t-\tau)}}\right]\right\}$$
$$\cdot\exp\left[-\frac{(y-y_0)^2}{4\eta_m(t-\tau)}\right]\Bigg/\sqrt{4\pi\eta_m(t-\tau)} \tag{6B-5}$$
$$\cdot\frac{\Delta z}{z_e}\left\{1+\frac{4z_e}{\pi\Delta z}\sum_{m=1}^{\infty}\frac{1}{m}\exp\left[-\frac{m^2\pi^2\eta_m(t-\tau)}{z_e^2}\right]\sin\frac{m\pi\Delta z}{2z_e}\cos\frac{m\pi z_0}{z_e}\cos\frac{m\pi z}{z_e}\right\}$$

In Equations (6B-2) to (6B-5), δ indicates the flux per unit length or area. For a continuous plane source which has a constant flux rate q_f, we have:

$$\delta=\frac{q_f}{\Delta x\Delta z} \tag{6B-6}$$

In addition, τ indicates the time at which the instantaneous flux occurs. For a continuous plane source which is continued from time τ_1 to time τ_2, the continuous source function can be obtained by integrating Equation (6B-5) from τ_1 to τ_2. As such, a continuous plane source function can be obtained:

$$\frac{1}{q_f}\Delta p(x,y,z,t)=\frac{1}{\phi_m c_{tm}\Delta x\Delta z}\int_{\tau_1}^{\tau_2}$$
$$\frac{1}{2}\left\{\operatorname{erf}\left[\frac{0.5\Delta x+(x-x_0)}{\sqrt{4\eta_m(t-\tau)}}\right]+\operatorname{erf}\left[\frac{0.5\Delta x-(x-x_0)}{\sqrt{4\eta_m(t-\tau)}}\right]\right\}\tau$$
$$\cdot\exp\left[-\frac{(y-y_0)^2}{4\eta_m(t-\tau)}\right]\Bigg/\sqrt{4\pi\eta_m(t-\tau)} \tag{6B-7}$$
$$\cdot\frac{\Delta z}{z_e}\left\{1+\frac{4z_e}{\pi\Delta z}\sum_{m=1}^{\infty}\frac{1}{m}\exp\left[-\frac{m^2\pi^2\eta_m(t-\tau)}{z_e^2}\right]\sin\frac{m\pi\Delta z}{2z_e}\cos\frac{m\pi z_0}{z_e}\cos\frac{m\pi z}{z_e}\right\}\mathrm{d}\tau$$

In Equation (6B-7), (x_0, y_0, z_0) represents the central position of the plane source, and Δx, Δz represents the dimension of the plane source. A flux of fracture segment (i, j) which is continued

from time t^{k-1} to t^k can cause a pressure drop at time t^n at fracture segment (I, J). On the basis of Equation (6B-7), this pressure drop can be expressed as:

$$\begin{aligned}\frac{1}{q_{f,i,j}^{k}}\Delta p_{f,I,J}^{n} &= \frac{1}{\phi_m c_{tm}\Delta x_{i,j}\Delta z_{i,j}}\int_{t^{k-1}}^{t^k} \\ &\frac{1}{2}\left\{\operatorname{erf}\left[\frac{0.5\Delta x_{i,j}+\left(x_{I,J}-x_{i,j}\right)}{\sqrt{4\eta_m\left(t^n-\tau\right)}}\right]+\operatorname{erf}\left[\frac{0.5\Delta x_{i,j}-\left(x_{I,J}-x_{i,j}\right)}{\sqrt{4\eta_m\left(t^n-\tau\right)}}\right]\right\}\tau \\ &\cdot\exp\left[-\frac{\left(y_{I,J}-y_{i,j}\right)^2}{4\eta_m\left(t^n-\tau\right)}\right]\Bigg/\sqrt{4\pi\eta_m\left(t^n-\tau\right)} \\ &\cdot\frac{\Delta z_{i,j}}{z_e}\left\{1+\frac{4z_e}{\pi\Delta z_{i,j}}\sum_{m=1}^{\infty}\frac{1}{m}\exp\left[-\frac{m^2\pi^2\eta_m\left(t^n-\tau\right)}{z_e^2}\right]\sin\frac{m\pi\Delta z_{i,j}}{2z_e}\cos\frac{m\pi z_{i,j}}{z_e}\cos\frac{m\pi z_{I,J}}{z_e}\right\}\mathrm{d}\tau\end{aligned} \tag{6B-8}$$

For convenience, we use the term $G_{I,J}^{n,k}(i, j)$ to represent the term on the right-hand side of Equation (6B-8), such that Equation (6B-8) can be rewritten as:

$$\Delta p_{f,I,J}^{n} = q_{i,j}^{k} G_{I,J}^{n,k}\left(i, j\right) \tag{6B-9}$$

The pressure drop at the fracture segment (I, J) at time t^n can be obtained by collecting the pressure drops caused by all of the fracture segments from time $t = 0$ to $t = t^n$, which can be written as:

$$\Delta p_{f,I,J}^{n} = \sum_{k=1}^{k=n}\sum_{j=1}^{j=N_j}\sum_{i=1}^{i=N_i} q_{f,i,j}^{k} G_{I,J}^{n,k}\left(i, j\right) + \sum_{k=1}^{k=n}\sum_{j=1}^{j=N_j}\sum_{i=1}^{i=N_i} q_{f,-i,-j}^{k} G_{I,J}^{n,k}\left(-i,-j\right) \tag{6B-10}$$

where the second term on the right-hand side of Equation (6B-10) indicates the pressure drop caused by the other unilateral non-uniform-width fracture. Fracture segment (-i, -j) indicates a fracture segment of the other unilateral non-uniform-width fracture corresponding to the fracture segment (i, j). Since we assume that the non-uniform-width fracture is symmetrical with respect to the wellbore, the fracture segment (-i, -j) should have the same flux rate and pressure with the fracture segment (i, j); thus, Equation (6B-10) can be simplified as:

$$\Delta p^{n}_{f,I,J} = \sum_{k=1}^{k=n} \sum_{j=1}^{j=N_j} \sum_{i=1}^{i=N_i} q^{k}_{f,i,j} \left[G^{n,k}_{I,J}(i,j) + G^{n,k}_{I,J}(-i,-j) \right] \tag{6B-11}$$

Applying Equation (6B-11) to all of the fracture segments, we will have N_f linear equations at each timestep.

Appendix 6C – Wellbore Equation

If the fracture segment (i, j) is connected to the wellbore, the flux rate from the fracture segment to the wellbore can be obtained by:

$$q^n_{f-w,i,j} = \frac{\beta_1 k_f w_{f,i,j} \Delta z_{i,j}}{B\mu} \frac{p^n_{f,i,j} - p^n_w}{0.5\Delta x_{i,j}} \tag{6C-1}$$

Applying Equating (6C-1) to the n_w fracture segments that are connected to the wellbore, we will have n_w linear equations. In addition, considering the wellbore storage, we can have the following well production rate equation (van Everdingen and Hurst, 1949):

$$q^n_w - 2\sum_{nw} q^n_{f-w,i,j} = C_w \frac{p^{n-1}_w - p^n_w}{\Delta t} \tag{6C-2}$$

The constant "2" in Equation (6C-2) indicates the summation of flux from the two unilateral fractures. It should be noted that, since the wellbore equation is handled with the numerical method, this model can be used to simulate various wellbore conditions (e.g., constant production rate condition, constant bottomhole pressure condition, varying production rate condition, and varying bottomhole pressure condition). In this work, only constant production rate condition is studied.

At each timestep, gathering the fracture flow equations, matrix flow equations, and the wellbore equations, we will have a system of linear equations which has $2N_f+n_w+1$ equations and $2N_f+n_w+1$ unknowns; therefore, this system of linear equation is close and can be solved.

References

Alramahi, B., and Sundberg, M.I. 2012. Proppant Embedment and Conductivity of Hydraulic Fractures in Shales. Paper ARMA-20121-291 presented at 46th U.S. Rock Mechanics/Geomechanics Symposium, Chicago, Illinois, 24-27 June.

Awoleke, O.O., Zhu, D., and Hill, A.D. 2016. New Propped-Fracture-Conductivity Models for Tight Gas Sands. *SPE J*. 21 (5): 1508-1517.

Belhaj, H.A., Agha, K.R., Butt, S.D., and Islam, M.R. 2003. A Comprehensive Numerical Simulation Model for Non-Darcy Flow including Viscous, Inertial and Convective Contributions. Paper SPE 85678 presented at Nigeria Annual International Conference and Exhibition, Abuja, Nigeria, 4-6 August.

Berg, R.R. 1970. Method for Determining Permeability from Reservoir Rock Properties. *Trans. GCAGS* 20: 303-335.

Brinkman, H.C. 1949. A Calculation of the Viscous Force Exerted by a Following Fluid on a Dense Swarm of Particles. *Appl. Sci. Res.* A1: 27-34.

Carman, P.C. 1956. *Flow of Gases through Porous Media*. Butterworths, London.

Carman, P.C. 1997. Fluid Flow through Granular Beds. *Trans. IChemE* 75: 32-48.

Comsol, 2019. Comsol, Inc, Burlington, Massachusetts, USA.

Darcy, H. 1856. Les Fontaines Publiques De La Ville De Dijon. Paris. Dalmont.

Darin, S.R., and Huitt, J.L. 1960. Effect of a Partial Monolayer of Propping Agent on Fracture Flow Capacity. *Trans. AIME*. 219 (3): 31-37.

Durlofsky, L., and Brady, J.F. 1987. Analysis of the Brinkman Equation as a Model for Flow in Porous Media. *Phys. Fluids* 30 (11): 3329-3341.

Ertekin, T., Abou-Kassem, J.H., and King, G.R. 2001. *Basic Applied Reservoir Simulation*. SPE Textbook Series.

Fredd, C.N., McConnell, S.B., Boney, C.L., and England, K.W. 2001. Experimental Study of Fracture Conductivity for Water-Fracturing and Conventional Fracturing Applications. *SPE J.* 6 (3): 288-298.

Glover, P.W., Zadjali, I.I., and Frew, K.A. 2006. Permeability Prediction from MICP and NMR Data using an Electro-Kinetic Approach. *Geophysics* 71 (4): 49-60.

Gringarten, A.C., and Ramey, H.J. 1973. The Use of Source and Green's Functions in Solving Unsteady-Flow Problems in Reservoirs. *SPE J.* 13 (5): 285-296.

Gu, H., and Leung, K.H. 1993. 3D Numerical Simulation of Hydraulic Fracture Closure with Application to Minifracture Analysis. *J. Pet. Tech.* 45 (3): 206-255.

Krumbein, W.C., and Monk, G.D. 1943. Permeability as a Function of Size parameters of Unconsolidated Sand. *Trans. AIME* 151 (1): 153-163.

Lacy, L.L., Rickards, A.R., and Bilden, D.M. 1998. Fracture Width and Embedment Testing in Soft Reservoir Sandstone. *SPE J*. 13 (1): 25-29.

Li, K., Gao, Y., Lyu, Y., and Wang, M. 2015. New Mathematical Models for Calculating Proppant Embedment and Fracture Conductivity. *SPE J*. 20 (3): 496-507.

Mack, D.J. 2000. Effects of Proppant Pack Concentration and Polymer Residue on Appalachian Stimulations. Paper SPE 65626 presented at SPE Eastern Regional Meeting, Morgantown, West Virginia, 17-19 October.

Morita, N., Whitfill, D.L., and Wahl, H.A. 1988. Stress-Intensity Factor and Fracture Cross-Sectional Shape Predictions from a Three-Dimensional Model for Hydraulically Induced Fractures. *J. Pet. Tech.* 40 (10): 1329-1342.

Nguyen, P.D., Dewprashad, B.T., and Weaver, J.D. 2000. New Approach for Enhancing Fracture Conductivity. *SPE Prod. Faci*. 15 (2): 83-89.

Parvazinia, M., Nassehi, V., Wakeman, R.J., and Ghoreishy M.H.R. 2006. Finite Element Modelling of Flow through a Porous Medium between Two Parallel Plates Using the Brinkman Equation. *Transp. Porous Med*. 63 (1): 71-90.

Pope, D.S., Leung, L.K.-W., Gulbis, J., and Constien, V.G. 1996. Effects of Viscous Fingering on Fracture Conductivity. *SPE Prod. Faci*. 11 (4): 230-237.

Rodriguez, F., Horne, R.N., and Cinco-Ley, H. 1984. Partially Penetrating Fractures: Pressure Transient Analysis of an Infinite Conductivity Fracture. Paper SPE 12743 presented at SPE California Regional Meeting, Long Beach, California, 11-13 April.

Sutera, S.P., and Skalak, R. 1993. The History of Poiseuille's Law. *Ann. Rev. Fluid Mech.* 25: 1-19.

Swaby, P.A., and Rawnsley, K.D. 1997. An Interactive 3D Fracture-Modeling Environment. *SPE J*. 9 (3): 82-87.

Teng, B., and Li, H. 2019. Pressure-Transient Behavior of Partially Penetrating Inclined Fractures with a Finite Conductivity. *SPE J*. 24 (2): 811-833.

van Baaren, J.P. 1979. Quick-Look Permeability Estimates Using Sidewall Samples and Porosity Logs. Transaction of the 6th Annual European Logging Symposium, Society of Professional Well Log Analysts.

van Everdingen, A.F., and Hurst, W. 1949. The Application of the Laplace Transformation to Flow Problems in Reservoirs. *Trans. AIME* 1 (12): 305-324.

Weaver, J.D., Rickman, R.D., and Luo, H. 2010. Fracture-Conductivity Loss Caused by Geochemical Interactions between Man-Made Proppants and Formations. *SPE J.* 15 (01):116-124.

Wright, C.A., Davis, E.J., Golich G.M., Ward, J.F., Demetrius, S.L., Minner, W.A., and Weijers, L. 1998. Downhole Tiltmeter Fracture Mapping: Finally Measuring Hydraulic Fracture Dimensions. Paper SPE 46194 presented at SPE Western Regional Meeting, Bakersfield, California, 10-13 May.

Zhang, J., Kamenov, A., Hill, A.D., and Zhu, D. 2013. Laboratory Measurement of Hydraulic Fracture Conductivities in the Barnett Shale. *SPE Prod. Oper.* 29 (03): 216-227.

Zhang, J., Zhu, D., and Hill, A.D. 2016. Water-Induced Damage to Propped-Fracture Conductivity in Shale Formations. *SPE Prod. Oper.* 31 (2): 147-156.

CHAPTER 7 CONTRIBUTIONS AND RECOMMENDATIONS

This is a paper-based thesis, and each chapter contains its own conclusions. Presented in this chapter are the major contributions of this thesis and the recommendetions for future research.

7.1 Scientific and Practical Contributions to the Literature and Industry

- In this thesis, the author proposes the semi-analytical models to characterize the transient flow behavior of HFs, PPIFs, reoriented refractures, and orthogonal refractures. Due to the nature of the semi-analytical method, these models can be used to efficiently predict the production of these complex fractures or conduct history matching work on these complex fractures. The details of constructing these models are well introduced in the thesis, such that one can readily replicate these models for real applications;
- The flow regimes of HFs and PPIFs are thoroughly investigated. The observed flow regimes of HF and PPIF are much more complex than what can be observed during the production of a vertical fracture. These recognized flow regimes can help one determine whether a studied fracture is a HF/PPIF or not;
- The productivity of the reoriented refracture and the orthogonal refracture can be influenced by many factors (i.e., permeability anisotropy, fracture geometry, azimuth of the refracture, etc). One could use the proposed semi-analytical molde of reoriented refractures to optimize the refracturing treatment; and
- A new fracture permeability model is proposed to characterize the relationship between the fracture permeability, fracture width, proppant-pack porosity, and proppant-pack permeability. By use of this new fracture permeability model, one can extend the proposed semi-analytical models to the scenarios involving non-uniform-width fractures.

7.2 Recommendations for Future Work

- In this thesis, all the semi-analytical model are developed for the single-phase oil flow, which is over-simplified for the real field cases. One can extend these models for the scenarios of multiphase flow by applying the concepts of pseudo-pressure and pseudo-time;
- Although various rapid semi-analytical models have been proposed to characterize the transient flow behavior of complex fractures, such models normally have not been widely applied for real applications. A pressure transient analysis software that is based on semi-analytical methods is commercially promising and worthwhile of being developed;
- The geometry and the orientation of the refracture can significantly influence the productivity of the refractures. One can develop an empirical method to estimate the geometry and the orientation of the refractures; and
- For the proposed fracture permeability model, only the effects of proppant-pack permeability, proppant-pack porosity, and fracture width on the fracture permeability are considered. In future work, more influencing factors, such as slippage and non-Newton fluid, can be taken into account.

BIBLIOGRAPHY

AccuMap, IHS, 2013.

Aghighi, M.A., Rahman, S.S., and Rahman, M.M. 2009. Effect of Formation Stress Distribution on Hydraulic Fracture Reorientation in Tight Gas Sands. Paper SPE 122723 presented at Asia Pacific Oil and Gas Conference & Exhibition, Jakarta, Indonesia, 4-6 August.

Al-Anazi, H., Al-Kanaan, A., Pacheco, E., and Rahim, Z. 2013. Evaluation and Selection of Stimulation Methods in Horizontal Gas Wells for Production Optimization Using Numerical Modeling of Well Performances. Paper SPE 167090 presented at SPE Unconventional Resources Conference and Exhibition-Asia Pacific, Brisbane, Australia, 11-13 November.

Alramahi, B., and Sundberg, M.I. 2012. Proppant Embedment and Conductivity of Hydraulic Fractures in Shales. Paper ARMA-20121-291 presented at 46th U.S. Rock Mechanics/Geomechanics Symposium, Chicago, Illinois, 24-27 June.

Asalkhuzina, G.F., Davletbaev, A.Ya., Fedorov, A.I., Yuldasheva, A.R., Efremov, A.N., Sergeychev, A.V., and Ishkin, D.Z. 2017. Identification of Refracturing Reorientation using Decline-Analysis and Geomechanical Simulator. Paper SPE 187750 presented at SPE Russian Petroleum Technology Conference, Moscow, Russia, 16-18 October.

Awoleke, O.O., Zhu, D., and Hill, A.D. 2016. New Propped-Fracture-Conductivity Models for Tight Gas Sands. *SPE J*. 21 (5): 1508-1517.

Baig, A., and Urbancic, T.I. 2012. Structural Controls on Vertical Growth of Hydraulic Fractures as Revealed Through Seismic Moment Tensor Inversion Analysis. Paper SPE 159795 presented at SPE Annual Technical Conference and Exhibition, San Antonio, Texas, USA, 8-10 October.

Belhaj, H.A., Agha, K.R., Butt, S.D., and Islam, M.R. 2003. A Comprehensive Numerical Simulation Model for Non-Darcy Flow including Viscous, Inertial and Convective Contributions. Paper SPE 85678 presented at Nigeria Annual International Conference and Exhibition, Abuja, Nigeria, 4-6 August.

Bello, R.O., and Wattenbarger, R.A. 2008. Rate Transient Analysis in Naturally Fractured Shale Gas Reservoirs. Paper SPE 114591 presented at CIPC/SPE Gas Technology Symposium 2008 Joint Conference, Calgary, Alberta, Canada, 16-19 June.

Benedict, D.S., and Miskimins, J.L. 2009. The Effects of Hydraulic Fracture Reorientation. Paper SPE 119355 presented at SPE Hydraulic Fracturing Technology Conference, the Woodlands, Texas, 19-21 January.

Berg, R.R. 1970. Method for Determining Permeability from Reservoir Rock Properties. *Trans. GCAGS* 20: 303-335.

Branch, G.A., and Drennan, K.M. 1991. Refracture Stimulations in the Norge Marchand Unit: A Case Study. Paper SPE 21642 presented at SPE Production Operations Symposium, Oklahoma City, Oklahoma, 7-9 April.

Brinkman, H.C. 1949. A Calculation of the Viscous Force Exerted by a Following Fluid on a Dense Swarm of Particles. *Appl. Sci. Res.* A1: 27-34.

Brown P.R. 1981. A Non-Interactive Method for the Automatic Generation of Finite Element Meshes Using the Schwarz-Christoffel Transformation. *Comput. Methods Appl. Mech. Eng.* 25 (1): 101-126.

Brown, M.L., Ozkan, E., Raghavan, R.S., and Kazemi, H. 2009. Practical Solutions for Pressure Transient Responses of Fractured Horizontal Wells in Unconventional Reservoirs. *SPE Res. Eval. Eng.* 14 (05): 663-676.

Carman, P.C. 1937. Fluid Flow through Granular Beds. *Trans. IChemE* 75: 32-48.

Carman, P.C. 1956. *Flow of Gases through Porous Media*. Butterworths, London.

Carslaw, H.S., and Jaeger, J.C. 1959. *Conduction of Heat in Solids,* second edition. Oxford, UK: Oxford University Press.

Chacon, A., Djebrouni, A., and Tiab, D. 2004. Determining the Average Reservoir Pressure from Vertical and Horizontal Well Test Analysis Using the Tiab's Direct Synthesis Technique. Paper SPE 88619 presented at SPE Asia Pacific Oil and Gas Conference and Exhibition, Perth, Australia, 18-20 October.

Chen, C., and Raghavan, R. 1997. A Multiply-Fractured Horizontal Well in a Rectangular Drainage Region. *SPE J.* 2 (04): 455-465.

Chen, H.Y. 1990. *Well Behavior in Naturally Fractured Reservoirs*. PhD Dissertation, Texas A&M University, College Station, Texas.

Chen, H.Y., Poston, S.W., and Raghavan, R. 1991. An Application of the Product Solution Principle for Instantaneous Source and Green's Functions. *SPE Form. Eval.* 6 (02): 161-167.

Chen, Z., Liao, X., Zhao, X., Lv, S., and Zhu, L. 2016. A Semianalytical Approach for Obtaining Type Curves of Multiple-Fractured Horizontal Wells with Secondary-Fracture Networks. *SPE J.* 21 (02): 538-549.

Chhina, H.S., Luhning, R.W., Bilak, R.A., and Best, D.A. 1987. A Horizontal Fracture Test in the Athabasca Oil Sands. Paper PETSOC-87-38-56 presented at Annual Technical Meeting, Calgary, Alberta, June 7 – 10.

Chun, K.H., and Ghassemi, A. 2012. Fracture Propagation under Poroelastic Loading. Paper ARMA 2012-274 presented at 46th U.S. Rock Mechanics/Geomechanics Symposium, Chicago, Illinois, 24-27 June.

Cinco-Ley, H., and Samaniego-V., F. 1981. Transient Pressure Analysis for Fractured Wells. *J Pet. Technol.* 33 (09): 1749-1766.

Cinco-Ley, H., Ramey, H.J., and Miller, F.G. 1975. Unsteady-State Pressure Distribution Created by a Well with an Inclined Fracture. Paper SPE 5591 presented at Fall Meeting of the Society of Petroleum Engineers of AIME, Dallas, Texas, 28 September-1 October.

Cinco-Ley, H., Samaniego-V., F., and Dominguez-A., N. 1978. Transient Pressure Behavior for a Well with a Finite-Conductivity Vertical Fracture. *SPE J.* 18 (04): 253-264.

Cipolla, C.L., and Wright, C.A. 2000. State-of-the-Art in Hydraulic Fracture Diagnostics. Paper SPE 64434 presented at SPE Asia Pacific Oil and Gas Conference and Exhibition, Brisbane, Australia, 16-18 October.

Comsol, 2019. Comsol, Inc, Burlington, Massachusetts, USA.

Conlin, J.M., Hale, J.L., Sabathier, J.C., Faure, F., and Mas, D. 1990. Multiple-Fracture Horizontal Wells: Performance and Numerical Simulation. Paper SPE 20960 presented at European Petroleum Conference, The Hague, Netherlands, 21-24 October.

Crawford, P.B., and Landrum, B.L. 1954. Estimated Effect of Horizontal Fractures on Production Capacity. Paper SPE 441-G presented at Fall Meeting of the Petroleum Branch of AIME, San Antonio, Texas, 17-20 October.

Crawford, P.B., Pinson, J., Simmons, J., and Landrum, B.L. 1963. Effect of Elliptical Fractures on Sweep Efficiencies in Water Flooding or Fluid Injection Programs. SPE-602-MS.

Culham, W.E. 1974. Pressure Buildup Equations for Spherical Flow Regime Problems. *SPE J.* 14 (06): 545-555.

Daneshy, A.A. 1973. A Study of Inclined Hydraulic Fractures. *SPE J.* 13 (02): 61-68.

Daneshy, A.A. 1978. Hydraulic Fracture Propagation in Layered Formations. *SPE J.* 18 (01) 33-41.

Darcy, H. 1856. Les Fontaines Publiques De La Ville De Dijon. Paris. Dalmont.

Darin, S.R., and Huitt, J.L. 1960. Effect of a Partial Monolayer of Propping Agent on Fracture Flow Capacity. *Trans. AIME*. 219 (3): 31-37.

Dinh, A.V., and Tiab, D. 2009. Transient-Pressure Analysis of a Well with an Inclined Hydraulic Fracture Using Tiab's Direct Synthesis Technique. Paper SPE 120545 presented at SPE Production and Operations Symposium, Oklahoma City, Oklahoma, 4-8 April.

Dinh, A.V., and Tiab, D. 2010. Transient-Pressure Analysis of a Well with an Inclined Hydraulic Fracture Using Type Curve Matching. *SPE Res. Eval. Eng.* 13 (06): 845-860.

Durlofsky, L., and Brady, J.F. 1987. Analysis of the Brinkman Equation as a Model for Flow in Porous Media. *Phys. Fluids* 30 (11): 3329-3341.

Elbel, J.L., and Mack, M.G. 1993. Refracturing: Observations and Theories. Paper SPE 25464 presented at SPE Production Operations Symposium, Oklahoma City, Oklahoma, 21-23 March.

Ertekin, T., Abou-Kassem, J.H., and King, G.R. 2001. *Basic Applied Reservoir Simulation*. SPE Textbook Series.

Escobar, F.H., and Montealegre, M. 2007. Conventional Analysis for the Determination of the Horizontal Permeability from the Elliptical Flow of Horizontal Wells. Paper SPE 105928 presented at Production and Operations Symposium, Oklahoma City, Oklahoma, U.S.A., 31 March-3 April.

Fredd, C.N., McConnell, S.B., Boney, C.L., and England, K.W. 2001. Experimental Study of Fracture Conductivity for Water-Fracturing and Conventional Fracturing Applications. *SPE J.* 6 (3): 288-298.

Gala, D.P., and Sharma, M.M. 2017. Effect of Fluid Type and Composition on Changes in Reservoir Stresses Due to Production: Implications for Refracturing. Paper ARMA-2017-0042 presented at 51st U.S. Rock Mechanics/Geomechanics Symposium, San Francisco, California, USA, 25-28 June.

Glover, P.W., Zadjali, I.I., and Frew, K.A. 2006. Permeability Prediction from MICP and NMR Data Using an Electro-Kinetic Approach. *Geophysics* 71(4): 49-60.

Gringarten, A.C., and Ramey, H.J. 1973. The Use of Source and Green's Functions in Solving Unsteady-Flow Problems in Reservoirs. *SPE J.* 13 (05): 285-296.

Gringarten, A.C., and Ramey, H.J. 1974. Unsteady-State Pressure Distributions Created by a Well with a Single Infinite-Conductivity Vertical Fracture. *SPE J.* 14 (04): 347-360.

Gringarten, A.C., and Ramey, H.J. 1974. Unsteady-State Pressure Distributions Created by a Well with a Single Horizontal Fracture, Partial Penetration, or Restricted Entry. *SPE J.* 14 (04): 413-426.

Gu, H., and Leung, K.H. 1993. 3D Numerical Simulation of Hydraulic Fracture Closure with Application to Minifracture Analysis. *J. Pet. Tech.* 45 (3): 206-255.

Habte, A.D., Dinh, A.V., and Tiab, D. 2010. Pressure Analysis of a Well with an Inclined Asymmetric Hydraulic Fracture Using Type Curves. Paper SPE 140638 presented at Nigeria Annual International Conference and Exhibition, Tinapa - Calabar, Nigeria31 July - 7 August.

Hubbert, M.K., and Willis, D.G. 1957. Mechanics of Hydraulic Fracturing. *Trans. AIME* 210: 153-168.

Issaka, M.B., Zaoral, K., Ambastha, A.K., and Mattar, L., 2000. Determination of Horizontal Permeability Anisotropy from Horizontal Well Test. Paper presented at SPE Saudi Arabia Section Technical Symposium, Dhahran, Saudi Arabia, 21-23 October.

Jeffrey, R.G., Bunger, A. LeCampion, B., Zhang, X., Chen, Z., van As, A., Allision, D.P., Beer. W.D., Dudley, J.W., Siebrits, E., Thiercelin, M.J., and Mainguy, M. 2009. Measuring Hydraulic Fracture Growth in Naturally Fractured Rock. Paper SPE 124919 presented at SPE Annual Technical Conference and Exhibition, New Orleans, Louisiana, 4-7 October.

Jia, P., Cheng, L., Huang, S., Liu, H. 2016. Pressure-Transient Analysis of a Finite-Conductivity Inclined Fracture Connected to a Slanted Wellbore. *SPE J.* 21 (02): 522-537.

Jiang, W., Cai, B., Li, Y., He, C., Yan, X., and Xu, Z. 2016. Optimum Time and Critical Re-Orientation Pressure of Re-Fracturing. Paper SPE 181837 presented at SPE Asia Pacific Hydraulic Fracturing Conference, Beijing, China, 24-26 August.

Johnson, R.L., Scott, M.P., Jeffrey, R.G., Chen, Z., Bennett, L., Vandenborn, C.B., and Tcherkashnev, S. 2010. Evaluating Hydraulic Fracture Effectiveness in a Coal Seam Gas Reservoir from Surface Tiltmeter and Microseismic Monitoring. Paper SPE 133063

presented at SPE Annual Technical Conference and Exhibition, Florence, Italy, 19-22 September.

Krumbein, W.C. and Monk, G.D. 1943. Permeability as a Function of Size parameters of Unconsolidated Sand. *Trans. AIME* 151 (1): 153-163.

Kucuk, F., and Brigham, W.E. 1979. Transient Flow in Elliptical Systems. *SPE J.* 19 (06): 401-410.

Lacy, L.L., Rickards, A.R., and Bilden, D.M. 1998. Fracture Width and Embedment Testing in Soft Reservoir Sandstone. *SPE J.* 13 (1): 25-29.

Lantz, T.G., Greene, D., Eberhard, M., Norrid, S., and Pershall, R. 2007. Refracture Treatments Proving Successful In Horizontal Bakken Wells: Richland Count, Montana. Paper SPE 108117 presented at Rocky Mountain Oil & Gas Technology Symposium, Denver, Colorado, U.S.A., 16-18 April.

Larsen, L. 2011. Horizontal Fractures in Single and Multilayer Reservoirs. Paper SPE 147004 presented at Canadian Unconventional Resources Conference, Calgary, Alberta, 15-17 November.

Larsen, L., and Hegre, T.M. 1994. Pressure Transient Analysis of Multifractured Horizontal Wells. Paper SPE 28389 presented at SPE Annual Technical Conference and Exhibition, New Orleans, Louisiana, 25-28 September.

Li, K., Gao, Y., Lyu, Y., and Wang, M. 2015. New Mathematical Models for Calculating Proppant Embedment and Fracture Conductivity. *SPE J.* 20 (3): 496-507.

Liu, H., Lan, Z., Zhang, G., Hou, F., He, X., and Liu, X. 2008. Evaluation of Refracture Reorientation in Both Laboratory and Field Scales. Paper SPE 112445 presented at SPE International Symposium and Exhibition on Formation Damage Control, Lafayette, Louisiana, USA, 13-15 February.

Luo, W., and Tang, C. 2015. Pressure-Transient Analysis of Multiwing Fractures Connected to a Vertical Wellbore. *SPE J.* 20 (02): 360-367.

Mack, D.J. 2000. Effects of Proppant Pack Concentration and Polymer Residue on Appalachian Stimulations. Paper SPE 65626 presented at SPE Eastern Regional Meeting, Morgantown, West Virginia, 17-19 October.

Medeiros, F., Kurtoglu, B., Ozkan, E., and Kazemi, H. 2010. Analysis of Production Data from Hydraulically Fractured Horizontal Wells in Shale Reservoirs. *SPE Res. Eval. Eng.* 13 (03): 559-568.

Medeiros, F., Ozkan, E., and Kazemi, H. 2008. Productivity and Drainage Area of Fractured Horizontal Wells in Tight Gas Reservoirs. *SPE Res. Eval. Eng.* 11 (05): 902-911.

Medlin, W.L., and Masse, L. 1984. Laboratory Experiments in Fracture Propagation. *SPE J.* 24 (03): 256-268.

Minner, W.A., Wright, C.A., Stanly, G.R., de Pater, C.J., Gorham, T.L., Eckerfield, L.D., and Hejl, K.A. 2002. Waterflood and Production-Induced Stress Changes Dramatically Affect Hydraulic Fracture Behavior in Lost Hills Infill Wells. Paper SPE 77536 presented at SPE Annual Technical Conference and Exhibition, San Antonio, Texas, 29 September-2 October.

Morita, N., Whitfill, D.L., and Wahl, H.A. 1988. Stress-Intensity Factor and Fracture Cross-Sectional Shape Predictions from a Three-Dimensional Model for Hydraulically Induced Fractures. *J. Pet. Tech.* 40 (10): 1329-1342.

Mukuhira, Y., Ito, T., Asanuma, H., and Haring, M. 2016. Stress State Analysis of a Fault Plane with Large Induced Seismicity. Paper ARMA-2016-360 presented at 50th U.S. Rock Mechanics/Geomechanics Symposium, Houston, Texas, 26-29 June.

Nguyen, P.D., Dewprashad, B.T., and Weaver, J.D. 2000. New Approach for Enhancing Fracture Conductivity. *SPE Prod. Faci*. 15 (2): 83-89.

Nicholl, M.J., and Glass, R.J. 2001. Simulation of Immiscible Viscous Displacement within the Plane of a Horizontal Fracture. Paper ARMA-01-0205 presented at the 38th U.S. Symposium on Rock Mechanics (USRMS), Washington, D.C., 7-10 July.

Ogunsanya, B.O., Oetama, T.P., Lea, J.F., Heinze, L.R., and Adisoemarta, P.S. 2006. A Robust Type Curve Solution for Analyzing Pressure-Transient Behaviors of both Vertical and Horizontal Fracture Systems. Paper SPE 105979 presented at Nigeria Annual International Conference and Exhibition, Abuja, Nigeria, 31 July-2 August.

Ozkan, E., and Raghavan, R. 1991. New Solutions for Well-Test-Analysis Problems: Part 1-Analytical Considerations. *SPE Form. Eval.* 6 (03): 359-368.

Ozkan, E., Brown, M.L., Raghavan, R., and Kazemi, H. 2011. Comparison of Fractured-Horizontal-Well Performance in Tight Sand and Shale Reservoirs. *SPE Res. Eval. Eng*. 14 (02): 248-259.

Palmer, I.D. 1993. Induced Stresses Due to Propped Hydraulic Fracture in Coalbed Methane Wells. Paper SPE 25861 presented at Low Permeability Reservoirs Symposium, Denver, Colorado, 26-28 April.

Pandey, V.J., and Agreda, A.J. 2014. New Fracture-Stimulation Designs and Completion Techniques Result in Better Performance of Shallow Chittim Ranch Wells. *SPE Prod. Oper*. 29 (04): 288-309.

Parvazinia, M., Nassehi, V., Wakeman, R.J., and Ghoreishy M.H.R. 2006. Finite Element Modelling of Flow through a Porous Medium between Two Parallel Plates Using the Brinkman Equation. *Transp. Porous Med*. 63 (1): 71-90.

Peaceman, D.W. 1990. Interpretation of Wellblock Pressures in Numerical Reservoir Simulation with Nonsquare Grid Blocks and Anisotropic Permeability. *SPE J.* 23 (03): 531-543.

Peaceman, D.W. 1990. Interpretation of Wellblock Pressures in Numerical Reservoir Simulation: Part 3 - Off-Center and Multiple Wells within a Wellblock. *SPE Res. Eng.* 5 (02): 227-232.

Pope, D.S., Leung, L.K.-W., Gulbis, J., and Constien, V.G. 1996. Effects of Viscous Fingering on Fracture Conductivity. *SPE Prod. Faci*. 11 (4): 230-237.

Potapenko, D.I., Tinkham, S.K., Lecerf, B., Fredd, C.N., Samuelson, M.L., Gillard, M.R., Le Calvez, J.H., and Daniels, J.L. 2009. Barnett Shale Refracture Stimulations Using a Novel Diversion Technique. Paper SPE 119636 presented at SPE Hydraulic Fracturing Technology Conference, The Woodlands, Texas, 19-21 January.

Rbeawi, S.AI, and Tiab, D. 2012a. Transient Pressure Analysis of a Horizontal Well with Multiple Inclined Hydraulic Fractures Using Type-Curve Matching. Paper SPE 149902 presented at SPE International Symposium and Exhibition on Formation Damage Control, Lafayette, Louisiana, USA, 15-17 February.

Rbeawi, S.AI, and Tiab, D. 2012b. Effect of Penetrating Ratio on Pressure Behavior of Horizontal Wells with Multiple-Inclined Hydraulic Fractures. Paper SPE 153788 presented at SPE Western Regional Meeting, Bakersfield, California, USA, 21-23 March.

Rbeawi, S.AI, and Tiab, D. 2013. Partially Penetrating Hydraulic Fractures: Pressure Responses and Flow Dynamics. Paper SPE 164500 presented at SPE Production and Operations Symposium, Oklahoma City, Oklahoma, USA, 23-26 March.

Restrepo, D.P., and Tiab, D. 2009. Multiple Fractures Transient Response. Paper SPE 121594 presented at Latin American and Caribbean Petroleum Engineering Conference, Cartagena de Indias, Colombia, 31 May-3 June.

Reynolds, A.C., Chen, J.C., and Raghavan, R. 1984. Pseudoskin Factor Caused by Partial Penetration. *J. Pet. Tech.* 36 (12): 2197-2210.

Rodriguez, F., Horne, R.N., and Cinco-Ley, H. 1984. Partially Penetrating Fractures: Pressure Transient Analysis of an Infinite Conductivity Fracture. Paper SPE 12743 presented at SPE California Regional Meeting, Long Beach, California, 11-13 April.

Roussel, N.P., and Sharma, M.M. 2010. Quantifying Transient Effects in Altered-Stress Refracturing of Vertical Wells. *SPE J.* 15 (3): 770-782.

Roussel, N.P., and Sharma, M.M. 2012. Role of Stress Reorientation in the Success of Refracture Treatments in Tight Gas Sands. *SPE Prod. Oper.* 27 (4): 346-355.

Roussel, N.P., and Sharma, M.M. 2013. Selecting Candidate Wells for Refracturing Using Production Data. *SPE Prod. Oper.* 28 (1): 36-45.

Ruhle, W. 2016. Refracturing: Empirical Results in the Bakken Formation. Paper URTEC 2461740 presented at Unconventional Resources Technology Conference, San Antonio, Texas, USA, 1-3 August.

Siebrits, E., Elbel, J.L., Detournay, E., Detouray-Piette, C., Christianson, M., Robinson, B.M., and Diyashev, I.R. 1998. Parameters Affecting Azimuth and Length of a Secondary Fracture During a Refracture Treatment. Paper SPE 48928 presented at SPE Annual Technical Conference and Exhibition, New Orleans, Louisiana, 27-30 September.

Siebrits, E., Elbel, J.L., Hoover, R.S., Diyashev, I.R., Griffin, L.G., Demntrius, S.L., Wright, C.A., Davidson, B.M., Steinsberger, N.P., and Hill, D.G. 2000. Refracture Reorientation Enhances Gas Production in Barnett Shale Tight Gas Wells. Paper SPE 63030 presented at SPE Annual Technical Conference and Exhibition, Dallas, Texas, 1-4 October.

Singh, K., and Whitson, C.H. 2010. Gas-Condensate Pseudopressure in Layered Reservoirs. *SPE Res. Eval. Eng*. 13 (02): 203-213.

Smith, M.B., and Montgomery, C. 2015. *Hydraulic Fracturing.* CRC Press.

Spivey, J.P. and Lee, W.J. 1998. New Solutions for Pressure Transient Response for a Horizontal or a Hydraulically Fractured Well at an Arbitrary Orientation in an Anisotropic Reservoir. Paper SPE 49236 presented at SPE Annual Technical Conference and Exhibition, New Orleans, Louisiana, 27-30 September.

Sutera, S.P., and Skalak, R. 1993. The History of Poiseuille's Law. *Ann. Rev. Fluid Mech.* 25: 1-19.

Swaby, P.A., and Rawnsley, K.D. 1997. An Interactive 3D Fracture-Modeling Environment. *SPE J.* 9 (3): 82-87.

Teng, B., and Li, H. 2018. A Semi-Analytical Model for Characterizing the Pressure Transient Behavior of Finite-Conductivity Horizontal Fractures. *Transp. Porous Med*. 123 (05): 1-36.

Teng, B., and Li, H. 2019. A Novel Analytical Fracture Permeability Model Dependent on Both Fracture Width and Proppant-Pack Properties. Submitted to *SPE J* for peer review.

Teng, B., and Li, H. 2019. A Semi-Analytical Model for Characterizing Transient Flow Behavior of Reoriented Refractures. *J. Pet. Sci. Eng.*177: 921-940.

Teng, B., and Li, H. 2019. A Semianalytical Model for Evaluating the Performance of a Refractured Vertical Well With an Orthogonal Refracture. *SPE J.* 24 (02): 891-911.

Teng, B., and Li, H. 2019. Pressure-Transient Behavior of Partially Penetrating Inclined Fractures with a Finite Conductivity. *SPE J.* 24 (2): 811-833.

Tran, T., Sinurat, P.D., and Wattenbarger, B.A. 2011. Production Characteristics of the Bakken Shale Oil. Paper SPE 145684 presented at SPE Annual Technical Conference and Exhibition, Denver, Colorado, USA, 30 October-2 November.

Tripathi, D., and Pournik, M. 2014. Effect of Acid on Productivity of Fractured Shale Reservoirs. Paper URTEC-1922960 presented at Unconventional Resources Technology Conference, Denver, Colorado, USA, 25-27 August.

Valko, P., and Economides, M.J. 1997. Transient Behavior of Finite Conductivity Horizontal Fractures. *SPE J.* 2 (02): 213-222.

Valko, P.P., and Amini, S. 2007. The Method of Distributed Volumetric Sources for Calculating the Transient and Pseudosteady-State Productivity of Complex Well-Fracture Configurations. Paper 106276 presented at SPE Hydraulic Fracturing Technology Conference, College Station, Texas, 29-31 January.

van Baaren, J.P. 1979. Quick-Look Permeability Estimates Using Sidewall Samples and Porosity Logs. Transaction of the 6th Annual European Logging Symposium, Society of Professional Well Log Analysts.

van Everdingen, A.F., and Hurst, W. 1949. The Application of the Laplace Transformation to Flow Problems in Reservoirs. *Trans. AIME* 1 (12): 305-324.

Wahl, H.A. 1965. Horizontal Fracture Design Based on Propped Fracture Area. *SPE J.* 17 (6): 723-730.

Wahl, H.A., and Campbell, J.M. 1963. Sand Movement in Horizontal Fractures. *SPE J.* 15 (11): 1239-1246.

Warpinski, N.R., and Branagan, P.T. 1989. Altered-Stress Fracturing. *J. Pet. Tech.* 41 (9): 990-997.

Warren, J.E., and Root, P.J. 1963. The Behavior of Naturally Fractured Reservoirs. *SPE J.* 3 (03): 245-255.

Watts, R.J., Yost, A.B., Farrell, H.H., Kennedy, J., Lowry, P. 1988. Devonian Shale Oil Production Analysis and Evaluation. Paper SPE 18552 presented at SPE Eastern Regional Meeting, Charleston, West Virginia, 1-4 November.

Weaver, J.D., Rickman, R.D., and Luo, H. 2010. Fracture-Conductivity Loss Caused by Geochemical Interactions between Man-Made Proppants and Formations. *SPE J.* 15 (01):116-124.

Weng, X., and Siebrits, E. 2007. Effect of Production-Induced Stress Field on Refracture Propagation and Pressure Response. Paper SPE 106043 presented at SPE Hydraulic Fracturing Technology Conference, College Station, Texas, U.S.A., 29-31 January.

Wolhart, S.L., and Mclntosh, G.E., Zoll, M.B., and Weijers, L. 2007. Surface Tiltmeter Mapping Shows Hydraulic Fracture Reorientation in the Codell Formation, Wattenberg Field, Colorado. Paper SPE 110034 presented at SPE Annual Technical Conference and Exhibition, Anaheim, California, U.S.A., 11-14 November.

Wolhart, S.L., Mclntosh, G.E., Zoll, M.B., and Weijers, L. 2007. Surface Tiltmeter Mapping Shows Hydraulic Fracture Reorientation in the Codell Formation, Wattenberg Field, Colorado. Paper SPE 106043 presented at SPE Hydraulic Fracturing Technology Conference, College Station, Texas, U.S.A., 29-31 January.

Wright, C.A. 1994. Reorientation of Propped Refracture Treatments in the Lost Hills Field. Paper SPE 27896 presented at SPE Western Regional Meeting, Long Beach, California, 23-25 March.

Wright, C.A., and Conant, R.A. 1995. Hydraulic Fracture Reorientation in Primary and Secondary Recovery from Low-Permeability Reservoirs. Paper SPE 30484 presented at SPE Annual Technical Conference and Exhibition, Dallas, Texas, 22-25 October.

Wright, C.A., Conant, R.A., Stewart, D.W., and Byerly, P.M. 1994. Reorientation of Propped Refracture Treatments. Paper SPE 28078 presented at Rock Mechanics in Petroleum Engineering, Delft, Netherlands, 29-31 August.

Wright, C.A., Davis, E.J., Golich G.M., Ward, J.F., Demetrius, S.L., Minner, W.A., and Weijers, L. 1998. Downhole Tiltmeter Fracture Mapping: Finally Measuring Hydraulic Fracture Dimensions. Paper SPE 46194 presented at SPE Western Regional Meeting, Bakersfield, California, 10-13 May.

Wright, C.A., Davis, E.J., Weijers, L., Minner, W.A., Hennigan, C.M., and Golich, G.M. 1997. Horizontal Hydraulic Fractures: Oddball Occurrences or Practical Engineering Concern? Paper 38324 presented at SPE Western Regional Meeting, Long Beach, California, 25-27 June.

Wright, C.A., Stewart, D.W., Emanuele, M.A., and Wright, W.W. 1994. Reorientation of Propped Refracture Treatments in the Lost Hills Field. Paper SPE 27896 presented at SPE Western Regional Meeting, Long Beach, California, 23-25 March.

Xia, K., Mondal. S., Fonseca, E., and Jones, R. 2017. Understanding Stress Reorientation Process in Shale Gas Play and Its Impact on Refracturing Time Window. Paper ARMA-2017-1012 presented at 51st U.S. Rock Mechanics/Geomechanics Symposium, San Francisco, California, USA, 25-28 June.

Xu, Y., Yu, W., and Sepehrnoori, K. 2017. Modeling Dynamic Behaviors of Complex Fractures in Conventional Reservoir Simulators. Paper URTEC-2670513 presented at SPE/AAPG/SEG Unconventional Resources Technology Conference, Austin, Texas, USA, 24-26 July.

Yang, D., Zhang, F., Styles, J.A., and Gao, J. 2015. Performance Evaluation of a Horizontal Well With Multiple Fractures by Use of a Slab-Source Function. *SPE J.* 20 (03): 652-662.

Yu, W., Wu, K., and Sepehrnoori, K. 2016. A Semianalytical Model for Production Simulation from Nonplanar Hydraulic-Fracture Geometry in Tight Oil Reservoirs. *SPE J.* 21 (03): 1028-1040.

Zhang, J., Kamenov, A., Hill, A.D., and Zhu, D. 2013. Laboratory Measurement of Hydraulic Fracture Conductivities in the Barnett Shale. *SPE Prod. Oper.* 29 (03): 216-227.

Zhang, J., Zhu, D., and Hill, A.D. 2016. Water-Induced Damage to Propped-Fracture Conductivity in Shale Formations. *SPE Prod. Oper.* 31 (2): 147-156.

Zhao, B., Zhang, G., and Lin, Q. 2016. The Application of Cryogenic Treatment during Refracture Process - Laboratory Studies. Paper ARMA-2016-552 presented at 50th U.S. Rock Mechanics/Geomechanics Symposium, Houston, Texas, 26-29 June.

Zhou, W., Banerjee, R., Poe, B.D., and Spath, J. 2014. Semianalytical Production Simulation of Complex Hydraulic-Fracture-Networks. *SPE J.* 19 (01): 6-18.